Order Number 9325162

Hot carrier dynamics in the satellite X valley and intervalley scattering in GaAs and AlGaAs

Wang, Wubao, Ph.D.

City University of New York, 1993

U·M·I
300 N. Zeeb Rd.
Ann Arbor, MI 48106

HOT CARRIER DYNAMICS IN THE SATELLITE X VALLEY AND INTERVALLEY SCATTERING IN GaAs and AlGaAs

by

WUBAO WANG

A dissertation submitted to the Graduate faculty in Physics in partial fulfillment of the requirements for the degree of Doctor of Philosophy, the City University of New York

---1993---

This manuscript has been read and accepted for the Graduate Faculty in Physics in satisfaction of the dissertation requirement for the degree of Doctor of Philosophy.

4/30/93
Date

Robert R. Alfano
Chair of Examining Committee
Professor R. R. Alfano

5/3/93
Date

Joseph B. Krieger
Executive Officer
Professor J. B. Krieger

Professor J. L. Birman

Professor J. Gersten

Professor K. Shum

Dr. N. Ockman

Professor S. K. Gayen

Supervisory Committee

The City University of New York

ABSTRACT

HOT CARRIER DYNAMICS IN THE SATELLITE X VALLEY AND INTERVALLEY SCATTERING IN GaAs and AlGaAs

by

WUBAO WANG

Adviser: Professor Robert R. Alfano

A femtosecond infrared (IR) pulse was generated in a $LiIO_3$ crystal by the method of seeded parametric amplification using a synchronously pumped dye laser with a pulse-dye-amplifier system. The time evolutions of the population of hot electrons in a $k \neq 0$ satellite valley, namely the X valley in GaAs and AlGaAs have been directly measured for the first time by a time-resolved visible-pump IR-probe absorption spectroscopy. The physics behind the measured temporal behavior of the hot carrier relaxation and the measured spectral characteristics corresponding to the hot carrier distribution among valleys have been studied.

The intervalley scattering back to the central Γ valley from the satellite valleys in GaAs and AlGaAs was found to play a dominant role in hot carrier relaxation because it acts as a source of heating of electrons in the Γ valley. This enables us to determine some intervalley scattering rates in

GaAs and AlGaAs from the measured carrier dynamics as described in this thesis. A temporal profile of measured total IR absorption was also found to be a function of the band structures and the IR absorption mechanisms. Some important band gap structure parameters for GaAs and AlGaAs could be determined from the measured temporal and spectral profile of the IR absorption as shown in this thesis.

The time-resolved IR absorption subsequent to the excitation at 527 nm in GaAs was measured and used to obtain the dynamics of hot electrons in the X valley. The rate equation analysis involving the intra-and-intervalley scattering are used to determine the $X_6 \rightarrow \Gamma_6$ intervalley scattering time of ~ 500 fs.

The transient $X_6 \rightarrow X_7$ band-to-band IR absorption spectrum in GaAs was measured by varying IR probe wavelength, from which the energy gap between the minima of the X_6 and X_7 bands has been directly determined to be 0.345 ± 0.017 eV, and the density of states effective mass for the X_7 band has been found to be 0.48 ± 0.06 m_0.

The temperature dependence of hot electron relaxation in GaAs has been observed in a temperature range of 4K to 300K. The much longer relaxation time of hot electrons at low temperature comparing with that at room temperature is attributed to the reduction of the number of phonons participating in the electron-phonon interaction and the decrease of the intra-and-intervalley scattering rates, in particular, the $L \rightarrow \Gamma$ scattering time.

The time evolution of the population of hot electrons in the bottom of the X valley in an indirect band gap semiconductor of $Al_{0.6}Ga_{0.4}As$ was monitored by a femtosecond IR probe pulse. The $L_6 \rightarrow X_6$ intervalley scattering time of ~ 200 fs has been determined by a rate equation analysis involving only the X and L valleys. Both phonon-assisted and alloy-disorder-induced intervalley scattering were considered and the L_6–X_6 intervally deformation potential of ~ 2.7×10^8 eV/cm has been determined.

The temporal profiles of the IR absorption for $Al_xGa_{1-x}As$ samples with different value of x were measured. The dynamics of the X valley electrons for samples with $x \leq 0.408$ was found to be completely different from that for samples with $x \geq 0.439$ which reflects their different type of band gaps. The critical value of x_c which corresponds to direct-to-indirect band gap transition for $Al_xGa_{1-x}As$ was determined to be 0.412 ± 0.009.

DEDICATION

This thesis is dedicated to
my parents, Dengfang Hu and Chengshun Wang,
my wife, Dalian Zhang, and
my daughters, Jing Wang and Shan Wang

ACKNOWLEDGEMENTS

I received a lot of encouragement, support, and help from many people during my thesis work. Now, I would like to deeply acknowledge and thank them.

My advisor, Professor Robert R. Alfano, has been not only an outstanding teacher and a capable director of our large institute, but also a distinguished scientist with a capability to search out new frontier research area. I would like to express my special thanks to him for his help in suggesting and defining the $k \neq 0$ transient dynamics as the heart of my thesis project, and for his patient guidance, and financial support during this thesis work.

I wish to thank Dr. N. Ockman and Professor S. K. Gayen for their help and useful discussions which opened many physical questions that helped me increase my understanding of carrier dynamics in semiconductors and solid state laser materials. I would like to acknowledge Dr. L. Rothberg of AT & T for his help for generating femtosecond IR pulses and Dr. A. J. Nozik of National Solar Energy Institute for suppling a series of AlGaAs samples with very high quality. I would like also to acknowledge Professors J. L. Birman, J. Gerstein, and K. Shum for serving on my graduate committee and helpful discussions.

It is with pleasure that I also thank all colleagues in the Institute of Ultrafast Spectroscopy and Lasers in City College of New York for their

cooperation, kindness, friendship, and help.

I would like to thank the Army Research Office and the CUNY Organized Research Office for their financial support for my thesis work.

My biggest debt of gratitude is to my family. I would like to express my sincere thanks to my mother and father, Dengfang Hu and Chengshun Wang, who have encouraged and supported my each step of the education for their entire life. I wish to give my special thanks to my dear wife, Dalian, who has continuously made tremendous sacrifices to support me to complete the thesis work. I also wish to thank my two lovely daughters, Jing and Shan, for their understanding and considerations which enabled me to pay my most attention to the thesis research. Without my family's encouragement, support, understanding and consideration, I would not have been able to finish this thesis work.

TABLE OF CONTENTS

LIST OF TABLES

LIST OF FIGURES

Chapter 1
INTRODUCTION

1.1. Background

Intervalley scattering of electrons between various valleys of the conduction bands in a semiconductor plays an important role in the initial relaxation of hot carriers, and in the determination of high-field transport properties of semiconductors. These intervalley scattering processes govern the physics of many high-speed devices.[1] As devices achieve submicron scales, carrier transit times decrease significantly and hot carrier phenomena can dominate device operations, and consequently, the fundamental carrier scattering processes in semiconductors will pose an ultimate limitation to device performance.[2] Studies of ultrafast carrier dynamics in semiconductors are of importance not only for an understanding of the basic physics of carrier scattering processes in semiconductors, but also for the development of high speed electronic and optoelectronic devices. GaAs and its alloys are the heart of these fast devices.

The energy band structure of GaAs is shown in Fig. 1.1.1.[3] The effective mass of electrons in the central conduction Γ valley is much smaller than that in the satellite L and X conduction valleys. When electrons scatter from the Γ valley of high mobility to the L and X valleys of lower mobility along the (111) or (100) directions, respectively, a large negative differential resistance will be exhibited. This gives rise to phenomena

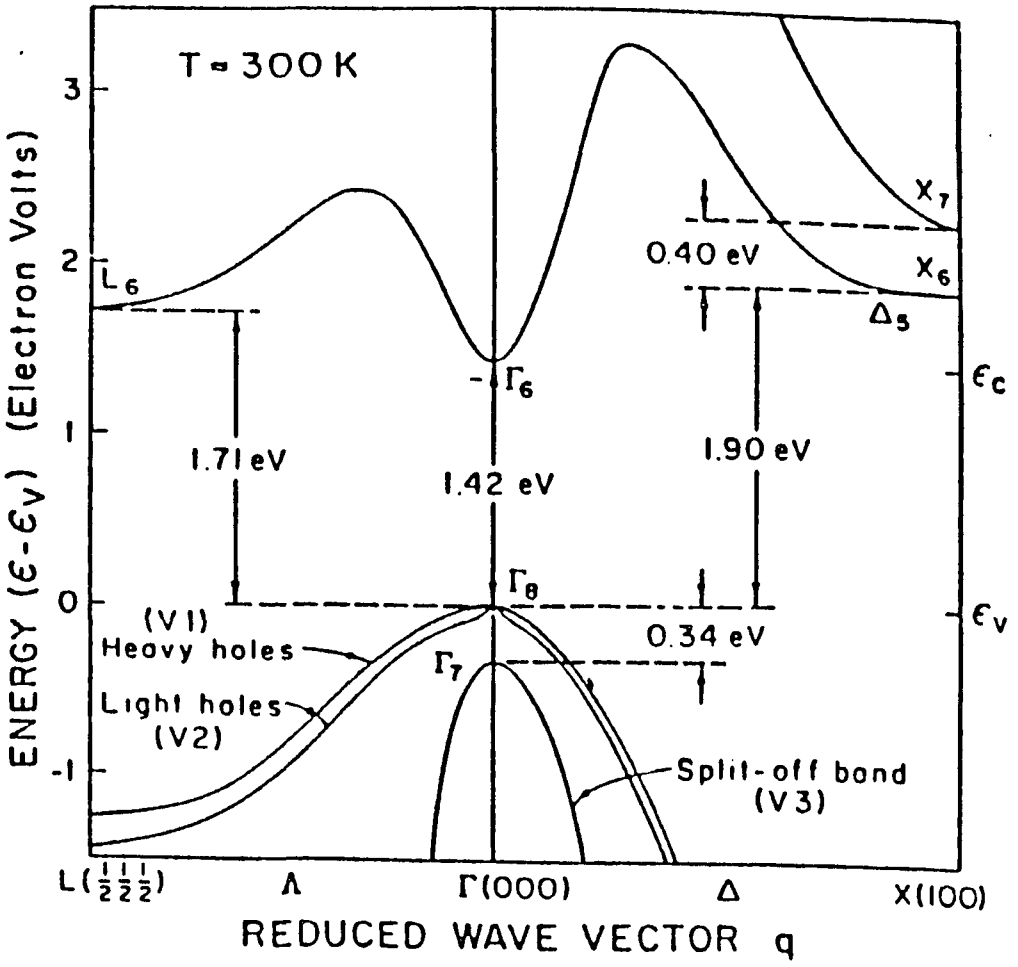

Fig. 1.1.1 Energy band structure for GaAs at room temperature and ordinary pressure [3]

like the Gunn effect.[4] Similar behavior appears in $Al_xGa_{1-x}As$ with small values of x because their band structures are similar to that of GaAs.[5] These characteristics of high field conductivity makes GaAs and $Al_xGa_{1-x}As$ more important than other materials for making photonic devices (lasers, light-emitting diodes, and photovoltaic converters) as well as for high speed electronic devices (high electron mobility transistors and resonant tunneling diodes). Furthermore, the variation of band gaps, effective masses of conduction band electrons, and deformation potentials in $Al_xGa_{1-x}As$ with x enables us to obtain desired band structures for studying expected scattering processes in different bulk and quantum well systems, and to design appropiate electronic or optoelectronic devices.

Because of this importance, investigation of hot carrier dynamics and intervalley scattering processes in GaAs and $Al_xGa_{1-x}As$ has been of significant interest in the very active field of hot-electron physics and high-speed, high-field device design in recent years. A number of theoretical and experimental groups[1-2,6-13] have investigated hot carrier dynamics and intervalley scattering times in GaAs and $Al_xGa_{1-x}As$. Conwell[6] has modeled the scattering mechanisms and calculated the intra- and intervalley scattering rates in GaAs by solving the Boltzmann equation. Zollner in Cardona's group[7] has calculated the intervalley deformation potentials and intervalley scattering times in GaAs, AlAs and other zinc blende semiconductors. Kann in Ferry's group[8] has considered the effect of electron-electron interaction on the intervalley transition rates and

calculated the carrier density dependence of intervalley scattering rates. Shah [1] has experimentally determined the Γ→L and L→Γ scattering rates in GaAs at room temperature by measuring up-conversion subpicosecond luminescence spectra and fitting his data using Monte Carlo calculations. Becker [9] has determined the Γ→X scattering time in GaAs at room temperature by degenerate pump-probe absorption spectroscopy. Ulbrich [10] and Mirlin [11] have measured recombination luminescence between non-equilibrium electrons and neutral acceptors in GaAs, and determined the Γ→L and Γ→X intervalley scattering times at low temperature. Katz and Alfano [12] have measured the population grating in GaAs using four wave mixing and determined the L→Γ back scattering time. Lin et al [2] have measured the dynamics of highly excited carriers in several $Al_xGa_{1-x}As$ samples by the pump-visible-probe transient absorption method. Wise [13] has measured the lifetime of hot electrons in the Γ valley for $Al_xGa_{1-x}As$.

However, all of the previously mentioned experimental methods only measured the time evolution of electrons in the central k=0 valley---Γ valley. [14] The hot electron dynamics in the X valley and the intervalley scattering times of $t_{X\to\Gamma}$, $t_{X\to L}$, and $t_{L\to X}$, which are important in high-field transport [15] and for the relaxation of hot electrons [2,9-11], have not been obtained in the previous experimental determinations as shown in Table 1.1.1. Therefore, direct measurements of the time evolution of the population of electrons in a $k\neq 0$ satellite valley in GaAs and $Al_xGa_{1-x}As$, and the determination of the X-valley-involved intervalley scattering rates

Table 1.1.1. The list of the previously measured intervalley scattering times and missed items for GaAs

---

$N_\Gamma(t)$ has been measured [1,9,10,12]

$N_X(t)$?

$t_{\Gamma L}=100fs$ [1]

$t_{L\Gamma}=2.5ps$ [1,9]

$t_{\Gamma X}=55fs$ [6]

$t_{X\Gamma}=?$

$t_{XL}=?$

$t_{LX}=?$

---

had become an urgent research problem in the field of hot carrier physics, and consequently was chosen to be a topic for this thesis.

Since the X valley plays an important role in high-field transport in GaAs, [15] the exploration of the properties of the X_6 and X_7 bands schematically shown in Fig.1.1.1 has attracted general interest in semiconductor physics. Over the past 20 years, there has been a number of investigations [3,16–18] to estimate the density of states effective mass for the X_6 band. However, no such measurements have been performed for the X_7 band before this thesis work. Furthermore, all of the determination of the energy separation, Δ_{7-6}, between the X_6 and X_7 bands at their minima from the previous steady-state absorption measurements [19–22] were indirect, and the obtained values varied in a large range from 0.35 eV to 0.58 eV. Therefore, the direct measurement of the $X_6 \rightarrow X_7$ absorption spectrum and the determination of Δ_{7-6} and the density of states effective mass of the X_7 band by measuring time-resolved IR absorption had been chosen to be the second topic for this thesis work.

Although the relationship of intervalley scattering times and crystal temperature has been theoretically studied, [6,7] there have been no previous measurements to systematically investigate the temperature dependence of intervalley scattering times. [14] Therefore, temperature dependence of hot electron relaxation in GaAs had been chosen to be another topic for this thesis.

The band structure of $Al_xGa_{1-x}As$ varies with x.[5] The design of $Al_xGa_{1-x}As$ devices relies on the x-dependence of its band structure, in particular on the critical value x_c which corresponds to the direct-to-indirect band gap transition as shown in Fig.1.1.2.[23] However, the values of x_c determined from recent fluorescence and other measurements[23,24-27] span the large range of 0.37-0.45. One could not design and construct high quality $Al_xGa_{1-x}As$ devices with such an uncertainty in x_c. Therefore, the precise determination of x_c remains very important for semiconductor physics and device design. Since the probability for indirect transitions is several orders of magnitude smaller than that for direct transitions, the intensity of fluorescence from the satellite valley is much weaker than that from the central valley. Consequently, it is difficult to monitor small changes of the electron distribution among different valleys with x, and to accurately determine x_c by measuring fluorescence from $Al_xGa_{1-x}As$.[28] The better way for determining the accurate value of x_c is to measure the time-resolved IR absorption in the X valley in $Al_xGa_{1-x}As$ because the temporal profile of the electron decay in the X valley in $Al_xGa_{1-x}As$ varies with x, and the measured change of the decay profile of the $X_6 \rightarrow X_7$ IR absorption is very sensitive to the band structure, especially when x approaches x_c. This thesis work has used this better technique---the pump-IR-probe absorption measurement to determine the critical value of x_c for $Al_xGa_{1-x}As$.

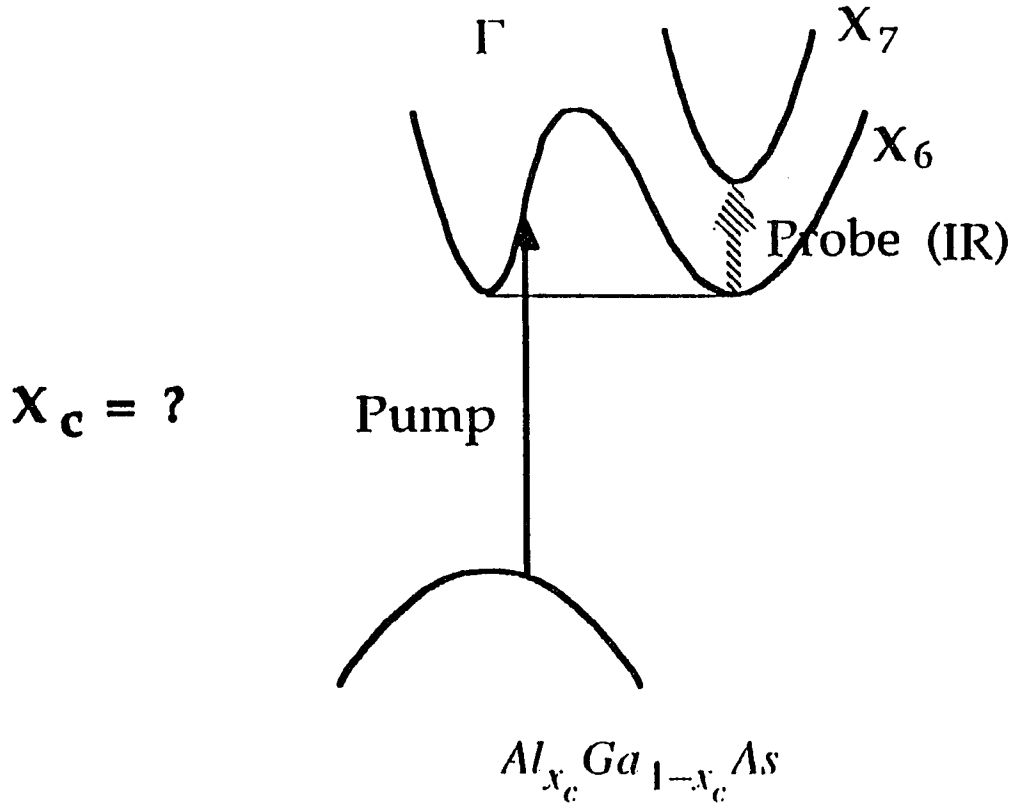

Fig. 1.1.2 The energy band structure for $Al_xGa_{1-x}As$ at $x=x_c$.[5]

1.2. Thesis Statement

This thesis work has directly measured the time evolution of the population of carriers in a k≠0 satellite valley by picosecond and femtosecond visible-pump and infrared(IR)-probe absorption spectroscopy for the first time, and has determined several X-valley-involved intervalley scattering times and band structure parameters for GaAs and $Al_xGa_{1-x}As$. This work can help one to understand the whole picture of intra-and-intervalley scattering processes in the X valley in GaAs and $Al_xGa_{1-x}As$.

The following five topics have been studied in this thesis work:

(1) Time evolution of the electron population in the X_6 valley and the $X_6 \rightarrow \Gamma_6$ scattering time in GaAs;

(2) Probe wavelength dependence of the $X_6 \rightarrow X_7$ absorption and the determination of the density of states effective mass of X_7 and the energy gap between the X_6 and X_7 conduction bands in GaAs;

(3) Crystal temperature dependence of hot carrier relaxation in GaAs;

(4) The X_6 valley hot carrier dynamics and the $L_6 \rightarrow X_6$ intervalley scattering time in $Al_{0.6}Ga_{0.4}As$; and

(5) Al content(x)-dependence of the temporal behavior of hot carriers in X_6 and the determination of the critical value x_c for the direct-to-indirect band gap transition in $Al_xGa_{1-x}As$.

1.3. Outline of Thesis

This thesis is organized into ten chapters:

In chapter 1, the previous theoretical and experimental studies on intervalley scattering in GaAs and $Al_xGa_{1-x}As$ are reviewed, and the main topics for this thesis work are introduced.

In chapter 2, a theoretical model is presented for intra-and-intervalley scattering in a semiconductor, and the matrix elements for different types of carrier-phonon interactions, and the selection rules for intervalley scattering are discussed.

In chapter 3, hot carrier dynamics in GaAs and $Al_xGa_{1-x}As$, the effect of intervalley scattering on hot carrier relaxation in GaAs, and the temporal profile of hot electron decay as a function of the band structure in $Al_xGa_{1-x}As$ are discussed.

In chapter 4, the experimental methods used for this thesis work are described. The picosecond and femtosecond pump-IR-probe absorption sets-up, and the time-resolved photoluminescence set-up are introduced. At the time when this thesis work started, femtosecond infrared (IR) pulses were not readily available in our lab. In order to study the time evolution of the electron population in the satellite X valley in GaAs, AlGaAs and other semiconductors, I have built a femtosecond pump-probe IR absorption set-up [29-31] which enable us to directly measure the femtosecond carrier dynamics in the X valley, and to investigate the X-valley-involved intervalley scattering processes and the X-valley related

band structure properties in semiconductors. This new femtosecond pump-IR-probe absorption set-up and the parameters important for the operation of the system are discussed in detail in Chapter 4.

In chapter 5, the experimental results on the time-resolved IR absorption in GaAs by a picosecond pump-IR-probe absorption spectroscopy is described. The dynamics of hot electrons in the X_6 valley subsequent to the excitation was obtained. From the time evolution of the population of the X_6 electrons, the intervalley $X_6 \rightarrow \Gamma_6$ scattering time was determined to be ~ 500 fs by a rate equation analysis. [32]

In chapter 6, the $X_6 \rightarrow X_7$ absorption spectrum for an intrinsic GaAs crystal measured by a picosecond pump-IR-probe absorption spectroscopy is presented. From the long-wavelength onset of the induced $X_6 \rightarrow X_7$ absorption spectrum, the energy gap between the minima of the X_6 and X_7 bands was directly determined to be 0.345 ± 0.017 eV. By fitting the measured $X_6 \rightarrow X_7$ absorption data, the density of states effective mass for the X_7 band was found to be 0.48 ± 0.06 m_0. [33]

In chapter 7, measurement on the temperature dependence of hot electron relaxation in GaAs in the range of 4K to 300K by a time-resolved photoluminescence spectroscopy is described. The electron relaxation times at low temperatures were found to be much longer than that at room temperature. This is attributed to the reduction of the number of phonons participating in the electron-phonon interaction and to the decrease of the intra-and-intervalley scattering rates, in particular, the $L \rightarrow \Gamma$ back

scattering rate. [34]

In chapter 8, the time evolution of the population of electrons in the bottom of the X_6 valley in $Al_{0.6}Ga_{0.4}As$ measured by a femtosecond pump-IR-probe absorption spectroscopy is described. The $L_6 \rightarrow X_6$ intervalley scattering time of ~ 200 fs was determined from the measured kinetic data. [30] The alloy-disorder-induced intervalley scattering in ternary semiconductors is compared with the phonon-assisted intervalley transition, and the L_6–X_6 intervalley deformation potential of ~ 2.7×10^{8} eV/cm was determined. [30]

In chapter 9, a measurement on the time evolution of the population of hot electrons in the satellite X valley for a series of $Al_xGa_{1-x}As$ samples with different values of x by femtosecond pump-probe absorption spectroscopy is presented. The dynamics of the X valley electrons for samples with $x \leq 0.408$ was found to be different from that for samples with $x \geq 0.439$ which reflects their different type of band gaps. The critical value of x_c which corresponds to the direct-to-indirect band gap transition for $Al_xGa_{1-x}As$ was determined to be 0.412 ± 0.009 from the composition dependence of the induced IR absorption. [35]

In chapter 10, future research directions related to this thesis work are discussed.

REFERENCES

[1] J. Shah, B. Deveaud, T. C. Damen, W. T. Tsang, A. C. Gossard, and P. Lugli, Phys. Rev. Lett. 59 , 2222 (1987).

[2] W. Z. Lin, M. J. LaGasse, R. W. Schoenlein, B. Zysset, and J. G. Fujimoto, SPIE, 942 , (March, 1988).

[3] J. S. Blakemore, J. Appl. Phys., 53 , R123 (1982).

[4] J. B. Gunn, Solid State Commun., 1 , 88 (1963).

[5] S. Adachi, J. Appl. Phys., 58 , R1 (1985).

[6] E. M. Conwell and M. O. Vassell, IEEE Trans. Electron. Devices, ED-13 , 22 (1966).

[7] S. Zollner, S. Gopalan, and M. Cardona, Appl. Phys. Lett., 54 , 614 (1989).

[8] M. J. Kann, A. M. Kriman, and D. K. Ferry, Phys. Rev., B41 , 12659 (1990).

[9] P. C. Becker, H. L. Fragnito, C. H. Brito Cruz, J. Shah, R. L. Fork, J. E. Cunningham, J. E. Henry, and C. V. Shank, Appl. Phys. Lett., 53 , 2089 (1988).

[10] R. G. Ulbrich, J. A. Kash, and J. C. Tsang, Phys. Rev. Lett., , 949 (1989).

[11] D. N. Mirlin, I. Ya. Karlik, and V. F. Sapega, Solid. State Commun, 65 , 171 (1988).

[12] A. Katz, and R. R. Alfano, Appl. Phys. Lett., 53 , 1065 (1988)

[13] F. W. Wise, I. A. Walmsley, and C. L. Tang, Appl. Phys. Lett., 51 , 605 (1986).

[14] N. Ockman, W. B. Wang, and R. R. Alfano, J. of Modern Phys., B5 , 3165 (1991).

[15] K. Berthold, A. F. J. Levi, J. Walker, and R. J. Malik, Appl. Phys. Lett., 54 , 813 (1989).

[16] G. D. Pitt and J. Lees, Phys. Rev. B2 , 4144 (1970).

[17] K. H. Nichols, C. M. L. Yee, and C. M. Wolfe, Solid State Electron, 23 , 109 (1980).

[18] D. E. Aspnes, Phys. Rev, B14 , 5331 (1976).

[19] D. L. Greenaway, Phys. Rev. Lett. 9 , 97 (1962).

[20] A. G. Thompson, M. Cardona, K. L. Shaklee, and J. C. Woolley, Phys. Rev. 146 , 601 (1966).

[21] L. W. James, R. C. Eden, J. L. Moll, and W. E. Spicer, Phys. Rev. 174 , 909 (1968).

[22] D. E. Aspnes and A. A. Studna, Phys. Rev. B7 , 4605 (1973).

[23] T. F. Kuech, D. J. Wolford, R. Potemski, J. A. Bradley, and K. H. Kelleher, App. Phys. Lett., 57 , 505 (1987).

[24] W. W. Ruhle, K. Leo, and E. Bauser, Phys. Rev., B40 , 1756 (1989).

[25] J. Shah, B. I. Miller, and A. E. DiGiovanni, J. Appl. Phys, 43 , 3434 (1972).

[26] E. E. Mendez, E. Calleja, and W. I. Wang, Phys. Rev., B34 , 6026 (1986).

[27] H. J. Lee, L. Y. Juravel, and J. C. Woolley, Phys. Rev., B21 , 659 (1980).

[28] H. A. Zarem, J. A. Lebens, K. B. Nordstrom, P. C. Sercel, S. Sanders, L. E. Eng, A. Yariv, and K. J. Vahala, Appl. Phys. Lett., 55 , 2622 (1989).

[29] T. M. Jedju, and L. Rothberg, Applied Optics, 27 , 615 (1988).

[30] W. B. Wang, Kai Shum, R. R. Alfano, D. Szmyd, and A. J. Nozik, Phys. Rev. Lett., 68 , 662 (1992).

[31] Kai Shum, W. B. Wang, R. R. Alfano, D. Szmyd, and A. J. Nozik, Phys. Rev. Lett., 68 , 3904 (1992).

[32] W. B. Wang, N. Ockman, M. Yan, and R. R. Alfano, J. of Lumin., 50 , 347 (1992).

[33] W. B. Wang, N. Ockman, M. A. Cavicchia, and R. R. Alfano, Appl. Phys. Lett., 57 , 395 (1990).

[34] W. B. Wang, Y. Takiguchi, and R. R. Alfano, to be submitted for publication.

[35] W. B. Wang, and R. R. Alfano, to be published in Phys. Rev. B46 , 15828 (1992).

Chapter 2
THEORY I: PHYSICAL MODEL ON INTRA-AND-INTERVALLEY SCATTERING

2.1. Classification of Carrier-Phonon Scattering

The electronic transitions in charge transport in semiconductors involving phonon absorption or emission is called carrier-phonon scattering shown schematically in Fig. 2.1.1. [1] It can be classified as intravalley scattering when the initial and final states of a scattered electron lie in the same valley as shown in Fig. 2.1.2, and intervalley scattering when the initial and final states of a scattered electron lie in different valleys as shown in Fig. 2.1.3. For the case of holes, intra-and-intervalley transitions are called intraband or interband scattering. [1]

The detailed classification of carrier-phonon scattering is shown in Table 2.1.1. [1] Both intravalley and intervalley scattering can be caused by interaction between a carrier and an acoustic or/and an optical phonon. Each acoustic-phonon-carrier or optical-phonon-carrier interaction can arise from the electrostatic interaction or/and deformation potential interaction discussed as follows.

If a semiconductor is made up of different atoms, their bond is partially ionic, and there is a lack of a symmetry center in its unit cell, it is then called a polar semiconductor. [2] Otherwise it is called a nonpolar

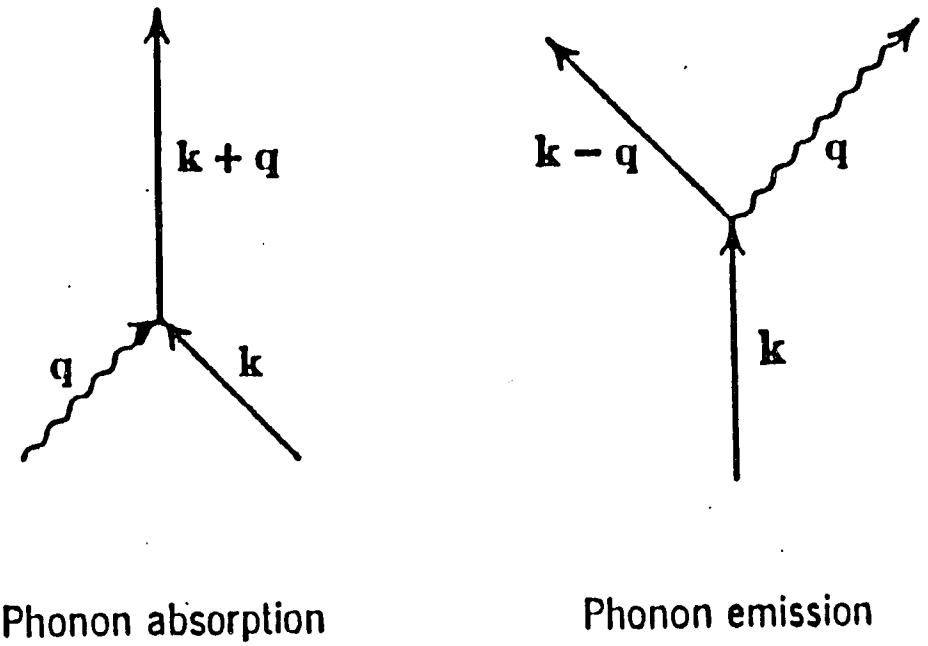

Fig. 2.1.1. Carrier-phonon scattering processes in first order. [1]

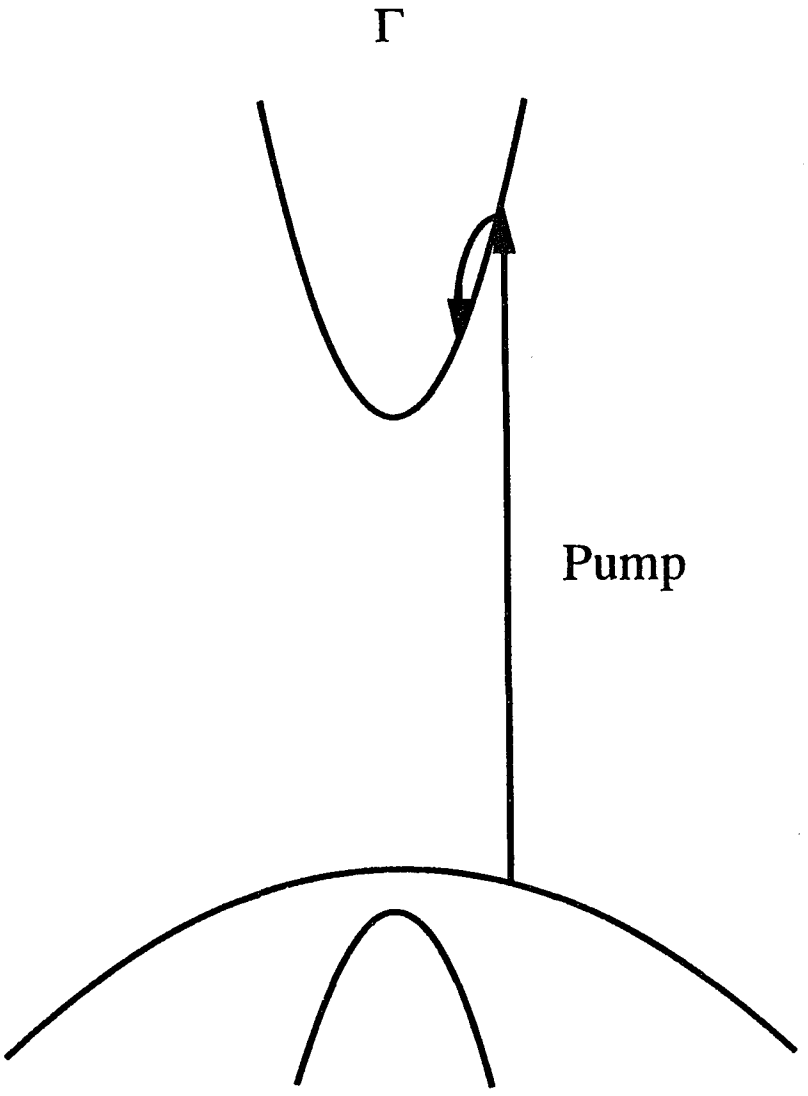

Fig. 2.1.2. Schematic diagram for intravalley scattering in the central Γ valley in GaAs.

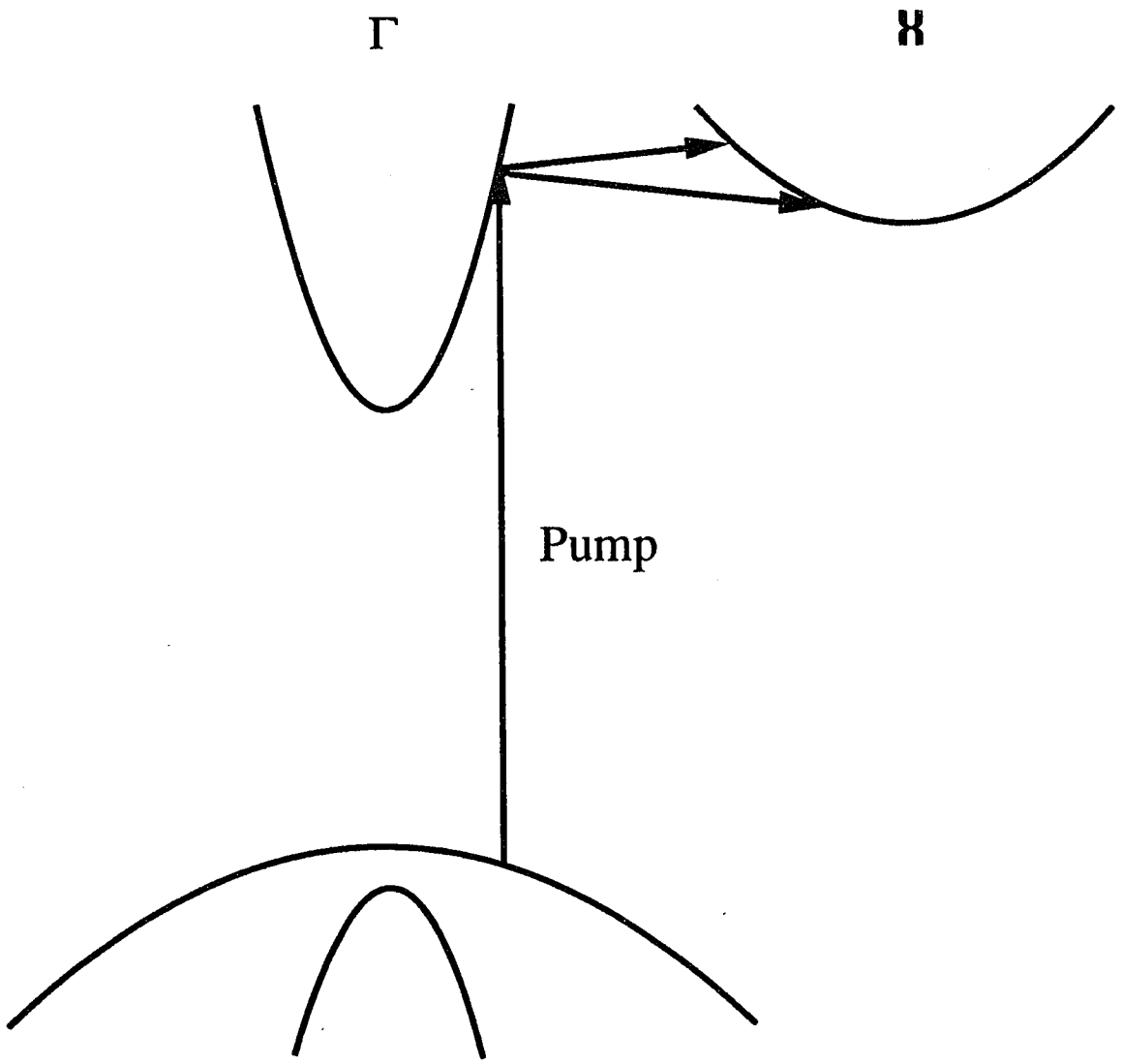

Fig. 2.1.3. Schematic diagram for intervalley scattering between the central Γ valley and the satellite X valley in GaAs.

semiconductor. For example, GaAs, InP, and AlAs are polar semiconductors, whereas Si and Ge are nonpolar semiconductors.

For an optical phonon wave in a polar semiconductor, lattice ions will oscillate around their equilibrium positions. The oscillation with a small amplitude can be described as [2]

$$\delta\vec{r}=\vec{A}\exp[\pm i(\vec{q}\cdot\vec{r}-\omega t)] \tag{2.1.1}$$

where $\vec{A}$, $\vec{q}$, and ω are the amplitude vector, wave vector, and angular frequency of the phonon wave, respectively. Due to the oscillation of lattice ions there arises a dipole moment per unit volume known as the "dielectric polarization" given by [2]

$$\vec{p}=N_u e_C \delta\vec{r}, \tag{2.1.2}$$

where N_u is the number of lattice cells per unit cm^3 and e_C is the effective charge for longitudinal optical modes. [2] Since the spatial displacement of carriers is negligible in comparison to the spatial displacement of the ions, there will be no space charge, and therefore, the dielectric displacement given by $D=\varepsilon_0 E+P$ [where ε_0 is the permittivity of free space] should vanish. Consequently, there is an alternating longitudinal electric field with the intensity given by [2]

$$\vec{E}=-\vec{P}/\varepsilon_0=-\frac{N_u e_C}{\varepsilon_0}\delta\vec{r}=\vec{E}_0\exp[\pm i(\vec{q}\cdot\vec{r}-\omega t)], \tag{2.1.3}$$

where $\vec{E}_0=-\frac{N_u e_C}{\varepsilon_0}\vec{A}$ is the amplitude vector of $\vec{E}$.

Because of this longitudinal field, an electron has an additional potential energy given by [2]

$$\delta\varepsilon=|e|V=|e|\int Edr=|e|\int E_0 e^{\pm i(\vec{q}\cdot\vec{r}-\omega t)}dr. \tag{2.1.4}$$

Carrying out the integral (2.1.4) gives [2]

$$\delta\varepsilon=\frac{|e|}{\pm iq}E_0 e^{\pm i(\vec{q}\cdot\vec{r}-\omega t)}=|e|\frac{E}{\pm iq}, \tag{2.1.5}$$

which is inversely proportional to the wave vector q of an optical wave. This small potential energy $\delta\varepsilon$ as a perturbation will cause phonon-carrier interaction, which is usually called polar scattering. [2]

For an acoustic phonon wave propagating in a polar semiconductor, the oscillation of ions will produce an electric field. Following the same approach given above, the electric field E due to the polarization P of the longitudinal acoustic lattice vibration can be written as

$$E=-P/\varepsilon_0, \tag{2.1.6}$$

and the corresponding potential energy of a carrier is given by

$$\delta\varepsilon=|e|\frac{E}{\pm iq}, \tag{2.1.7}$$

which is inversely proportional to the wave vector q of an acoustic phonon wave. This small perturbation energy $\delta\varepsilon$ will cause phonon-carrier interaction, which is usually called piezoelectric scattering.

When an acoustic phonon wave propagates in a nonpolar semiconductor, lattice atoms will oscillate around their equilibrium positions. The

oscillation with a small amplitude can also be described [2] by equation (2.1.1). However, the oscillation could not produce any electric field. An acoustic displacement can not affect the energy since neighboring unit cells all move by almost the same amount. Only the differential displacement, namely strain, is of importance [3]. The relative displacement of two neighboring atoms is given by

$$|\delta\vec{r}(a)-\delta\vec{r}(o)| = a(\nabla_r \delta\vec{r}). \tag{2.1.8}$$

This strain will cause a small change of lattice constant, and therefore, cause a small shift in energy at the edge of the valence and conduction bands which is given by [2]

$$\delta\varepsilon = \varepsilon_{DP}(\nabla_r \delta\vec{r})a \tag{2.1.9}$$

where ε_{DP} is a coefficient, and $\delta\varepsilon$ is independent of the phonon wave vector q. The shift in energy at the band edge per unit elastic strain is called the deformation potential. [2] As a perturbation, energy shift $\delta\varepsilon$ shown by (2.1.9) can cause carrier-phonon interaction, which is called acoustic deformation potential scattering.

For an optical phonon wave in nonpolar materials, the vibration of lattice atoms could not produce any electric field. The displacement of the oppositely moved atoms may affect the electronic energy directly. [3] The corresponding shift in energy at the edge of the valence and conduction bands is given by [2]

$$\delta\varepsilon = D\,\delta r, \tag{2.1.10}$$

where δr is the relative displacement of two atoms in an unit cell; and the coefficient D is called the optical deformation potential. The energy shift $\delta\varepsilon$ is independent of the phonon wave vector q. As a perturbation, $\delta\varepsilon$ can cause phonon-carrier interaction called optical deformation potential or nonpolar optical scattering.

The acoustic and optical deformation potential scattering exists not only in nonpolar materials, but also in polar materials. In polar semiconductors, besides the piezoelectric or polar optical scattering, the deformation potential interaction will produce additional scattering for both acoustic and optical phonon modes.

2.2. Matrix Elements For Carrier-Phonon Scattering

2.2.1. Acoustic Deformation Potential Scattering

Scattering due directly to strain caused by an acoustic phonon wave is called acoustic deformation potential scattering. The main idea of the deformation potential approach is that the matrix element is practically equal to that obtained by replacing $H(\vec{r})$ by the shift $\delta\varepsilon$ of the band edge energy that would be produced by a homogeneous strain of magnitude equal to the local strain at $\vec{r}$ set up by the mode $\vec{q}$. Since the strains involved are small, the shift may be described with only linear terms in

Table 2.1.1. Classification of carrier-phonon scattering. [1]

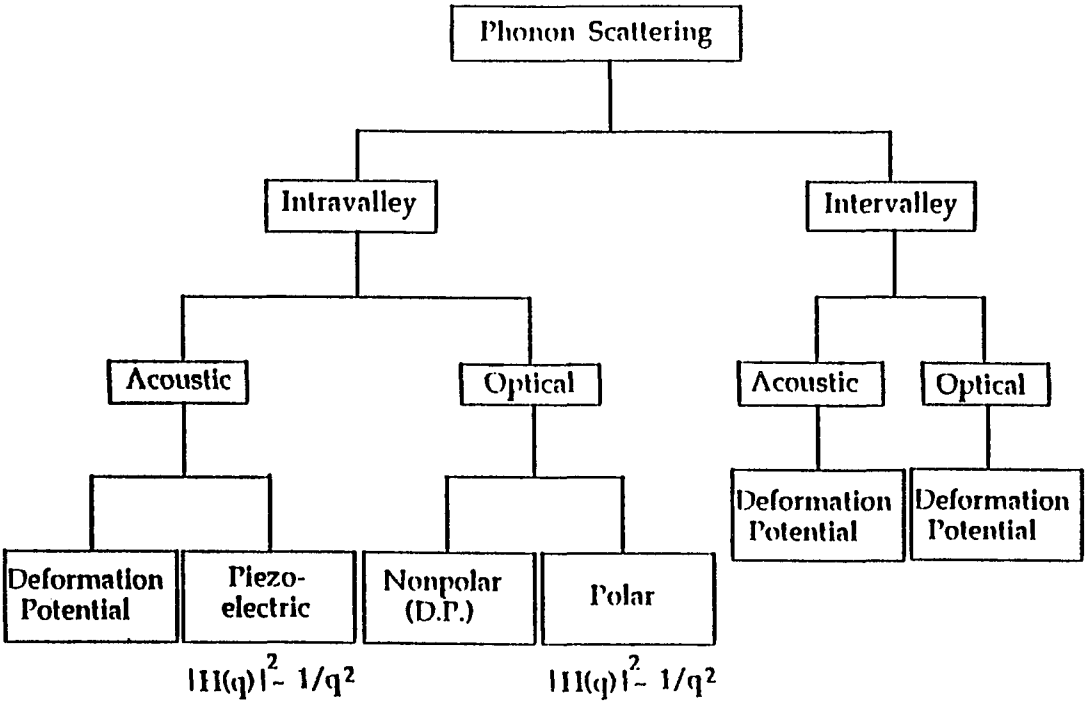

the strain. For spherical constant energy surfaces and acoustic mode scattering, one may write for the shift of the band edge [4]

$$\delta\varepsilon=E_1(e_{xx}+e_{yy}+e_{zz})=E_1\Delta \tag{2.2.1}$$

where e_{ii} are diagonal components of the strain tensor, their sum being equal to the dilatation Δ, and E_1 is the shift of the band edge per unit dilatation. Using the relation $\Delta=\nabla\cdot\delta\vec{r}$, where $\delta\vec{r}$ is the displacement at the point $\vec{r}$, one obtains the result that only longitudinal lattice waves scatter the carriers, the squared matrix element for this scattering being [4]

$$|(\vec{k}\pm\vec{q}|\,H_{adp}\,|\vec{k})|^2=\frac{E_1^2\hbar\omega_q}{2V\rho u_l^2}[N_q+\frac{1}{2}+\frac{\delta N_q}{2}] \tag{2.2.2}$$

where V is the volume of the crystal, u_l is the velocity of the longitudinal wave, ρ the density of the crystal, and $\delta N_q=-1$ for absorption of a phonon and $\delta N_q=+1$ for emission of a phonon. The quantity $\hbar\omega_q(N_q+\frac{1}{2}+\frac{\delta N_q}{2})$ is the average energy of the lattice oscillator involved in the transition.

2.2.2. Piezoelectric (Acoustic Electrostatic) Scattering

Scattering due to the electric field arising from an acoustic phonon wave in polar materials as discussed in section 2.1 is called piezoelectric or acoustic electrostatic scattering. The produced electric field, E, is parallel to the propagation direction of an acoustic wave. For a wave propagating in the i-direction, the produced electric field is given by [4]

$$E_i = -P_{ijk} e_{jk} / k \tag{2.2.3}$$

where p_{ijk} is the appropriate component of the piezoelectric tensor, e_{jk} is the component of the strain tensor, and k is the dielectric constant.

Because of this longitudinal field, an electron has an additional potential energy given by [4]

$$-eV = -ep_{ijk} e_{jk} / qk \tag{2.2.4}$$

where q is the wave vector of the acoustic wave.

When (2.2.4) is used as the perturbing potential, the electron wave functions taken to be plane waves, and equipartition assumed for the acoustic modes, the squared matrix element for either emission or absorption is found to be [4]

$$| (\vec{k} \pm \vec{q} | H_{pie} | \vec{k}) |^2 = \frac{1}{2} \frac{e^2 p^2}{q^2 k^2} \frac{K_B T}{V \rho u_l^2} \tag{2.2.5}$$

where V, ρ, and u_l have the same meaning as that in (2.2.2), and k is the dielectric constant.

2.2.3. Nonpolar Optical (Optical Deformation Potential) Scattering

Scattering due to strain caused by an optical phonon wave is called nonpolar optical or optical deformation potential scattering. It may exist in nonpolar crystals as well as in polar crystals.

Consideration of the nonpolar optical matrix element [2] has shown that it may be either zero or of higher order in the wave vector of the phonon

or of the carrier, the wave vector in the lattice case being measured from the edge of the valley. When the matrix element is of higher order, it is much smaller, and the optical mode scattering may be neglected. Therefore, one considers only the case that the squared matrix element is of zeroth order which can be written as [4]

$$|(\vec{k}\pm\vec{q}|H_{npo}|\vec{k})|^2=\frac{D_t^2K^2\hbar}{2V\rho\omega_0}[N_q+\frac{1}{2}\pm\frac{\delta N_q}{2}] \qquad (2.2.6)$$

where ρ, V, ω, N_q, and δN_q have the same meaning as that in (2.2.2); D_t is an interaction constant having the dimension of energy; K is a reciprocal lattice vector. For convenience, one uses D replacing $D_t K$ and calls it the deformation potential which is the shift of the band edge energy per unit relative displacement of the sublattices.

2.2.4. Polar Optical (Optical Electrostatic) Scattering

In polar crystals, the dielectric polarization arising from the vibrations of the longitudinal optical branch results in an additional interaction with carriers, or scattering, the so-called polar optical scattering. This is generally expected to be stronger than the nonpolar optical scattering. It has been shown that [4] polar optical scattering is the dominant scattering mechanism over a considerable temperature range in GaAs.

For high-mobility materials and the case of weak coupling between carriers and phonons, the perturbation theory can be used to describe these interactions. The squared matrix element may be written as [4]

$$|(\vec{k}\pm\vec{q}|H_{po}|\vec{k})|^2=\frac{2\pi\hbar^2eE_0}{Vmq^2}[N_q+\frac{1}{2}+\frac{\delta N_q}{2}] \qquad (2.2.7)$$

where E_0 is an effective field defined by

$$eE_0=\frac{me^2\hbar\omega_l}{\hbar^2}(\frac{1}{k_\infty}-\frac{1}{k_0}), \qquad (2.2.8)$$

and is usually used as a measure of the strength of coupling to the polar mode. In (2.2.8), ω_l is the longitudinal optical mode frequency, k_0 and k_∞ are the dielectric constants for zero and infinite frequencies, respectively.

2.3. The Dominant Mechanisms for Intra-or-Intervalley Scattering

The squared matrix elements used for acoustic deformation potential, optical deformation potential, piezoelectric, and polar optical scatterings are given in Table 2.3.1, which indicates that the squared matrix elements $|H(q)|^2$ are independent of q for deformation potential scattering, and inversely proportional to the square of q ($|H(q)|^2\alpha\frac{1}{q^2}$) for piezoelectric and polar optical scatterings, where q is the momentum of the phonon involved in the scattering, and is proportional to the value of the corresponding phonon wave vector.

Most intravalley scattering processes require only a small electron momentum transfer, i.e. a small phonon momentum q. For example, the intravalley scattering near the zero momentum point in the Γ valley in GaAs requires a phonon having a very small momentum of ~ 2.5 $\times10^{-21}$

erg.sec/cm for the electron momentum transfer. Since the squared matrix elements for the piezoelectric and polar optical scatterings are inversely proportional to q^2, these two scattering mechanisms will dominate the whole intravalley scattering process. It has been shown that polar optical scattering is indeed the dominant mechanism of scattering in pure III-V and II-VI compounds. [3]

Most intervalley scattering processes occur at or near the Brillouin zone edge (depending on whether the valley minimum is at or near the zone edge), and involve a large momentum transfer for electrons. Therefore, the momentum q of a phonon participating in intervalley scattering is required to be large. For example, the intervalley scattering between the Γ and X valleys and between the Γ and L valleys in GaAs requires a phonon with a large momentum of ~ 8.4×10^{-18} erg.sec/cm for the electron momentum transfer. Since the squared matrix element for electrostatic scatterings (both piezoelectric acoustic scattering and polar optical scattering) are inversely proportional to q^2, they are very small and can be neglected for intervalley scattering. Consequently, only deformation potential induced scattering is considered for intervalley scattering.

Table 2.3.1. Squared matrix elements $|H(q)|^2$ for different carrier-phonon scattering mechanisms. [2,4]

Acoustic Deformation Potential Scattering *

$$|(\vec{k}\pm\vec{q}|H_{adp}|\vec{k})|^2=\frac{E_1{}^2\hbar\omega_q}{2V\rho u_l{}^2}[N_q+\frac{1}{2}+\frac{\delta N_q}{2}]$$

Piezoelectric (Acoustic Electrostatic) Scattering

$$|(\vec{k}\pm\vec{q}|H_{pie}|\vec{k})|^2=\frac{1}{2}\frac{e^2p^2}{q^2k^2}\frac{K_BT}{V\rho u_l{}^2}$$

Optical Deformation Potential or Nonpolar Optical Scattering *

$$|(\vec{k}\pm\vec{q}|H_{npo}|\vec{k})|^2=\frac{D_t{}^2K^2\hbar}{2V\rho\omega_0}[N_q+\frac{1}{2}\mp\frac{\delta N_q}{2}]$$

Polar Optical (Optical Electrostatic) Scattering

$$|(\vec{k}\pm\vec{q}|H_{po}|\vec{k})|^2=\frac{2\pi\hbar^2eE_0}{Vmq^2}[N_q+\frac{1}{2}+\frac{\delta N_q}{2}]$$

---

* which are dominant for intervalley scattering.

2.4. Intervalley Scattering Rates

The inter-or-intravalley scattering time τ_{ij} can be obtained starting from the Fermi-Golden Rule. The probability of a transition taking place during time t between states of energy ε_1 and ε_2 may be written as

$$P_{12}(t)=\frac{2\pi t}{\hbar}|H'_{12}|^2\delta(\varepsilon_1-\varepsilon_2) \tag{2.4.1}$$

where H'_{12} is the matrix element of the perturbing potential H' between the initial and final states.

From equation (2.4.1), the probability per unit time of a carrier being scattered out of $\vec{k}$ can be written as [4]

$$\frac{1}{\tau}=\frac{2\pi}{\hbar}\sum_{\vec{q}}[|(\vec{k}+\vec{q};N_q-1|H'|\vec{k},N_q)|^2\delta(\varepsilon_{\vec{k}+\vec{q},N_q-1}-\varepsilon_{\vec{k},N_q})$$

$$+|(\vec{k}-\vec{q};N_q+1|H'|\vec{k},N_q)|^2\delta(\varepsilon_{\vec{k}-\vec{q},N_q+1}-\varepsilon_{\vec{k},N_q})] \tag{2.4.2}$$

where the first term is the transition probability due to phonon absorption, the second due to phonon emission; N_q stands for the steady-state average number of phonons with wave vector $\vec{q}$, and is given by the Bose-Einstein distribution function

$$N_q=1/[\exp(\hbar\omega_q/K_BT)-1] \tag{2.4.3}$$

where $\hbar\omega_q$ is the energy of a phonon with momentum q, K_B is the Boltzmann constant, T is the lattice temperature.

For a simple spherical energy surface and a parabolic band with a free carrier effective mass m, the term in the δ function of equation (2.4.2) for the case of phonon absorption can be written as

$$\varepsilon_{\vec{k}+\vec{q},N_q-1}-\varepsilon_{\vec{k},N_q}=\frac{\hbar^2}{2m}(2\vec{k}\cdot\vec{q}+q^2)-\hbar\omega_q \tag{2.4.4}$$

It is convenient to transform the summation over $\vec{q}$ to an integration over spherical coordinates q, θ, ϕ with the $\vec{k}$-direction taken as the z-axis. Then equation (2.4.4) becomes

$$\varepsilon_{\vec{k}+\vec{q},N_q-1}-\varepsilon_{\vec{k},N_q}=\frac{\hbar^2}{2m}(2kq\cos\theta+q^2)-\hbar\omega_q \tag{2.4.5}$$

and equation (2.4.2) becomes [4]

$$\frac{1}{\tau}=\frac{2\pi}{\hbar}\int_{q=0}^{q_0}\int_{\theta=0}^{\pi}\int_{\phi=0}^{2\pi}\frac{V}{(2\pi)^3}q^2\sin\theta\,d\theta\,d\phi\,dq\,[|(\vec{k}+\vec{q},N_q-1|H'|\vec{k},N_q)|^2\delta(\frac{\hbar^2}{m}kq\cos\theta+\frac{\hbar^2q^2}{2m}-\hbar\omega_q)$$

$$+|(\vec{k}-\vec{q},N_q+1|H'|\vec{k},N_q)|^2\delta(\frac{\hbar^2}{m}kq\cos\theta+\frac{\hbar^2q^2}{2m}-\hbar\omega_q)]. \tag{2.4.6}$$

Since the matrix element $|(\vec{k}\pm\vec{q},N_q\mp1)|H'|\vec{k},N_q)|^2$ is independent of θ and ϕ, and only depends on the magnitude of q, the integral over θ and ϕ in equation (2.4.6), designated by $I(\vec{k}+\vec{q})$ for the first term and by $I(\vec{k}-\vec{q})$ for the second term, can be carried out.

For intervalley scattering, the $\vec{q}$ of the phonon involved will be approximately equal to the difference between the $\vec{k}$ vectors of the valley minimum, and the energy of the phonon involved will be a significant

fraction of the optical phonon and $\geq K_B T$ for most of the temperature range of interest. Therefore, the matrix element for intervalley scattering may be treated much like nonpolar optical (optical deformation potential) scattering, for which the integrated results are given by [4]

$$I_{op}(\vec{k}+\vec{q})=\frac{2\phi m}{\hbar^2 kq} \tag{2.4.7}$$

for

$$k[(1+\frac{\hbar\omega_0}{\varepsilon})^{1/2}-1]<q<k[(1+\frac{\hbar\omega_0}{\varepsilon})^{1/2}+1]$$

and

$$I_{op}(\vec{k}-\vec{q})=\frac{2\phi m}{\hbar^2 kq} \tag{2.4.8}$$

for

$$k[1-(1-\frac{\hbar\omega_0}{\varepsilon})^{1/2}]<q<k[1+(1-\frac{\hbar\omega_0}{\varepsilon})^{1/2}]$$

where ε is the carrier energy which satisfies $\varepsilon>\hbar\omega_0$. Substituting equations (2.4.7) and (2.4.8) into (2.4.6), one obtains

$$\frac{1}{\tau_{op}}=\frac{mV}{2\pi\hbar^3 k}\left[\int_{k(1+\hbar\omega/\varepsilon)^{1/2}-k}^{k(1+\hbar\omega/\varepsilon)^{1/2}+k}|(\vec{k}+\vec{q}|H'_{op}|\vec{k})|^2 qdq+\int_{k-k(1-\hbar\omega/\varepsilon)^{1/2}}^{k+k(1-\hbar\omega/\varepsilon)^{1/2}}|(\vec{k}-\vec{q}|H'_{op}|\vec{k})|^2 qdq\right]. \tag{2.4.9}$$

As mentioned in 2.2.3, the squared matrix element for nonpolar optical scattering may be written as

$$|(\vec{k}\pm\vec{q}|H'_{op}|\vec{k}|)^2=\frac{D_t^{\,2}K^2\hbar}{2V\rho\omega_0}[N_q+\frac{1}{2}\pm\frac{\delta N_q}{2}] \tag{2.4.10}$$

where D_t is an interaction constant having the dimension of energy, K is a reciprocal lattice vector, δN_q=+1 for phonon emission and δN_q=−1 for phonon absorption. The product of $D_t K$ is usually marked as D and called the deformation potential which gives the shift of the band edge per unit relative displacement of the sublattice.

Substituting (2.4.10) into (2.4.9), and carrying out the integration, the nonpolar optical intravalley scattering rate becomes [4]

$$\frac{1}{\tau_{op}}=\frac{D^2 m^{2/3}}{2^{1/2}\pi\hbar^3\rho\omega_0}[N_q(\varepsilon+\hbar\omega_0)^{1/2}+(N_q+1)(\varepsilon-\hbar\omega_0)^{1/2}]. \qquad (2.4.11)$$

The intervalley scattering rate from the ith valley to the jth valley can be obtained by replacing D, ω_0 in equation (2.4.11) by D_{ij}, ω_{ij}, respectively. In addition, if we choose the minimum energy of the ith valley as zero, the minimum energy of the jth valley will be $\delta E_{ij}=E_{oj}-E_{oi}$, and ε_2 is measured from the bottom of the jth valley. Consequently, the intervalley scattering time of carriers with initial energy ε in the ith valley can be written as: [4]

$$\frac{1}{\tau_{ij}}=\frac{D_{ij}^2 m_j^{3/2} N_j}{2^{1/2}\pi\hbar^3\rho\omega_{ij}}[N_{q_{ij}}(\varepsilon+\hbar\omega_{ij}-\varepsilon_{oj})^{1/2}+(N_{q_{ij}}+1)(\varepsilon-\hbar\omega_{ij}-\varepsilon_{oj})^{1/2}] \qquad (2.4.12)$$

where the subscript j refers to the valley into which electrons are scattered, N_{ij} is the number of equivalent valleys (1 for Γ, 3 for X, and 4 for L), and D_{ij} refers to the coupling constant or deformation potential for the process. The first term in the angular bracket represents transitions

involving emission of a phonon with angular frequency ω_{ij} while the second term represents transitions involving phonon absorption.

For example, the $\Gamma \rightarrow X$ intervalley scattering time in GaAs, $t_{\Gamma X}$, as a function of initial energy ε, deformation potential $D_{\Gamma X}$ and crystal temperature T can be calculated using equation (2.4.12) and the values of the parameters m_j, ρ, $\hbar\omega_{ij}$, N_j and ε_{0j} given by Blakemore [5].

The calculated $\Gamma \rightarrow X$ intervalley scattering time, $t_{\Gamma X}$, as a function of the kinetic energy of electrons in the Γ valley, ε, for GaAs at 300 K is shown in Fig. 2.4.1. When ε is smaller than the bottom energy of the X valley, ε_{0X}, by the energy of a phonon, $\hbar\omega_{\Gamma X}$, then both intervalley scattering channels by absorption and emission of a phonon becomes impossible so that the intervalley scattering rate becomes zero. When ε increases to be greater than $\varepsilon_{0X}-\hbar\omega_{\Gamma X}$, but smaller than $\varepsilon_{0X}+\hbar\omega_{\Gamma X}$, intervalley scattering by absorption of a phonon becomes possible, therefore, the intervalley scattering rate becomes nonzero. When ε increases to beyond $\varepsilon_{0X}+\hbar\omega_{\Gamma X}$, both intervalley scattering channels by absorption and emission of a phonon becomes possible, therefore, the scattering rates increase rapidly. When ε is much greater than $\varepsilon_{0X}+\hbar\omega_{\Gamma X}$, the intervalley scattering rate increases slowly with $\varepsilon^{1/2}$. Fig. 2.4.1 also shows that the intervalley scattering rate at each fixed ε increases very rapidly with deformation potential, $D_{\Gamma X}$. This is expected because the intervalley scattering rate is proportional to the square of the deformation potential as shown in

equation (2.4.12).

The calculated $\Gamma \rightarrow X$ intervalley scattering time as a function of crystal temperature, T, for GaAs at ε=0.83eV is shown in Fig. 2.4.2. At very low temperatures (T < 50 K), the average number of phonons participating in the electron-phonon scattering, $N_{q_{\Gamma X}}$, is almost zero according to equation (2.4.3). Therefore, intervalley scattering rates reach their smallest values. When T>50 K, $N_{q_{\Gamma X}}$ increases with temperature, and therefore, intervalley scattering rates increase with temperature.

The calculated $X \rightarrow \Gamma$ intervalley scattering time, $t_{X\Gamma}$, as a function of crystal temperature for GaAs, and a proposed measurement for the temperature dependence of $t_{X\Gamma}$ will be discussed in chapter 10.

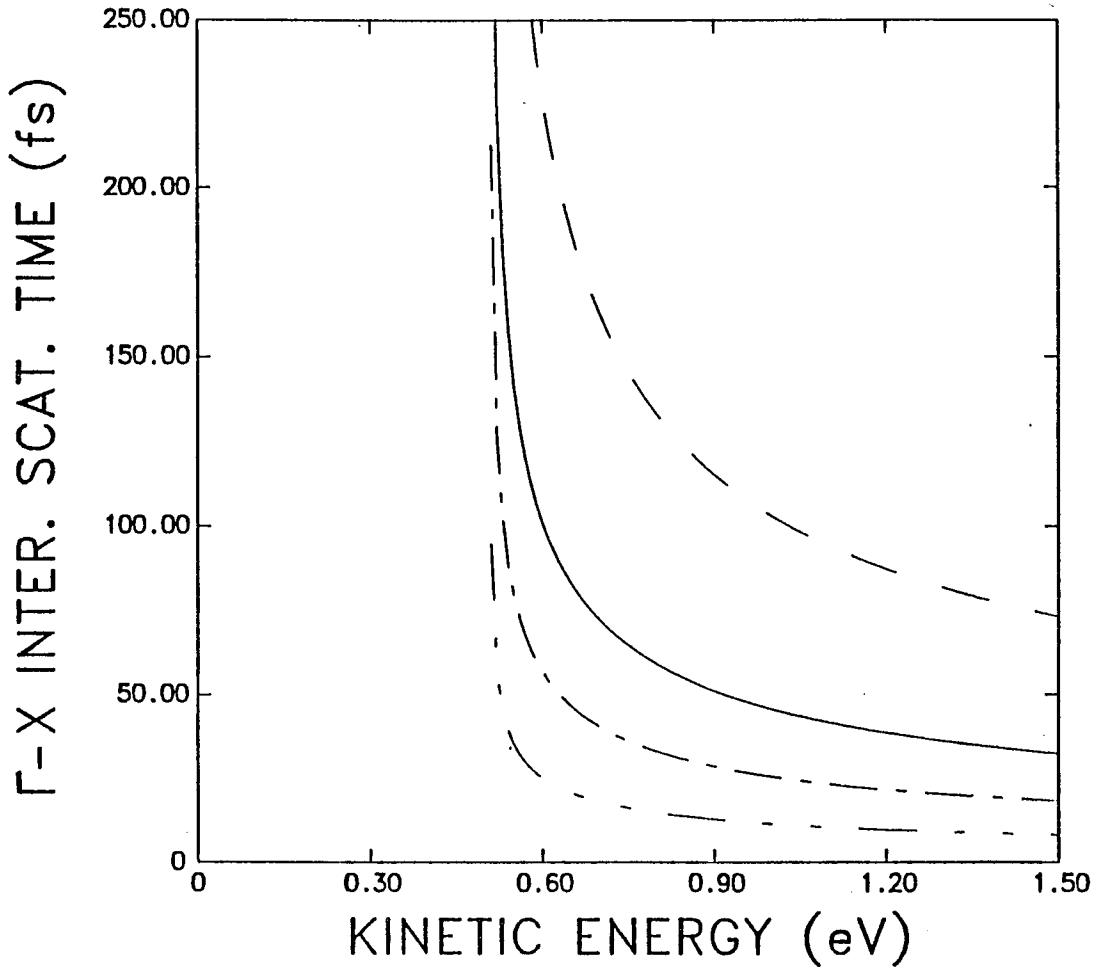

Fig. 2.4.1. The calculated Γ→X intervalley scattering time as a function of kinetic energy of electrons and deformation potential $D_{\Gamma X}$ for GaAs at 300 K. The dash, solid, dot-dash and dot-dot-dash curves correspond to $D_{\Gamma X}$ = 2.0, 3.0, 4.0 and 6.0×10^{8} eV/cm, respectively.

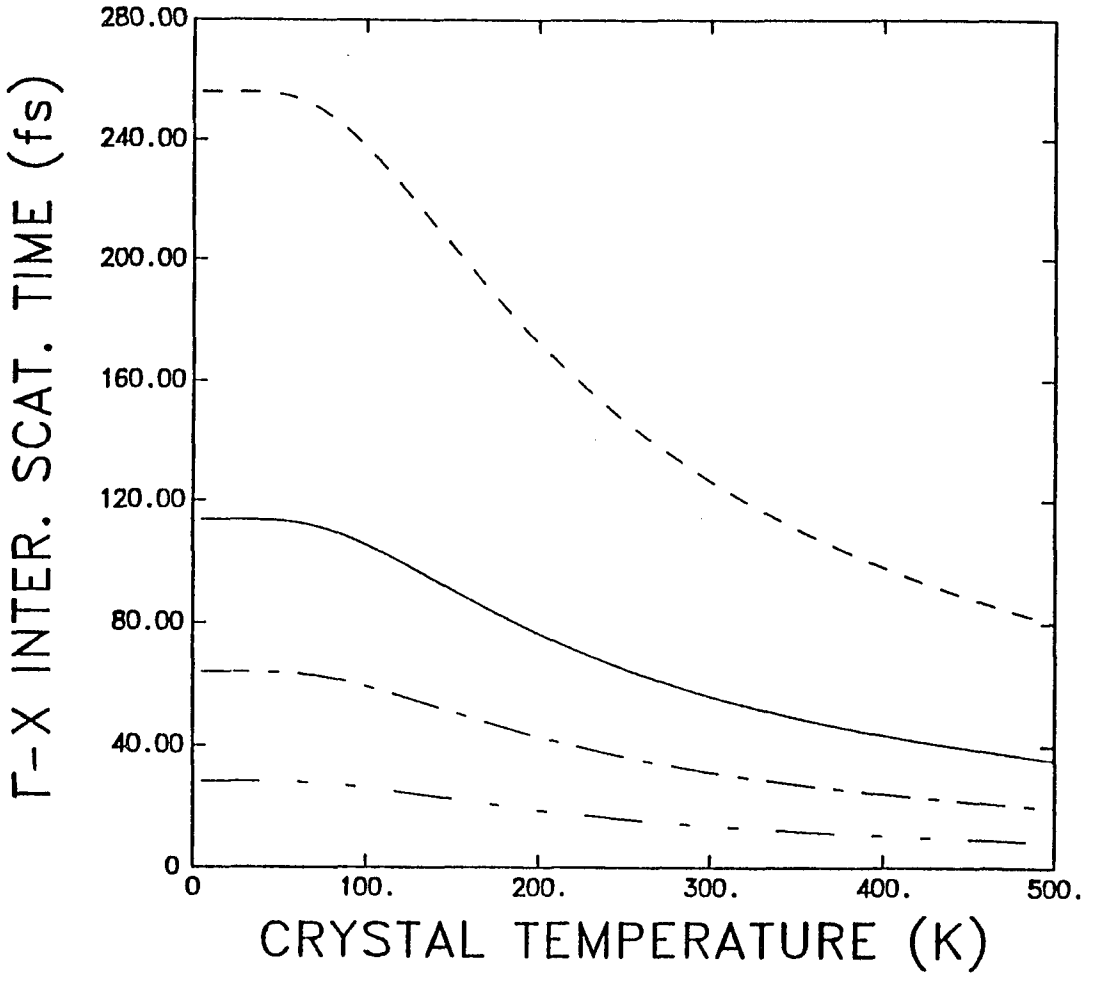

Fig. 2.4.2. The calculated Γ→X intervalley scattering time as a function of crystal temperature and deformation potential for GaAs at ε (kinetic energy of electrons in the Γ valley)=0.83 eV. The dash, solid, dot-dash and dot-dot-dash curves correspond to $D_{\Gamma X}$ = 2.0, 3.0, 4.0 and 6.0×10^{8} eV/cm, respectively.

2.5. Selection Rules for Intervalley Scattering in III-V Semiconductors

Selection rules for intervalley scattering in III-V semiconductors has been obtained using group theory by Birman et al. [6,7]

The matrix element for intervalley scattering from state $|\vec{k}>$ to state $|\vec{k}\pm\vec{q}>$ by absorption or emission of a phonon $|\vec{q}_j>$ in the absence of an external field is

$$<\vec{k}\pm\vec{q}|H|\vec{k}> \qquad (2.5.1)$$

where H is the first term in the Taylor Expansion of the potential versus phonon displacements. As H has the symmetry of the phonon involved, the transition, according to Wigner-Echart Theory, is forbidden unless the representation belonging to the state $|\vec{k}\pm\vec{q}>$ is contained in the product of the representations belonging to $|\vec{q}_j>$ and $|\vec{k}>$; or the representation belonging to phonon $|\vec{q}_j>$ is contained in the product of the representations belonging to $|\vec{k}>$ and $|\vec{k}\pm\vec{q}>$.

The symmetries of the Γ, L and X (lowest X valley in conduction band) valleys in GaAs are the following; [6]

Γ (000):	Γ_1
L (111):	L_1
X (100):	X_1

(2.5.2)

For the intervalley scattering between different types of valleys, the Kronecker (direct) products of the space-group representations are required to be the following; [6]

$$\Gamma \rightarrow X: \quad \Gamma_1 \times X_1 = X_1$$

$$\Gamma \rightarrow L: \quad \Gamma_1 \times L_1 = L_1$$

$$L \rightarrow X: \quad L_1 \times X_1 = L_1 + L_3 \qquad (2.5.3)$$

The phonon symmetries in different valleys in GaAs are as follows; [7]

$$\Gamma: \quad \Gamma_{15}\ (\text{Optic}) + \Gamma_{15}\ (\text{Acoustic})$$

$$L: \quad L_3(TO) + L_1(LO) + L_1(LA) + L_3(TA) \qquad (2.5.4)$$

$$X: \quad X_5(TO) + X_1(LO) + X_3(LA) + X_5(TA)$$

The intervalley transitions can occur only if the symmetries of the phonons listed in (2.5.4), which are needed for the transition of an electron between the states whose symmetries are listed on the left-hand sides of (2.5.3), are the same as the symmetries of the irreducible representation listed on the right-hand side of (2.5.3). Therefore, combining (2.5.3) and (2.5.4), the following selection rules for intervalley scattering in GaAs were obtained: [7]

$$\Gamma \rightarrow X: \quad LO$$

$$\Gamma \rightarrow L: \quad LO + LA$$

$$L \rightarrow X: \quad LO + LA + TO + TA \qquad (2.5.5)$$

Equation (2.5.5) shows that if the phonon momentum q involved in the intervalley scattering is at the Brillouin zone edge, only LO phonons can participate in the $\Gamma \rightarrow X$ intervalley scattering in GaAs. The LA and transverse phonons (TO and TA) in the X valley have X_3 and X_5 symmetries, respectively, and do not contribute to the $\Gamma \rightarrow X$ scattering. The situation for the $\Gamma \rightarrow L$ scattering is different as both the LA and LO phonons have L_1 symmetry and contribute to the $\Gamma \rightarrow L$ scattering processes, whereas transverse phonons (TO and TA) have L_3 symmetry, and therefore the transverse phonon scattering is forbidden. For $L \rightarrow X$ scattering, all of the phonon modes (LO, LA, To and TA) are permitted.

If the higher valleys are not exactly at the Brillouin zone edge, the selection rules mentioned above will become less restrictive. For example, the Δ valley in GaAs lies on the path from Γ to X as shown in Fig. 2.5.1, both LA and LO can cause $\Gamma \rightarrow \Delta$ scattering.

The selection rules for GaAs given in (2.5.5) can be used for AlAs and AlSb because the anion (group V atoms) is heavier than the cation (group III atoms), and the X_1 state (with the anion at rest) has higher energy (LO) than the X_3 state (LA) in those materials. In the reverse case such as in InP, GaP, and InAs, the anion is lighter than the cation, and the LA (LO) phonon has X_1 (X_3) symmetry. Therefore, LA phonons can contribute to the $\Gamma \rightarrow X$ intervalley scattering, but not LO phonons in InP, GaP and InAs.

Using the selection rules given in (2.5.5) for GaAs and corresponding selection rules for the other III-V semiconductors, Zollner in Cardona's group [8] has calculated the intervalley deformation potentials in zinc-blende semiconductors as shown in Table 2.5.1.

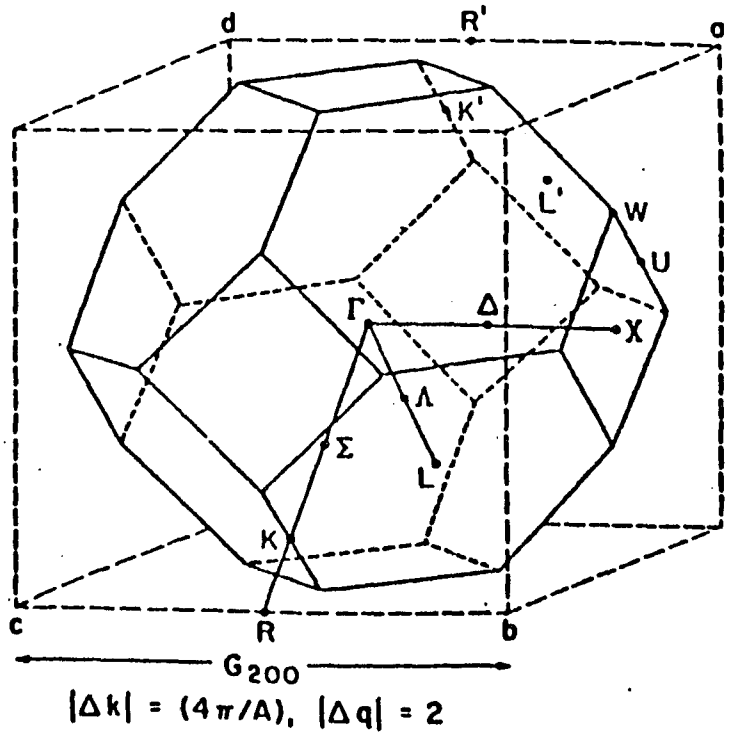

Fig. 2.5.1. First Brillouin zone structure for GaAs. [5]

Table 2.5.1. Calculated intervalley deformation potentials for III-V semiconductors ($\times 10^8$ eV/cm). [8]

	$D_{\Gamma L}$		$D_{\Gamma X_1}$		$D_{\Gamma X_3}$		D_{LL}		$D_{X_1X_3}$			D_{LX_3}		
	LA	LO	LA	LO	LA	LO	LA	LO	LA	LO	TA	LA	LO	TO
AlAs[a,b]	2.3	2.2	0	4.4	2.7	0	0.2	2.2	0	6.6	1.1	1.7	0.6	2.4
AlSb[c,d]	2.3	3.4	0	4.9	1.3	0	0.5	0.6	0	9.5	1.1	0.8	2.4	3.7
GaAs[c,b]	4.1	0.6	0	4.1	4.7	0	0.1	1.7	0	7.0	1.2	0.5	2.5	2.6
GaSb[c,b]	2.8	2.7	0	4.5	2.5	0	0.6	1.2	0	6.0	1.0	1.4	1.5	2.2
InSb[f,g]	4.3	1.1	0	4.9	3.3	0	0.6	0.3	0	6.8	1.2	0.2	2.9	2.5
InP[c,g]	1.6	3.0	2.3	0	0	3.7	0.4	1.2	4.4	0	1.0	0.7	4.0	1.7
InAs[c,g]	2.5	1.4	3.2	0	0	2.8	1.4	0.7	3.6	0	0.9	0.8	2.7	1.6
GaP[c,b]	1.2	1.0	1.5	0	0	1.2	0.3	0.8	4.3	0	0.5	1.0	2.2	1.0

2.6. Intravalley Scattering Rates

Ehrenreich has compared the results of the experimentally observed temperature-dependence of the low-field mobility with the dependence predicted theoretically for some scattering processes or combination processes, and has concluded that the predominant intervalley scattering mechanism in some of the III-V compounds such as GaAs, InP, InAs, and InSb over a considerable temperature range is polar optical scattering. [9]

The probability per unit time of a carrier being scattered out of the state $\vec{k}$ by a polar optical interaction may be calculated in the same way as that for the nonpolar optical (optical deformation potential) case. As mentioned in section 2.4., equation (2.4.9) is valid for either type of optical scattering. Therefore, the probability per unit time of polar optical scattering can be obtained by replacing H'_{op} in (2.4.9) by H'_{po}:

$$\frac{1}{\tau_{po}}=\frac{mV}{2\pi\hbar^3 k}\left[\int_{k(1+\hbar\omega/\varepsilon)^{1/2}-k}^{k(1+\hbar\omega/\varepsilon)^{1/2}+k} |(\vec{k}+\vec{q}|H'_{po}|\vec{k})|^2 qdq+\int_{k-k(1-\hbar\omega/\varepsilon)^{1/2}}^{k+k(1-\hbar\omega/\varepsilon)^{1/2}} |(\vec{k}-\vec{q}|H'_{po}|\vec{k})|^2 qdq\right]. \quad (2.6.1)$$

where the first and second terms correspond to transitions due to absorption and emission of a phonon, respectively.

The squared matrix element for polar optical scattering is given by (2.2.7) and (2.2.8). Substituting (2.2.7) into (2.6.1), and integrating over q, one obtains the polar optical scattering rate as

$$\frac{1}{\tau_{po}}=\frac{2eE_0}{(2m\varepsilon)^{1/2}}\left[N_q \sinh^{-1}\left(\frac{\varepsilon}{\hbar\omega_q}\right)^{1/2}+(N_q+1)\sinh^{-1}\left(\frac{\varepsilon-\hbar\omega_q}{\hbar\omega_q}\right)^{1/2}\right], \quad (2.6.2)$$

where E_0 is given by (2.2.8), ε is the kinetic energy of a carrier, $\hbar\omega_q=\hbar\omega_l$ is the energy of a longitudinal optical phonon, N_q is the thermal equilibrium occupation number of phonons given by (2.4.3), the first and second terms in the angular bracket correspond to absorption and emission of a phonon, respectively. The latter appears only if $\varepsilon>\hbar\omega_l$.

The expression (2.6.2) can be used to give a qualitative picture of the variation of scattering rate $1/\tau_{po}$. For $\varepsilon\ll\hbar\omega_q$, it is seen from (2.6.2) that only absorption of phonons is possible, and the scattering rate $1/\tau_{po}$ is small. When ε increases so that emission of phonons becomes possible, the scattering rate $1/\tau_{po}$ will increase. In the limit of $\varepsilon\gg\hbar\omega_q$, (2.6.2) becomes; [10]

$$\frac{1}{\tau_{po}}=\frac{eE_0(2N_q+1)}{(2m\varepsilon)^{1/2}}. \qquad (2.6.3)$$

The scattering rate $1/\tau_{po}$ decreases with increasing ε, essentially as $\varepsilon^{-1/2}$. Since $E_0 \alpha m$ as shown in (2.2.8), the polar optical scattering rate $1/\tau_{po}$ shown in (2.6.3) increases with increasing m, essentially as $m^{1/2}$.

The polar optical intravalley scattering times, τ_{po}, in the Γ valley in GaAs as a function of kinetic energy of electrons (ε) and crystal temperature (T) can be calculated from the equation (2.6.3) using equation (2.4.3) and the parameters given by Blakemore [5].

The calculated τ_{po} as a function of the kinetic energy of electrons, ε, is shown in Fig.2.6.1. The polar optical intravalley scattering rates

decrease with ε as a function of $\varepsilon^{1/2}$.

The calculated τ_{po} as a function of crystal temperature, T, is shown in Fig.2.6.2. At low temperatures T < 50 K, the average number of phonons, N_q, participating in intravalley scattering is almost zero, and therefore, the intravalley scattering rates are very small. When T increases to be greater than 50K, N_q and the intravalley scattering rates increase with T.

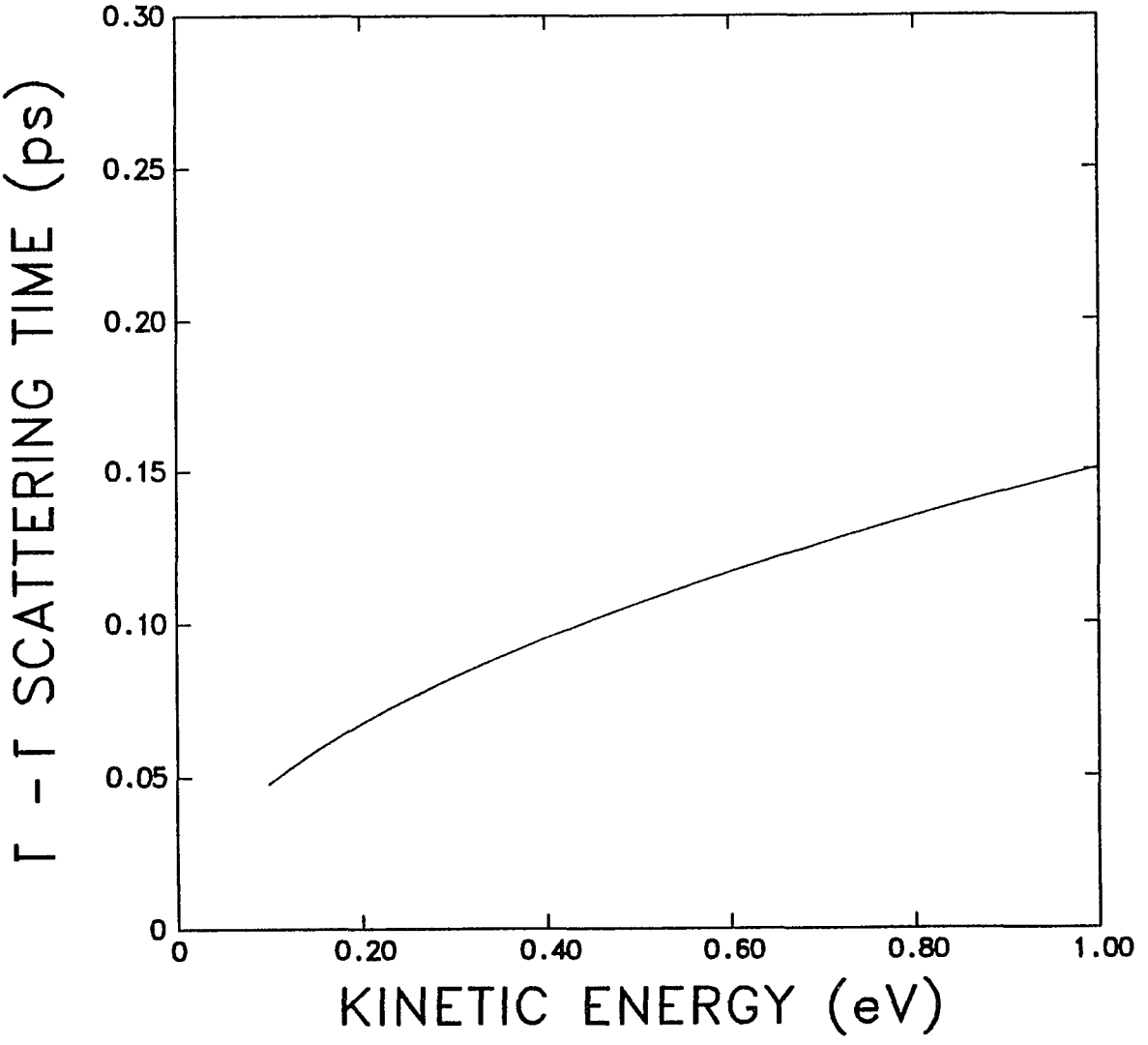

Fig. 2.6.1. Polar optical intravalley scattering time τ_{po} as a function of kinetic energy of electrons.

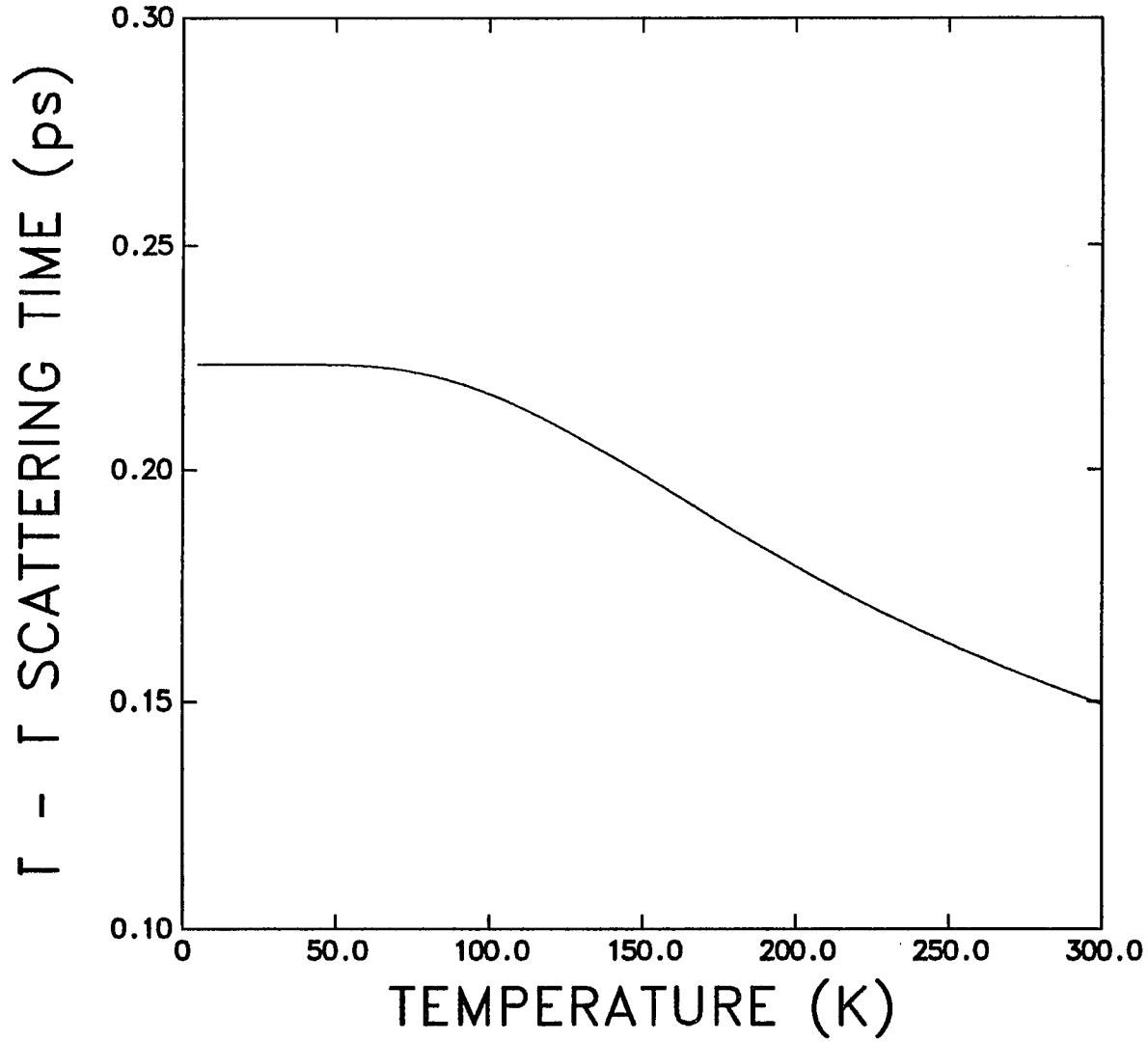

Fig. 2.6.2. Polar optical intravalley scattering time τ_{po} as a function of crystal temperature.

The relaxation rate of carrier energy due to polar optical scattering can be simply obtained from that $\hbar\omega_q$ times the difference between the probability per unit time for phonon absorption and the probability per unit time for phonon emission. The probabilities of absorption and emission of a phonon are given by the first and the second terms of (2.6.2), respectively. The rate of the change in carrier energy due to the polar interaction can then be written

$$(\frac{d\varepsilon}{dt})_{po}=\frac{2eE_0\hbar\omega_q}{(2m\varepsilon)^{1/2}}[N_q\sinh^{-1}(\frac{\varepsilon}{\hbar\omega_q})^{1/2}-(N_q+1)\sinh^{-1}(\frac{\varepsilon-\hbar\omega_q}{\hbar\omega_q})^{1/2}] \quad (2.6.4)$$

For $\varepsilon\gg\hbar\omega_l$, the net energy change is, of course, a loss, given actually by the spontaneous emission, since absorption and stimulated emission essentially cancel in this limit.

There is another channel for electrons to lose their energy by electron-electron interaction. The rate of energy loss of a fast electron to other electrons is given by [10]

$$(\frac{d\varepsilon}{dt})_{e-e}=-\frac{4\pi ne^{*4}}{(2m\varepsilon)^{1/2}}, \quad (2.6.5)$$

where n is the electron density, e^* an effective charge, usually approximated by e divided by the square root of the average dielectric constant, ε and m are energy and effective mass of electrons, respectively.

The electron-electron interaction establishes a Fermi-Dirac distribution without changing their mean energy if elastic scattering is assumed.

Whereas, electron-phonon interaction can change the mean energy of electrons and reduce their effective temperature. For low electron densities, electrons first lose their energy by electron-phonon interactions, then reach their thermal distribution by electron-electron interaction. For high electron densities, a thermalized distribution of hot electrons can be achieved by electron-electron interaction before there is significant energy loss from hot electrons to the lattice.

The electron density required to make these two energy loss rates due to electron-phonon and electron-electron interactions equal is usually called the critical density, n_c. If the carrier density is greater than the critical density, $n>n_c$, the energy loss rate by electron-electron interactions will be greater than that by electron-phonon interaction. Therefore, a thermalized Fermi-Dirac distribution formed by electron-electron interaction can be achieved before there is significant energy loss from the hot electrons to the lattice. [10,11] If $n<n_c$, the hot electrons will first lose their energy to the lattice by electron-phonon interaction, and then achieve their thermalized equilibrium distribution by electron-electron interaction.

The critical electron density, n_c, can be obtained by equating (2.6.4) to (2.6.5) as shown by

$$\frac{4\pi n_c e^{*4}}{(2m\varepsilon)^{1/2}}=\frac{2eE_0\hbar\omega_q}{(2m\varepsilon)^{1/2}}[N_q\sinh^{-1}(\frac{\varepsilon}{\hbar\omega_q})^{1/2}-(N_q+1)\sinh^{-1}(\frac{\varepsilon-\hbar\omega_q}{\hbar\omega_q})^{1/2}]. \quad (2.6.6)$$

Consequently,

$$n_c=\frac{2eE_0\hbar\omega_q}{4\pi e^{*4}}[N_q\sinh^{-1}(\frac{\varepsilon}{\hbar\omega_q})^{1/2}-(N_q+1)\sinh^{-1}(\frac{\varepsilon-\hbar\omega_q}{\hbar\omega_q})^{1/2}], \quad (2.6.7)$$

where E_0 and N_q are given by (2.2.8) and (2.4.3), respectively. Using the values of m, $\hbar\omega_l$, χ_∞ and χ_0 for GaAs,[5] the critical density n_c for electrons in the Γ valley as a function of the kinetic energy of electrons is calculated and shown in Fig.2.6.3, which shows that n_c is in the range of $3–6\times10^{17}cm^{-3}$ and increases slightly with ε. In an experimental analysis, the Fermi-Dirac distribution can be used for each relaxation step of hot electrons only if the carrier density n in that experiment is greater than the corresponding critical density n_c.

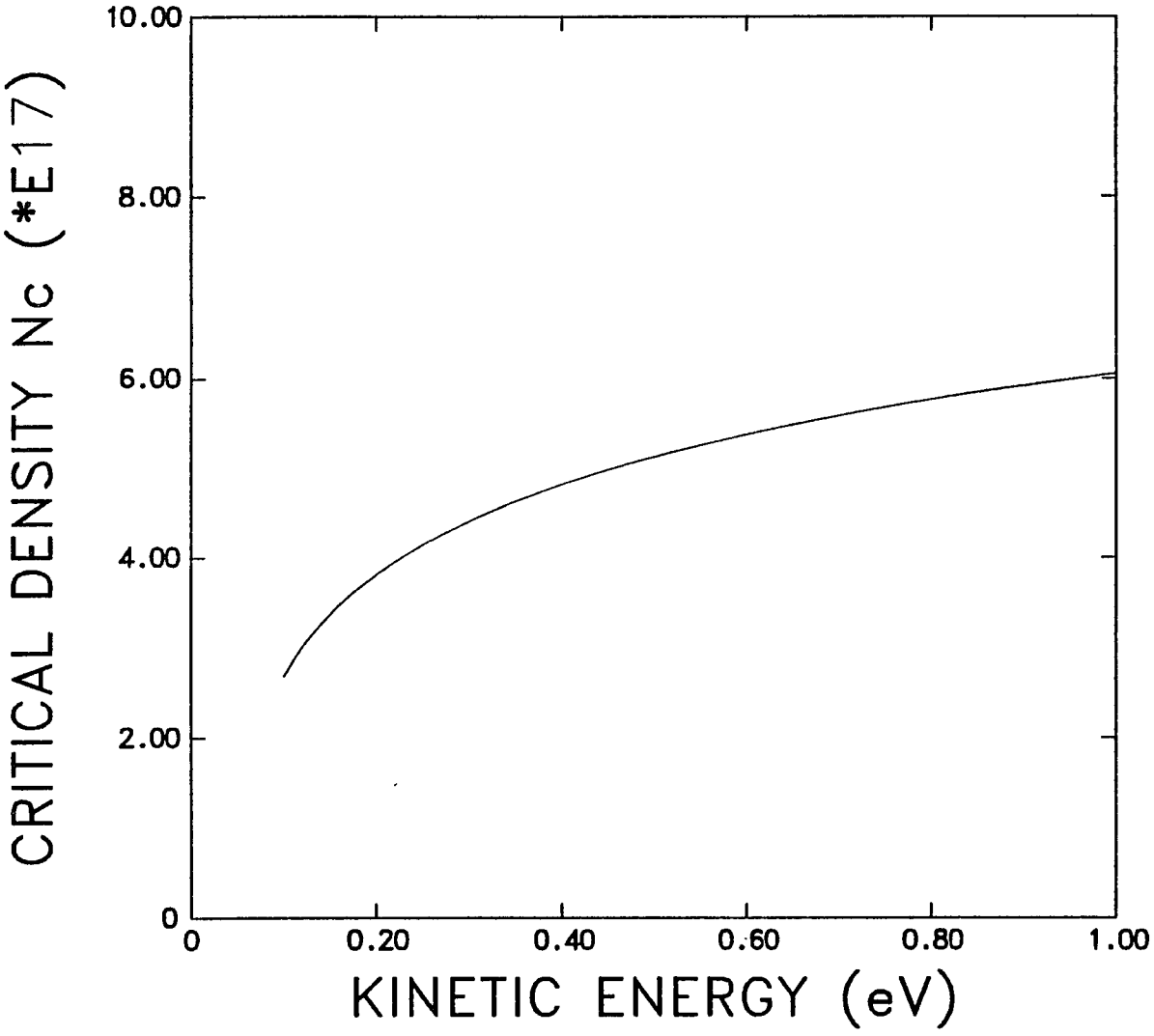

Fig. 2.6.3. The calculated critical density of electrons in the Γ valley to match e-e interactions with e-ph interaction as a function of the kinetic energy of electrons.

REFERENCES

[1] L. Reggiani, in "Hot-Electron Transport in Semiconductors", Springer-Verlag, New York, (1984), ch.2.

[2] K. Seeger, "Semiconductor Physics", Springer-Verlag, Vienna, 1973, Ch. 6 & 7.

[3] B. K. Ridley, "Quantum Processes in Semiconductors", the Second Edition, Oxford Science Publications, Oxford, 1988, Ch. 3.

[4] E. M. Conwell, in "High Field Transport in Semiconductors", Academic Press, New York, (1967), Ch.3.

[5] J. S. Blakemore, Appl. Phys., 53 , R 123 (1982).

[6] J. L. Birman, M. Lax and R. London, Phys. Rev., 145 , 620 (1966).

[7] J. L. Birman, Phys. Rev., 131 , 1489 (1963).

[8] S. Zollner, S. Gopalan, and M. Cardona, Appl. Phys. Lett., 54 , 614 (1989).

[9] H. Ehrenreich, Phys. Rev., 120 , 1951 (1960).

[10] E. M. Conwell, and M. O. Vassell, IEEE Trans. Electron. Devices, ED-13 , 22 (1966).

[11] J. C. Tsang, and J. A. Kash, Phys. Rev., B34 , 6003 (1986).

Chapter 3

THEORY II: HOT CARRIER DYNAMICS IN GaAs and AlGaAs

3.1. Band Structure for GaAs

Over the years, physicists have been concerned with the order of the eigen energies of three types of Brillouin zone locations where the lowest conduction band dips to a minimum, namely Γ(000), L(111), and X(100). Prior to 1976, many band structure calculations and experiments [1] showed that the conduction band order for GaAs was Γ-X-L. However, in 1976, a measurement of the UV Schottky barrier electron-reflectance by Aspnes et al [2] clearly demonstrated the Γ-L-X ordering. The literature on GaAs in subsequent years has made a rapid adjustment to the abruptly altered perception of the conduction bands. Now, the Γ-L-X ordering for energies of the conduction band valleys in GaAs, shown in Fig.3.1.1, has been widely accepted to be the true one. [1] The energy gaps, E_g^{Γ}, E_g^{L}, and E_g^{X}, measured from the top of the valence bands to the bottoms of the Γ_6, L_6, and X_6 conduction valleys are 1.42 eV, 1.71 eV, and 1.90 eV, respectively.

The energy gaps of E_g^{Γ}, E_g^{L}, and E_g^{X} change with temperature and pressure. The temperature dependence of the energy gaps was suggested to be (in eV) [1]

$$E_g^{\Gamma}(T)=1.519-5.405\times10^{-4}T^2/(T+204), \qquad (3.1.1)$$

$$E_g^{L}(T)=1.815-6.05\times10^{-4}T^2/(T+204), \qquad (3.1.2)$$

$$E_g^X(T)=1.981-4.60\times10^{-4}T^2/(T+204). \quad (3.1.3)$$

The pressure dependence of the energy gaps can be approximately considered to be linear as [3]

$$dE_g^\Gamma(P)/dP=+11.5\times10^{-3}eV/Kbar, \quad (3.1.4)$$

$$dE_g^L(P)/dP=+2.8\times10^{-3}eV/Kbar, \quad (3.1.5)$$

$$dE_g^X(P)/dP=-0.8\times10^{-3}eV/Kbar. \quad (3.1.6)$$

The density of states effective mass for each of the conduction and valence bands in GaAs are shown in Table 3.1.1. [1] The phonon frequency and energy for each of the Brillouin zone high symmetry locations in GaAs are listed in Table 3.1.2.

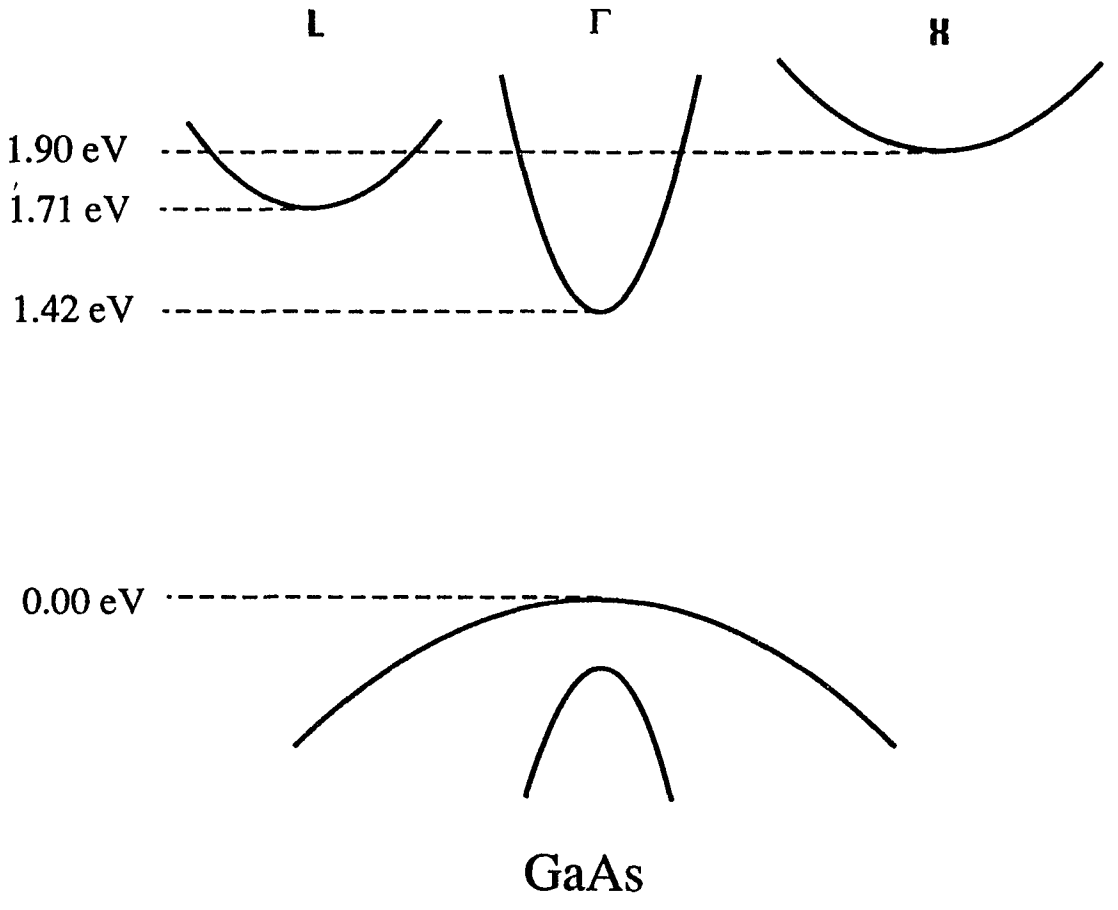

Fig.3.1.1. The Γ-L-X ordering for energies of the conduction band valleys for GaAs. [1]

Table 3.1.1. The density of states effective mass for each of the conduction and valence bands in GaAs. [1]

For Γ_6 conduction band:	$m_{\Gamma_6}=0.0632m_0$
For L_6 conduction band:	$m_{L_6}=0.55m_0$
For X_6 conduction band:	$m_{X_6}=0.85m_0$
For heavy-hole band:	$m_{hh}=0.50m_0$
For light-hole band:	$m_{lh}=0.088m_0$
For split-off band:	$m_{so}=0.15m_0$

Table 3.1.2. The phonon frequency and energy for each of the Brillouin zone high symmetry locations in GaAs. [1]

Reciprocal space location	Mode character	ν (10^{12} Hz)	$h\nu$ (meV)
Γ ($q = 000$)	LO	8.55 ± 0.2	35.4 ± 0.8
	TO	8.02 ± 0.08	33.2 ± 0.3
X ($q = 100$) and R ($q = 0\bar{1}1$)	TO	7.56 ± 0.08	31.3 ± 0.3
	LO	7.22 ± 0.15	29.9 ± 0.6
	LA	6.80 ± 0.06	28.1 ± 0.25
	TA	2.36 ± 0.015	9.75 ± 0.06
$L\left(q = \frac{1}{2}\frac{\bar{1}}{2}\frac{1}{2}\right)$	TO	7.84 ± 0.12	32.4 ± 0.5
	LO	7.15 ± 0.07	29.6 ± 0.3
	LA	6.26 ± 0.10	25.9 ± 0.4
	TA	1.86 ± 0.02	7.70 ± 0.08
$K\left(q = 0\frac{\bar{3}}{4}\frac{3}{4}\right)$	$TO_{\parallel}$	7.90 ± 0.15	32.7 ± 0.6
	$TO_{\perp}$	7.51 ± 0.12	31.1 ± 0.5
	LO	6.44 ± 0.12	26.6 ± 0.5
	LA	5.65 ± 0.12	23.4 ± 0.5
	$TA_{\parallel}$	3.48 ± 0.06	14.4 ± 0.25
	$TA_{\perp}$	2.38 ± 0.04	9.58 ± 0.15

3.2. Direct-to-Indirect Band Gap Trasition in $Al_xGa_{1-x}As$

A considerable number of theoretical and experimental groups have investigated the electronic band structure of $Al_xGa_{1-x}As$ and determined the compositional dependence of its energy gaps (E_g's).[3] Casey and Ponish[4] suggested that the Γ direct gap (E_g^{Γ}), and the L and X indirect gaps (E_g^{L} and E_g^{X}, respectively) at 300 K may be represented by (in eV)

$$E_g^{\Gamma}(x)=1.424+1.247x+1.147\Theta(x-0.45)(x-0.45)^2 \qquad (3.2.1)$$

$$E_g^{L}(x)=1.708+0.642x \qquad (3.2.2)$$

$$E_g^{X}(x)=1.900+0.125x+0.143x^2 \qquad (3.2.3)$$

where $\Theta(x-0.45)$ is a Θ function which is 0 for $x<0.45$ and 1 for $x>0.45$.

Lee et al[5] also quoted the dependence of E_g's on x at room temperature in $Al_xGa_{1-x}As$ alloy as (in eV)

$$E_g^{\Gamma}(x)=1.425+1.155x+0.37x^2 \qquad (3.2.4)$$

$$E_g^{L}(x)=1.734+0.574x+0.055x^2 \qquad (3.2.5)$$

$$E_g^{X}(x)=1.911+0.005x+0.245x^2 \qquad (3.2.6)$$

The band gaps of E_g^{Γ}, E_g^{L} and E_g^{X}, as functions of x calculated using equations (3.2.1) to (3.2.3) are shown in Fig.3.2.1, which indicates that $Al_xGa_{1-x}As$ with a small value of x has a direct band gap, whereas with a large value of x has an indirect band gap. The value of Al content x at which a direct-to-indirect band gap transition occurs is called the

critical value or crossover value marked as x_c and shown in Fig.1.1.2. This value can be obtained by solving the equation $E_g^X(x_c)=E_g^\Gamma(x_c)$.

Since the values of $E_g^\Gamma(x)$ vary greatly from 1.424 eV for x=0 to 3.018 eV for x=1, and the values of $E_g^X(x)$ change slightly from 1.900 eV for x=0 to 2.168 eV for x=1, [3] the more sensitive one for determining x_c is not the function $E_g^X(x)$, but $E_g^\Gamma(x)$. Therefore, most of the previous band structure investigations have paid more attention to the determination of the coefficient for the change in the direct gap, $\alpha=\Delta E_g^\Gamma/\Delta x$, suggested to be linear with x in the range of $x<x_c$, and the critical value of x_c. However, the reported values span a large range from 12.47 meV/% to 14.55 meV/% for $\alpha=\Delta E_g^\Gamma/\Delta x$, and from 0.37 to 0.45 for x_c. [4,6] The difference of the values of $E_g^\Gamma(x)$ for $x\leq x_c$ calculated using Ref.4 and Ref.6 are shown in Fig.3.2.2. The method to determine the value of x_c for $Al_xGa_{1-x}As$ by pump-IR-probe measurement will be discussed in section 3.6 and chapter 9.

The density of states effective masses for each of the conduction and valence bands in $Al_xGa_{1-x}As$ as a function of x are shown in Table 3.2.1.

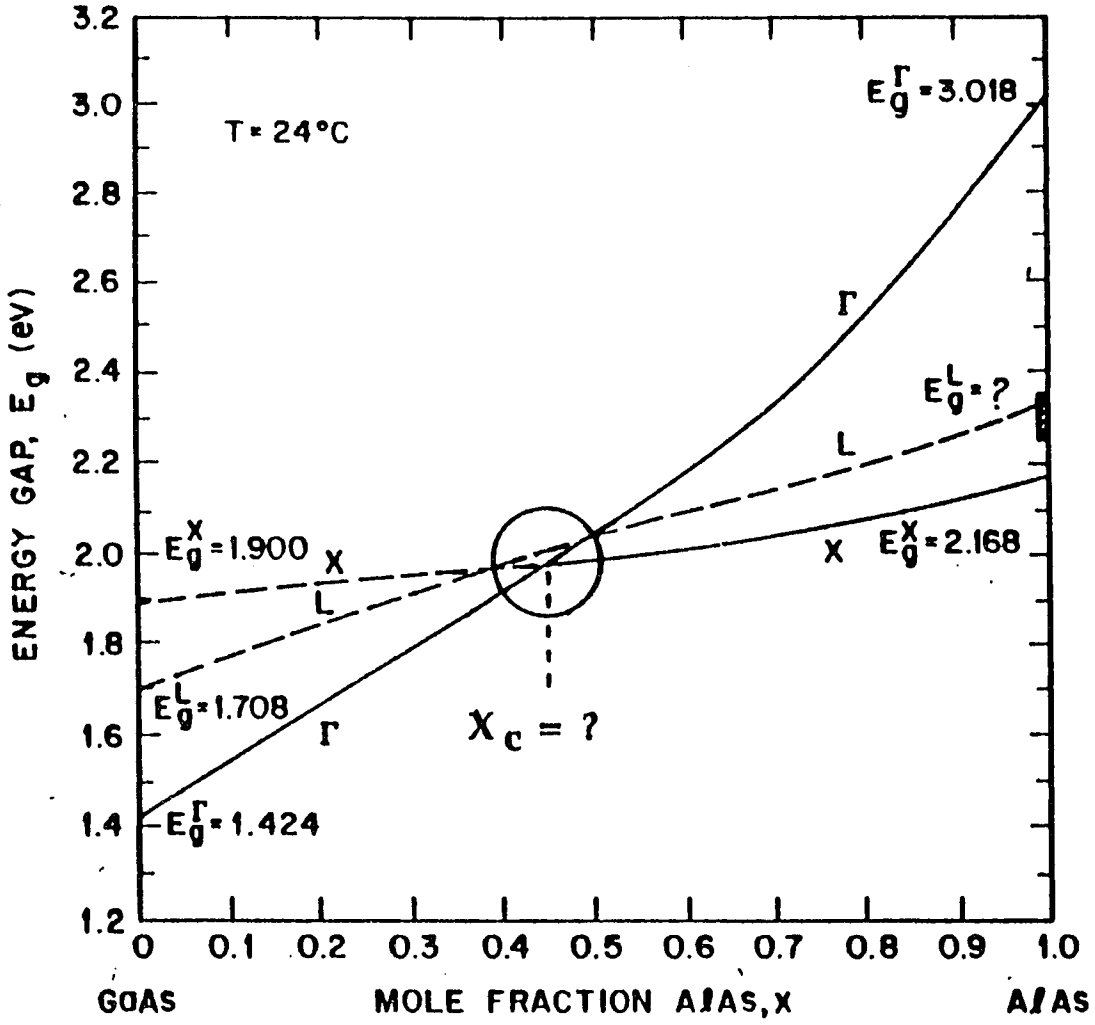

Fig.3.2.1. The band gaps of $E_g{}^\Gamma(x)$, $E_g{}^L(x)$, and $E_g{}^X(x)$ as functions of x in $Al_xGa_{1-x}As$ calculated using equations given by Casey.[4]

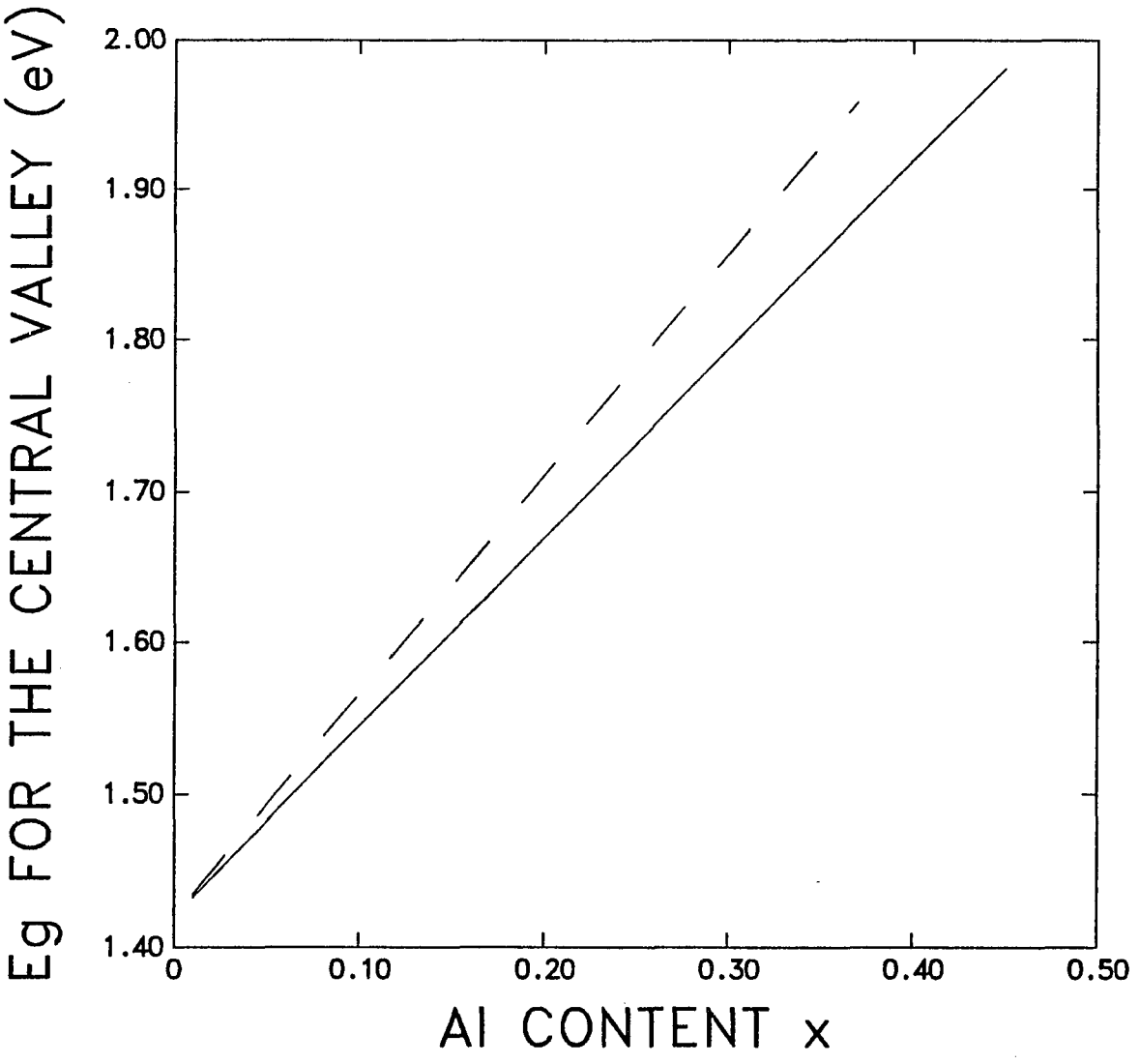

Fig.3.2.2. The values of $E_g^{\Gamma}(x)$, in the range of $x \leq x_c$ as a function of x for $Al_xGa_{1-x}As$ calculated using the values[4] of $\alpha=\Delta E_g^{\Gamma}/\Delta x=12.47$ meV/% and $x_c=0.45$ (solid line), and that[6] of $\Delta E_g^{\Gamma}/\Delta x=14.55$ meV/% and $x_c=0.37$ (dashed line).

Table 3.2.1. The density of states effective mass for each of the conduction and valence bands in $Al_xGa_{1-x}As$ [3]

$m_e^{\Gamma}=0.067+0.083x$

$m_e^{L}=0.56+0.1x$

$m_e^{X}=0.85-0.14x$

$m_{hh}=0.62+0.14x$

$m_{lh}=0.087+0.063x$

$m_{s-off}=0.15+0.09x$

3.3. Effect of Intervalley Scattering on Hot Carrier Relaxation

If electrons in GaAs excited by photons or high electric fields obtain a kinetic energy less than $\Delta E_{L\Gamma}=E_g{}^L-E_g{}^\Gamma$, they can only undergo intravalley scattering in the Γ valley, and their relaxation time will be fast. For example, with a pump of 1.66 eV photons for GaAs, only intravalley scattering is involved because $1.66\ eV < E_g{}^L$ as shown in Fig.3.3.1. It takes only ~ 2 ps for electrons to relax from their initial energy of ~ 0.21 eV to the bottom of the Γ valley measured by Oberli [7] as shown in Fig.3.3.2. This result agrees with the time-dependent spontaneous Raman measurement on GaAs by Kash et al, [8] who have resolved the growth time of ~ 2 ps of the optically induced nonequilibrium LO-phonon population and deduced an average electron-phonon scattering time of 165 fs in the Γ valley. [8]

In the case of hot electrons excited to the Γ valley with sufficient energy to undergo $\Gamma\rightarrow L$ scattering, the decay of the hot electrons from their initial energy to the bottom of the Γ valley will be much slower than that without intervalley scattering. For example, with a pump of 2.04 eV ($> E_g{}^L$ for GaAs) photons, electrons can undergo the $\Gamma\rightarrow L$ intervalley scattering as well as intravalley scattering inside each of the Γ and L valleys [1] as shown in Fig.3.3.1. The total relaxation time of the electrons from their initial energy to the bottom of the Γ valley was measured to be ~ 10 ps [7] which is much longer than that of ~ 2 ps without the $\Gamma\rightarrow L$ intervalley scattering in GaAs with $E_{pump}=1.66eV$ [7].

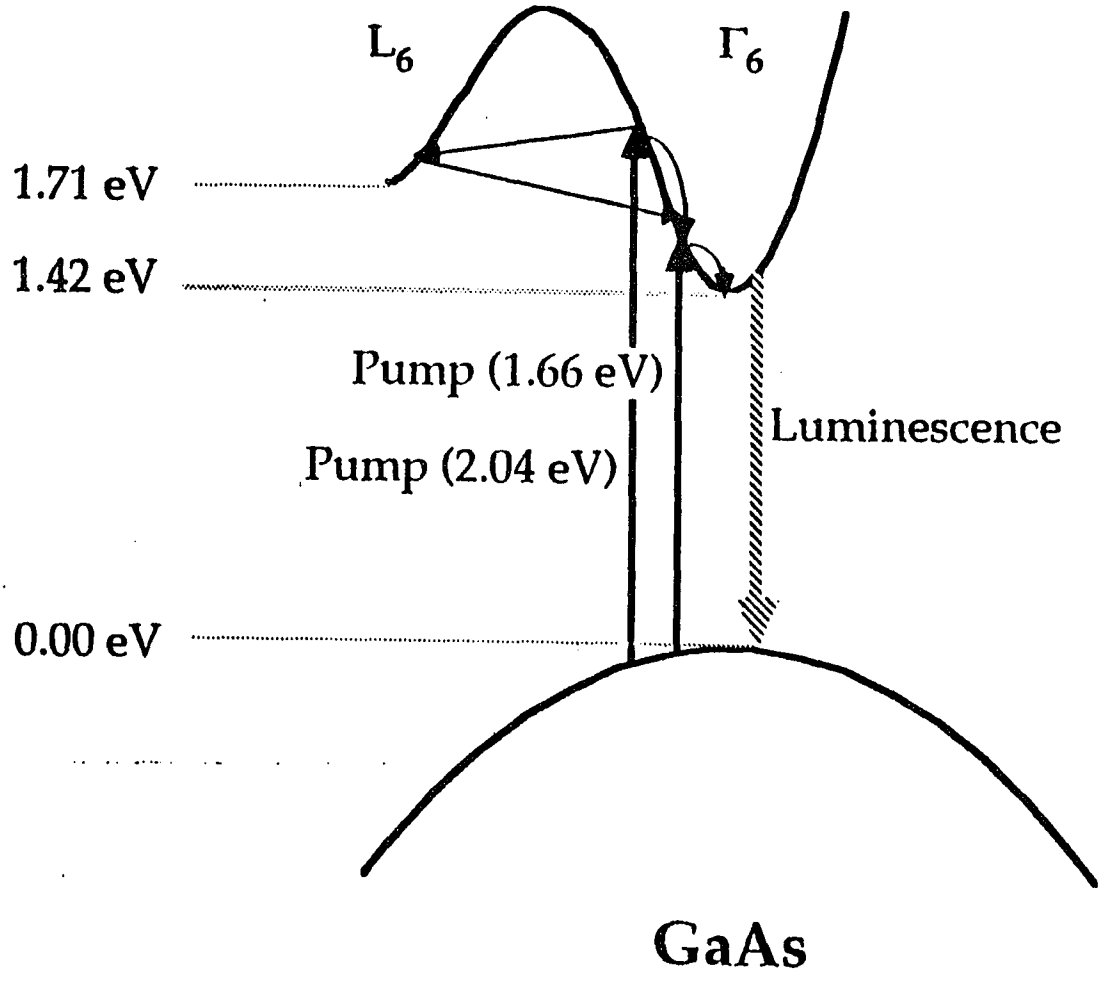

Fig. 3.3.1. Schematic diagram for the comparison of pumps with 1.66 eV and 2.04 eV photons in GaAs. The $\Gamma \rightarrow L$ intervalley scattering is involved for the pump at 2.04 eV because 2.04 eV > $E_g{}^L$, but not involved for the pump at 1.66 eV because 1.66 eV < $E_g{}^L$.

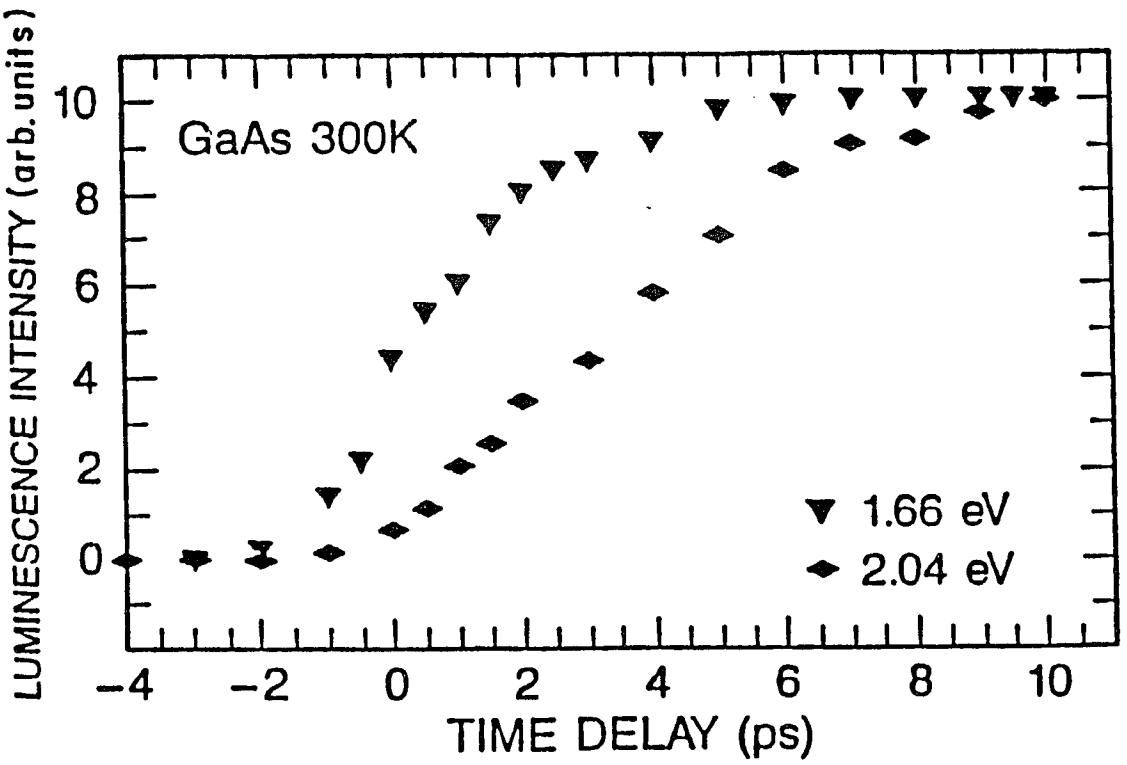

Fig. 3.3.2. The comparison of the time evolution of near-band-gap luminescence intensity in GaAs at 300 K for excitation at 1.66 eV (triangles) and 2.04 eV (squares).[7] The risetime of ~ 2 ps for the pump at 1.66 eV, in which no intervalley scattering is involved, is much shorter than that of ~ 10 ps for the pump at 2.04 eV, in which the $\Gamma \rightarrow L$ intervalley scattering is involved. This shows that intervalley scattering acts as a source for heating of electrons in the Γ valley.

Another example showing the effect of intervalley scattering in hot carrier relaxation are the measurements on GaAs and InP with the same pump of 2.04 eV photons[9]. Since $E_{0L}<2.04eV$ for GaAs, and $E_{0L}>2.04eV$ for InP, there is no intervalley scattering involved in InP as shown in Fig.3.3.3. The hot electron relaxation times were measured to be ~ 2 ps for InP and ~ 10 ps for GaAs as shown in Fig.3.3.4.

Both of the measurements mentioned above show that intervalley scattering slows down the relaxation of hot electrons. In fact, if the $L \rightarrow \Gamma$ back scattering time is longer than the $\Gamma \rightarrow L$, $\Gamma \rightarrow \Gamma$, and $L \rightarrow L$ scattering times, electrons in the L valley will decay to the bottom of the L valley and stay there for a relatively longer time. When those electrons scatter back to the Γ valley, they will release their extra potential energy and heat the Γ valley electrons. Therefore, intervalley scattering between different conduction band valleys acts as a source for heating of electrons, and increases the relaxation time of hot electrons.

Since intervalley scattering increases the relaxation time of hot electrons, the measured relaxation time of hot electrons can be used to determine corresponding intervalley scattering times by rate equation or other types of analysis. For example, the time evolution of the population of the Γ valley electrons in GaAs obtained from a time-resolved hot-luminescence measurement[9] yields the determination of $t_{\Gamma L}$=100 fs and $t_{L\Gamma}$= 2.5 ps by a Monte-Carlo analysis as shown in Fig. 3.3.4.[9]

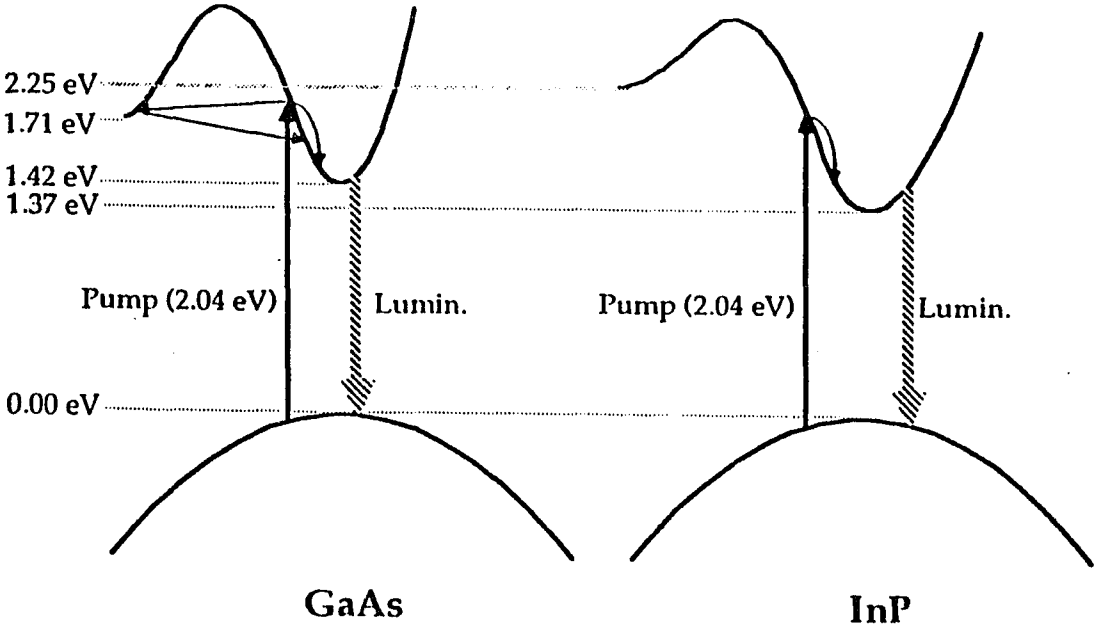

Fig.3.3.3. Schematic diagram for the comparison of excitation at 2.04 eV for GaAs and InP. The $\Gamma \rightarrow L$ intervalley scattering is involved for GaAs because its $E_g{}^L$ is smaller than 2.04 eV, but not involved for InP because its $E_g{}^L$ is greater than 2.04 eV.

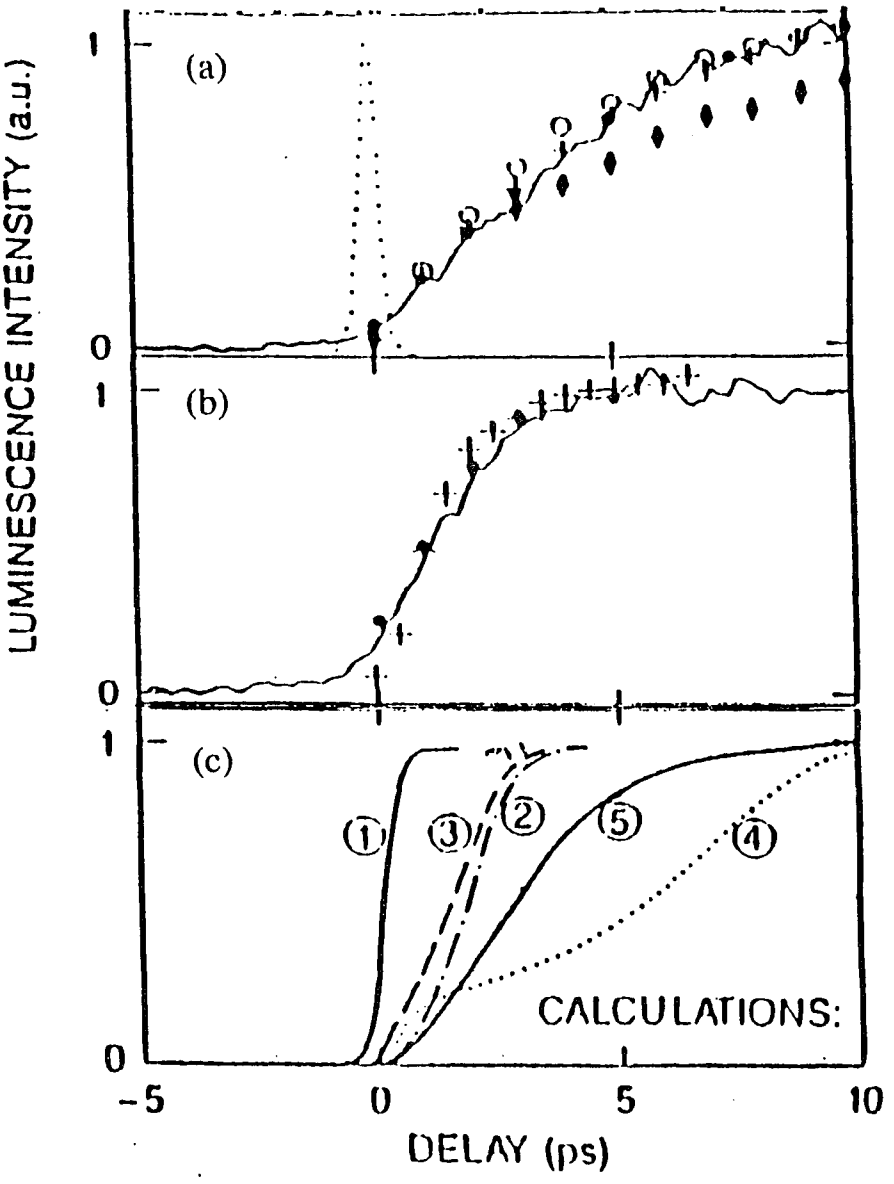

Fig. 3.3.4. The Comparison of the rise portion of the near band gap luminescence at 300 K versus delay time excited by 2.04 eV photons for (a) GaAs, (b) InP, and (c) different fitting curves for (a) calculated by Monte-Carlo method in which curve (5) gives the best fit to the experimental data which corresponds to $t_{\Gamma L}$ = 100 fs and $t_{L\Gamma}$ = 2.5 ps.[9]

3.4. Time Evolution of Electron Population in the X Valley in GaAs

If excited electrons in GaAs obtain a kinetic energy greater than 0.48 eV, they will undergo not only the $\Gamma \rightarrow L$ but also the $\Gamma \rightarrow X$ intervalley scattering. For example, electrons excited by 527 nm photons from the heavy-hole and light-hole bands to the Γ conduction band will obtain a kinetic energy of about 0.83 eV which is sufficient for electrons to scatter to the L and X valleys from which they can scatter to other valleys as schematically shown in Fig. 3.4.1. At the same time, electrons in each of the valleys lose their energy by intravalley scattering. The x valley-involved intervalley scattering can occur many times before the electrons in the Γ and L valleys have insufficient energy ($<$ 0.48 eV for the Γ valley electrons and $<$ 0.19 eV for the L valley minimum) to scatter to the X valley. Therefore, with increasing delay time, the population of electrons in the X_6 band should rapidly increase at first due mostly to the $\Gamma_6 \rightarrow X_6$ scattering, reach a maximum, and then decrease due to the $X_6 \rightarrow \Gamma_6, L_6$ back intervalley scattering and the intravalley scattering in the Γ_6 and L_6 valleys. Since a measurement by Seymour and Alfano [10] showed that it takes ~ 25 ps for hot electrons to decay from an initial kinetic energy of 0.83 eV to the bottom of the Γ_6 valley, the time for hot electrons to lose their initial energy of 0.83 eV to the X_6 minimum energy of 0.48 eV should be shorter than 25 ps. When the energy of hot electrons falls below the X_6 minimum energy, the population of the X_6 electrons would be expected to approach zero.

This time evolution of electron population in the X valley in GaAs, namely N_X, characterized by a rapid risetime and a short decay time can be monitored by the $X_6 \rightarrow X_7$ IR interconduction band absorption (ICA) as shown in Fig.3.4.1. Since the kinetic energy of the excited electrons in the Γ valley is insufficient to make strong $\Gamma_6 \rightarrow X_7$ intervalley scattering, [11] the X_7 band is almost empty. Therefore, the time-dependence of the $X_6 \rightarrow X_7$ absorption directly reflects the time-evolution of the electron population in the X_6 valley.

The decay time of the electron population in the X_6 valley is dominated by the back scattering time from the X_6 valley to the Γ_6 and L_6 valleys. A direct measurement of the time evolution of the electron population in the X_6 valley by a 527 nm-pump and IR-probe absorption spectroscopy yielded a determination of the $X \rightarrow \Gamma$ back scattering time of 500 ± 350 fs for GaAs, [12] which will be discussed in detail in chapter 5.

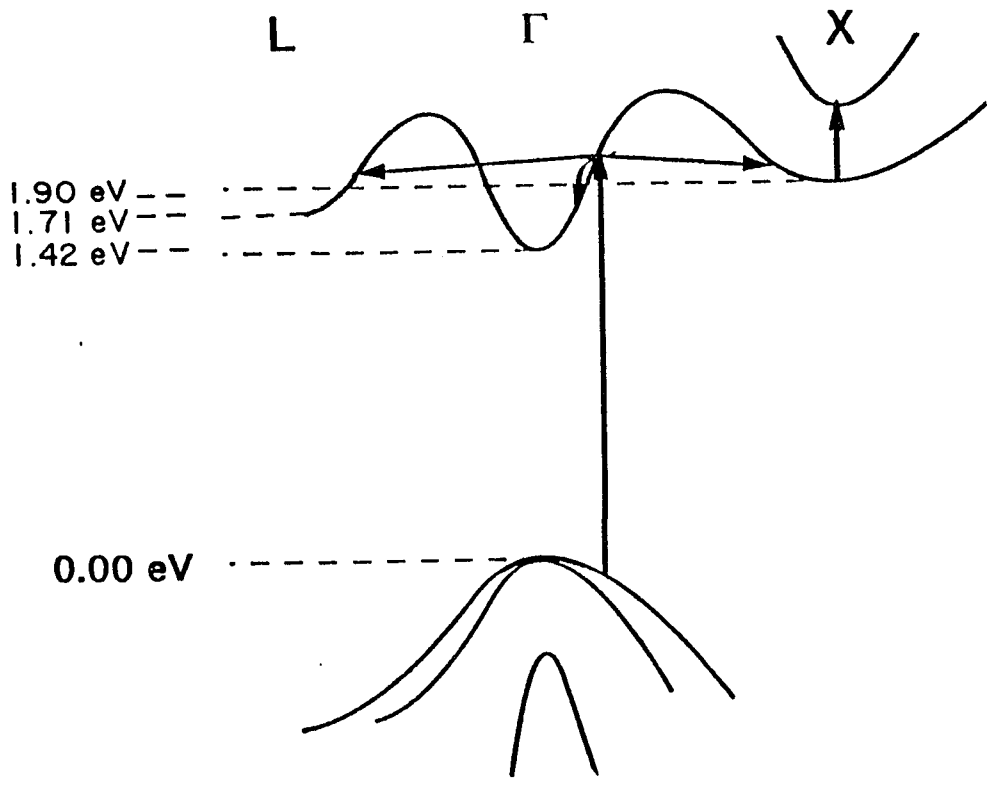

Fig.3.4.1. Schematic diagram for the three valley (Γ, L and X)-involved intervalley scattering and the $X_6 \rightarrow X_7$ IR absorption for GaAs.

3.5. Temporal Profile of the Electron Population in the X valley in $Al_xGa_{1-x}As$

The temporal profile of the decay of the electron population in the X_6 valley in $Al_xGa_{1-x}As$ depends on its band structure which varies with x.

An $Al_xGa_{1-x}As$ sample with $x<x_c$ has a GaAs-like direct band gap.[3] Electrons pumped, for example, by 585 nm photons obtain sufficient energy to undergo intervalley scattering from the Γ valley to the L and X valleys[3]. Similar to that in GaAs, the population of electrons at the bottom of the X valley, N_X, rapidly increases at first to its maximum due to the $\Gamma \rightarrow X$ and $L \rightarrow X$ intervalley scattering and the $X \rightarrow X$ intravalley scattering. Since the minimum of the X_6 valley is much higher than that of the Γ and L valleys, electrons stay in the X_6 valley for only a short time, and then scatter to the Γ and L valleys. Therefore, N_X and the $X_6 \rightarrow X_7$ ICA as a function of t_d should have a short decay as shown in Fig.3.5.1, in which the flat decay corresponds to free carrier absorption.

An $Al_xGa_{1-x}As$ sample with $x>x_c$ has an AlAs-like indirect band gap.[3] If pump photons have sufficient energy to excite electrons to reach the X, L and Γ valleys, electrons will undergo inter-and-intravalley scattering. Since the X_6 minimum is lower than the Γ and L minima, almost all of the electrons will finally scatter into the X_6 valley and stay at its bottom until they recombine with holes in a few hundred nanoseconds[14]. Therefore, the decay of the $X_6 \rightarrow X_7$ ICA should be flat in a small range of delay time, such as 50 ps, as shown in Fig.3.5.2. The rise time of the $X_6 \rightarrow X_7$

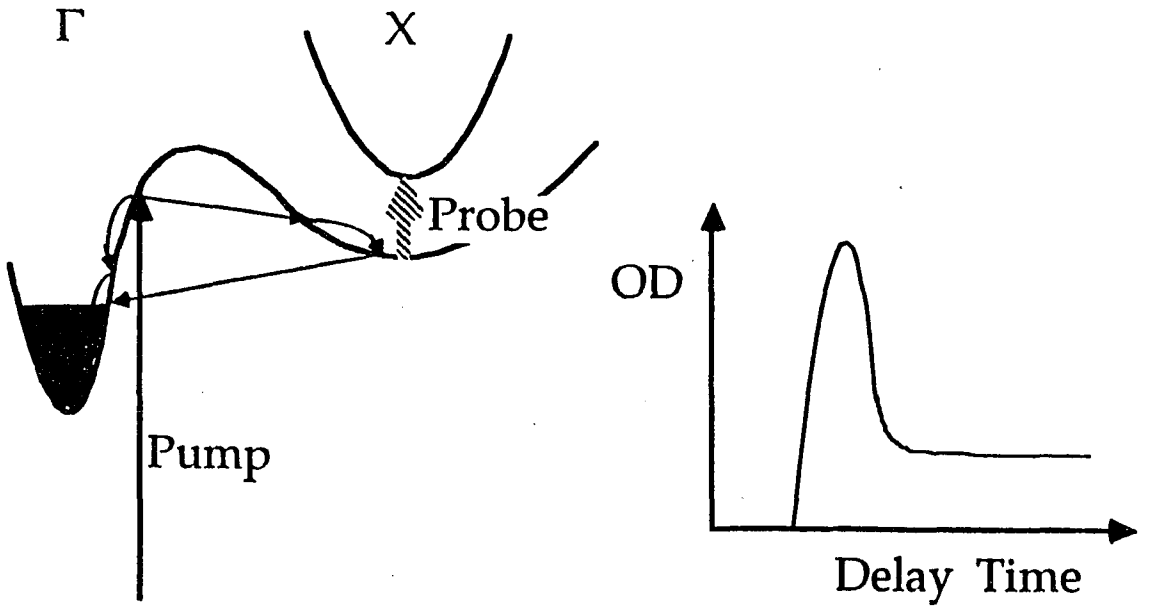

Fig. 3.5.1. Band structure of $Al_xGa_{1-x}As$ with $x \ll x_c$ and the corresponding IR absorption profile.

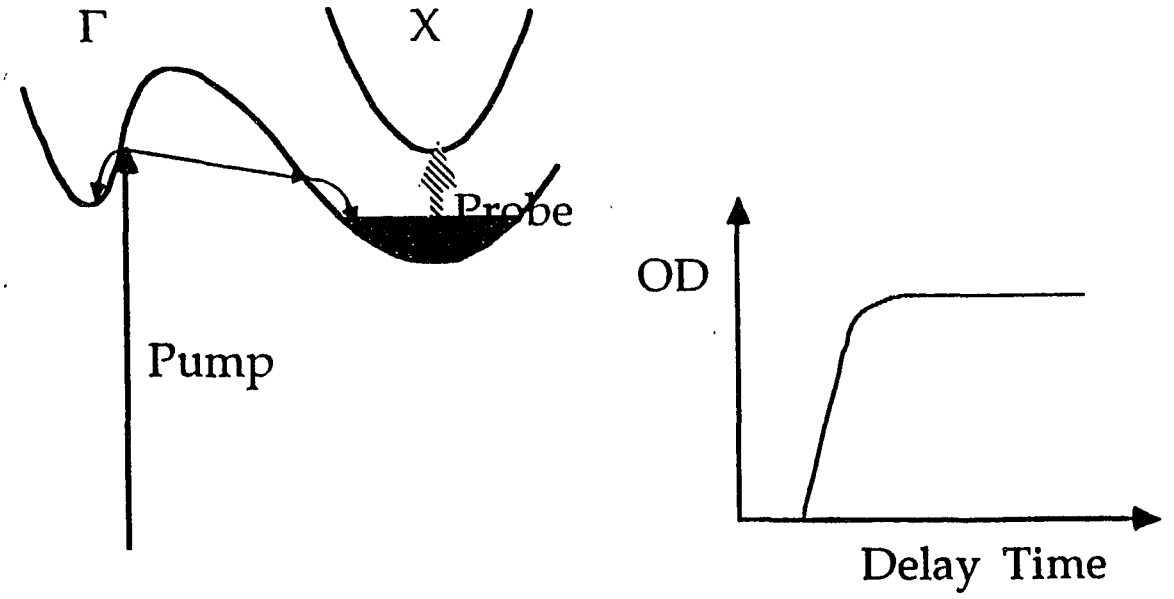

Fig. 3.5.2. Band structure of $Al_xGa_{1-x}As$ with $x \gg x_c$ and the corresponding IR absorption profile.

absorption is dominated by the inter-and-intravalley scattering times. Therefore, measurement of the time-resolved $X_6 \rightarrow X_7$ IR absorption can yield the determination of the corresponding scattering time. For example, a measurement on $Al_{0.6}Ga_{0.4}As$ using a 585 nm-pump and IR-probe gave a determination of the $L \rightarrow X$ intervalley scattering time of ~ 200 fs, [15] which will be discussed in chapter 8.

In order to understand the change of the decay portion of the IR absorption profile with x, the case for $x \approx x_c$ should be considered. When x increases to almost x_c, the minimum of the X valley is slightly higher than that for the Γ valley. When final thermal equilibrium among the electrons in the Γ, L, and X valleys is obtained, not all of the electrons will be in the Γ valley but some of them will occupy the L and X valleys as schematically shown in Fig.3.5.3. In other words, not all of the X_6 valley electrons will scatter back to the Γ and L valleys, but some of them will stay in the X_6 valley for a long time, which will result in the $X_6 \rightarrow X_7$ ICA having a long flat decay. For this type of direct band gap $Al_xGa_{1-x}As$ alloys, the $X_6 \rightarrow X_7$ ICA would have both short and flat decay components as shown in Fig.3.5.4. When the energy difference between the X and Γ minima, $\Delta E_{X\Gamma}=E_g^X-E_g^\Gamma$, decreases, the number of electrons in the X valley relative to the total number of electrons in thermal equilibrium will increase, and as a result, the flat decay portion of ICA will become larger, and the short decay portion of ICA will decrease. Consequently, the measured percentage of the short decay portion of ICA relative to the total

absorption, defined as a parameter $K_{short}=(OD)_{short}/(OD)_{total}$, directly reflects the value of $\Delta E_{X\Gamma}$ for an $Al_xGa_{1-x}As$ alloy. The critical value of x_c for which $\Delta E=0$ can be obtained from the measured x dependence of ΔE.

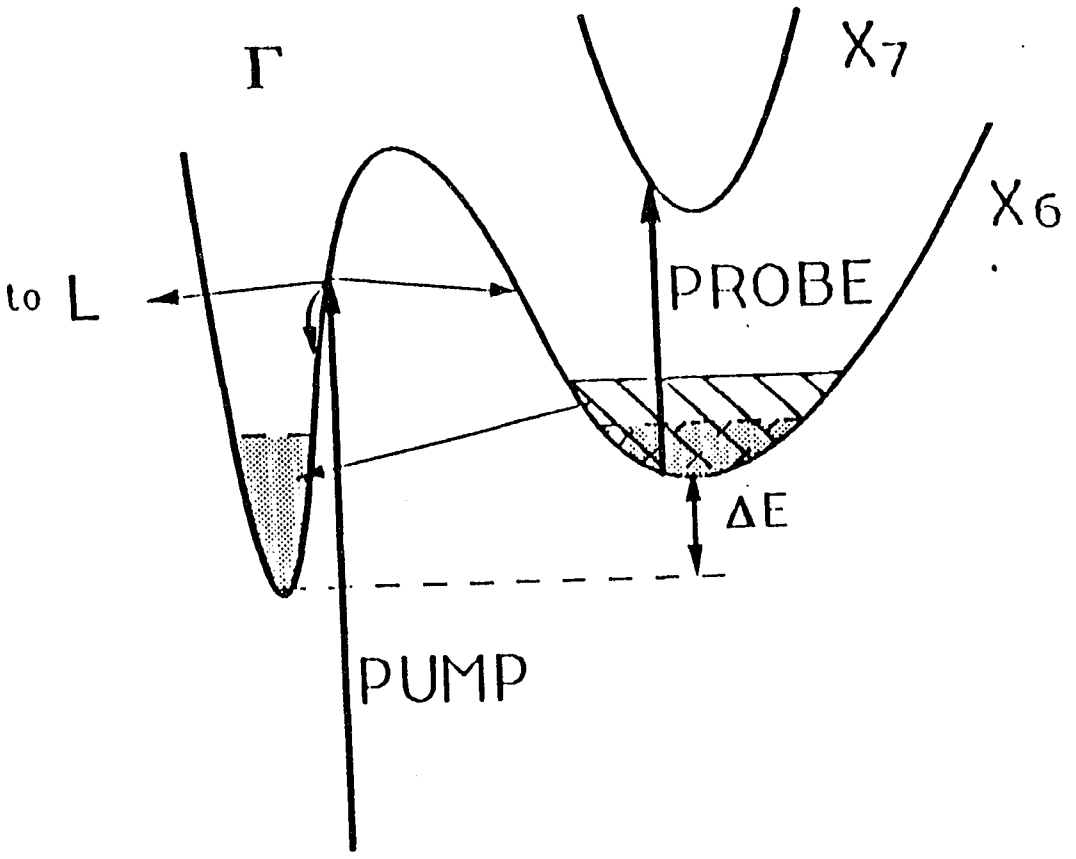

Fig. 3.5.3. Schematic diagram indicating band structure involving the Γ and X valleys in $Al_xGa_{1-x}As$ for x slightly smaller than x_c showing ΔE, N_X at t_{peak} (diagonal solid lines) and t_{flat} (shaded area with diagonal dashed lines) as defined in the text. [13]

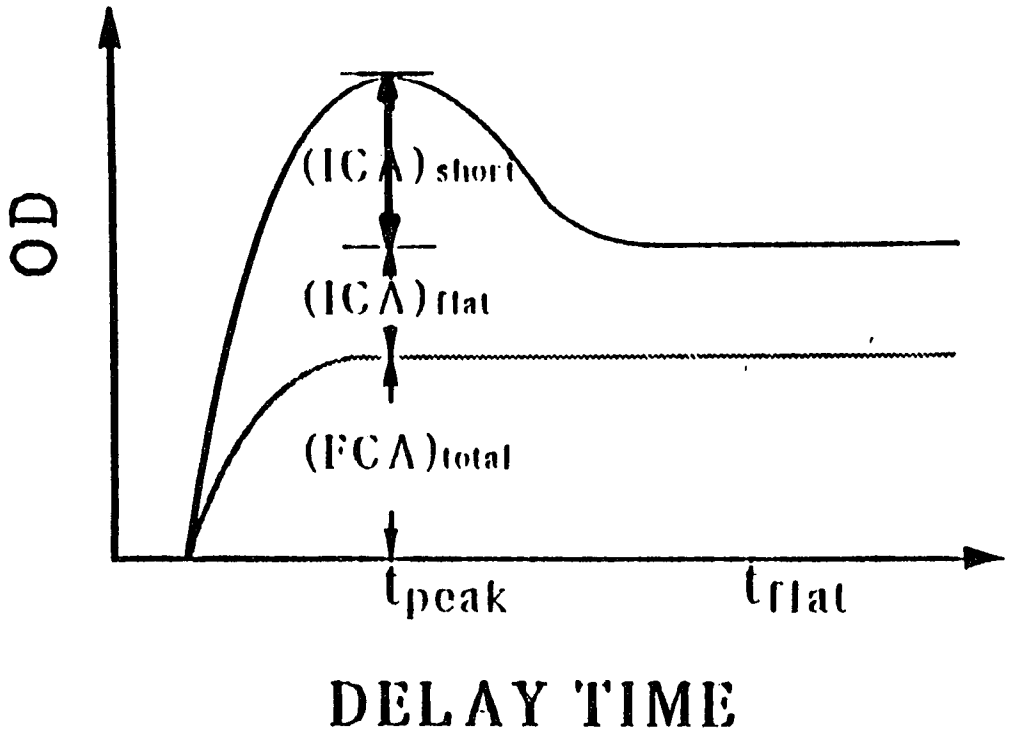

Fig. 3.5.4. A profile of the induced total absorption for $Al_xGa_{1-x}As$ with $x \sim x_c$ showing absorption portions $(ICA)_{short}$, $(ICA)_{flat}$, and $(ICA)_{total}$, and delay times t_{peak} and t_{flat} as described in the text. [13]

3.6. Short Decay Component of N_X and Determination of x_c

In order to mathematically describe the change of the short decay component with x, we write the parameter K_{short} as [13]

$$K_{short}=(ICA)_{short}/[(ICA)_{total}+(FCA)_{total}], \tag{3.6.1}$$

where $(FCA)_{total}$, $(ICA)_{total}=(ICA)_{short}+(ICA)_{flat}$, and $(ICA)_{short}$, indicated in Fig.3.5.4, correspond to the total absorption for FCA and ICA, and the short decay component of ICA at the absorption peak, respectively.

The $(FCA)_{total}$ and $(ICA)_{total}$ are given by

$$(FCA)_{total}=\sigma_{FC}N, \tag{3.6.2}$$

and

$$(ICA)_{total}=\sigma_{IC}p_X N, \tag{3.6.3}$$

where σ_{FC} and σ_{IC} are cross sections for FCA and ICA, respectively; N is the total carrier density; p_x is the fraction of the carrier density in the X valley relative to the total carrier density at the delay time corresponding to the absorption peak, t_{peak} (see Fig.3.5.4).

The flat decay component of ICA is given by

$$(ICA)_{flat}=\sigma_{IC}f_X N, \tag{3.6.4}$$

where f_X is the fraction of carrier density in the X valley relative to the total carrier density at the delay time corresponding to the flat absorption region, t_{flat} (see Fig.3.5.4). The short decay component of ICA can be

written as

$$(ICA)_{short}=(ICA)_{total}-(ICA)_{flat}=\sigma_{IC}N[p_X-f_X]. \qquad (3.6.5)$$

Substituting the expressions for $(ICA)_{short}$, $(ICA)_{flat}$, and $(ICA)_{total}$ into equation (3.6.1), K_{short} becomes

$$K_{short}=[1/(\sigma_{FC}/\sigma_{IC}+p_X)][p_X-f_X], \qquad (3.6.6)$$

The expression for $p_X(x)$ can be written as [16,17]

$$p_X(x)=[1/t_{\Gamma X}(x)]/[1/t_{\Gamma X}(x)+1/t_{\Gamma L}(x)+1/t_{\Gamma\Gamma}(x)] \qquad (3.6.7)$$

where $t_{\Gamma X}(x)$, $t_{\Gamma L}(x)$, and $t_{\Gamma\Gamma}(x)$ are inter-and-intravalley scattering times, and vary with Al content x and the experimental conditions such as crystal temperature, kinetic energy of electrons, and so on.

The inter-and-intravalley scattering times for GaAs were previously measured to be $t_{\Gamma X}=55\pm11$ fs for electrons with kinetic energy centered at 0.51 eV [17], $t_{\Gamma L}=100\pm20$ fs for 0.5 eV electrons [9], and $t_{\Gamma\Gamma}=165\pm20$ fs for the central valley electrons relaxing from kinetic energy of 0.61 eV [8]. These measured results can be normalized, using Conwell's theory [18], to obtain corresponding values of those parameters for GaAs in our experimental conditions.

The x-dependence of the scattering rates arises from the x-dependence of the effective masses, the deformation potentials and the alloy-disorder-assisted intervalley scattering rates. The x-dependence of the effective masses of $m_\Gamma=0.067+0.083x$, $m_L=0.56+0.1x$, and $m_X=0.85-0.14x$ are

given in the literature [3]. The calculations by Cardona's group [19] have shown that the deformation potentials D_{ij} (i,j= Γ, L, X) for $Al_xGa_{1-x}As$ changes slightly with x, and can therefore be approximately treated as a linear function of x. The x-dependence of alloy-disorder-assisted intervalley scattering (zero-phonon transition) rates can be estimated from the measured results of Kalt et al. [20] The expressions for the x-dependence of the effective mass, the deformation potentials, and the alloy-disorder intervalley scattering rates enable one to obtain the x-dependence of the scattering rates and to calculate $p_X(x)$ as a function of x.

Since both intra-and-intervalley scattering occur on a time scale which is much shorter than the recombination time of electrons and holes [8,9,12,15,17], electrons in the conduction bands at t_{flat} may be assumed to be in thermal equilibrium and characterized by a Boltzmann distribution. [11] Therefore, $f_X(x)$ can be written as [16]

$$f_X(x)=1/[1+(\frac{t_X}{t_\Gamma})(\frac{m_\Gamma}{m_X})^{3/2}e^{\Delta E_{X\Gamma}/K_BT}+(\frac{t_X}{t_L})(\frac{m_L}{m_X})^{3/2}e^{\Delta E_{XL}/K_BT}], \quad (3.6.8)$$

where t_i and m_i are the lifetime and density of states effective mass of electrons in the ith valley, respectively, where i=Γ, L, and X; K_B is the Boltzmann constant; $\Delta E_{X\Gamma}=E_g{}^X-E_g{}^\Gamma$; and $\Delta E_{XL}=E_g{}^X-E_g{}^L$. The previous band-gap determinations suggest a linear dependence [3,6] of $E_g{}^\Gamma(x)$ for $x<x_c$ given by $E_g{}^\Gamma(x)=1.424+\alpha x$. Since the value of $E_g{}^\Gamma(x)$ varies greatly with x as mentioned in section 3.2, and the previously determined values of α

scatter in the large range from 12.47 meV% [4] to 14.55 meV% [6], α has to be kept as an unknown parameter to be determined. Since the value of $E_g^X(x)$ changes slightly with x, and the difference of its calculated values using different expressions of E_g^X is small [3], we can chose the most used expression [4] of $E_g^X(x)=1.90+0.125x+0.143x^2$ for E_g^X(x). For a similar reason, we can chose [4] $E_g^L(x)=1.704+0.642x$ for E_g^L(x). Substituting the expressions of t_i(x), m_i(x), E_g^i(x) (i=Γ, L and X) into equation (3.6.8), f_x(x) can be obtained with one unknown parameter α.

The ratio of σ_{FC}/σ_{IC} can be found from equation (3.6.6) using the calculated values of p_X and f_X, and the measured value of K_{short} for GaAs (x=0). Substituting the expressions of p_X(x) and f_X(x), and the value of σ_{FC}/σ_{IC} into equation (3.6.6) shows K_{short} to be a complex function of x with an unknown parameter α.

As examples, the calculated values of K_{short} as a function of x using equations (3.6.6) to (3.6.8) are shown in Fig.3.6.1. The solid, dot-dash, and dot-dot-dash curves were obtained by using the parameters of $\alpha=\Delta E_g^{\Gamma}/\Delta x$=13.42 meV/% [13], 12.47 meV/% [4], and 14.55 meV/% [6], respectively.

In order to determine the value of α for $Al_xGa_{1-x}As$, it can be treated as a variable parameter to fit the calculated values of K_{short} to its measured value. The best fit will yield a correct value of α, and the critical value of

x_c can be obtained by solving the equation of $E_g^{X}(x_c)=E_g^{\Gamma}(x_c)$ using the determined value of α.

Since the number of electrons in the X_6 valley relative to the total number of electrons in thermal equilibrium increases significantly when x approaches to x_c (i.e. $\Delta E_{X\Gamma}\rightarrow 0$), the change in $(ICA)_{short}$ is extremely sensitive to the change in $\Delta E_{X\Gamma}$. Therefore, the determination of α and x_c by pump-IR-probe absorption spectroscopy has a high accuracy, which will be discussed in chapter 9.

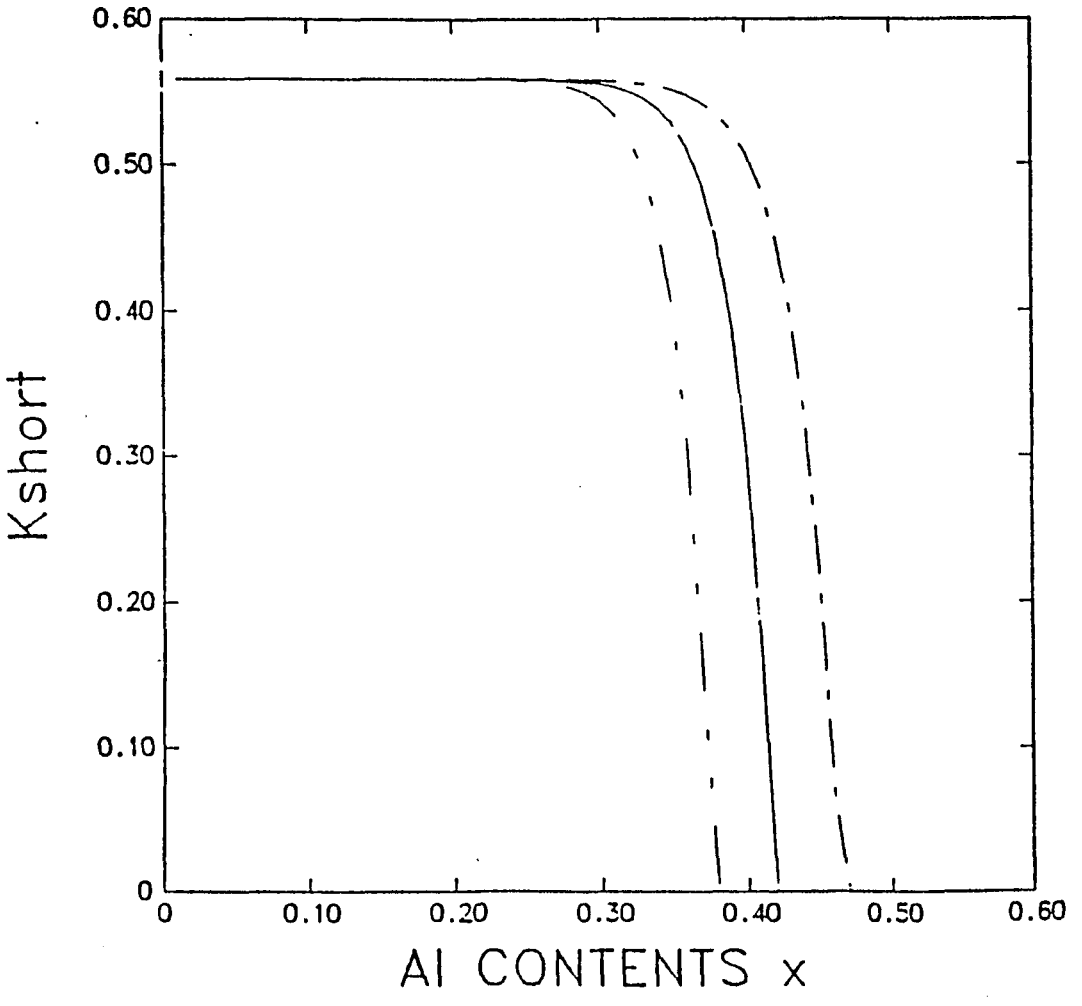

Fig. 3.6.1. The percentage of the short decay portion of ICA in the induced total absorption at the delay time corresponding to the absorption peak, K_{short}, as a function of x. The dot-dash, solid, and dot-dot-dash curves were obtained by using the values of α = 13.42 meV/% [13], 12.47 meV/% [4], and 14.55 meV/% [6], respectively.

REFERENCES

[1] J. S. Blakemore, Appl. Phys., 53 , R 123 (1982).

[2] D. E. Aspnes, C. G. Olson, and D. W. Lynch, Phys. Rev. Lett., 378 , 766 (1976).

[3] S. Adachi, J. Appl. Phys., 58 , R1 (1985).

[4] H. C. Casey, Jr, and M. B. Ponish, " Heterostructure lasers", Academic, New York, 1978, Paris A and B.

[5] H. J. Lee, L. Y. Juravel, and J. C. Woolley, Phys. Rev., B21 , 659 (1980).

[6] T. F. Kuech, D. J. Wolford, R. Potemski, J. A. Bradley, and K. H. Kelleher, App. Phys. Lett., 57 , 505 (1987).

[7] D. Y. Oberli, J. Shah, and T. C. Daman, Phys. Rev., B40 , 1323 (1989-I).

[8] J. A. Kash, J. C. Tsang, and J. M. Hvam, Phys. Rev. Lett., 54 , 2151 (1985).

[9] J. Shah, B. Deveaud, T. C. Damen, W. T. Tsang, A. C. Gossard, and P. Lugli, Phys. Rev. Lett. 59 , 2222 (1987).

[10] R. J. Seymour, M. R. Junnarkar, and R. R. Alfano, Solid State Commun., 41 , 657 (1982).

[11] W. B. Wang, N. Ockman, M. A. Cavicchia, and R. R. Alfano, Appl. Phys. Lett., 57 , 395 (1990).

[12] W. B. Wang, N. Ockman, M. Yan, and R. R. Alfano, J. of Lumin., 50 , 347 (1992).

[13] W. B. Wang, R. R. Alfano, D. Szmyd, and A. J. Nozik, Phys. Rev., B46 , 15828 (1992).

[14] H. A. Zarem, J. A. Lebens, K. B. Nordstrom, P. C. Sercel, S. Sanders, L. E. Eng, A. Yariv, and K. J. Vahala, Appl. Phys. Lett., 55 , 2622 (1989).

[15] W. B. Wang, K. Shum, R. R. Alfano, D. Szmyd, and A. J. Nozik, Phys. Rev. Lett., 68 , 662 (1992).

[16] J. Shah, B. I. Miller, and A. E. DiGiovanni, J. Appl. Phys, 43 , 3434 (1972).

[17] P. C. Becker, H. L. Fragnito, C. H. Brito Cruz, J. Shah, R. L. Fork, J. E. Cunningham, J. E. Henry, and C. V. Shank, Appl. Phys. Lett., 53 , 2089 (1988).

[18] E. M. Conwell, and M. O. Vassell, IEEE Trans. Electron. Devices, ED-13 , 22 (1966).

[19] S. Zollner, S. Gopalan, and M. Cardona, Appl. Phys. Lett., 54 , 614 (1989).

[20] H. Kalt, W. W. Ruhle, K. Reimann, M. Rinker, and E. Bauser, Phys. Rev., B43 , 12364 (1991-II).

Chapter 4
EXPERIMENTAL METHODS

As mentioned in Chapter 1, all of the previous experimental methods for investigation of hot carrier dynamics in semiconductors, such as hot-luminescence and degenerate pump-probe visible absorption only measured carrier dynamics in the central k=0 valley---the Γ valley. Our picosecond and femtosecond visible-pump and IR-probe absorption spectroscopy allows us to measure the time evolution of the population of hot electrons in a k≠0 satellite valley---the X valley. The measured carrier dynamics in the X valley for GaAs and AlGaAs enables us to determine corresponding intervalley scattering times and band structure parameters. The experimental methods used in this thesis work, such as picosecond (ps) and femtosecond (fs) pump-IR-probe absorption spectroscopies will be discussed in this chapter. A single shot 7 ps glass laser and a 10 Hz, 500 fs dye laser were used for the former and the latter systems, respectively.

4.1. Picosecond Pump-IR-Probe Absorption Spectroscopy

4.1.1. Nd:Glass Laser and Its Amplifier System

A passively mode-locked Nd:glass laser system includes a cavity, a single pulse selector, and a three-stage amplifier as schematically shown in Fig. 4.1.1. The cavity consists of a Nd:glass laser rod surrounded by a flash lamp and a saturable absorber dye between two high-reflectivity

mirrors. The ends of the rod are cut at Brewster's angle to prevent subcavities, feedback, and reflection losses from the surface. The flash lamp surrounding the laser rod provides the optical energy necessary to excite the laser-active ions in the rod. The end mirrors are dielectric coated, the one at the back being 100% reflecting and the other in the front being 50% reflecting at the emission band of the laser medium.

The absorption characteristics of the dye (Kodak 9860 in dichloroethane) are such that at low-incident intensity the absorption is constant, but as the intensity increases and exceeds a certain critical value (~ 50 MW/cm ^{2}), the absorption decreases. The nonlinear absorption of the saturable absorber produces ultrashort pulses. [1] The output of the Nd:glass laser is a train of pulses separated by the round-trip time of the cavity at ~ 1.054 μm. In order to obtain a good single mode, a small aperture is placed on the optical path within the cavity. In addition, a parallel thin film working as a Fabry-Perot interferometer is also placed in the optical path to decrease the bandwidth of the laser pulse to the Fourier-transform limited one of 0.5 nm at 1.054 μm for FWHM.

A single pulse selection system, consisting of a Pockels cell and two polarizers, [1] is arranged behind the oscillator to obtain a single pulse from a pulse train. The Pockels cell, made of a KDP crystal cut perpendicular to its optical axis, is placed between two dielectric cross-polarizers. The pulses will pass through the first polarizer but not through the second one. If, however, a half-wave voltage is applied to the Pockels cell, the plane

of the polarization of a laser pulse will be rotated by 90 °, and this pulse can pass through the second polarizer. When the applied voltage lasts for a short time less than the round-trip time in the cavity, only one pulse is allowed to pass through the second polarizer. Consequently, a single pulse which is vertically polarized will be selected from a pulse train.

The amplifier system for the selected single pulse consists of three stages. Each stage is practically identical with the laser without mirrors. The amplifier medium is the same as that used in the oscillator, but the diameter of the rods used in the amplification stages are progressively larger. This reduces the chance of surface damage to the rods. The rods are doped at a lower concentration for more uniform pumping. The ends of the rods are cut at a small angle of about 6 °, to avoid lasing action off the ends and the formation of multiple pulses [1]. The average energy and the pulse duration of the amplified single pulses are ~ 50 mJ and ~ 7 ps, respectively.

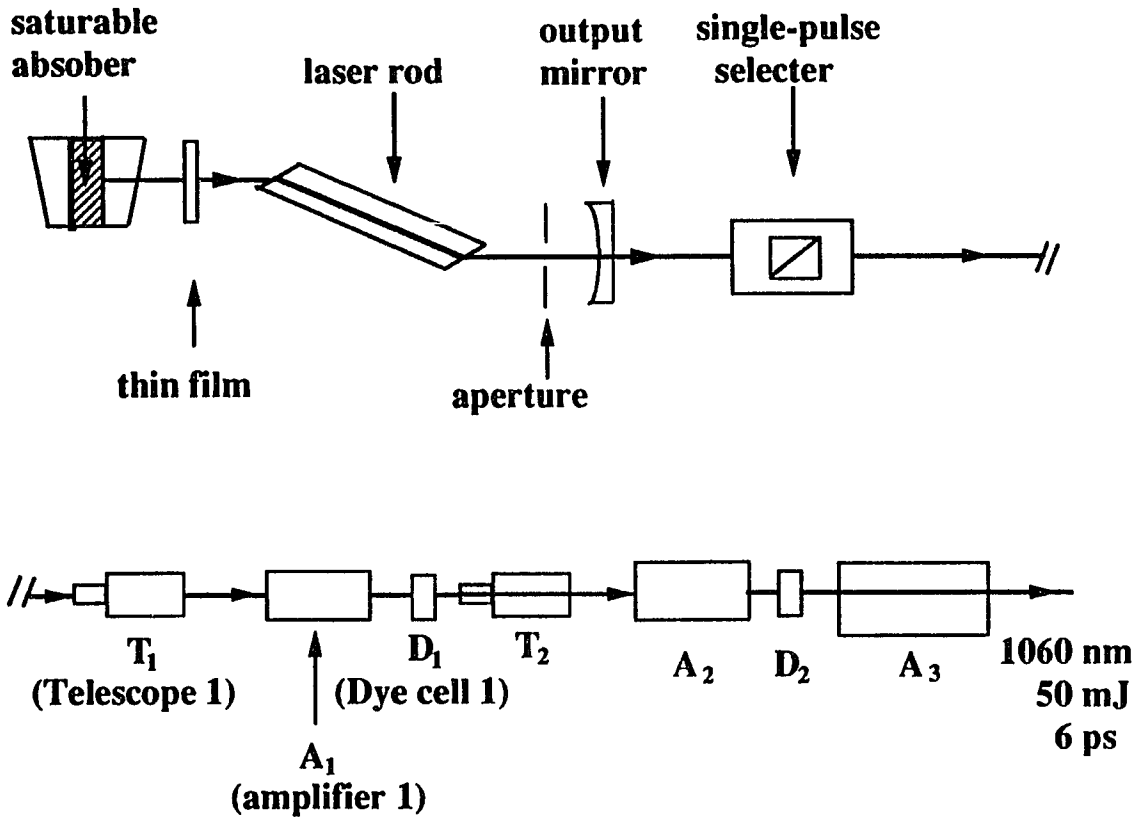

Fig. 4.1.1. Schematic diagram of a mode-locked Nd:glass laser system including a cavity, a single pulse selector and a three-stage amplifier.

4.1.2. Picosecond Pump-IR-Probe Absorption System

The picosecond pump-IR-probe absorption setup [2-4] using a Nd:glass laser with three stages of amplifiers is schematically shown in Fig. 4.1.2. The amplifiered 1.054 μm laser beam is split into two beams. The first is focused into a KDP crystal to generate a frequency doubling pulse of 527 nm with a shorter pulse duration of ~ 5 ps and a horizontal polarization, which is then focused on a sample as a pump. The second beam is directed through two $LiNbO_3$ crystals to generate a horizontally polarized IR beam tunable from 2 μm to 5 μm by parametric optical amplification used as a probe. The energy, bandwidth, and tuning curve of the generated IR pulses will be discussed in section 4.1.3. The transmitted IR intensity from the sample is collected by a Perkin-Elmer model 1B monochromator equipped with a cooled (77 K) Infrared Associates InSb detector. The output from the detector is amplified by a Comlinear-100 wide-band preamplifier and displayed-and-recorded by a Tektronix 7844 oscilloscope or an integrator. To avoid the effect of the fluctuation of the incident IR laser pulses, a beam splitter reflects a fraction of the incident IR beam through an identical detector-preamplifier-recorder system as a reference channel. The change of the transmittance with and without a pump can be accurately obtained from the change of the ratio of the signal-to-reference IR intensities.

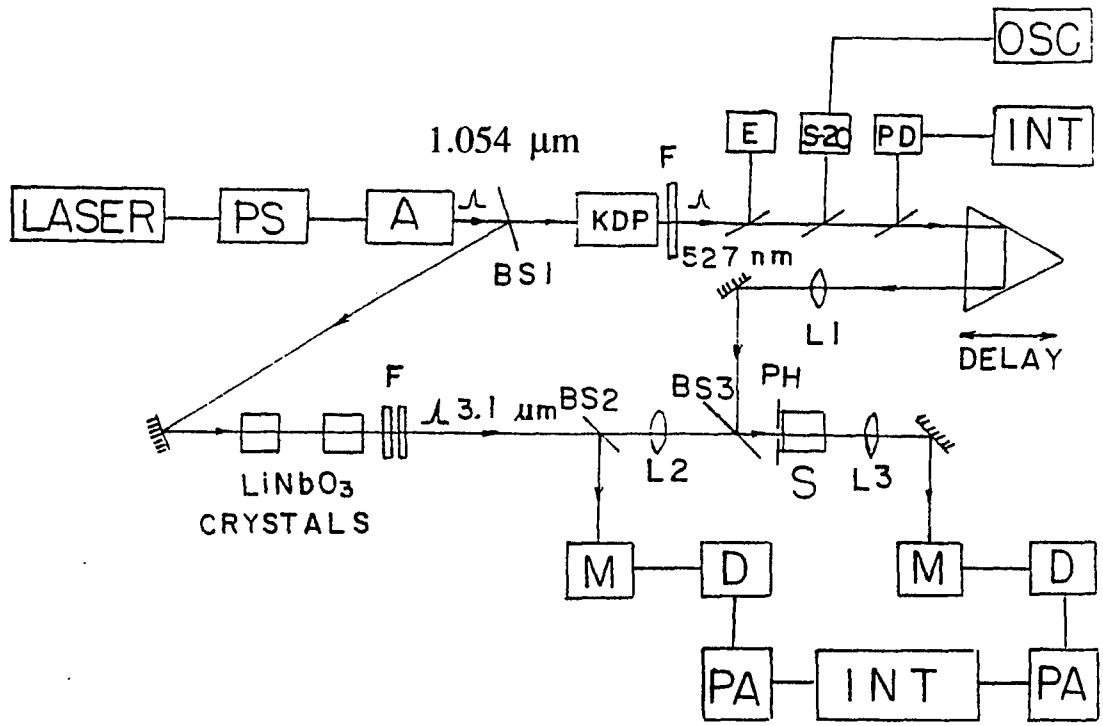

Fig. 4.1.2. Schematic diagram of the single shot picosecond pump-IR-probe absorption set up.

4.1.3. Generation of Tunable IR Pulses by Parametric Optical Amplification

The heart of our picosecond pump-IR-probe absorption system is the generation of the tunable IR pulses by the method of parametric optical amplification. The powerful short 1.054 μm pulses pass through the non-linear $LiNbO_3$ crystals and serve as a pump for parametric three-photon amplification. The $LiNbO_3$ crystal used in our set up is 3-cm long with a 5×5 mm crossection and cut at 45 ^{0} from its optical axis. Starting from spontaneous parametric fluorescence, two light pulses are generated at the signal and idler frequencies, ω_s and ω_i, respectively. The phase-matching condition of the parametric processes, $\Delta\vec{k}=\vec{k}_s+\vec{k}_i-\vec{k}_p=0$, determines the frequencies of the signal and idler pulses.

Neglecting depletion of the pump peak intensity I_p, the maximum intensity I_s and I_i of the signal and idler pulses may be written as [5]:

$$I_s(z)=2I_{so}\sinh^2(\gamma z)+I_{so} \tag{4.1.1}$$

$$I_i(z)=I_{so}(2\omega_i/\omega_s)\sinh^2(\gamma z)+I_{so}\,\omega_i/\omega_s, \tag{4.1.2}$$

where

$$\gamma=\left(\frac{32\pi^3}{c^3}\frac{\omega_s\omega_i}{n_s n_i n_p}\chi_{eff}{}^2 I_p-\frac{(\Delta k)^2}{4}\right)^{1/2}, \tag{4.1.3}$$

z is the interaction length, I_{so} is intensity of spontaneous noise, n_s , n_i and n_p are the refractive indices, χ_{eff} denotes the effective second-order

nonlinear susceptibility. Equations (4.1.1) and (4.1.2) indicate that experimental gain of the signal and idler is achieved at high pump intensities ($\gamma z \gg 1$). Maximum gain proportional to $I_p^{1/2}$ occurs for $\Delta k=0$, in which the energy of the signal pulse rises exponentially with increasing pump intensity over more than four orders of ten within a path length of a few centimeters. The gain decreases with increasing mismatch; amplification is reduced by a factor of 2 at $\Delta k_{1/2}=2\phi/z$.

The energy of the generated IR pulses from our set up was measured to be ~ 15 μJ per pulse. The duration of the generated IR pulses is estimated to be 2-3 ps, which is shorter than the input pulse approximately by a factor of more than 2.

The measured IR wavelength as a function of tuning number for the crystal position corresponding to phase matching angles is plotted in Fig.4.1.3 which presents results of our spectral investigations of the parametrically produced IR beam. This curve shows that rotation of the crystal by several degrees covers a large wavelength range from ~ 2 μm to ~ 4.5 μm. The bandwidth of the generated IR pulses increases with the IR wavelength, and was measured to be approximately ±50 nm for 4.5 μm, and ±80 nm for 2.5 μm.

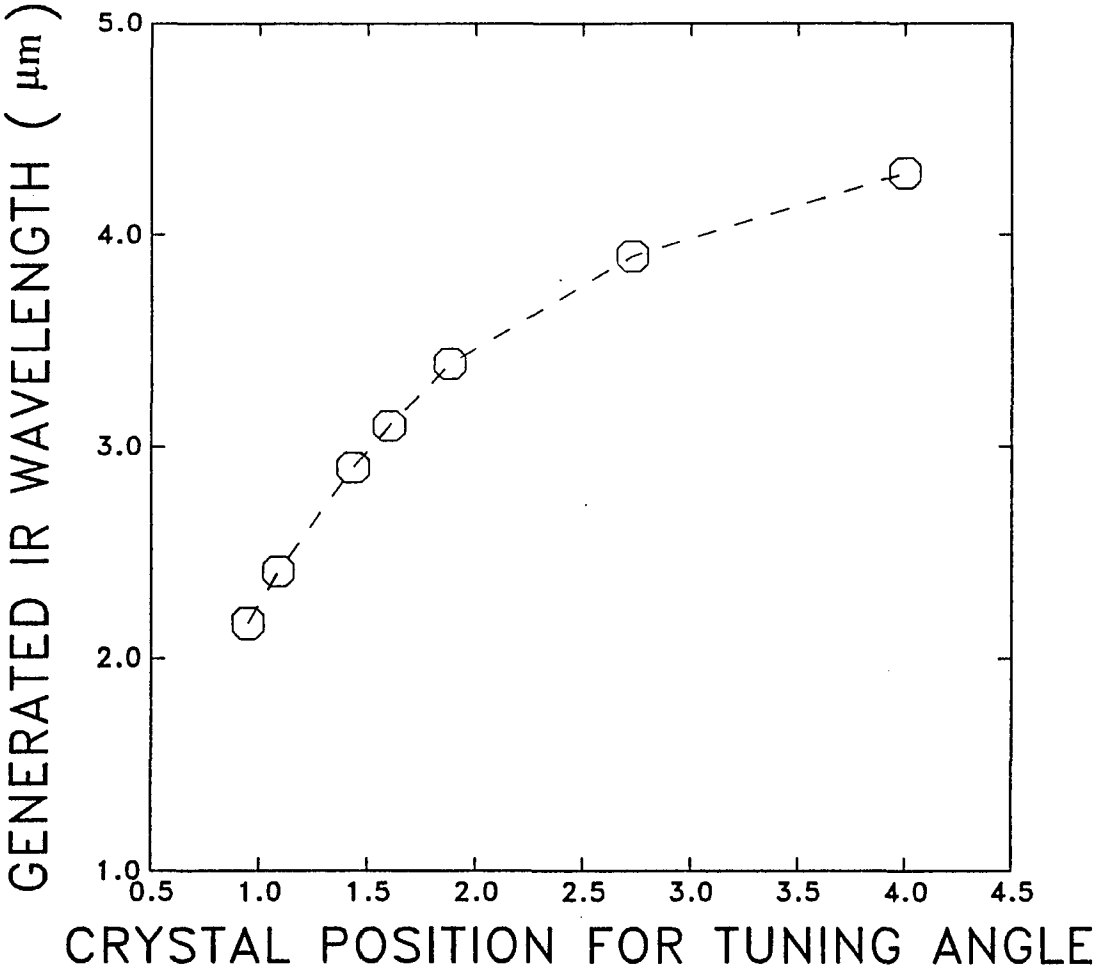

Fig. 4.1.3. Generated IR wavelength as a function of tuning numbers for the $LiNbO_3$ crystal position corresponding to the phase matching angles.

4.2. Femtosecond Pump-IR-Probe Absorption Spectroscopy

4.2.1. Mode-Locked Nd:YAG Laser and Synchronously Pumped Dye laser System

The schematic diagram of the dye laser synchronously pumped by a mode-locked Nd:YAG laser used in this thesis work is shown in Fig. 4.2.1.[6] A continuous-wave (CW) mode-locked Nd:YAG laser (Spectra-Physics 3000) with a fiber-grating pulse-compression and second harmonic generation system (Spectra-Physics 3690) is used to synchronously pump a dye laser (Spectra-Physics 375B). The active medium of this mode-locked laser is a 4 mm diameter rod of neodymium-doped yttrium alumium garnet (Nd:YAG) approximately 80 mm long placed at one focus of a gold-coated elliptical reflector. The rod is pumped by a krypton arc lamp which is located at the other focus of the elliptical reflector.[7]

A crystal with a radio frequency (rf) driver working as an acousto-optic modulator is placed within the cavity of the Spectra-Physics 3000 Nd:YAG laser for active mode-locking. The frequency of the modulation is equal to or a multiple of $f=c/(2L)$, where L is the length of a cavity, c is the speed of light, and f is the frequency difference between two adjacent modes.[8] In our Nd:YAG laser system, L is ~ 1.82 m, f~82.4×10^6 Hz, and the frequency actually used for the modulation is ~ 41.1860 MHz.

The mode-locked laser is a laser that operates with all or most of the

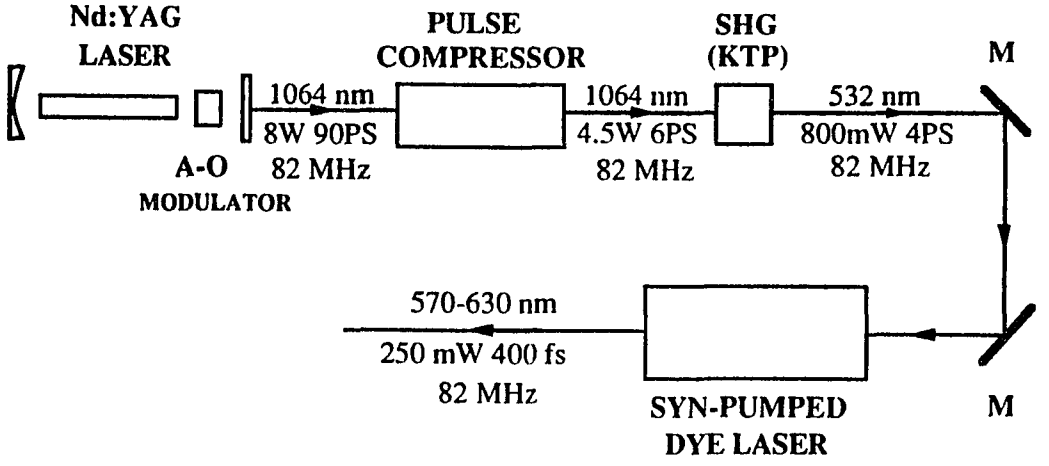

Fig. 4.2.1. Schematic diagram of the dye laser synchronously pumped by a mode-locked Nd:YAG laser.

longitudinal laser modes "locked" together with identical phases. [1] In active mode locking, the phases of longitudinal modes are linked by periodic modulation of the parameters of the resonator.

An active temperature stabilization system (Spectra-Physics 3270) for the mode-locker eliminates "thermal runaway" of the acousto-optic modulator resonant frequency. The system monitors the acousto-optic resonance frequency and compares it to the rf driver frequency. If they disagree, it adjusts the temperature of the modulator until the resonance frequency agrees with that of the driver. If the driver frequency changes, the modulator temperature will change to keep the frequencies locked together.

The output of this active mode-locked Nd:YAG laser is a train of ~ 90 ps pulses with a average power of ~ 8 W and a repetition rate of 82 MHz at 1.064 μm. In order to shorten the pulses, a fiber-grating pulse-compression system is used. The output pulses are first focused to pass through a single-mode optical fiber, thus increasing the bandwidth of the laser pulses via self-phase modulation and group velocity dispersion. [9] The pulses are then compressed by using a grating pair in the double-pass geometry as shown in Fig.4.2.2. This technique enables the Nd:YAG pulses of ~ 90 ps to be compressed to ~ 5 ps with a average power of ~ 4.5 W.

The compressed 1.064 μm pulses are then focused into a potasium titanyl phosphate crystal ($KTiOPO_4$---KTP) to generate second harmonic pulses at 532 nm with a shorter pulse duration of ~ 4 ps and an average

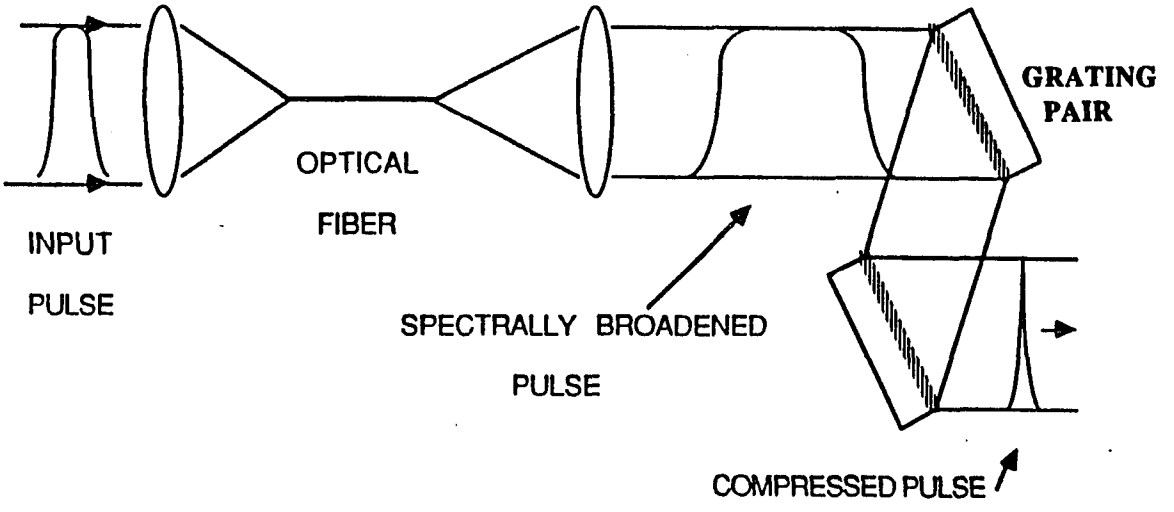

Fig. 4.2.2. Schematic diagram for optic fiber-grating pulse compression system.

power of ~ 800 mW. The nonlinear optical frequency doubling efficiency of KTP is much higher[6] than that of KH_2PO_4 (KDP) and $Ba_2NdNb_5O_{15}$ crystals due to its higher damage threshold of ~ 250 MW/cm^2 compared with the other two, allowing one to focus tighter to obtain higher intensities. In our laser system, the beam diameter within the crystal is about 40 μm, which suggested a power density of over 50 MW/cm^2.

The continuous pulse train at 532 nm with a pulse duration of ~ 4 ps is used to synchronously pump the Spectra-Physics 375B dye laser. If the round-trip time of the dye laser cavity is equal to, or a submultiple of that of the pumping laser, the gain of the dye laser will be impulsively driven in synchronism with the round-trip repetition rate, and a train of ultrafast pulses will be generated from the dye laser. In order to produce the short pulses from the dye laser, the pulse duration of the pumping source should be as short as possible because the temporal duration of the dye laser pulses is proportional to the square root of the ratio of the pump pulse duration to the intracavity bandwidth.[7] That is why we need the fiber-grating pulse compression system for the pump laser.

The Spectra-Physics 375B dye laser cavity is a four-mirror astigmatically compensated design with a cavity length equal to that of the Nd:YAG laser as shown in Fig.4.2.3. The image of the pump laser beam is focused on the dye stream, which is at Brewster's angle to the intracavity beam of the dye laser. The collimating mirror is focused on the

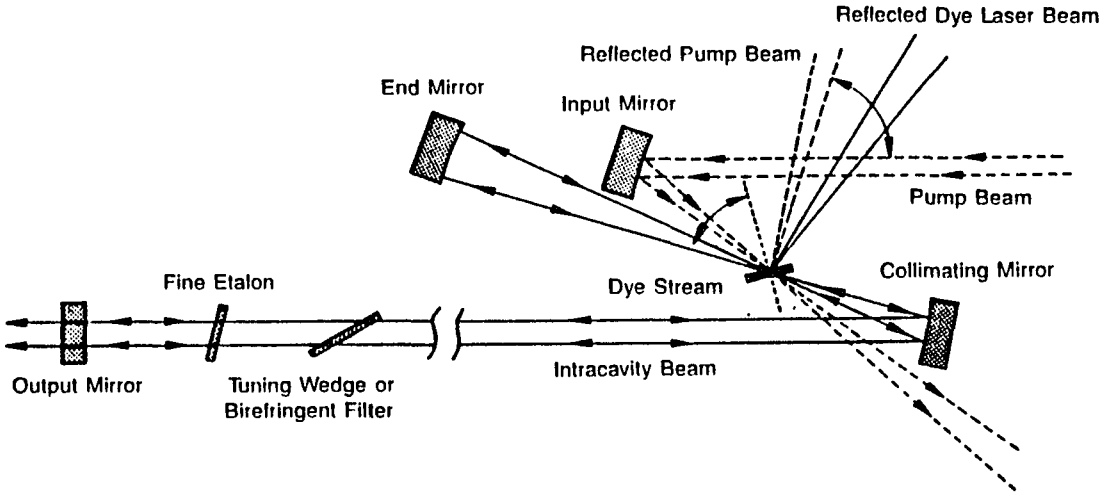

Fig. 4.2.3. The schematical diagram for the cavity of the Spectra-Physics 375B continuum dye laser.

resulting fluorescent spot within the dye stream. When the mirror is correctly aligned and focused, the image of the spot will be focused 60 cm in front of the output coupler. The end mirror is also focused on the fluorescent spot. The image of the spot, as reflected by the end mirror, is also focused by the collimated mirror 60 cm in front of the output coupler. Lasing will occur when the output coupler is aligned with the intracavity beam, perpendicular to it in both the horizontal and vertical planes. The precision with which each of the optics is aligned and focused, the uniformity of the dye stream where it is struck by the pump beam, and the power and mode structure of the pump beam all contribute to dye laser output power.

Dye laser optics are selected to provide output with a given dye. The input mirror reflects wavelengths within the absorption spectrum of the dye while absorbing all others. The cavity mirrors reflects wavelengths within the tuning range of the dye while absorbing all others. The output coupler must also transmit a fraction of the intracavity power; transmission efficiency depends on the gain of the dye used. The spectra of the output from Spectra-Physics 375B for different dyes are shown in Fig.4.2.4.

The dye solution consists of a solution of rhodamine 6G (2.0×10^{-3} M/liter) in methanol (0.03 liter), and Ethylene (1.47 liter) for the output tuned from 570-630 nm used in our experiments. The pulse duration, repetition rate, and average power at 585 nm are ~ 400 fs, 82 MHz, and ~ 250 mW, respectively. The output wavelength can be tuned by the tuning

wedge and the fine etalon. The tuning wedge is a variable-cavity Fabry-Perot etalon. A fused-silica wedge separates its mirrored surfaces so that the peak transmission frequencies depend on the position of the wedge relative to the dye laser beam. Turning the tuning control slides the wedge across the beam path, changing the thickness of the etalon and the resonant frequencies. The fine etalon control tilts the etalon, changing its thickness relative to the beam and, thus, its transmission frequencies. Using the fine etalon control, an accuracy of ± 0.025 nm for the output wavelengths can be achieved.

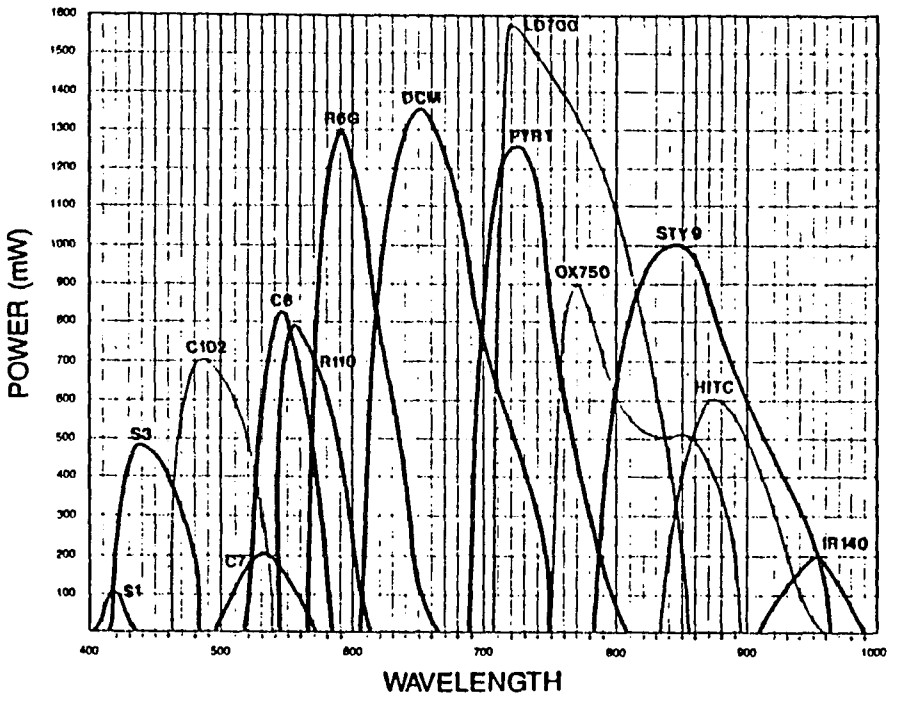

Fig. 4.2.4. Tuning curves of the dyes for the Spectra-Physics 375B synchronously pumped dye laser.

4.2.2. Pulse-Dye-Amplifier System

The average energy of a pulse obtained from the dye laser is only ~ 3 nJ which has to be amplified so that it can be used to generate IR pulses.

The schematical diagram for the pulse-dye-amplifier (PDA) system used in our set up (Quanta-Ray PDA-1) is shown in Fig.4.2.5. The pump pulses of 532 nm per pulse for the PDA-1 system are generated from a frequency doubled Q-switch Nd:YAG laser (Quanta-Ray DCR-2). The output of ~ 300 mW per pulse of a 10 Hz Q-switch Nd:YAG laser is synchronized with the rf driver for the modulation crystal of the mode-locked Nd:YAG laser, and ten pulses per second are selected for pumping. This pump beam is split into three parts: the first two are focused using cylindrical lenses for transversely pumping the first and the second cells, respectively, and the third one is focused for longitudinally pumping the third dye cell. Each of the dye cells is filled with organic dye solution in water placed at Brewster's angle. The PDA-1 system amplifies the input within the tuning range of the given amplifier dye. The tuning curves for different dyes are shown in Fig.4.2.6. Since our output wavelength is desired to be 585 nm, the Kiton Red 620 (KR620) was chosen as our amplifier dye.

Two micro-apertures of 50 μm and 150 μm are placed between the two adjacent dye cells working as spatial filters to isolate gain states from one another to reduce the amplified spontaneous emission (A.S.E) to less than 2%. The amplification of ~ 5×10^{5} is achieved from the PDA-1

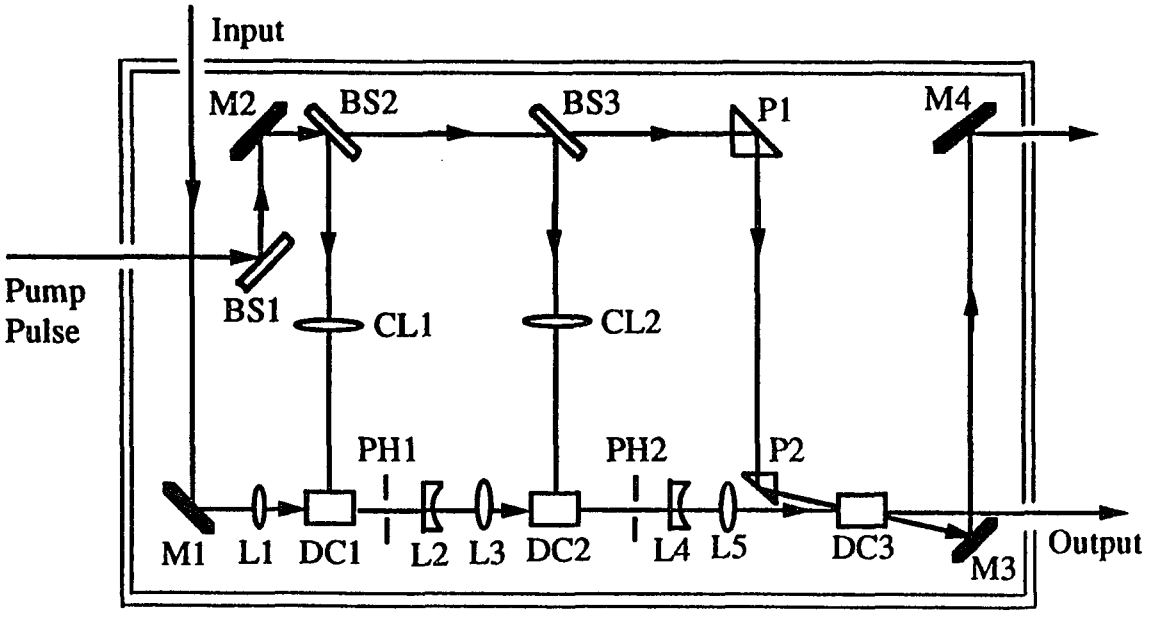

Fig. 4.2.5. Schematic diagram of the PDA-1 pulse dye amplifier system. (M---mirror, L---lens, DC---dye cell, PH---pin hole, BS---beam splitter, P---prism, CL---cylindrical lens)

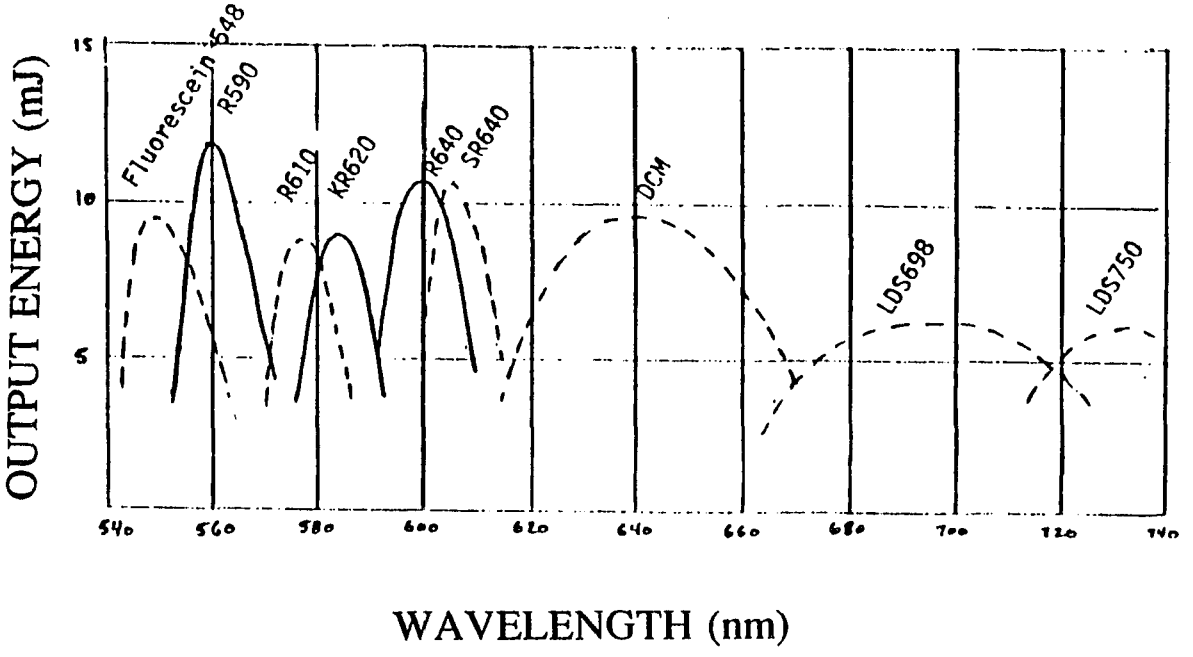

Fig. 4.2.6. The tuning curves of dyes used for PDA-1.

system which provides output pulses with an average energy of ~ 0.5 mJ per pulse measured by an energy meter.

There are three important requirements for obtaining satisfactory amplification with a very small percentage of A.S.E. for PDA-1: (1) synchronization of input laser pulses and the pump pulses with a synchronization electronics system SM-1; (2) alignment of the three stages of the amplifier dye cells using diffraction patterns; and (3) optimization of the dye concentration. The high concentration of the amplifier dye solution will generate more gain for both spontaneous and stimulated emission, therefore, one has to choose a proper concentration to obtain the large amplification for stimulated emission with a small A.S.E. The suggested (by Spectra-Physics) best dye concentrations of 20 mg/L for the first and the second cells, and 8 mg/L for the third cell must be carefully checked by their absorption spectra, especially the absorption coefficient at 532 nm. Figs. 4.2.7 and 4.2.8 show typical absorption curves (optical density versus wavelength) of the amplifier dye solutions for the first-and-second, and the third cells, respectively. The optical density at 532 nm are 2.08 for the first-and-second cells, and 0.86 for the third cell.

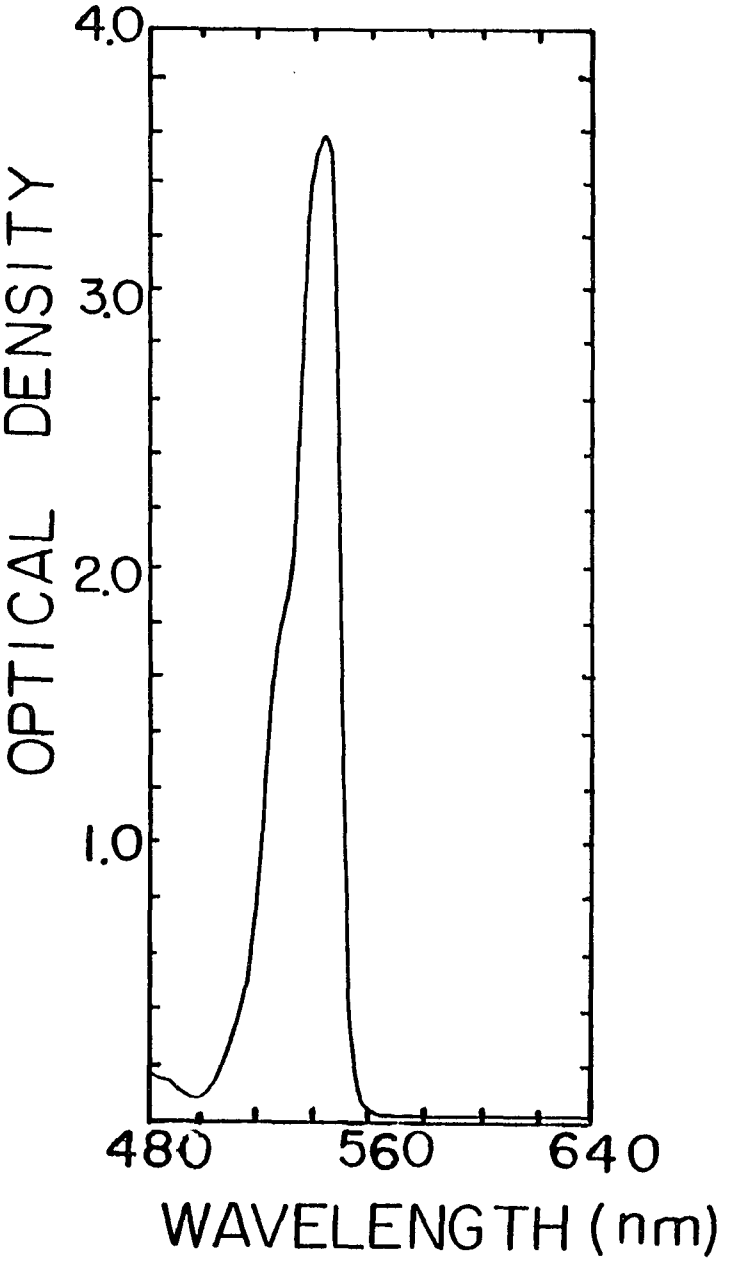

Fig. 4.2.7. The absorption curve of the dye solution for the first-and-second amplifier cells.

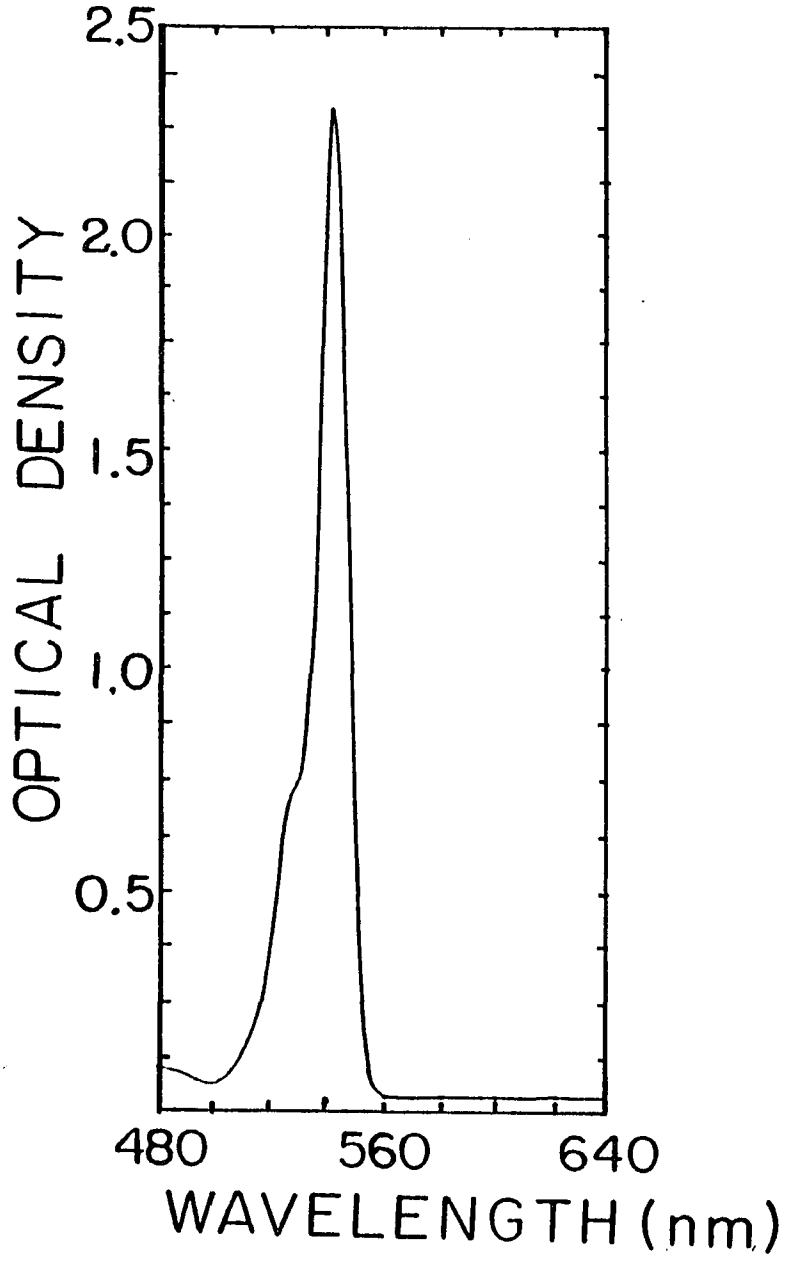

Fig. 4.2.8. The absorption curve of the dye solution for the third amplifier cell.

4.2.3. Femtosecond Pump-IR-Probe Absorption Setup

The femtosecond pump-IR-probe absorption set up using the amplified laser pulses from the synchronously pumped dye laser is schematically shown in Fig. 4.2.9. [10-12]

The output beam of 585 nm from PDA-1 is divided into three parts: one of them is focused on the sample as a pump, and the second is focused into a cell contained D_2O or methyl alcohol to generate a white light continuum which is mixed with the third beam (585 nm) in a $LilO_3$ crystal to produce IR pulses tuned from 2.5 μm to 5.5 μm by difference frequency mixing (also called seeded optical parametric amplification). The energy, bandwidth, and tuning curve of the generated IR pulses will be discussed in section 4.2.4. These IR pulses are used as a probe to monitor the induced IR absorption in the sample after excitation.

The transmitted IR intensity is measured by a liquid-nitrogen-cooled InSb photovoltaic detector (Infrared Associates G-132-1S). The signal obtained from the detector is amplified by a PPA-15-IS preamplifier, and is then recorded by a box car integrator-and-computer system.

To avoid the effect of the fluctuation of the incident IR laser pulses, a beam splitter directs a fraction of the probe beam through an identical detector-preamplifier-recorder system to monitor the intensity of a fraction of the incident probe pulse. The pump induced IR absorption can be accurately monitored from the change of the ratio of signal-to-reference IR intensities with and without the pump.

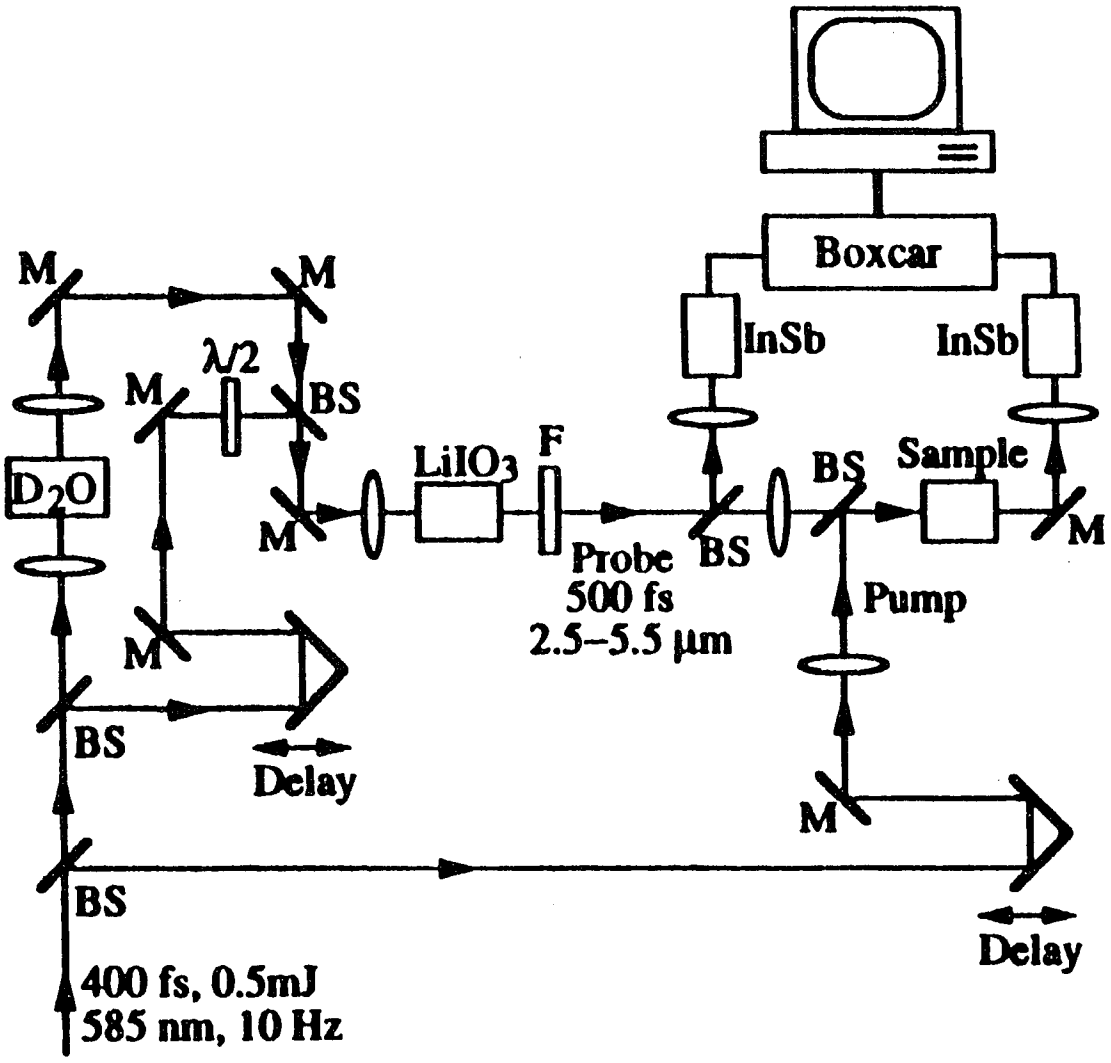

Fig. 4.2.9. Schematic diagram of the 10 Hz femtosecond pump-IR-probe absorption set up. [11]

4.2.4. Generation of IR Pulses by Difference Frequency Mixing

The key step for the femtosecond pump-IR-probe absorption set up is the generation of IR by mixing the white light continuum and 585 nm beams in a $LiIO_3$ crystal. The white light continuum which typically extends from ~ 300 nm to ~ 900 nm, and the third 585 nm beam are combined and loosely focused with a beam size of ~ 1 mm^2 into an 1-mm thin $LiIO_3$ crystal cut at 22^0 from its optic axis for type I phase matching. The polarizations of the continuum and the generated IR are along the crystal's ordinary axis, whereas the polarization of the 585 nm beam is along the crystal's extraordinary axis to achieve the proper effective index for phase matching.

The wavelength of the generated IR pulses is determined by which components of the continuum are phase matched at the given crystal angle. The IR wavelengths for different tuning numbers for phase matching angles measured by using IR narrow band filters are shown in Fig.4.2.10.

The group velocity difference between a component of the white light continuum pulses with an o-polarization and the 585 nm pulses with an e-polarization limits their interaction length within the pulse duration. The maximum interaction length for generating 3.1 μm IR pulses within our pulse duration of ~ 500 fs was calculated to be 1.2 mm.

The intensity of the generated IR at each wavelength is determined by intensities of the third 585 nm beam and the corresponding components of the white light continuum used to obtain this IR wavelength. Since the

distribution of intensity of the white light continuum varies with different continuum generation liquids, the IR intensity as a function of wavelength will also change with the liquids. As examples, Fig.4.2.11 shows the intensity of generated IR as a function of wavelength (therefore the crystal tuning angle) [13] in four different continuum liquids: H_2O, D_2O, CH_3OH, and C_3D_6O. The IR outputs are peaked corresponding to the Raman allowed vibrational modes of the various liquids, as illustrated in the figure. In H_2O and D_2O, the high frequency Raman modes are diffuse due to inhomogeneous broadening from hydrogen bonding. Using different liquids provides a way of optimizing the IR intensity and stability for a given wavelength.

The typical energy and pulse duration of the generated IR pulses were measured to be ~ 1 nJ per pulse, and ~ 500 fs, respectively. The bandwidth of the generated IR pulses varies with wavelength, and were measured to be 500 cm^{-1}, 370 cm^{-1}, 460 cm^{-1}, and 470 cm^{-1} for the wavelengths of 2.5 μm, 3.25 μm, 3.5 μm, and 4.75 μm, respectively. [13]

The method we used here has some advantages over difference frequency mixing the outputs of two separate amplified lasers. There is no timing jitter between lasers to limit the IR pulse length. Our method is also more efficient than that of standard optical parametric amplification [5] where output is built up solely from noise in the nonlinear crystal. For subpicosecond pulses, the crystal lengths are constrained to be very short by group velocity dispersion. Using a seeded beam, one is not as severely

restricted by the damage threshold of the nonlinear crystal because spontaneous emission noise is replaced by white light continuum generated in liquids.

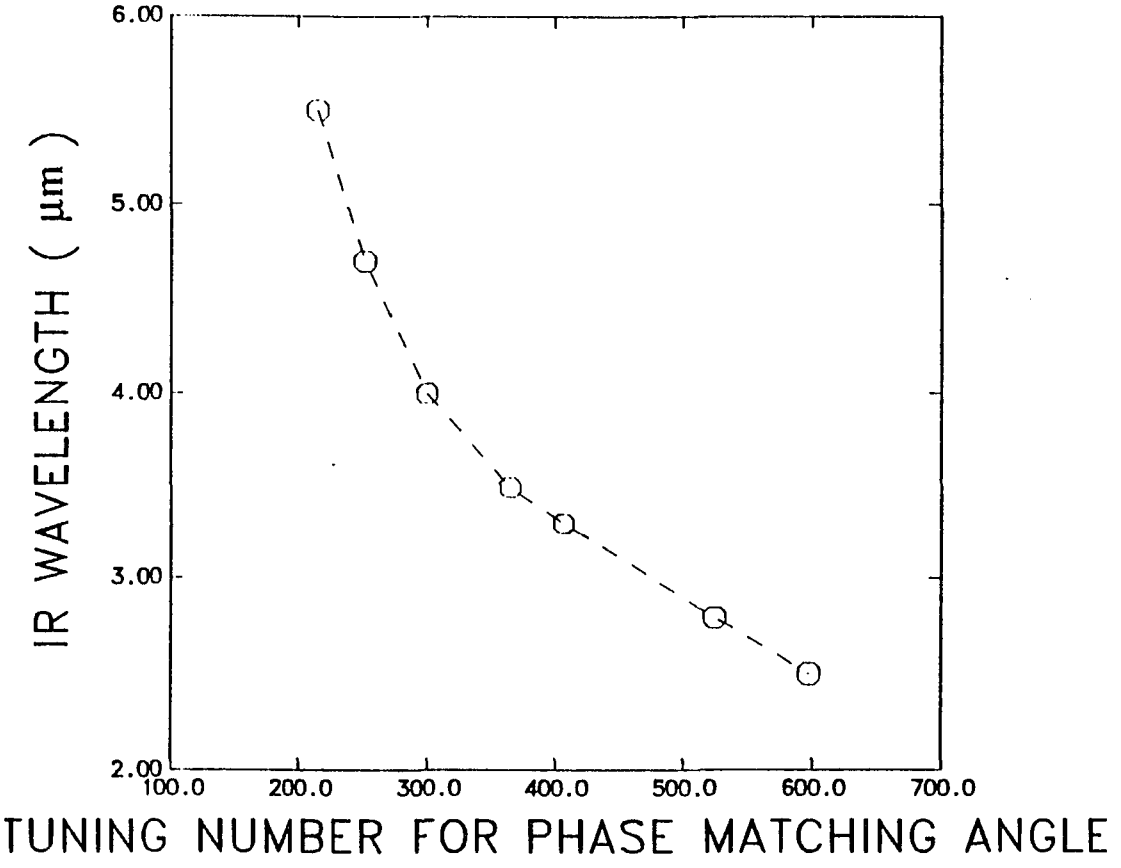

Fig. 4.2.10. The generated IR wavelength as a function of phase matching angle in $LiIO_3$. The dashed line is drawn to guide the eye.

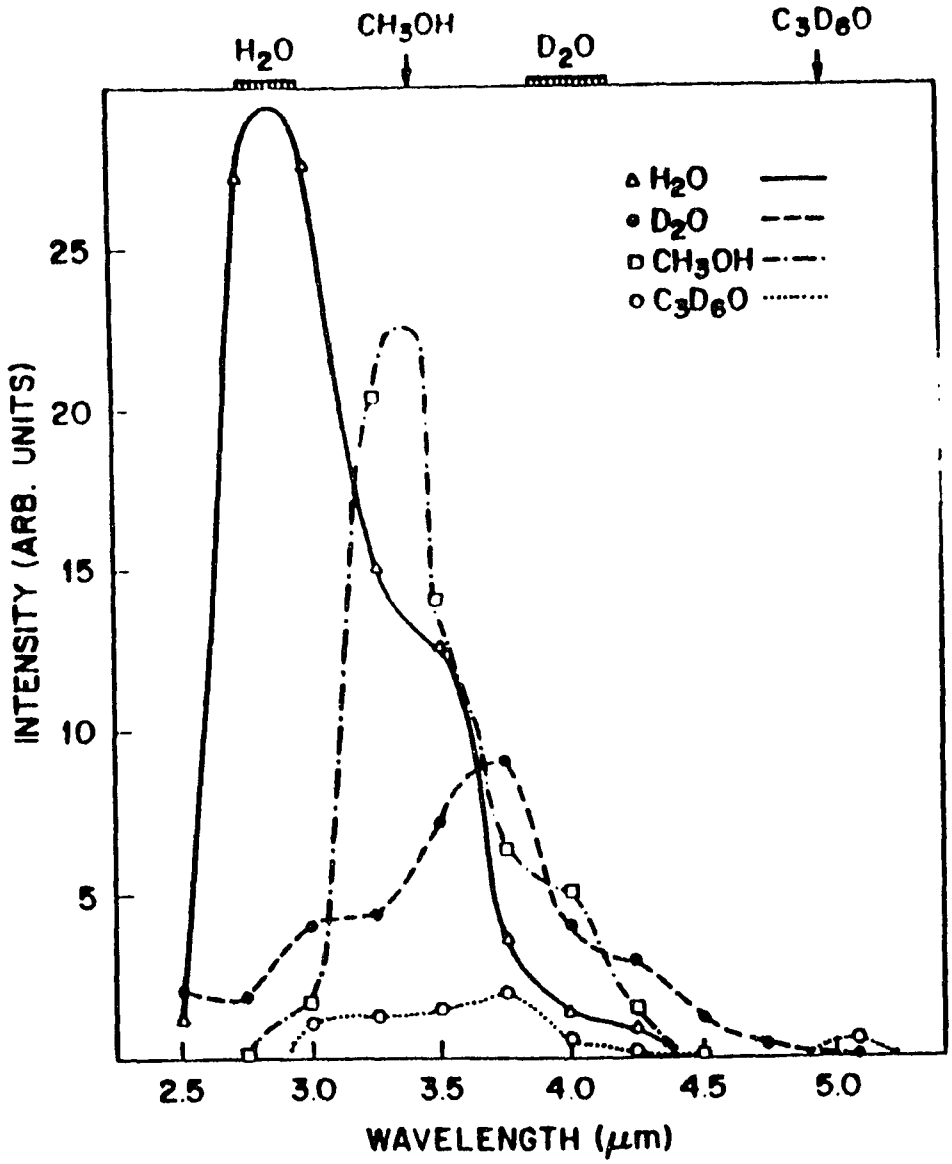

Fig. 4.2.11. The intensity of generated IR pulses as a function of wavelength for four different continuum generation liquids. The lines connecting data points are merely to guide the eye.

4.3. Time-Resolved Photoluminescence Spectroscopy

The time-resolved photoluminescence set up used in our experiments is schematically shown in Fig.4.3.1. [14] The output pulses of 532 nm, 82 MHz, ~ 4 ps and 800 mW from the frequency doubled Nd:YAG laser are focused onto a sample for photoexcitation. The photoluminescence (PL) from the sample is collected and sent into a SPEX 1681B spectrograph which incorporates a 600 grooves/mm reflection grating. The output from SPEX 1681B is directed onto the input slit of an S-20 photocathode in a Hamamatsu C1587 synchroscan streak camera.

A streak camera is most widely used for time-resolved luminescence measurements. [15,16] It converts the temporal character of luminescence into spatial information, and enables one to study processes affecting this emission which occur on a picosecond time scale. A streak camera system consists of a streak tube, imaging optics, fast sweeping electrodes, and video display/computer equipment. The principle of the streak tube is schematically shown in Fig.4.3.2. The light emitted from a sample photoexcited by a ultrafast laser pulse is focused onto the photocathode of a streak tube at a given time and is proportional to the intensity of incident light hitting the photocathode at that time. These photoelectrons are accelerated and deflected across a phosphor screen by a voltage ramp applied by a pair of electrodes. Since the incident light has a temporal intensity profile, the electrons released from the photocathode at different times have different intensities. These electrons are deflected linearly with time and strike the

phosphor screen at different positions. This produces a streak, which has a spatial intensity profile directly proportional to the incident temporal intensity profile of the luminescence. The phosphorescent track is analyzed electronically using a direct readout system including a silicon intensified target (SIT) vidicon camera, a temporal analyzer, and a TV monitor.

Since the pumping pulses are CW pulses at a repetition rate of ~ 82 MHz, a synchroscan streak camera (SSC) which operates in synchronism with the CW laser should be used. [16] A SSC uses a regular streak tube, but the applied sweeping voltage has a sinusoidal form and can be synchronized to the incident light pulse at the repetition rate. The streak images are continuously generated and accumulated at fixed positions on the phosphor screen. The time integration of the streak images can be performed either on the phosphor screen or on the direct readout system making it possible to detect low-level signals with a large signal-to-noise ratio.

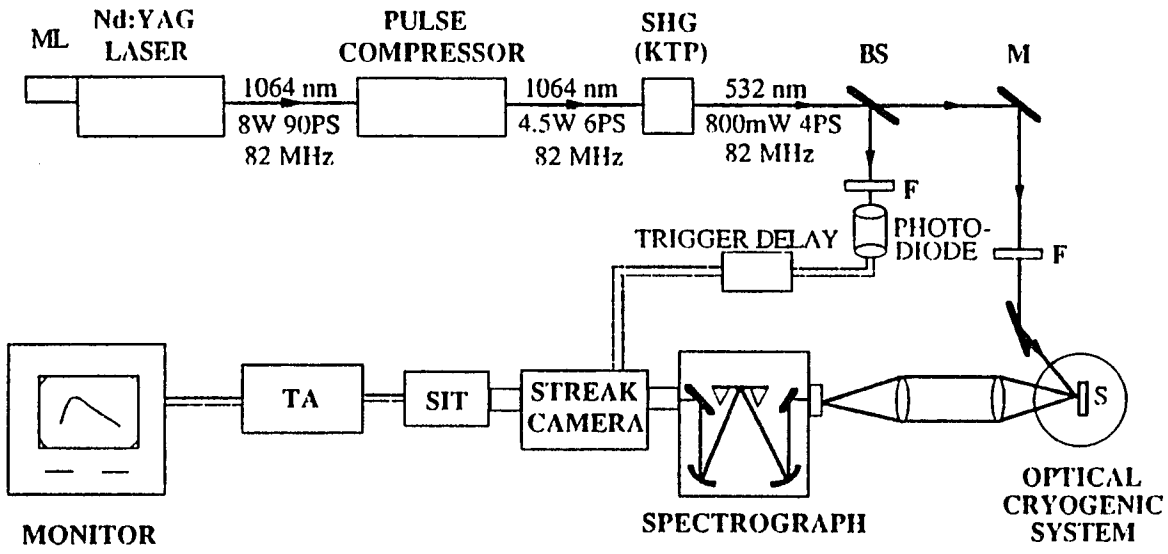

Fig. 4.3.1. Schematic diagram of the time-resolved photoluminescence set up.[14] (BS---beam splitter, M---mirror, F---filter, S---sample, SIT---silicon intensified target, TA---temporal analyzer)

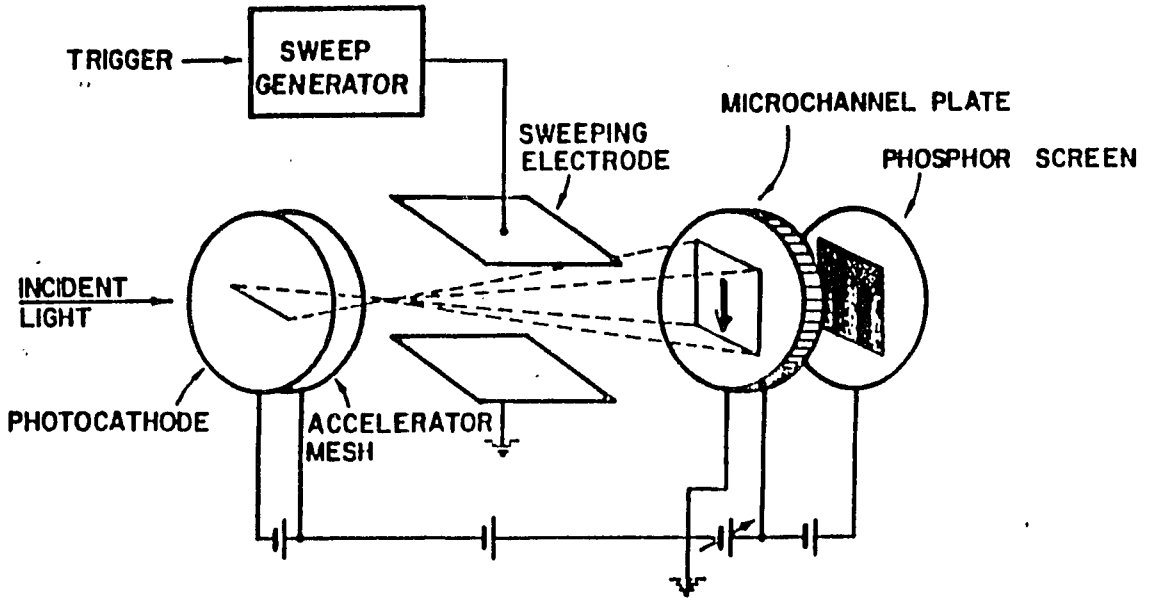

Fig. 4.3.2. Schematic diagram of a streak camera tube. [7,15]

REFERENCES

[1] A. G. Doukas, J. Buchert, and R. R. Alfano, in "Biological Events Probed by Ultrafast Laser Spectroscopy," edited by R. R. Alfano, Academic Press, New York, (1982), Ch.17.

[2] S. K. Gayen, W. B. Wang, V. Petricevic, R. Dorsinville, and R. R. Alfano, Appl. Phys. Lett., 47 , 455 (1985).

[3] N. Ockman, R. Dorsinville, W. B. Wang, and R. R. Alfano, IEEE J, Quantum Electron., QE-23 , 2008 (1987).

[4] W. B. Wang, N. Ockman, M. Yan, and R. R. Alfano, J. of Lumin., 50 , 347 (1992).

[5] A. Laubereau, L. Greiter, and W. Kaiser, Appl. Phys. Lett., 25 , 87 (1974).

[6] T. Sizer, J. D. Kafka, I. N. Duling, C. W. Gabel, and G. A. Mourou, IEEE, QE-19, , 506 (1983).

[7] P. J. Delfyett, S. K. Gayen, and R. R. Alfano, "Encyclopedia of Physical Science and Technology", 14 , Academic Press. Inc. 169, (1987).

[8] A. Yariv, "Optical Electronics", third edition, CBS College Publisher, The Dryden Press., (1985).

[9] R. R. Alfano, and S. L. Shapiro, Phys. Rev. Lett., 29 , 1655 (1972).

[10] T. M. Jedju and L. Rothberg, Appl. Optics, 27 , 615 (1987).

[11] W. B. Wang, Kai Shum, R. R. Alfano, D. Szmyd, and A. J. Nozik, Phys. Rev. Lett., 68 , 662 (1992).

[12] Kai Shum, W. B. Wang, R. R. Alfano, D. Szmyd, and A. J. Nozik, Phys. Rev. Lett., 68 , 3904 (1992).

[13] T. M. Jedju, and L. Rothberg, Appl. Optics, 26 , 2877 (1988).

[14] W. B. Wang, Y. Tokiguchi, and R. R. Alfano, to be submitted for publication.

[15] N. Ockman, W. B. Wang, and R. R. Alfano, J. of Modern Phys., B5 , 3165 (1991).

[16] N. H. Schiller, in "Semiconductors Probed by Ultrafast Laser Spectroscopy, Vol.II, edited by R. R. Alfano, Academic Press., (1984).

Chapter 5
HOT ELECTRON DYNAMICS AND $X_6 \rightarrow \Gamma_6$ SCATTERING TIME IN GaAs

5.1. Historical Review

Because of the significant effect of intra-and-inter-valley scattering rates on GaAs device operation [1], several theoretical groups [2-6] have investigated the energy relaxation process and the intervalley scattering rates of hot electrons in GaAs. Recently, a number of measurements [1,7-10] have been performed on the dynamics of electrons in the Γ_6 valley and have determined the $\Gamma_6 \rightarrow L_6$, $L_6 \rightarrow \Gamma_6$ and $\Gamma_6 \rightarrow X_6$ intervalley scattering times in GaAs. However, to our best knowledge, there have been no previous measurements of the time evolution of the population of hot electrons in a $K \neq 0$ satellite valley, and there have been no previous determinations of the $X_6 \rightarrow \Gamma_6$ back scattering time before this thesis work. The dynamics of electrons in the X_6 valley [11] are directly related to the $X \leftrightarrow \Gamma$ and $X \leftrightarrow L$ intervalley scattering rates and can be used to study their contribution to the energy relaxation of hot electrons.

I have directly measured the hot carrier dynamics in the X valley in GaAs by a picosecond pump-probe IR absorption spectroscopy, and, as a consequence, have determined the $X_6 \rightarrow \Gamma_6$ back intervalley scattering rate for the first time. [12]

5.2. Experimental Setup and Result

The details of the picosecond pump-IR-probe experimental setup have been described in chapter 4 and elsewhere [13]. In this measurement, a 527 nm, 5 ps pulse creates hot electrons and holes. An infrared probe pulse of ~ 3 ps tunable from 2 μm to 5 μm was used to monitor several processes, including the growth and decay of the population of electrons in the X valley subsequent to the pump. The steady-state infrared transmission spectrum of the intrinsic GaAs sample was measured and found to have no appreciable absorption at the probe wavelengths.

The measured change in optical density as a function of delay time between pump and probe pulses, t_d, at λ_{PROBE}=3.1 μm for GaAs at room temperature is displayed in Fig.5.2.1(a). The salient features of the curve are a resolution-limited risetime followed by a multicomponent decay: the fast one has a decay time of 13 ps which was resolved by our 5-ps pump and 3-ps probe system, and the slow one does not show any significant change in absorbance within the experimental time scale of ~ 200 ps. The measured change in optical density as a function of delay time, t_d, at λ_{PROBE}=3.9 μm for GaAs at room temperature is displayed in Fig.5.2.1(b), which is characterized by a flat decay.

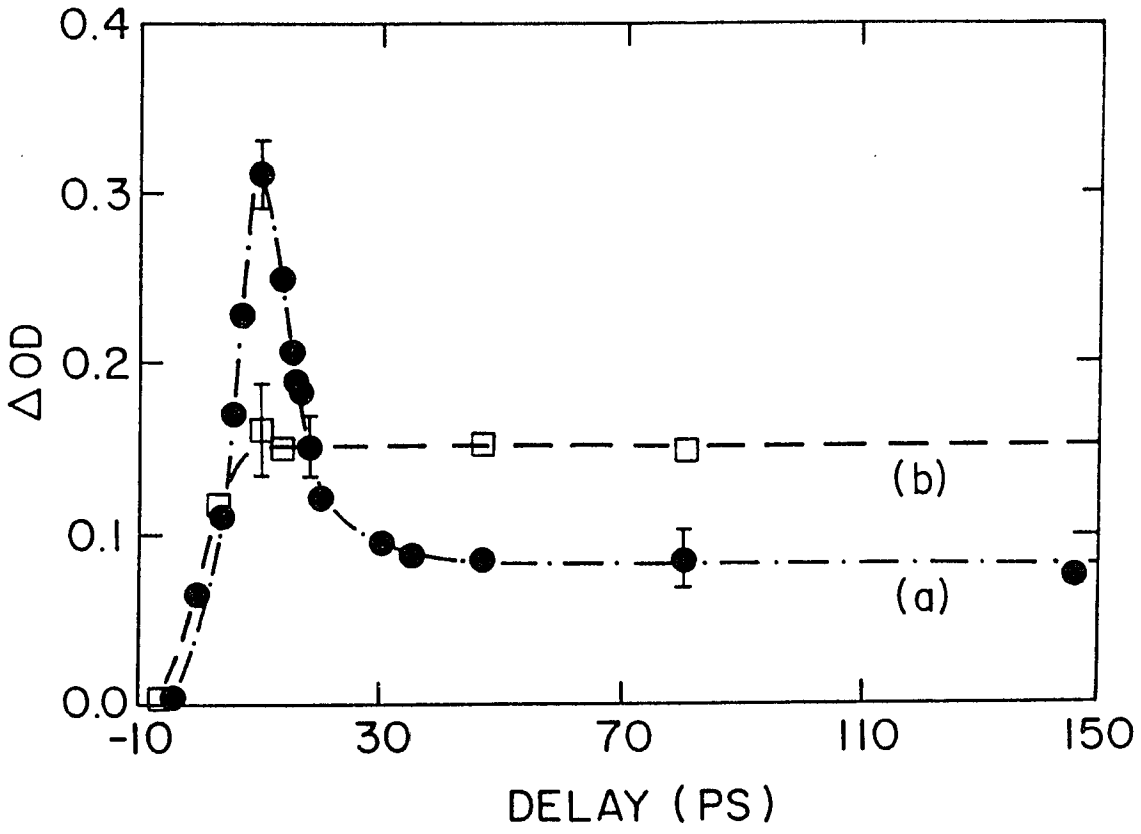

Fig. 5.2.1. Time evolution of the total change in induced optical density at (a) 3.1 μm (filled circles) and (b) 3.9 μm (squares) for GaAs at room temperature. The error flags indicate standard deviation. [12]

5.3. Hot Electron Dynamics in the X_6 Valley

Electrons were excited from all of the valence bands at the Γ point to the conduction band by 2.36 eV (527 nm) pump photons, attaining an energy of about 0.83 eV as measured from the bottom of the Γ conduction valley for electrons from the heavy-hole and light-hole bands, and about 0.42 eV energy above the Γ conduction valley minimum for those from the split-off band (see Fig.5.3.1). The energy of 0.83 eV is sufficient for electrons to scatter from the Γ valley to the L_6 and X_6 valleys.

The induced total absorption at λ_{PROBE}=3.1 μm can be attributed to the following three possible processes after excitation: (1) Intervalence band absorption (IVA) by electrons from the split-off to the heavy-hole and light-hole bands, and by electrons from the light-hole to the heavy-hole bands; (2) Free carrier absorption (FCA) by hot electrons in the Γ, L and X valleys, and by hot holes in the three valence bands; and (3) Inter-conduction band absorption (ICA) by electrons from the X_6 to the X_7 valleys. Their temporal behavior is discussed as the following:

Intervalence band absorption should be characterized by a resolution limited risetime and a flat decay. The fast risetime is due to both the instantaneous excitation of the hot carriers and the few picoseconds redistribution time of the initial and the final state holes for the IVA transitions [6,9], which is shorter than the resolution time of our system. The decay of IVA should be flat within our experimental range of ~ 200 ps since the radiative and Auger recombination time of electrons and holes in GaAs at

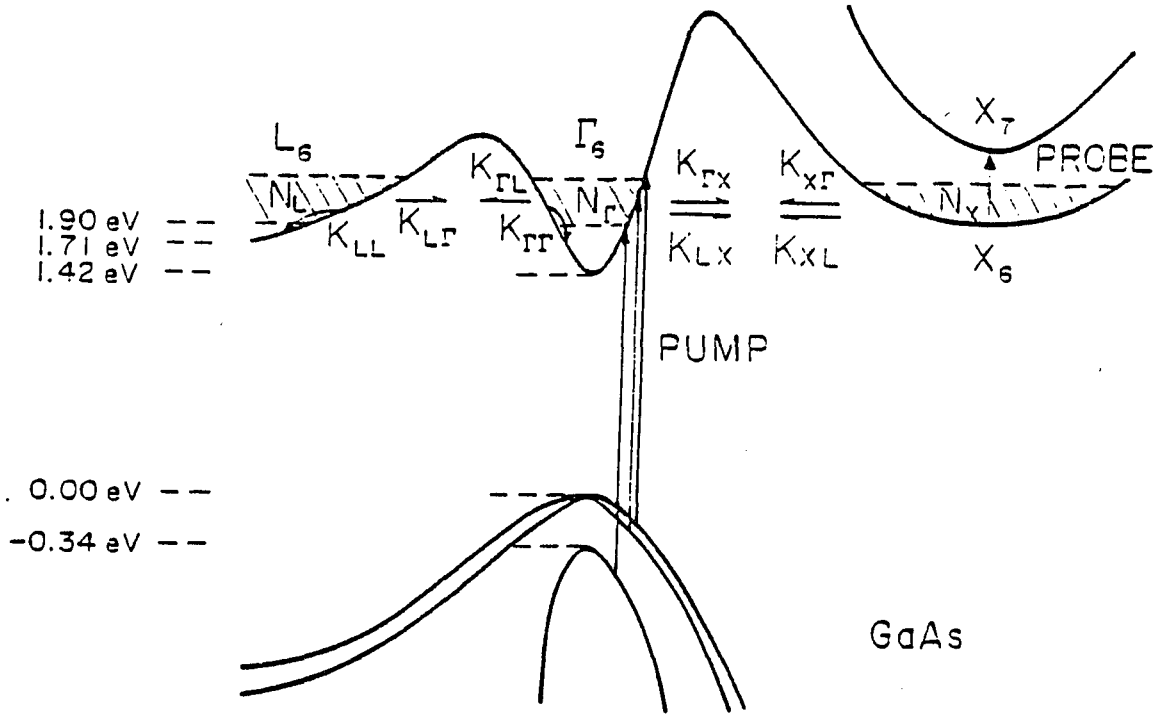

Fig. 5.3.1. The energy band structure diagram showing the excitation transitions, relevant scattering processes and the corresponding transition rates. In the shaded area, electrons in the three valleys have energies 0.48-0.83 eV relative to the bottom of the Γ_6 valley. [12]

room temperature is several nanoseconds and there are no L and X valleys to which holes can scatter[9]. Furthermore, the calculated optical density of IVA at 3.1 μm, obtained by using the cross section from Braunstein[14] and our electron densities of states in the split-off and the light-hole bands, is much smaller than that observed. Therefore, IVA can be essentially neglected.

Free carrier absorption, for similar reasons, can also be characterized by a resolution-limited risetime and a flat decay. To verify this conclusion, the measurement was extended to a probe wavelength of 3.9 μm. At this wavelength, only FCA is possible because (1) the energy of a 3.9 μm (0.318 eV) photon is less than the energy gap of 0.345 eV between the minima of the X_6 and X_7 valleys[15], therefore, the probe photons could not make the transitions for ICA; (2) the absorption cross section for IVA at 3.9 μm given by Braunstein[14] is so small that the calculated optical density of IVA at this wavelength is only 0.003 which is much smaller than the observed value of 0.15 shown in Fig.5.2.1(b), and, therefore, can be neglected. Consequently, the measured change in optical density at 3.9 μm shown in Fig.6.1.1(b) which has a resolution limited risetime followed by a flat decay is due only to FCA. In addition, the optical density of 0.15 ± 0.03 for the flat decay at 3.9 μm agrees with that calculated for FCA by using the cross section from Blakemore[16].

However, the $X_6 \rightarrow X_7$ interconduction band absorption is characterized by a short decay. The electrons excited from the heavy-hole and light-hole

bands to the Γ valley obtained sufficient energy (0.83 eV) to scatter to the L and X valleys from which they can scatter to other valleys. At the same time, electrons in each of these valleys lose their energy by intravalley scattering. Scatterings to and from the X valley can occur many times before the electrons in the Γ and L valleys have insufficient energy (< 0.48 eV for the Γ valley electrons and < 0.19 eV for the L valley electrons, as measured from the conduction Γ valley minimum) to return to the X valley. Therefore, with increasing delay time, the population of electrons in the X_6 band should rapidly increase at first due mostly to $\Gamma_6 \rightarrow X_6$ scattering, reach a maximum, and then decrease due to the back $X_6 \rightarrow \Gamma_6$, L_6 intervalley scattering and the intravalley scattering in the Γ_6 and L_6 valleys. Since Seymour's measurement [17] showed that it takes ~ 25 ps for hot electrons to decay from an initial kinetic energy of 0.83 eV to the bottom energy of the Γ_6 valley, the time for hot electrons to lose their initial energy of 0.83 eV to the X_6 minimum energy of 0.48 eV should be shorter than 25 ps. When the energy of hot electrons falls below the X_6 minimum energy, the population of X_6 electrons would be expected to become zero. Since the $X_6 \rightarrow X_7$ interconduction band absorption follows this behavior, its decay time should be less than 25 ps.

Consequently, for the curve of λ_{PROBE}=3.1 μm, we attribute the flat decay to FCA and the fast decay to the $X_6 \rightarrow X_7$ ICA. The difference in the temporal behavior of ICA from that of FCA and IVA is the key to

separate the interconduction band $X_6 \rightarrow X_7$ absorption from the total absorption. The measured value of $\Delta OD = 0.085 \pm 0.017$ in the flat decay region in Fig.5.2.1(a) gives the value of FCA at 3.1 μm. Consequently, a curve similar to Fig.5.2.1(b) but with the appropriate flat decay value of $(\Delta OD)_{FC}$ for 3.1 μm is subtracted from the curve of $(\Delta OD)_{TOTAL}$ (Fig.5.2.1(a)) to give the change in optical density attributed only to the $X_6 \rightarrow X_7$ absorption at 3.1 μm, $(\Delta OD)_{X_6 \rightarrow X_7}(t)$. From this quantity, as will be shown, the time evolution of the population density of electrons in the X_6 valley, $N_X(t)$, can be obtained.

The optical density $(\Delta OD)_{X_6 \rightarrow X_7}(t)$ at $\lambda_{PROBE} = 3.1$ μm, obtained in the manner described above, was used to determine the corresponding transmittance by the relation $\Delta OD(t_d) = -\log T(t_d)$. This transmittance as a function of delay time is given in terms of $N_X(t)$ by:

$$T(t_d) = \int_{-\infty}^{\infty} dt I(t - t_d) e^{-N_X(t)\sigma_X d} / \int_{-\infty}^{\infty} dt I(t), \qquad (5.3.1)$$

where I(t) is the instantaneous intensity of the probe pulse, σ_X the absorption cross section for the $X_6 \rightarrow X_7$ transition, and d the effective length of the sample. The probe pulse is assumed to have a Gaussian profile with a 3.0 ± 0.5 ps FWHM. The function $N_X(t_d)$ describing the hot electron dynamics in the X valley is obtained by deconvoluting the transmittance data $T(t_d)$ and the probe pulse I(t) from equation (5.3.1), and is shown in Fig.5.3.2.

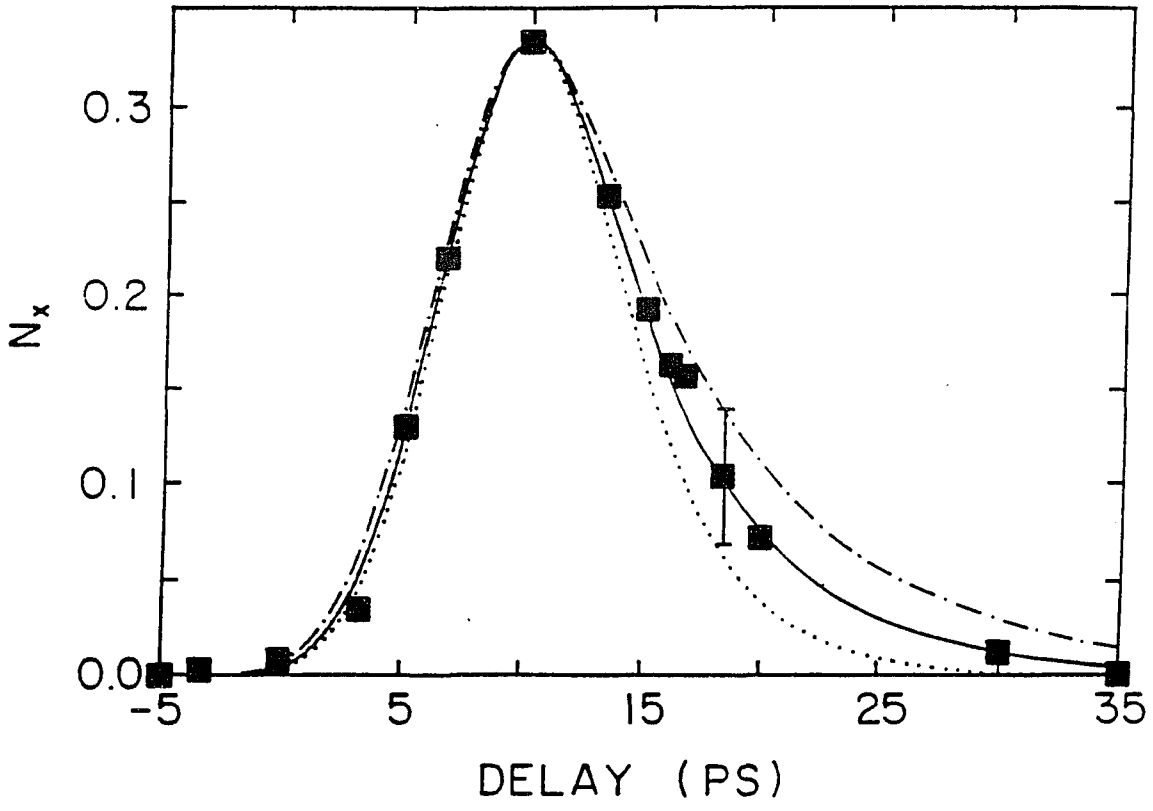

Fig. 5.3.2. The result of fitting the numerical solution of rate equations (5.4.1) to (5.4.3) to the experimental data of N_X. The filled squares represent the experimental data. The value of N_X at the peak position corresponds to the carrier density of 2.8×10^{19} cm^{-3} in the X_6 valley. The dot-dot, solid, and dot-dot-dash curves are the computer fits corresponding to $X\rightarrow\Gamma$ scattering times of 0.20, 0.50, and 0.80 ps, respectively, with the fixed values of $t_{\Gamma L}$=151 fs, $t_{L\Gamma}$=1.5 ps, $t_{\Gamma X}$=28 fs, and $t_{\Gamma\Gamma}$ = 1.48 ps. [12]

5.4. Rate Equation Analysis and Determination of the $X_6 \rightarrow \Gamma_6$ Intervalley Scattering Time

The time evolution of the population of electrons in the X_6 valley shown in Fig.5.3.2 can be used to extract the value of the $X \rightarrow \Gamma$ intervalley scattering time by a rate equation analysis. The inter-and-intravalley scattering rates are indicated in Fig.5.3.1. The rate equations governing the kinetics of the populations of electrons in the energy range of 0.48eV--0.83 eV relative to the bottom of the Γ valley (shaded area in Fig.5.3.1) are

$$\frac{dN_\Gamma(t)}{dt} = -K_{\Gamma L}N_\Gamma(t)+K_{L\Gamma}N_L(t)-K_{\Gamma X}N_\Gamma(t)+K_{X\Gamma}N_X(t)-K_{\Gamma\Gamma}N_\Gamma(t)+\alpha dP(t) \quad (5.4.1)$$

$$\frac{dN_X(t)}{dt} = K_{\Gamma X}N_\Gamma(t)-K_{X\Gamma}N_X(t)+K_{LX}N_L(t)-K_{XL}N_X(t) \quad (5.4.2)$$

$$\frac{dN_L(t)}{dt} = K_{\Gamma L}N_\Gamma(t)-K_{L\Gamma}N_L(t)+K_{XL}N_X(t)-K_{LX}N_L(t)-K_{LL}N_L(t) \quad (5.4.3)$$

where N_i(t) = instantaneous population density of electrons in the ith valley whose kinetic energies are in the shaded area, and i=Γ, L, X; P(t)=pump photon flux density; $K_{ij}=1/t_{ij}$, scattering rates, where i,j= Γ, L, X; t_{ij}=intervalley scattering time from i to j valleys for i$\neq$j; and t_{ii}=average time of electrons in the ith valley to undergo an energy loss from the top to the bottom of the shaded area by intravalley scattering; α is the absorption coefficient of the sample for the pump pulse at 527 nm; and d=1/α is the effective length of the sample.

The rate equations (5.4.1) to (5.4.3) were solved for $N_X(t)$ numerically by using the recently determined values of $t_{L\Gamma} = 2.5 \pm 0.5$ ps [7,8] for 0.5 eV electrons at room temperature with a carrier density up to 10^{19} cm^{-3}, $t_{\Gamma L} = 540 \pm 120$ fs for 0.48 eV electrons, and $t_{\Gamma X} = 180 \pm 40$ fs for 0.58 eV electrons [10] at 2 ^{0}K with an injected-carrier density of 3×10^{15} cm^{-3}. These values can not be directly substituted into the rate equations (5.4.1) to (5.4.3) because their experimental conditions were different from ours. The intervalley scattering times vary with the experimental parameters such as crystal temperature, T, kinetic energy of electrons in the initial valley, ε_i, and the density of excited electrons participating in the intervalley scattering process, n_{ele}. [2,3,18] Normalizing these previously determined values of $t_{L\Gamma}$, $t_{\Gamma L}$, and $t_{\Gamma X}$ to our experimental conditions using Conwell's theory [2] for the function $t_{ij}(T, \varepsilon_i)$ and Kann's calculated results [18] for the relation $t_{ij}(n_{ele})$ gives values of $t_{L\Gamma} = 1.5 \pm 0.3$ ps, $t_{\Gamma L} = 151 \pm 34$ fs and $t_{\Gamma X} = 28 \pm 6$ fs. The parameter $t_{\Gamma\Gamma}$ was determined to be 1.48 ± 0.18 ps by combining the average electron-phonon scattering time of 165 ± 20 fs [19] with the required emission of 9 LO phonons by 0.83 eV electrons in the Γ valley to reduce their energy to near the bottom of the X valley. The relations between K_{LL} and $K_{\Gamma\Gamma}$, K_{LX} and K_{XL}, and K_{XL} and $K_{X\Gamma}$, used for solving the rate equations, were determined by using Conwell's theory [2,5], and the parameters $m_\Gamma = 0.063\ m_0$ (m_0 is the free electron mass), $m_L = 0.55 m_0$, $m_X = 0.85 m_0$, $\varepsilon_{0\Gamma} = 0$, $\varepsilon_{0L} = 0.29$ eV, $\varepsilon_{0X} = 0.48$ eV [16], and the values for the deformation potentials, $D_{X\Gamma}$ and D_{XL} [4].

All of the three parameters $K_{X\Gamma}$, K_{XL} and K_{LX} have, so far, not been determined by previous experiments. Since they are related by intervalley scattering theory, any one of them, in our analysis, can be chosen as an unknown parameter to be determined from our experimental data. However, since $K_{X\Gamma}$ is directly related to hot electron relaxation in the central Γ valley which is more important than the L valley for GaAs and GaAs-like systems and devices characterized by a direct band gap, we are more interested in the $X \rightarrow \Gamma$ scattering time, $t_{X\Gamma}=1/K_{X\Gamma}$. Therefore, this quantity was chosen as a variable parameter to fit the numerical solution for $N_X(t)$ to the experimental data. With the value of $t_{\Gamma\Gamma}=1.48$ ps, the three curves for numerical solutions of $N_X(t)$ for the three values of $t_{X\Gamma}$; 0.20, 0.50, and 0.80 ps, are shown in Fig.5.3.2. Comparing these curves with the experimental data gives a value of $t_{X\Gamma}$ of 500 fs for the best fit. The probable error for the data point at $N_X=0.105$ at the delay time between the probe and pump pulses of $t_d=18.3$ ps was found to be $\pm$ 0.037, taking into consideration the standard deviations in both the data ($t_d=18.3$ ps) and background ($t_d=80$ ps) points (see Fig.5.2.1(a)). A comparison of the error flag with the curves in Fig.5.3.2 gives an uncertainty in $t_{X\Gamma}$ of $\pm$300 fs. The total contribution of errors in the parameters used to solve the rate equations was also considered and found to give an uncertainty in $t_{X\Gamma}$ of $\pm$ 190 fs. Therefore, the total uncertainty in $t_{X\Gamma}$ arising from both experimental and parameter errors should be $\pm\sqrt{300^2+190^2}=\pm 350 fs$.

5.5. Discussion

Shah's subpicosecond luminescence measurements [7] show that if hot electrons excited by 2.0 eV photons can undergo Γ–L scattering, the decay of their energies to the bottom of the Γ valley is much slower (~ 10 ps for GaAs) than the decay without intervalley scattering(~ 2 ps for InP). The electrons returning to the Γ valley from the L valley, consequently, act as a source of heating of electrons in the Γ valley. In our experiment, hot electrons have enough energy to scatter to both the L and X valleys from the Γ valley. The $X \rightarrow \Gamma$ back scattering acts as an additional source of heating of the electrons in the Γ valley, and further slows their net cooling. Also, the $X \rightarrow L$ scattering acts as a source of heating of electrons in the L valley, and slows the cooling rate of the entire hot electron system. By combining our results with those of Shah, the total time for electrons to decay from their initial energy of 0.83 eV to the bottom of the Γ valley due to intra-and-intervalley scattering is estimated to be ~ 23 ps which is consistent with the value of ~ 25 ps obtained by Seymour et all. [17]

A theoretical support for our determination is the Monte-Carlo calculation by Kann et al [18]. They estimated the X to Γ intervalley scattering time to be ~ 400 fs which is in good agreement with our determined value of 500 ± 350 fs.

Our determined value of $t_{X\Gamma}$ is comparable with the value expected from the $t_{\Gamma X}$ measurement of Ulbrich et al [10]. As previously mentioned,

based on their measurement, the $\Gamma \rightarrow X$ intervalley scattering time was normalized to be 28 ± 6 fs for our experimental conditions. Using this normalized value of $t_{\Gamma X}$ and the intervalley scattering theory [2], the $X \rightarrow \Gamma$ back scattering time $t_{X\Gamma}$ corresponding to our experimental conditions was calculated to be 689 ± 148 fs which is slightly longer but within the experimental errors of our determined value of 500 ± 350 fs.

Since our determination, combined with others, [1,7-10] shows that $t_{\Gamma X} < t_{\Gamma L}$ and $t_{X\Gamma} < t_{L\Gamma}$, hot electrons scatter back and forth between the Γ and X valleys as well as between the L and X valleys more frequently than between the Γ and L valleys. The time evolution of the population of the electrons in the X valley presented here gives detailed knowledge of the contribution of the X-valley-involved intervalley scattering to the relaxation of hot electrons. Consequently, our results provide new insight into the dynamics of hot electrons in GaAs.

REFERENCES

[1] W. Z. Lin, M. J. LaGasse, R. W. Schoenlein, B. Zysset, and J. G. Fujimoto, SPIE, 942 , (March, 1988).

[2] E. M. Conwell and M. O. Vassell, IEEE Trans. Electron. Devices, ED-13 , 22 (1966).

[3] S. Zollner, S. Gopalan, and M. Cardona, Appl. Phys. Lett., 54 , 614 (1989).

[4] L. Reggiani, in " Hot-Electron Transport in Semiconductors ", edited by L. Reggiani, Springer-Verlag, New York, (1984), ch.2.

[5] E. M. Conwell, in " High Field Transport in Semiconductors ", Academic Press, New York, (1967), Ch.5.

[6] M. A. Osman and D. K. Ferry, Phys. Rev. B36 , 6018 (1987).

[7] J. Shah, B. Deveaud, T. C. Damen, and W. T. Tsang, A. C. Gossard, and P. Lugli, Phys. Rev. Lett., 59 , 2222 (1987).

[8] A. Katz, and R. R. Alfano, Appl. Phys. Lett., 53 , 1065 (1988).

[9] P. C. Becker, H. L. Fragnito, C. H. Brito Cruz, J. Shah, R. L. Fork, J. E. Cunningham, J. E. Henry, and C. V. Shank, Appl. Phys. Lett., 53 , 2089 (1988).

[10] R. G. Ulbrich, J. A. Kash, and J. C. Tsang, Phys. Rev. Lett., 62 , 949 (1989).

[11] Since subscript for all of the bands under discussion is labled #6, this #6 will be deleted from here on unless noted otherwise.

[12] W. B. Wang, N. Ockman, M. Yan, and R. R. Alfano, J. of Lumin., 50 , 347 (1992).

[13] N. Ockman, R. Dorsinville, W. B. Wang, and R. R. Alfano, IEEE J, Quantum Electron, QE-23 , 2008 (1987).

[14] R. Braunstein, and L. Magid, Phys. Rev., 111 , 480 (1958).

[15] W. B. Wang, N. Ockman, M. A. Cavicchia, and R. R. Alfano, Appl. Phys. Lett., 57 , 395(1990).

[16] J. S. Blakemore, J. Appl. Phys., 53 , R123 (1982).

[17] R. J. Seymour, M. R. Junnarkar, and R. R. Alfano, Solid State Commun, 41 , 657 (1982).

[18] M. J. Kann, A. M. Kriman, and D. K. Ferry, Phys. Rev., B41 , 12659 (1990).

[19] J. A. Kash, J. C. Tsang, and J. M. Hvam, Phys. Rev. Lett., 54 , 2151 (1985).

Chapter 6
DENSITY OF STATES EFFECTIVE MASS OF THE X_7 BAND in GaAs

6.1. Introduction

It has been pointed out that the $\Gamma \rightarrow X$ intervalley transfer is one of the dominant scattering mechanisms for high-energy Γ valley electrons [1-4]. The X valley plays an important role in high-field transport in GaAs [3]; therefore, the exploration of the properties of the X_6 and X_7 bands has attracted general interest in semiconductor physics, and is significant for further understanding the band structure of GaAs as well as for hot carrier transport studies for fast electronic devices. Over the past 20 years, there has been a number of investigations [5-8] to estimate the density of states effective mass for the X_6 band. To our best knowledge, no such measurement has been performed for the determination of the density of states effective mass for the X_7 band. Furthermore, there has been a number of steady-state absorption measurements to investigate the energy separation, Δ_{7-6}, between the X_6 and X_7 bands at their minima [9-12]. All of the determinations of Δ_{7-6} from those experiments were indirect, and the obtained values varied from 0.35 eV to 0.58 eV.

I have measured the $X_6 \rightarrow X_7$ prompt absorption spectrum in an intrinsic GaAs crystal using a time-resolved picosecond pump-IR-probe technique. From the long wavelength onset of the induced $X_6 \rightarrow X_7$ absorption

spectrum, the energy gap between the minima of the X_6 and X_7 bands was directly determined to be 0.345 ± 0.017 eV. By fitting the $X_6 \rightarrow X_7$ absorption data, the density of states effective mass for the X_7 band was found to be $0.48 \pm 0.06\ m_0$.[13]

6.2. The $X_6 \rightarrow X_7$ IR Absorption Spectrum

The experimental setup has been described in Section 4.1.[13-15] In this experiment, a 527 nm pump pulse of 5 ps duration was used to create hot electrons with sufficient energy to scatter into the X_6 band. An IR probe pulse of ~ 3 ps tuned from 2 μm to 5 μm was used to monitor the time-resolved absorption including the transition from the X_6 to the X_7 bands. The steady-state infrared transmission spectrum of the intrinsic GaAs sample was measured and found to have no appreciable absorption at the probe wavelengths.

The changes in optical density as a function of delay time at various probe wavelengths from 3.9μm to 2.16μm for GaAs at room temperature are displayed in Fig.6.2.1. Although the risetimes of all of these curves are resolution-limited, their decay behavior show some differences. The curve in Fig.6.2.1(c) for λ_{probe}=3.1μm shows a multicomponent decay: the fast one with a decay time of ~ 13ps, and the slow one which is flat within the experimental time scale of ~ 200ps. The total measured absorption can be attributed[4] to (1) intervalence band absorption (IVA) by electrons from the split-off to the heavy-hole and light-hole bands; (2) free carrier absorption (FCA) by hot electrons in the Γ, L, and X conduction valleys and hot holes in the three valence bands; and (3) the interconduction band absorption (ICA) by electrons making the transition from

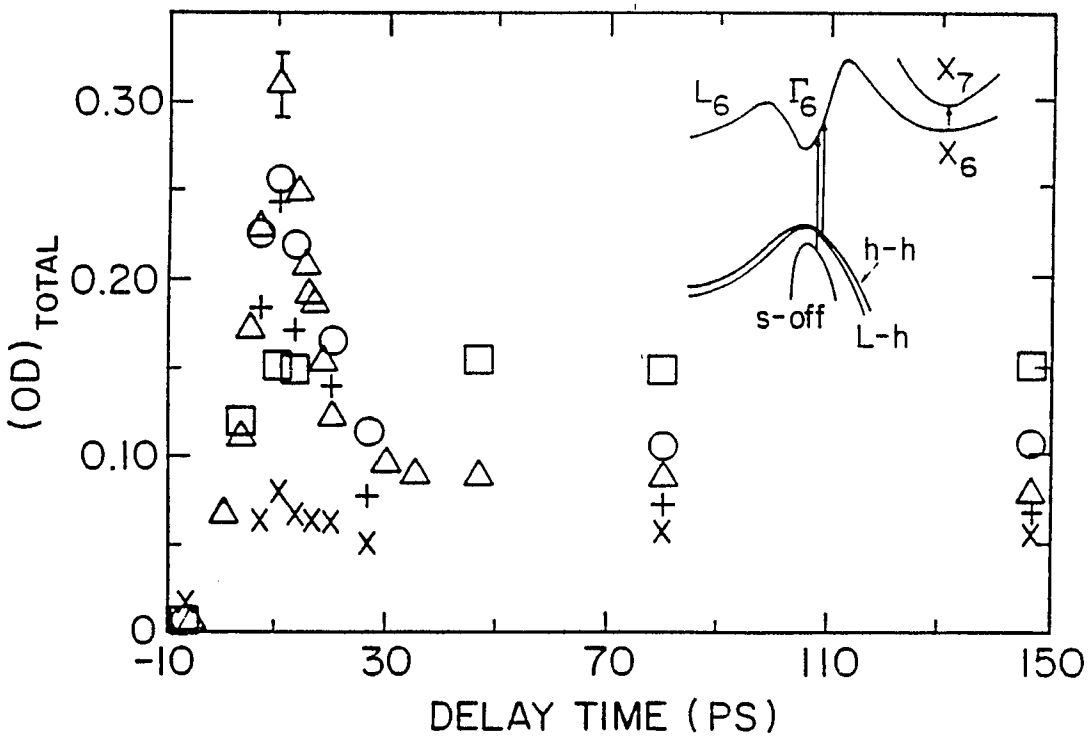

Fig.6.2.1 Time evolution of the total change in induced optical density at (a) 3.9 μm (squares), (b) 3.4μm (circles), (c) 3.1μm (triangles), (d) 2.9μm (pluses), and (e) 2.16μm (cross lines) for GaAs at room temperature. The error flags indicate standard deviation. The band structure of GaAs is shown in the inset. [13]

the X_6 to the X_7 bands. As mentioned in Section 5.3, the intervalence band absorption and the free carrier absorption are characterized by a resolution limited risetime and a flat decay; while the $X_6 \rightarrow X_7$ interconduction band absorption is characterized by a short (< 25 ps) decay.

Consequently, for λ_{probe}=3.1 μm, we attribute the flat decay to FCA and IVA, and the fast decay only to the $X_6 \rightarrow X_7$ ICA. This difference of the temporal behavior of ICA from that of FCA and IVA is the key to separate the $X_6 \rightarrow X_7$ absorption from the total absorption. The measured value of 0.085 ± 0.017 in the flat decay region in Fig.6.2.1(c) gives the sum of FCA and IVA at 3.1 μm, consequently, a curve parallel to Fig.6.2.1(a) but with the appropriate flat decay value of $(\Delta OD)_{FC+IV}=0.085 \pm 0.017$ for 3.1μm is subtracted from $(\Delta OD)_{TOTAL}$ (Fig.6.2.1(c)) to give the change in optical density attributed only to the $X_6 \rightarrow X_7$ ICA at 3.1 μm.

The curves in Figs.6.2.1(b), (d), and (e) show similar decay behavior to that in Fig.6.2.1(c). To obtain the detailed absorption spectrum, the measurements were extended to the probe wavelengths of 3.65μm, 3.60μm, 3.55μm, and 2.45μm. Their decay behavior are similar to that of 3.9μm for the first two, and to that of 3.1 μm for the last two. The values of $(\Delta OD)_{TOTAL}$ and $(\Delta OD)_{FC+IV}$, obtained in a similar manner to their determinations for 3.1 μm, for all of the probe wavelengths at t_d=10 ps are shown in Figs.6.2.2(a),(b), respectively. Subtracting the sum of FCA and IVA (Fig.6.2.2(b)) from the total absorption (Fig.6.2.2(a)) gives the

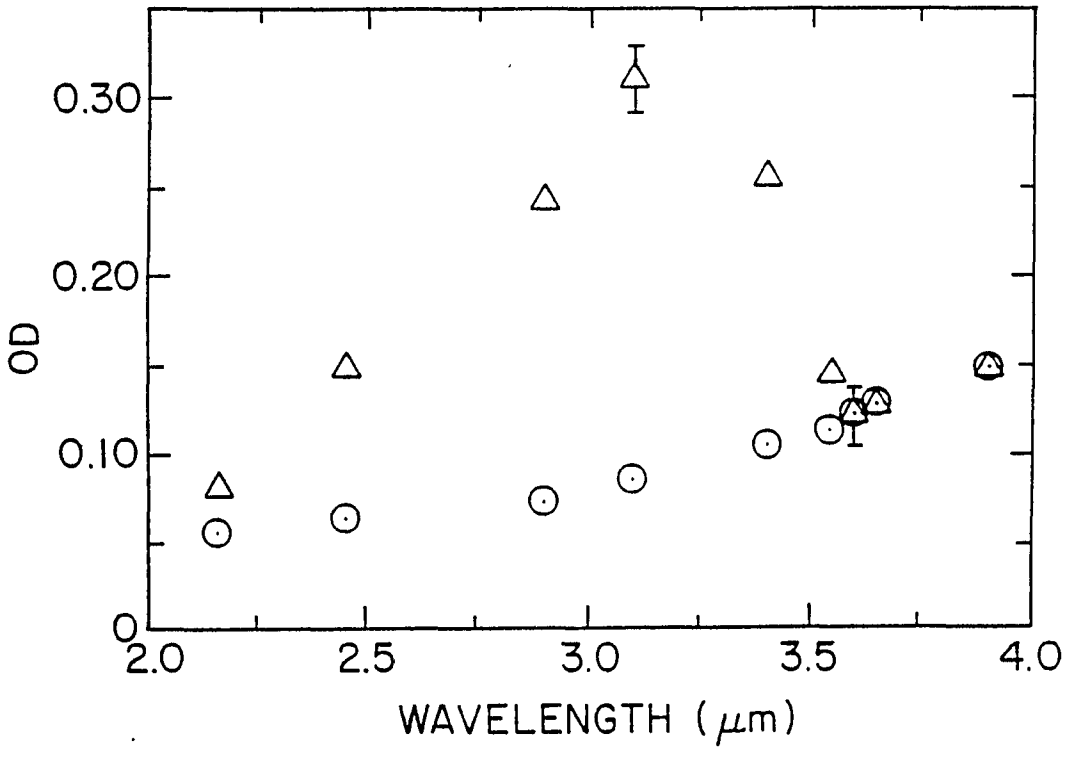

Fig.6.2.2 Absorption spectra for (a) total induced absorption at the peak position (t_d ~ 10 ps) (triangles), and (b) sum of the free carrier and intervalence band absorptions at the flat decay region (circles). [13]

$X_6 \rightarrow X_7$ absorption data, $(\Delta OD)_{X_6 \rightarrow X_7}$, shown in Fig.6.2.3.

The long wavelength threshold of 3.6 μm of the $X_6 \rightarrow X_7$ absorption shown in Fig.6.2.3 indicates an energy separation of 0.345 eV between the X_6 and X_7 bands at their minima. A comparison of the error flag with the data at 3.6 μm gives an uncertainty of 0.017 eV for the value of Δ_{7-6}.[16] Although this parameter has been reported to be anywhere from less than 0.3 eV to 0.9 eV by calculations[17,18] and from 0.35 eV to 0.58 eV by a number of indirect measurements[9-12], our first direct measurement enables us to clarify this large range of discrepancies in the energy separation between the X_6 and X_7 bands at their minima.

It should be emphasized that IVA has nothing to do with the absorption spectrum shown in Fig.6.2.3 because of its temporal behavior discussed above. In addition, the calculated optical densities of IVA as a function of probe wavelengths, obtained by using the crossections from Braunstein[20] and our electron densities in the split-off band, showed that its shape and magnitudes do not match the measured absorption as shown in Fig.6.2.4.

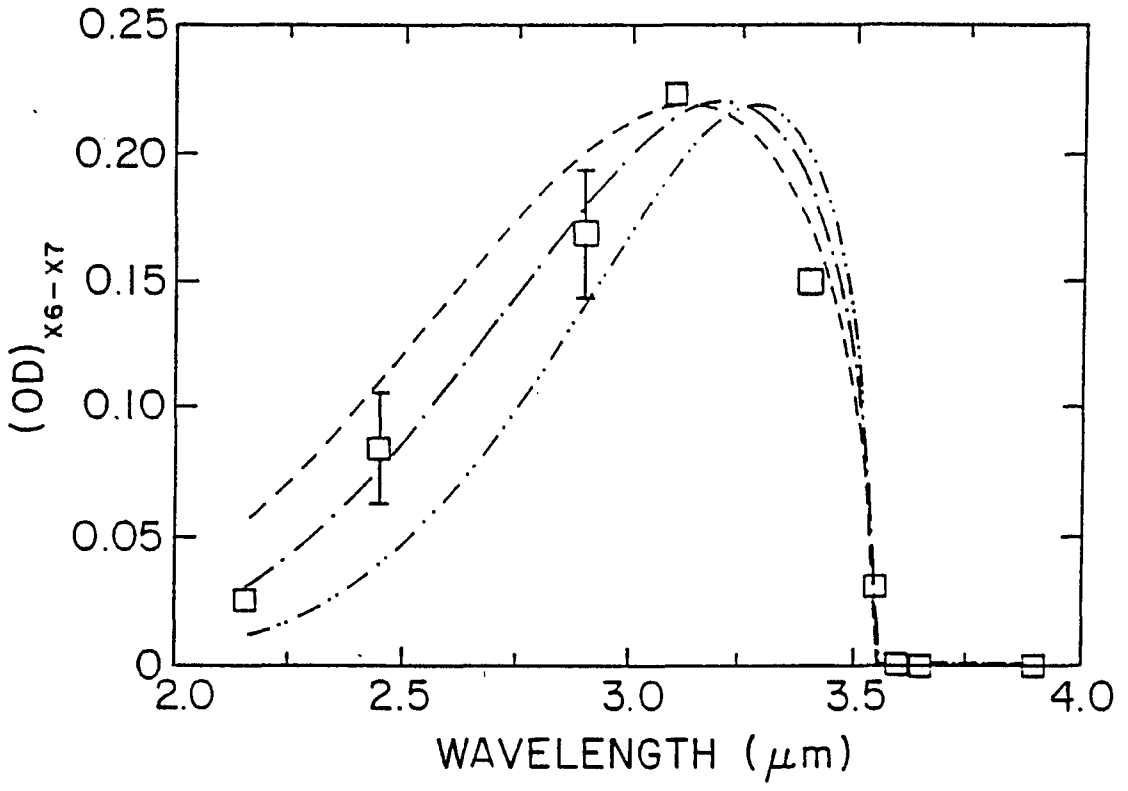

Fig.6.2.3 The result of fitting the calculated optical density for the $X_6 \rightarrow X_7$ transition to the measured $X_6 \rightarrow X_7$ absorption spectrum. The squares are the experimental data at t_d = 10 ps. The dash-dash, dot-dash, and dot-dot-dash curves are the computer fit corresponding to the density of states effective mass of $0.44m_0$, $0.48m_0$, and $0.54m_0$ for the X_7 band, respectively. [15]

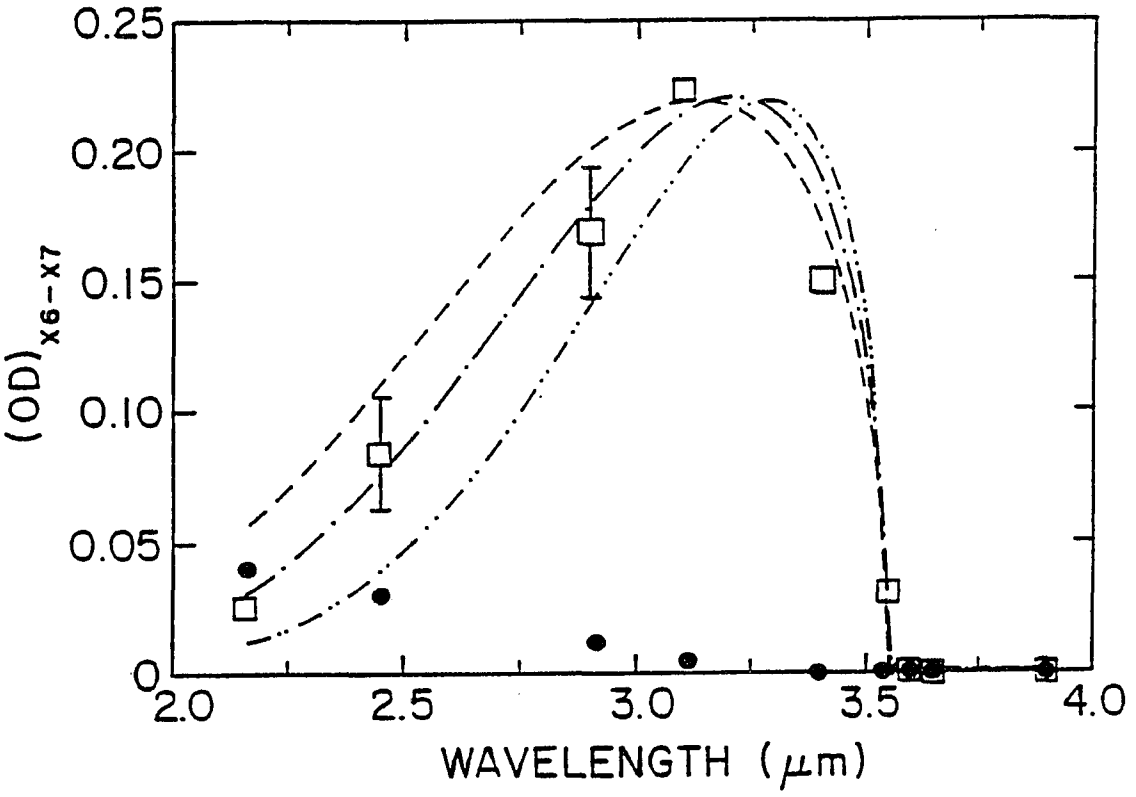

Fig.6.2.4. The comparison of the intervalence band absorption (IVA) (dots) with the observed $X_6 \rightarrow X_7$ IR absorption (squares) spectra in GaAs with 527 nm pump.

6.3. Density of States Effective Mass for the X_7 Bands

The $X_6 \rightarrow X_7$ absorption spectrum shown in Fig.6.2.3 can be used to estimate the density of states effective mass for the X_7 band. Since all of the momentum-conserving transitions from the X_6 band to the X_7 band are allowed,[5] every initial state in the X_6 band is associated with a final state in the X_7 band such that $E_7-E_6=\hbar\omega$ corresponding to an $X_6 \rightarrow X_7$ transition, where E_7 and E_6 are the energies of electrons in the X_7 and X_6 bands, respectively, and $\hbar\omega$ is the energy of an absorbed photon. According to the Fermi-Golden Rule, the probability rate for a transition from the X_6 band to the X_7 band is given by

$$W_{6\rightarrow 7}=(2\pi/\hbar)|H_{6\rightarrow 7}|^2\delta(E_7-E_6-\hbar\omega), \qquad (6.3.1)$$

where $H_{6\rightarrow 7}$ is the perturbation matrix element. The total number of the net transitions per second in a crystal of effective volume V is given by:[20]

$$N_{6\rightarrow 7}=\frac{2V}{\pi\hbar}\int_0^\infty d(k-k_{X0})|H|_{6\rightarrow 7}{}^2\delta(E_7-E_6-\hbar\omega)(k-k_{X0})^2[f_6(E_6)-f_7(E_7)], \qquad (6.3.2)$$

where k_{xo} is the absolute value of the k vector at the band edge (100), $f_6(E_6)$, $f_7(E_7)$ are the probabilities that an electron has the energies E_6, E_7 in the X_6 and X_7 bands, respectively.

As mentioned in section 2.6, if the electron density n is higher than the critical electron density n_c, a thermalized Fermi-Dirac distribution can be achieved before there is significant energy loss from the hot electrons

to the lattice.[21,22] Therefore, the probability that a state is occupied by an electron in the X_6 band is given by

$$f_6(E_6)=\frac{1}{\exp[E_6-(E_F)_6]/k_BT+1} \tag{6.3.3}$$

where $(E_F)_6$ is the Fermi energy for X_6 electrons. If the kinetic energy of the excited electrons in the Γ_6 valley is sufficient for the $\Gamma_6 \rightarrow X_6$ scattering but insufficient to allow strong $\Gamma_6 \rightarrow X_7$ intervalley scattering, there are few hot electrons in the X_7 band. Therefore, $f_7(E_7) \sim 0$.

Since the $X_6 \rightarrow X_7$ transition is assumed to be of the electric dipole type, the perturbation matrix element can be written as

$$H_{6\rightarrow 7}(k)=(eE_0/2)\int dV U^*_{6k}(\vec{r})XU_{7k}(\vec{r}) \tag{6.3.4}$$

where $U_{6k}(\vec{r})$, $U_{7k}(\vec{r})$ are the wave functions for X_6 and X_7 electrons, respectively, and eX is the component of the electron dipole moment along the direction of the electric field of the light. Since H(k) varies with k only a few percent,[23] it can be approximately treated as a constant.

Substituting the expressions for $f_6(E_6)$, $f_7(E_7)$ and $H_{6\rightarrow 7}(k)$ into equation (6.3.2) gives:

$$N_{6\rightarrow 7}=\frac{2V}{\pi\hbar}|H|^2\int_0^\infty d(k-k_{X0})\delta(E_7-E_6-\hbar\omega)\frac{(k-k_{X0})^2}{(\exp[E_6-(E_F)_6]/k_BT+1)} \tag{6.3.5}$$

Since we are only interested in the determination of the state effective mass of the X_7 band, the rotational ellipsoids for both the X_6 and X_7 bands

can be treated as spherical surfaces with the corresponding density of states effective mass. If the $X_6 \rightarrow X_7$ transition in an experiment only corresponds to small values of $(k-k_{XO})$, then E_6 and E_7 as a function of $(k-k_{XO})$ can be approximated by paraboloids, and then

$$E_7-E_6=\Delta_{7-6}+[\hbar^2(k-k_{X0})^2]/(2m_r) \tag{6.3.6}$$

where Δ_{7-6} is the energy gap between the X_7 and X_6 bands at their minima, and m_r is defined by

$$m_r=m_6m_7/(m_6-m_7) \tag{6.3.7}$$

in which m_6 and m_7 are the effective masses for electrons in the X_6 and X_7 bands, respectively. With the above approximation, m_6 and m_7 are proportional to the density of states effective mass of the X_6 and X_7 bands, respectively, and the constant of proportionality is $(1/3)^{2/3}$ (3 is the degeneracy of the X_6 and X_7 bands). Substituting the expression for E_7-E_6 into equation (6.3.5), and considering the properties of the δ-function, equation (6.3.5) can be integrated to give:

$$N_{6\rightarrow 7}=\frac{V}{\pi}|H|^2\frac{(2m_r)^{3/2}}{\hbar^4}\frac{(\hbar\omega-\Delta_{7-6})^{1/2}}{\exp[\frac{m_r}{m_6}(\hbar\omega-\Delta_{7-6})-(E_F)_6]/k_BT+1}, \tag{6.3.8}$$

According to the definition of the absorption coefficient, the $X_6 \rightarrow X_7$ absorption coefficient $\alpha_{6\rightarrow 7}(\omega)$ can be expressed by: [20]

$$\alpha_{6\to 7}(\omega) = \frac{|H|^2}{N_0 \pi \hbar^4} \frac{(\hbar\omega - \Delta_{7-6})^{1/2}(2m_r)^{3/2}}{\exp[\frac{m_r}{m_6}(\hbar\omega - \Delta_{7-6}) - (E_F)_6]/k_B T + 1}, \qquad (6.3.9)$$

where N_0 is the total number of incident probe photons per second in a crystal of effective volume V.

According to the relationship of $OD = \alpha l/2.3$ (l is the effective thickness), the change of the optical density for the transition from the X_6 to the X_7 bands is given by:

$$(\Delta OD)_{X_6 \to X_7} = C \frac{(\hbar\omega - \Delta_{7-6})^{1/2}(2m_r)^{3/2}}{\exp[\frac{m_r}{m_6}(\hbar\omega - \Delta_{7-6}) - (E_F)_6]/k_B T + 1}, \qquad (6.3.10)$$

where m_r was defined by (6.3.7); $(E_F)_6$ is the Fermi-energy for the X_6 electrons; $\Delta_{7\to 6}$ is the energy gap between the X_6 and X_7 bands at their minima; $C = l|H|^2/(2.3 N_0 \pi \hbar^4)$ is a constant (N_0 is the total number of incident probe photons per second in a crystal of effective volume V, and $|H|^2$ is the square of the perturbation matrix element).

To fit our experimental data, we substituted into Equation (6.3.10) our measured value of the energy gap $\Delta_{7\to 6} = 0.345 eV$, the density of states effective mass of $0.85 m_0$ for the X_6 band[5], T= 293 K, and the calculated value of $(E_F)_6$=-0.064 eV obtained from evaluating the Fermi-Dirac integrals for our experimental conditions. The density of states effective mass for the X_7 band was treated as a variable parameter to fit the

calculated changes of the optical density to the experimental data. The three curves for the calculated $(\Delta OD)_{X_6 \to X_7}$ for the three values of the variable parameter: $0.44m_0$, $0.48m_0$, and $0.54m_0$, are displayed in Fig.6.2.3 to show the fit of the profiles to the data. The best fit gives the value of 0.48 m_0 for the density of states effective mass in the X_7 band. A comparison of the experimental error bars with the curves in Fig.6.2.3 gives an uncertainty of $\pm 0.06m_0$ in this determined parameter.

Our results provided two parameters, Δ_{7-6} and the density of states effective mass for the X_7 band, which are important both in semiconductor physics and in studying the high speed electronic devices because these two parameters can be used together with the corresponding large deformation potential $D_{\Gamma_6 \to X_7}$ [24] for determining the intervalley scattering rate from Γ_6 to X_7 for electrons with sufficient energy (greater than 0.825 eV) to make this transition. Our experiment also demonstrates the potential of the pump-IR-probe technique to investigate semiconductors with high energy satellite valley conduction bands separated by an energy difference in the IR. Materials with appropriate X valley structures are: GaP, InP, InSb and their alloys.

REFERENCES

[1] E. M. Conwell, in " High Field Transport in Semiconductors ", Academic Press, New York, (1967), Ch.5.

[2] P. C. Becker, H. L. Fragnito, C. H. Brito Cruz, J. Shah, R. L. Fork, J. E. Cunningham, J. E. Henry, and C. V. Shank, Appl. Phys. Lett., 53 , 2089 (1988).

[3] K. Berthold, A. F. J. Levi, J. Walker, and R. J. Malik, Appl. Phys. Lett, 54 , 813 (1989).

[4] W. B. Wang, N. Ockman, M. Yan, and R. R. Alfano, Solid State Electron., 32 , 1337 (1989).

[5] J. S. Blakemore, J. Appl. Phys., 53 , R123 (1982).

[6] G. D. Pitt and J. Lees, Phys. Rev. B2 , 4144 (1970).

[7] K. H. Nichols, C. M. L. Yee, and C. M. Wolfe, Solid State Electron, 23 , 109 (1980).

[8] D. E. Aspnes, Phys. Rev, B14 , 5331 (1976).

[9] D. L. Greenaway, Phys. Rev. Lett. 9 , 97 (1962).

[10] A. G. Thompson, M. Cardona, K. L. Shaklee, and J. C. Woolley, Phys. Rev. 146 , 601 (1966).

[11] L. W. James, R. C. Eden, J. L. Moll, and W. E. Spicer, Phys. Rev. 174 , 909 (1968).

[12] D. E. Aspnes and A. A. Studna, Phys. Rev. B7 , 4605 (1973).

[13] W. B. Wang, N. Ockman, M. A. Cavicchia, and R. R. Alfano, Appl. Phys. Lett., 57 , 395(1990).

[14] N. Ockman, R. Dorsinville, W. B. Wang, and R. R. Alfano, IEEE J, Quantum Electron, QE-23 , 2008 (1987).

[15] S. K. Gayen, W. B. Wang, V. Petricevic, K. M. Yoo, and R. R. Alfano, Appl. Phys. Lett. 50 ,1494 (1987).

[16] W. B. Wang, N. Ockman, M. A. Cavicchia, M. Yan, and R. R. Alfano, SPIE, 1282 , 86 (1990).

[17] H. Ehrenreich, H. R. Philipp, and J. C. Philips, Phys. Rev. Letts, 8 , 59 (1962).

[18] W. Paul, J. Appl. Phys, 32 , 2082 (1961).

[19] R. Braunstein, and L. Magid, Phys. Rev., 111 , 480 (1958).

[20] A. Yariv, in "Quantum Electronics" John Wiley * Sons Inc., New York, (1975), Ch.10.

[21] E. M. Conwell, and M. O. Vassell, IEEE Trans. Electron. Devices, ED-13 , 22 91966).

[22] J. C. Tsang, and J. A. Kash, Phys. Rev., B34 , 6003 (1986).

[23] D. Brust, Phys. Rev., 134 , A1337 (1964).

[24] S. Zollner, S. Gopalan, and M. Cardona, Appl. Phys. Lett., 54 , 614 (1989).

Chapter 7

TEMPERATURE DEPENDENCE OF THE INTRA-AND-INTERVALLEY ELECTRON-PHONON INTERACTION IN GaAs

7.1. Introduction

The hot carrier relaxation via carrier-phonon interaction in GaAs has been intensively studied because of its importance in the development of high speed electronic and optoelectronic devices [1]. Several theoretical groups [2-5] have modeled the mechanism of scattering and calculated hot electron relaxation in GaAs as a function of deformation potentials, crystal temperatures, carrier energy, carrier densities, and effective mass. A number of picosecond and femtosecond measurements [6-14] have been performed to investigate the inter-and-intravalley scattering processes in GaAs at their fixed experimental temperatures. However, there have been no previous measurements to systematically investigate the temperature dependence of hot carrier relaxation and the carrier-phonon interaction [15].

I have systematically measured the temperature (T) dependence of hot electron relaxation in GaAs. The temporal profiles of the near-band-gap photoluminescence (PL) for GaAs over the temperature range of 4 K to 300 K were measured by time-resolved photoluminescence spectroscopy. The risetime of the PL at low temperatures were found to be much longer than that at room temperature. This results from the reduction of the number of phonons participating in the electron-phonon interaction and the

decrease of the intra-and-intervalley scattering rates, in particular, the $L \rightarrow \Gamma$ back scattering rate [16].

From the measured $t_{L\Gamma}(D,T) \sim$ T curve, the $L-\Gamma$ deformation potential was determined to be $D_{L\Gamma}=4.4\times10^8$ eV/cm. This result determined from our data over a large range of temperature from 4 K to 300 K is more accurate than that of 6.5×10^8 eV/cm determined from the measurement performed at a particular temperature of 300 K, [6] and 3.2×10^8 eV/cm obtained from the measurement performed at another particular temperature of 4 K. [17]

7.2. Time-Resolved Photoluminescence

The experimental set up used for this measurement is schematically shown in Fig.4.3.1. The output pulses of 532 nm, 82 MHz, ~ 4 ps, ~ 800 mW from a frequency-doubled, pulse-compressed mode-locked Nd:YAG laser were focused onto a sample for photoexcitation. The photoluminescence (PL) from the sample is collected and sent to a SPEX 1681B spectrograph which incorporates a 600 grooves/mm reflection grating and then directed onto the input slit of an S-20 photocathode in a Hamamatsu C1587 synchroscan streak camera. The time-resolved fluorescence image picked up by a silicon intensified target (SIT) vidicon camera was stored in an image memory and analyzed by a temporal analyzer (TA, an image processing computer) to exact temporal and spectral information on the luminescence. The spectral and temporal resolution of this laser-streak-

camera system were measured to be about 1 nm and 10 ps, respectively. The sample was placed inside an Optical Cryogenic system so that its temperature (T) can be easily changed and controlled.

The temporal profiles of the near-band-gap PL at temperatures varying from 4 K to 300 K were measured. As examples, the time-resolved photoluminescence intensity at 4 K, 140 K, and 274 K are displayed in Fig.7.2.1. In order to clearly compare the time-evolution of hot carrier relaxation at those three temperatures, the maximum value of each curve has been normalized to unity, and the rise portions of the three curves have been expanded on the time scale and are shown in Fig.7.2.2. The salient feature of the curves is that the rise time at 4 K is much longer than that at 274 K, and the decays of all three curves are slow which corresponds to a long recombination time of hot electrons and holes [10,13,14]. At many other temperatures, the decay profiles of the PL were observed to be as slow as that of the three curves shown in Fig.7.2.1, but their rise-times increase from 15 ps to 26 ps with decreasing temperature. The rise-time (time for the intensity of PL to increase from 10% to 90% of its peak) of PL for each temperature was measured and displayed in Fig.7.2.3, which shows that the change of the rise time is very small in the temperature range of 4 K to 50 K, and is much greater for T > 50 K.

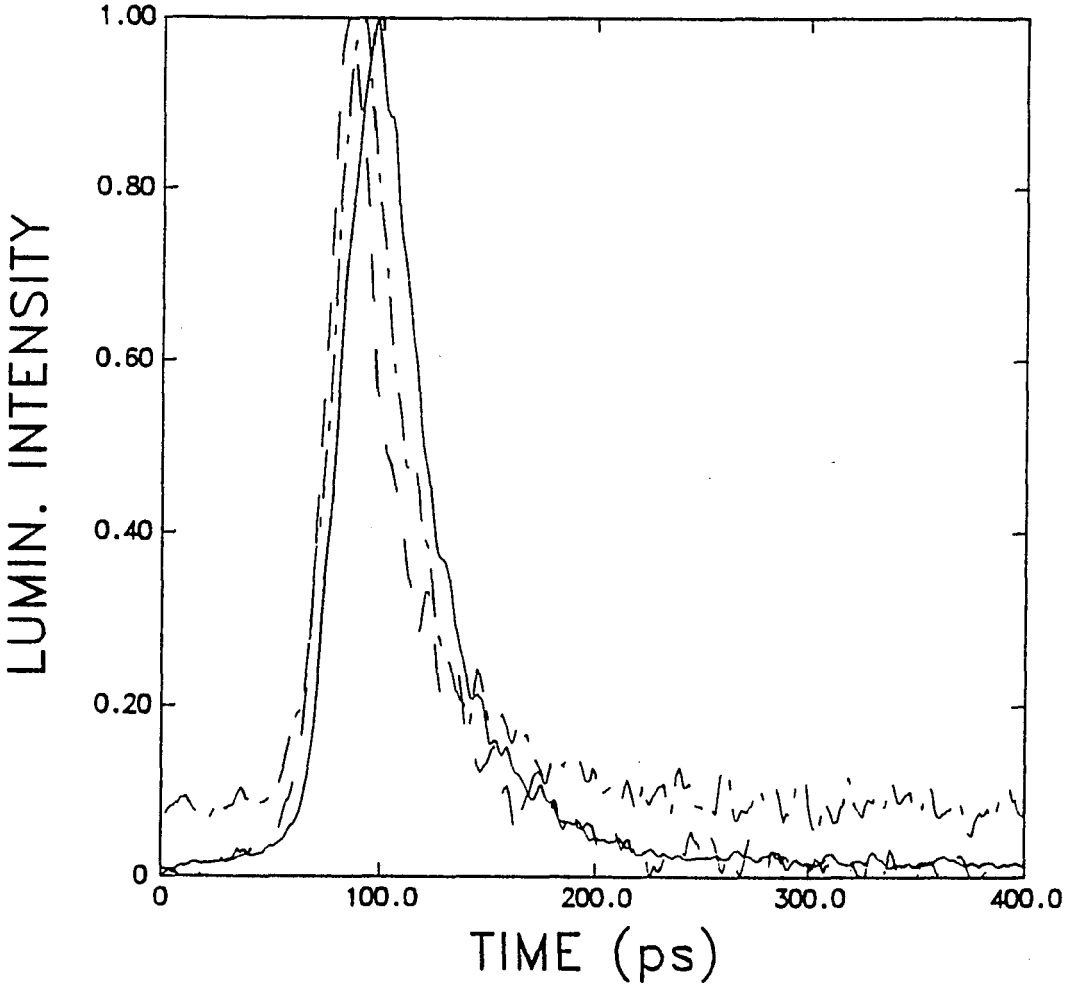

Fig.7.2.1. The measured change in photoluminescence intensity as a function of delay time and crystal temperature. The dash, dot-dash, and solid lines correspond to T=274 K, 140 K, and 4 K, respectively. [16]

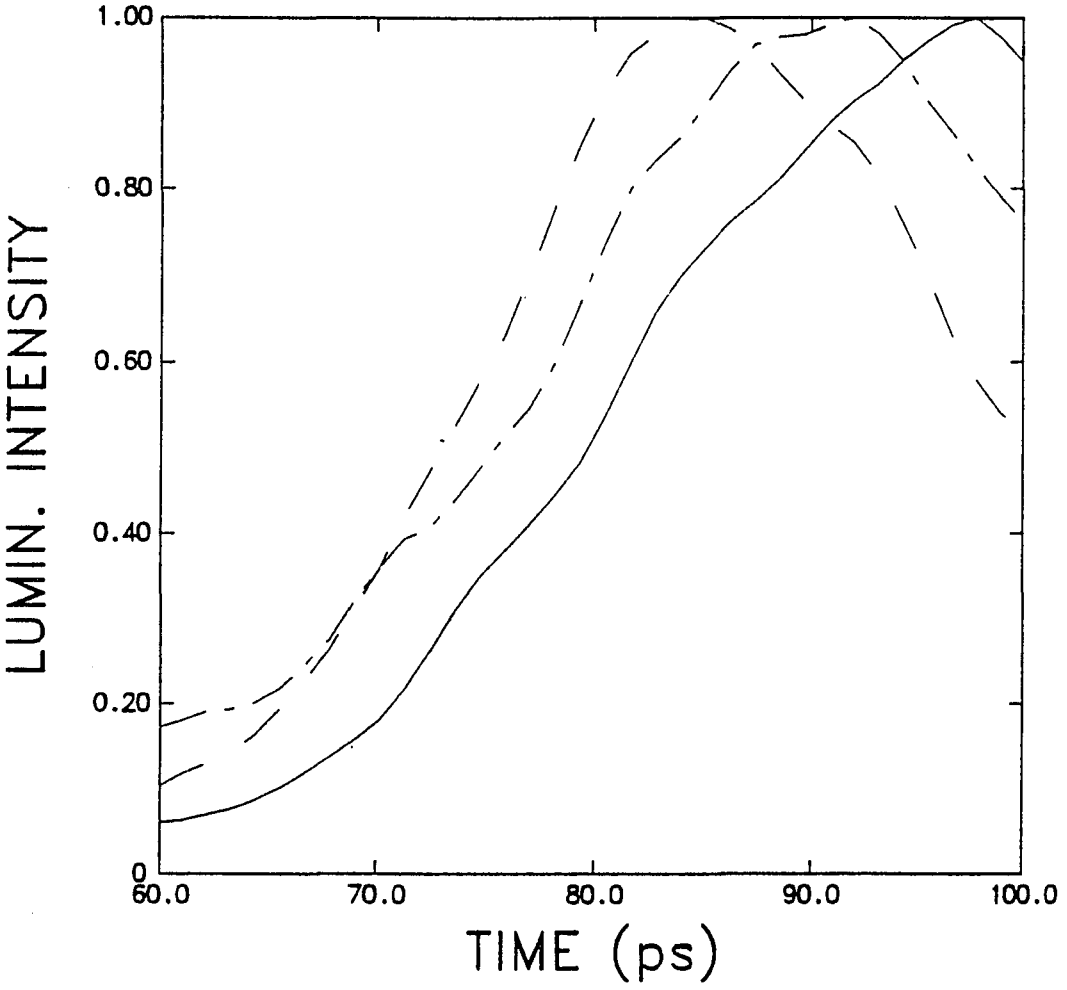

Fig.7.2.2. The rise portions of the three curves in Fig.7.2.1. [16]

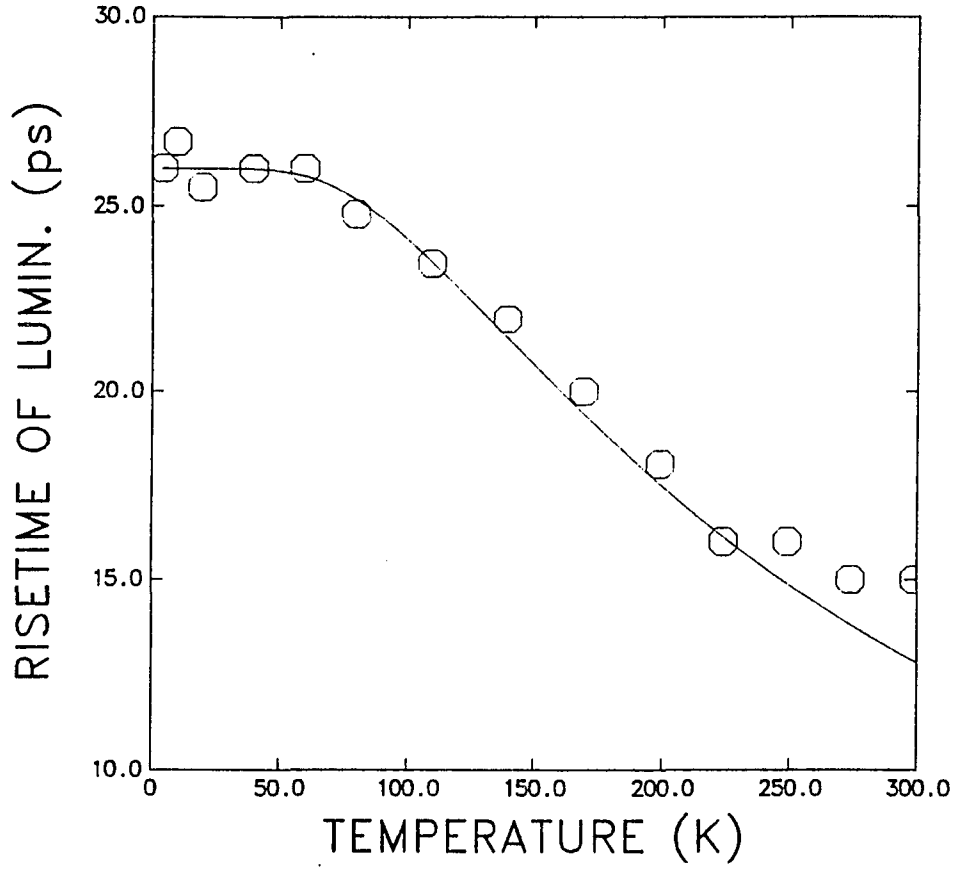

Fig.7.2.3. The temperature dependence of the risetime of photo-luminescence and the $L \rightarrow \Gamma$ intervalley scattering time. The circles represent the measured rise time of the PL as a function of T. The solid curve indicates the best fit of the calculated values of $t_{L\Gamma}$ with a value of $D_{L\Gamma}=4.4\times10^{8} eV/cm$. [16] The values of $t_{L\Gamma}$ at each T has been multiplied by a factor of 3 because electrons make about three trips in scattering between the L and Γ valleys.

7.3. Hot Electron Relaxation Subsequent to the Pump

With a 532 nm pump, electrons were excited from all of the valence bands at the Γ point to the conduction band attaining an energy of about 0.83 eV (at room temperature) above the minimum energy of the Γ conduction valley, E_Γ, for electrons from the heavy-hole and light-hole bands, and about 0.41 eV energy above E_Γ for those from the split-off band [18]. The energy of 0.83 eV is sufficient for electrons to scatter from the Γ valley to the L and X valleys. Therefore, those electrons will undergo intervalley scattering among the Γ, L and X valleys and intravalley scattering inside each of the valleys. Since the minimum of the Γ valley is lower than that of the L and X valleys, all of electrons will finally scatter back to the Γ valley and decay to its bottom. Similar relaxation processes occur for hot electrons of 0.4 eV excited from the split-off band but only involve the L and Γ valleys. Electrons relaxed to the bottom of the Γ valley will stay there until they recombine with holes emitting radiation. Therefore, the risetime of the near-band-gap PL reflects the relaxation time of electrons from their initial kinetic energy, ε_{ini}, obtained from the pump photon, to the bottom of the Γ valley.

The relaxation of hot electrons from ε_{ini} to the bottom of the Γ valley, schematically shown in Fig.7.3.1, can be considered to have the following steps corresponding to six energy ranges of the hot electrons: (1) at ε near ε_{ini}, where ε is the average kinetic energy of hot electrons --- since the previously measured values of $t_{\Gamma L}$=100±20 fs [6], $t_{\Gamma X}$=55±11 fs [8], and

$t_{\Gamma\Gamma}$=165±20 fs [11] show that $t_{\Gamma X} < t_{\Gamma L} < t_{\Gamma\Gamma}$, almost all of the excited electrons will scatter into the X and L valleys after several $\Gamma \rightarrow X$, $\Gamma \rightarrow L$ and $\Gamma \rightarrow \Gamma$ scatterings; (2) in the range of $\varepsilon_{ini} > \varepsilon > \varepsilon_{0X}$, where ε_{0X} is the bottom energy of the X valley measured from E_Γ --- since the previously measured results of $t_{X\Gamma}$=0.50±0.35 ps [9], $t_{L\Gamma}$=2.5±0.5 ps [6], t_{LX}=200±100 fs [12], $t_{\Gamma\Gamma}$=165±20 fs [11] and Conwell's theory [2] giving $t_{ii} \propto 1/m_{ii}^{1/2}$ (t_{ii} and m_{ii} are intravalley scattering time and effective mass in the ith valley, respectively, for i=Γ, L, and X) show that $t_{LL} << t_{L\Gamma}$, $t_{XX} << t_{X\Gamma}$, most of the hot electrons in the X and L valleys will undergo the X→X and L→L intravalley scatterings and the L←→X intervalley scattering rather than the X→Γ and L→Γ back scattering; (3) near ε_{0X} --- since the previous measurements [1,9,12] show that $t_{XL} < t_{X\Gamma}$, about 80% of the electrons near the bottom of the X valley will scatter into the L valley [19]. Only 20% of the X valley electrons scatter into the Γ valley from which they will also scatter into the L valley via the $\Gamma \rightarrow L$ or the $\Gamma \rightarrow X \rightarrow L$ scattering. As a result, almost all of the hot electrons will scatter into the L valley after several times of back-and-forward scattering among these three valleys; (4) in the range of $\varepsilon_{0X} > \varepsilon > \varepsilon_{0L}$, where ε_{0L} is the energy of electrons at the bottom of the L valley as measured from E_Γ --- since $t_{LL} << t_{L\Gamma}$, electrons will undergo the intravalley scattering inside the L valley rather than the $L \rightarrow \Gamma$ intervalley scattering and will decay to the bottom of the L valley; (5) near ε_{0L} --- electrons will scatter into the Γ valley after several transits of L←→Γ scatterings; and (6) in the range of $\varepsilon_{0L} > \varepsilon > 0$ --- electrons will relax

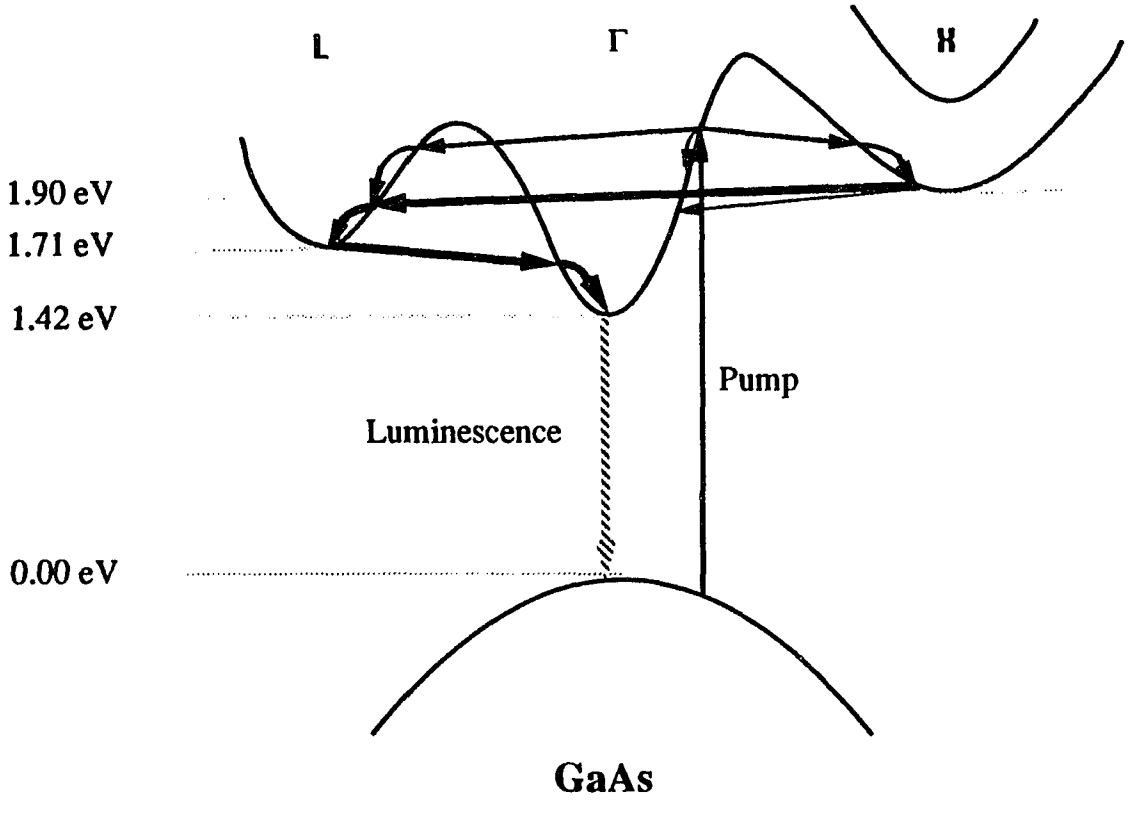

Fig.7.3.1. Schematic diagram of the relaxation processes of hot electrons of ε=0.83 eV to the bottom of the Γ valley in GaAs. [16]

to the bottom of the Γ valley via intravalley scattering.

When the crystal temperature goes down, the number of phonons participating in the electron-phonon scattering will decrease. Therefore, each of the intra-and-intervalley scattering processes mentioned above will become longer, and the total relaxation time from ε_{ini} to E_Γ will increase.

7.4. Intra-and-Intervalley Scattering Rate as a Function of T

As mentioned in Chapter 2, the dominant intravalley scattering mechanism for GaAs is the polar optical one, whereas the dominant intervalley scattering mechanism for GaAs is the deformation potential one [2,20]. The intravalley scattering time t_{ii} at which an electron of energy ε ($\varepsilon > \hbar\omega_{ii}$) is scattered into the same valley by a polar optical interaction is given by [2]

$$\frac{1}{t_{ii}} = \frac{2eE_0}{(2m\varepsilon)^{1/2}} [N_{ii} \sinh^{-1}(\frac{\varepsilon}{\hbar\omega_{ii}})^{1/2} + (N_{ii}+1)\sinh^{-1}(\frac{\varepsilon-\hbar\omega_{ii}}{\hbar\omega_{ii}})^{1/2}] \quad (7.4.1)$$

where e is the electron charge, m the effective mass of the electrons, $\hbar\omega_{ii}$ is the energy of an optical phonon, N_{ii} is the average number of optical phonons in thermal equilibrium and is given by the Planck distribution function

$$N_{ii} = 1/[e^{\hbar\omega_{ii}/KT} - 1], \quad (7.4.2)$$

and E_0 is an effective field defined [2] by $eE_0 = (me^2\hbar\omega_{ii}/\hbar^2)(1/k_\infty - 1/k_0)$, where k_0, k_∞ are the dielectric constants for zero and infinite frequency,

respectively. The first and second terms in the angular bracket represent scatterings involving absorption and emission of a phonon, respectively.

The intervalley scattering time t_{ij} (i, j=Γ, L, and X, but i≠j) for an electron from the initial ith valley with energy ε to the final jth valley is given by [2,3]

$$\frac{1}{t_{ij}}=\frac{D_{ij}^{2}N_j m_j^{3/2}}{2^{1/2}\pi\hbar^{3}\rho\omega_{ij}}[(N_{ij}+1)(\varepsilon-\hbar\omega_{ij}-\varepsilon_{oj})^{1/2}+N_{ij}(\varepsilon+\hbar\omega_{ij}-\varepsilon_{oj})^{1/2}] \quad (7.4.3)$$

where N_j is the number of equivalent valleys (1 for Γ, 3 for X, and 4 for L), m_j is the effective mass of electrons in the jth valley, ρ is the density of the crystal, $\hbar\omega_{ij}$ is the energy of a phonon for the i→j intervalley transition, N_{ij} is the number of intervalley scattering phonons which is given by a similar formula as equation (7.4.2), ε_{oj} is the energy at the bottom of the jth valley measured from E_Γ, and D_{ij} is the deformation potential between the ith and jth valleys. The first and the second terms in the angular bracket in equation (7.4.3) represent intervalley transitions involving emission and absorption of a phonon, respectively.

The average number of phonons N_{ii} or N_{ij} varies with temperature as shown in equation (7.4.2). As examples, the calculated values of $N_{\Gamma\Gamma}$ and $N_{\Gamma X}$ at different temperatures are shown in Fig.7.4.1. In the range of low temperatures, T < 50 K, the values of N_{ii} and N_{ij} are almost zero and unchanged with T. In this limit, scattering of electrons by absorption of a phonon becomes almost impossible, and the scattering rate by emission of

a phonon reaches its minimum. Therefore, the intra-and-intervalley scattering rates should reach their smallest values. When T > 50 K, N_{ii} and N_{ij} increase with temperature.

The minimum energy for the Γ, L and X conduction valleys in GaAs as functions of temperature have been previously determined [21]. Therefore, the energy terms in the equations (7.4.1) and (7.4.3) can be written as $\varepsilon_{0\Gamma}=0$, $\varepsilon_{0L}=0.296-6.45\times10^{-5}T^2/(T+204)$, $\varepsilon_{0X}=0.462-8.05\times10^{-5}T^2/(T+204)$, and $\varepsilon_{ini}=[\hbar\omega_{pump}-E_\Gamma]\times m_h/(m_\Gamma+m_h)$ where $E_\Gamma=1.519-5.405\times10^{-4}T^2/(T+204)$, and m_Γ and m_h are the effective masses of Γ valley electrons and holes participating in the recombination, respectively. Since the values of ε_{ini} and ε_{0j} (j=Γ, L and X) change slightly with temperature, their effect on the change of the intra-and-intervalley scattering times, t_{ii} and t_{ij}, is small. Therefore, the temperature dependence of t_{ii} and t_{ij} mainly arises from the temperature dependence of the number of phonons.

The values of t_{ii} and t_{ij} as functions of temperature can be calculated using expressions of $N_{ii}(T)$, $N_{ij}(T)$, $\varepsilon_{ini}(T)$, $\varepsilon_{0j}(T)$, and the previously determined values of the parameters [3,21,22] D_{ij}, ρ, m_j, and $\hbar\omega_{ij}$ in equations (7.4.1) and (7.4.3). The calculated results show that although all of the inter-and-intravalley scattering times in GaAs increase with decreasing crystal temperature, the absolute values of the changes of $t_{L\Gamma}$ and $t_{X\Gamma}$ are

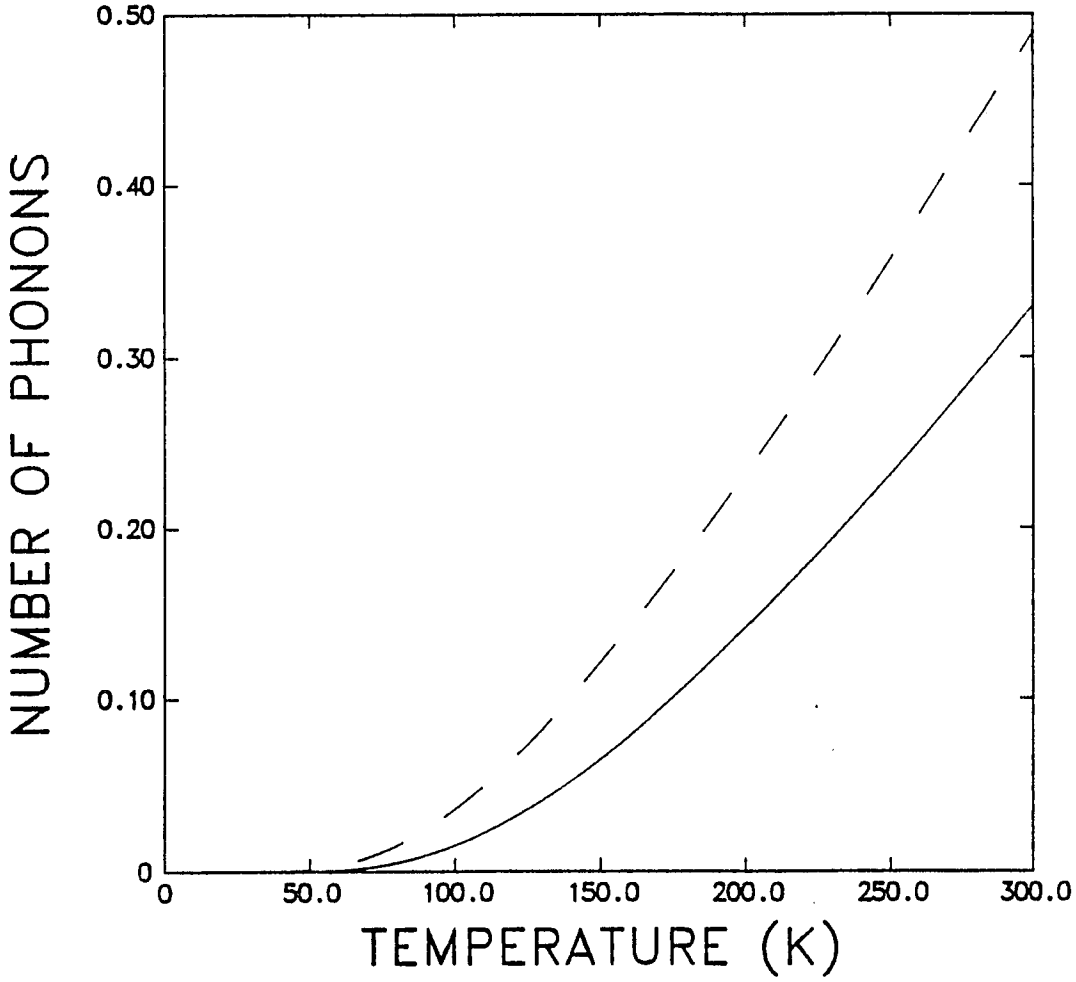

Fig.7.4.1. The calculated average number of phonons of N_{rr} (dash line) and N_{rx} (dot-dash line) as a function of T. [16]

much larger than that of $t_{\Gamma\Gamma}$, $t_{\Gamma L}$, $t_{\Gamma X}$, t_{LX}, and t_{XL} at each temperature. This agrees with the previous measurements.[6-9,11,12] Therefore, the contribution of $t_{\Gamma\Gamma}$, $t_{\Gamma L}$, $t_{\Gamma X}$, t_{LX}, and t_{XL} to the risetime of the PL can be neglected. Only the contribution of $t_{L\Gamma}$ and $t_{X\Gamma}$ should be considered.

The previous measurements[1,9,12] and the calculation[19] show that $t_{XL} < t_{X\Gamma}$, and about 80% of electrons in the X valley scatter into the L valley, whereas only 20% of them scatter into the Γ valley from which they will also scatter into the L valley via the $\Gamma \rightarrow L$ and $\Gamma \rightarrow X \rightarrow L$ scattering. Therefore, most of the hot electrons relax to the Γ valley via the the $L \rightarrow \Gamma$ channel rather than the $X \rightarrow \Gamma$ channel, and the function $t_{L\Gamma}(T)$ dominates the change of the risetime of the PL with T.

The calculated values of $t_{L\Gamma}(T)$ using equation (7.4.3) are shown in Fig.7.2.3, which shows that (1) in the low temperature range, the values of $t_{L\Gamma}$ reach their maximum and remain unchanged; and (2) as temperature goes up, the values of $t_{L\Gamma}$ decrease. In order to compare the calculated values of $t_{L\Gamma}$ with the experimental data, the maximum value of the calculated $t_{L\Gamma}$ has been normalized to the measured maximum value with normalization factor[7] of 3. The best fit of the calculated values of $t_{L\Gamma}$ to the experimental data shown in Fig. 7.2.3 gives the value of $D_{L\Gamma}=4.4\times10^{8} ev/cm$, which is in good agreement with the theoretical value[3] of $D_{L\Gamma}=4.1\times10^{8} ev/cm$. The values of $D_{L\Gamma}$ determined from the previous single-temperature measurements[6,17] span a large range from

$D_{L\Gamma}$=3.2×10^8*ev/cm* to $D_{L\Gamma}$=6.5×10^8*ev/cm*. Our determination clarifies these discrepancies.

The good agreement of the calculated values of $t_{L\Gamma}$ with the experiment data indicates that the slowing of hot electron relaxation by hot-phonon effects and the reduction of electron-phonon interaction rates by screening can be neglected in our experimental conditions. In fact, since hot electrons excited by 532 nm photons undergo intervalley scattering with emission or absorption of a zone-boundary or near zone-boundary LO phonon, the volume in k space in which the phonons are created is very large. Therefore, no appreciable nonthermal phonon population density can be generated by such a process, and the hot-phonon effect on slowing the hot electron relaxation should be very small [23]. Because the critical carrier density for the onset of screening for phonon-assisted intervalley transitions in GaAs [24] is on the order of 10^{21} cm^{-3}, which is much larger than our carrier density, the effect of screening on reducing the electron-phonon interaction rates should also be small.

In conclusion, the temperature dependence of hot electron relaxation in GaAs has been observed from the time-resolved photoluminescence spectroscopy. The much longer relaxation time of electrons at low temperatures comparing with that at room temperature is mainly attributed to the increase of the $L \rightarrow \Gamma$ back scattering time. The deformation potential of $D_{L\Gamma}$ was determined to be 4.4×10^8*eV/cm* from the measured T-dependence of $t_{L\Gamma}$.

REFERENCES

[1] R. W. Schoenlein, W. Z. Lin, E. P. Ippen, and J. G. Fujimoto, Appl. Phys. Lett., 51 , 1442 (1987).

[2] E. M. Conwell and M. O. Vassell, IEEE Trans. Electron. Devices, ED-13 , 22 (1966).

[3] S. Zollner, S. Gopalan, and M. Cardona, Appl. Phys. Lett., 54 , 614 (1989).

[4] M. A. Osman and D. K. Ferry, Phys. Rev. B36 , 6018 (1987).

[5] M. J. Kann, A. M. Kriman, and D. K. Ferry, Phys. Rev., B41 , 12659 (1990).

[6] J. Shah, B. Deveaud, T. C. Damen, and W. T. Tsang, A. C. Gossard, and P. Lugli, Phys. Rev. Lett., 59 , 2222 (1987).

[7] A. Katz, and R. R. Alfano, Appl. Phys. Lett., 53 , 1065 (1988).

[8] P. C. Becker, H. L. Fragnito, C. H. Brito Cruz, J. Shah, R. L. Fork, J. E. Cunningham, J. E. Henry, and C. V. Shank, Appl. Phys. Lett., 53 , 2089 (1988).

[9] W. B. Wang, N. Ockman, M. Yan, and R. R. Alfano, J. of Lumin., 50 , 347 (1992).

[10] R. J. Seymour, M. R. Junnarkar, and R. R. Alfano, Solid State Commun, 41 , 657 (1982).

[11] J. A. Kash, J. C. Tsang, and J. M. Hvam, Phys. Rev. Lett., 54 , 2151 (1985).

[12] W. B. Wang, Kai Shum, R. R. Alfano, D. Szmyd, and A. J. Nozik, Phys. Rev. Lett., 68 , 662 (1992).

[13] R. F. Leheny, J. Shah, R. L. Fork, C. V. Shank, and A. Migus, Solid State Commun., 31 , 809 (1979).

[14] S. Tanaka, H. Kobayashi, H. Saito, and S. Shionoya, Solid State Commun., 33 , 167 (1980).

[15] N. Ockman, W. B. Wang, and R. R. Alfano, Internat. J. Modern Physics, B5 , 3165 (1992).

[16] W. B. Wang, K. Tokiguchi, and R. R. Alfano, to be submitted for publication.

[17] R. G. Ulbrich, J. A. Kash, and J. C. Tsang, Phys. Rev. Lett., 62 , 949 (1989).

[18] W. B. Wang, N. Ockman, M. A. Cavicchia, and R. R. Alfano, Appl. Phys. Lett., 57 , 395(1990).

[19] S. Zollner, S. Gopalan, and M. Cardona, SPIE, 1677 , 614 (1990).

[20] L. Reggiani, in "Hot-Electron Transport in Semiconductors", edited by L. Reggiani, Springer-Verlag, New York, (1984), ch.2.

[21] J. S. Blakemore, J. Appl. Phys., 53 , R123 (1982).

[22] S. Adachi, J. Appl. Phys., 58 , R1 (1985).

[23] W. W. Ruhle, K. Leo, and E. Bauser, Phys. Rev., B40 , 1756 (1989).

[24] E. J. Yoffa, Phys. Rev., B23 , 1909 (1981).

Chapter 8

THE $L_6 \rightarrow X_6$ INTERVALLEY SCATTERING TIME IN $Al_{0.6}Ga_{0.4}As$

8.1. Introduction

A large number of experiments have been performed to determine intervalley scattering times such as $t_{\Gamma\rightarrow L}$, $t_{\Gamma\rightarrow X}$, $t_{L\rightarrow\Gamma}$, and $t_{X\rightarrow\Gamma}$ in GaAs [1-4]. Due to the direct gap nature and the initial excitation of the Γ valley electrons rather than the satellite valley electrons, the L_6–X_6 intervalley scattering in GaAs can not be directly monitored. [5,6] However, it can be estimated from the L-X intervalley scattering measurement for GaAs alloys such as AlGaAs. To our best knowledge, no such measurements have been performed before this thesis work. Therefore, the importance of L-X intervalley scattering for the hot electron relaxation in GaAs has not yet been experimentally revealed.

I have measured the time evolution of electrons in the X_6 valley in $Al_{0.6}Ga_{0.4}As$ using a femtosecond visible-pump and infrared(IR)-probe absorption spectroscopy described in Section 4.2. The indirect band gap structure of $Al_{0.6}Ga_{0.4}As$ enables us to eliminate the Γ valley-involved intervalley scattering and to directly investigate the L_6–X_6 intervalley scattering process as shown in Fig.8.1.1. The experimental results yield the first determination of the $L\rightarrow X$ intervalley scattering time and the deformation potential between the L and X valleys for $Al_{0.6}Ga_{0.4}As$, and give the upper limit of the L-X intervalley scattering time for GaAs. [6]

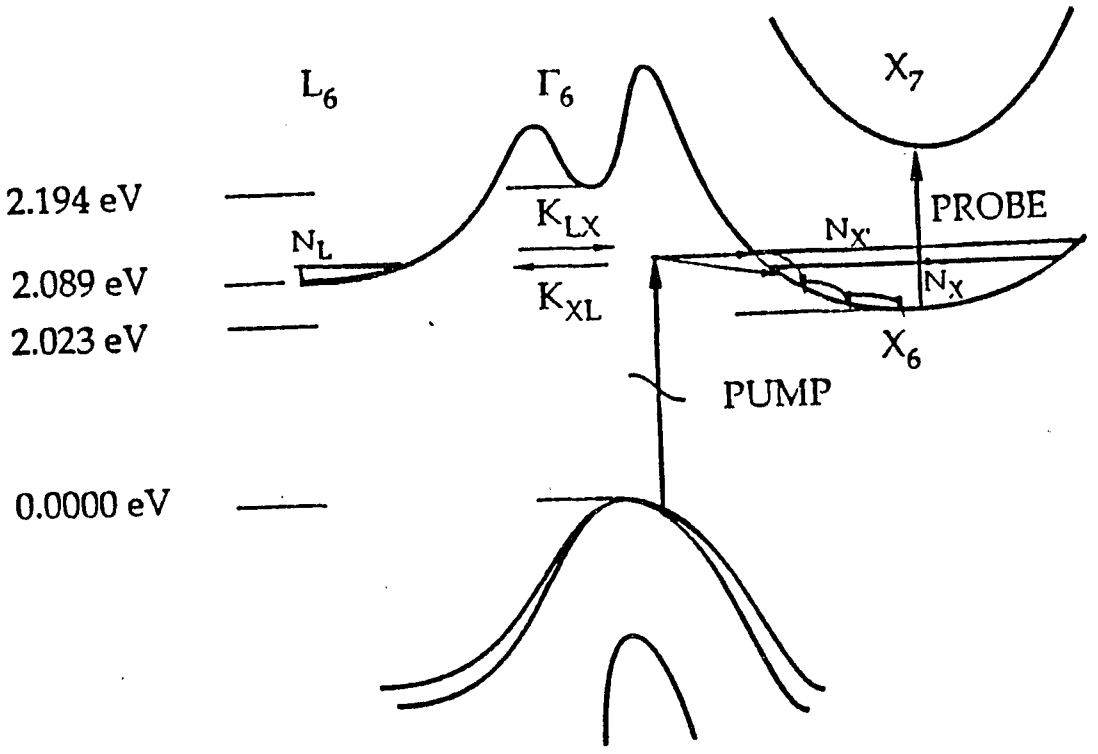

Fig.8.1.1. Band structure of $Al_{0.6}Ga_{0.4}As$ showing visible-excitation and the $X_6 \rightarrow X_7$ IR absorption. [6]

8.2. Sample and Experimental Arrangement

An undoped 2 μm-thick $Al_{0.6}Ga_{0.4}As$ epilayer sample was grown by the MOCVD process in a vertical reactor at a temperature of 725 ^{0}C with a growth rate of 12-14 A/sec. The Al content of the sample was determined via electron microprobe analysis and the gas phase composition measurement with an uncertainty of $\pm$0.005. The GaAs substrate was completely removed to eliminate the excitation and absorption from the substrate. The steady-state IR transmission spectra of the samples were measured and found to have no appreciable absorption at the probe wavelengths.

A femtosecond visible-pump and IR-probe setup [6-8] shown in Fig.4.2.9 was used in this experiment. A 585 nm, ~ 500 fs pulse obtained from a synchronously pumped dye laser and its amplifier was used as a pump to produce hot carriers with a carrier density of 2.8×10^{18} cm^{-3} through a photoexcited indirect transition. The IR pulses tuned from 2.5 μm to 5.5 μm generated from a $LiIO_3$ crystal by a difference frequency method were used as a probe to monitor the induced IR absorption.

8.3. Measured IR Absorption and Time Evolution of the Electron Population in the X_6 Valley

The measured time-resolved IR absorption at λ_{PROBE}=3.3μm and 4.0μm for $Al_{0.6}Ga_{0.4}As$ are displayed in Fig.8.3.1. The rise parts of these two curves were normalized for their maximum values, and shown in Fig.8.3.2. Although the decay of the both curves are flat, the risetime of

the 3.3 μm curve is longer than that of the 4.0 μm and has two components. To understand the physics behind the differences between the risetimes of the two curves in Fig.8.3.2, the measurements were extended to other wavelengths between 2.5 μm and 4.7 μm to obtain the probe-wavelength dependence of the induced IR absorption at a fixed delay time of t_d=20 ps. The measured results are shown in Fig.8.3.3 which indicates an interband transition in the IR.

The induced total IR absorption is attributed to the following three absorption processes: [6,9] (1) interconduction band absorption (ICA) by electrons from the X_6 to the X_7 valleys (see Fig.8.1.1.); (2) intervalence band absorption (IVA) by electrons from the split-off to the heavy-hole and light-hole bands and by electrons from the light-hole to the heavy-hole bands; and (3) free carrier absorption (FCA) by hot electrons in the L and X valleys and by hot holes in the three valence bands.

The calculated optical densities of IVA for $\lambda \geq 3.1\mu m$, obtained by using the cross sections for IVA given by Braunstein [10] and our electron densities in the split-off and the light-hole bands, are less than 0.004 which are much smaller than the observed values shown in Fig.8.3.3. Therefore, IVA can be neglected for $\lambda_{probe} \geq 3.1\mu m$.

The characteristics of FCA can be obtained from Figs.8.3.1. to 8.3.3. The absorption for $\lambda_{probe} \geq$ 4.0 μm in Fig.8.3.3 simply increases with probe wavelengths and does not show any interband transition structure. This indicates that the energy of probe photons for $\lambda_{probe} \geq$ 4.0 μm are

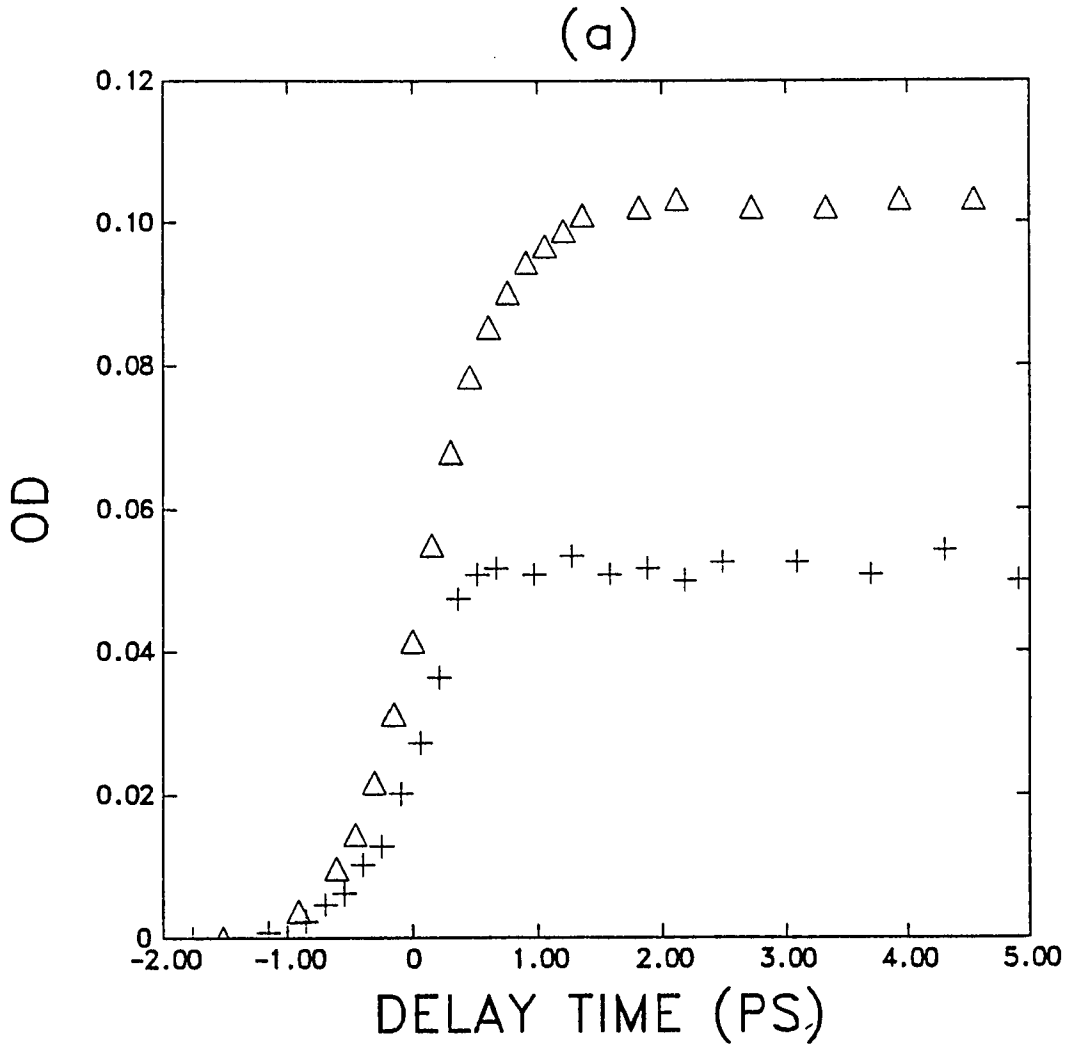

Fig.8.3.1. The measured change in induced optical density at 3.3 μm (triangles) and 4.0 μm (pluses, *1/2) for $Al_{0.6}Ga_{0.4}As$ at room temperature. [6]

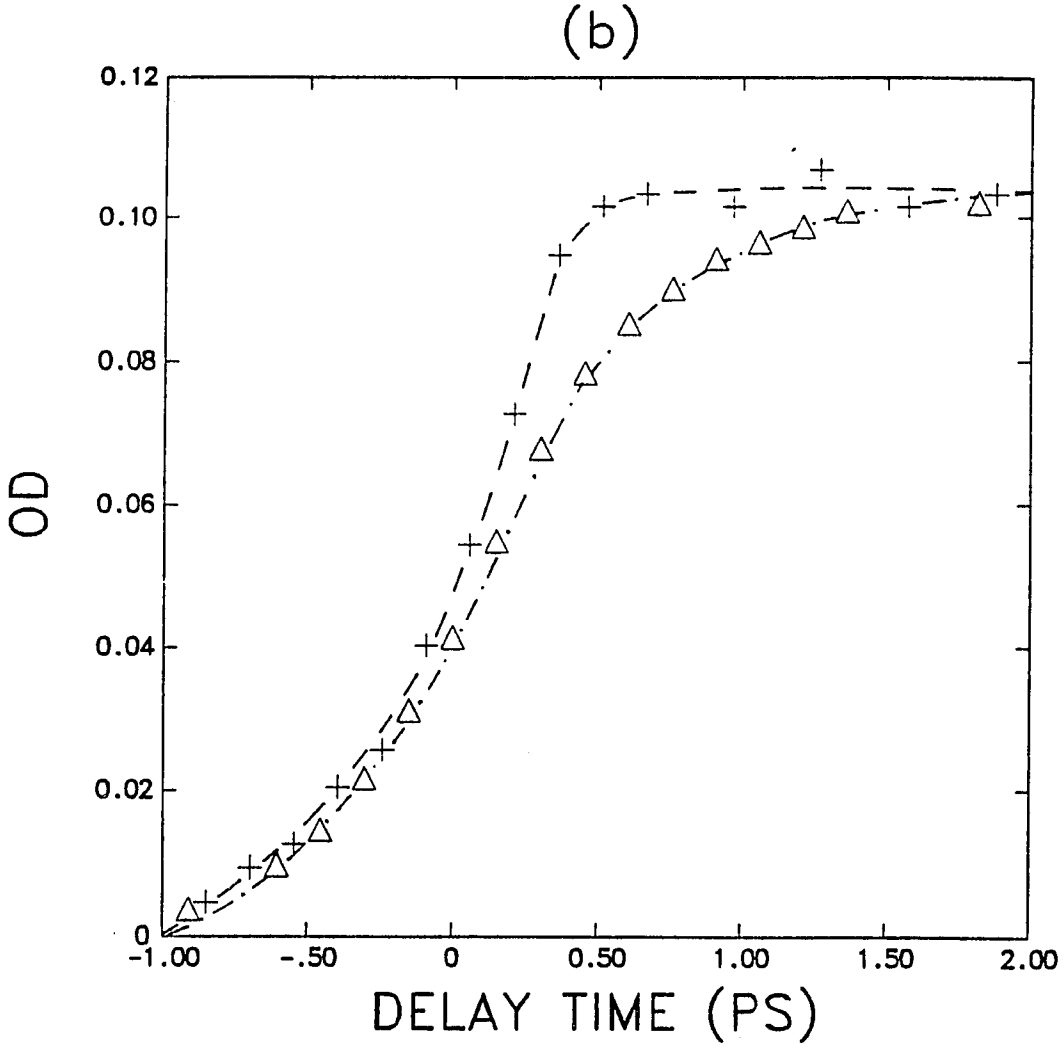

Fig.8.3.2. The rise portions of both curves in Fig.8.3.1 normalized for their maximum values. [6]

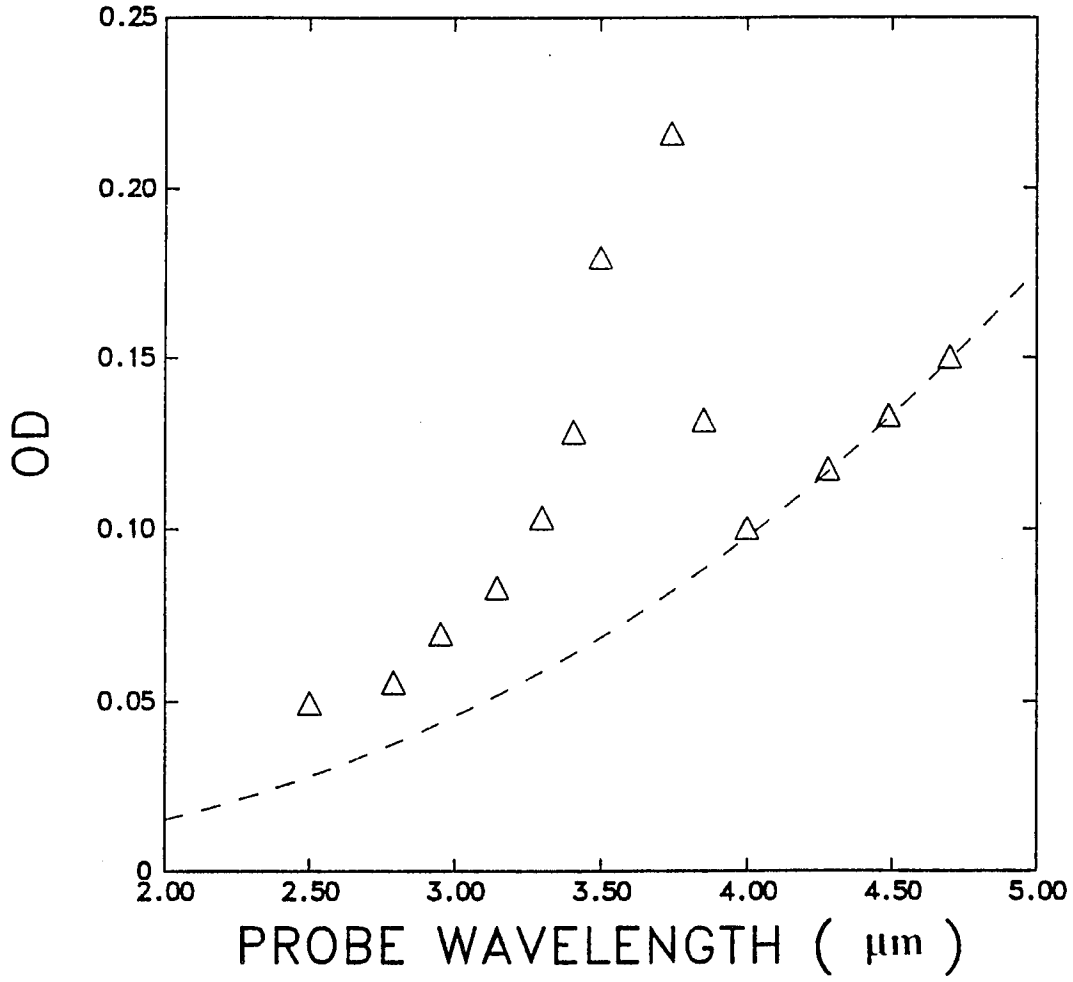

Fig.8.3.3. The probe wavelength dependence of the induced total IR absorption (triangles) and the free carrier absorption (dashed line). [6]

not sufficient to make transitions for ICA. Consequently, the absorption for those longer wavelengths only arise from FCA. The curve fitting to the data for $\lambda_{probe} \geq 4.0\mu m$ by using the relation of $(OD)_{FCA} \propto \lambda^n$, and its extension to shorter probe wavelengths, shown in Fig.8.3.3, give an appropriate value of FCA at each λ_{probe} with the value of n=2.2. The temporal behavior of FCA at each λ_{probe}, for example, at λ_{probe}= 3.3μm, should be similar to the curve for 4.0μm in Fig.8.3.1 with its appropriate flat value.

Consequently, the total IR absorption at 3.3 μm is attributed to both FCA and ICA because a 3.3 μm photon is energetic enough to make the $X_6 \rightarrow X_7$ transitions [6,9,11,12]. Since the temporal behavior of FCA at 3.3 μm should be similar to that of 4.0 μm, the time-resolved $X_6 \rightarrow X_7$ ICA at 3.3 μm, $(OD)_{X_6->X_7}(t)$, can be obtained by subtracting its FCA curve of $(OD)_{FCA}(t)$ from its measured total absorption curve of $(OD)_{total}(t)$.

Since the X_7 states are almost empty, the time-resolved $X_6 \rightarrow X_7$ absorption, $(OD)_{X_6 \rightarrow X_7}(t)$ obtained by the manner mentioned above, reflects the time evolution of the population of the X_6 electrons, $N_X(t)$. In fact, $N_X(t)$ can be obtained by deconvoluting the transmittance data $T_{X_6 \rightarrow X_7}(t)$, corresponding to the absorption data of $(OD)_{X_6 \rightarrow X_7}$, and the probe pulse $I_{probe}(t)$ using the equation:

$$T_{X_6 \rightarrow X_7}(t_d) = \int_{-\infty}^{\infty} dt I_{probe}(t-t_d) e^{-N_X(t)\sigma_X d} / \int_{-\infty}^{\infty} dt I_{probe}(t) \qquad (8.3.1)$$

where I_{probe}(t) is the instantaneous intensity of the probe pulse assumed to have a Gaussian profile, d is the length of the sample, σ_X is the $X_6 \rightarrow X_7$ absorption cross section, which can be calculated using the value of $(OD)_{X_6 \rightarrow X_7}$(t) in the flat decay region and the carrier density. The deconvoluted result for N_X(t) is shown in Fig.8.3.4.

In contrast, with the X valley electrons undergoing both ICA and FCA, the L valley electrons only undergo FCA because there are no upper IR active bands for them to undergo ICA. Therefore, the relative IR absorption in the L valley is very small.

8.4. The $L_6 \rightarrow X_6$ Intervalley Scattering Time

The time evolution of the population of the X_6 electrons, N_X(t), was used to extract the value of the L→X intervalley scattering time from a rate equation analysis. Electrons excited from the heavy-hole and light-hole bands by 2.12 eV (585 nm) pump photons obtained sufficient energy to reach both the X and L valleys [12] from which they can scatter to each other as well as scatter inside each valley. Although the emission and absorption of a phonon increases and decreases the intravalley scattering rate, respectively, both of them increase the intervalley scattering rate [13]. Since the energy of the X minimum (2.023 eV measured from the top of the Γ valence band) is lower than that of the L minimum (2.089 eV) by the energy of two phonons, after a few times of the X←→L back-and-forward intervalley scattering, electrons in the L valley will scatter into the X

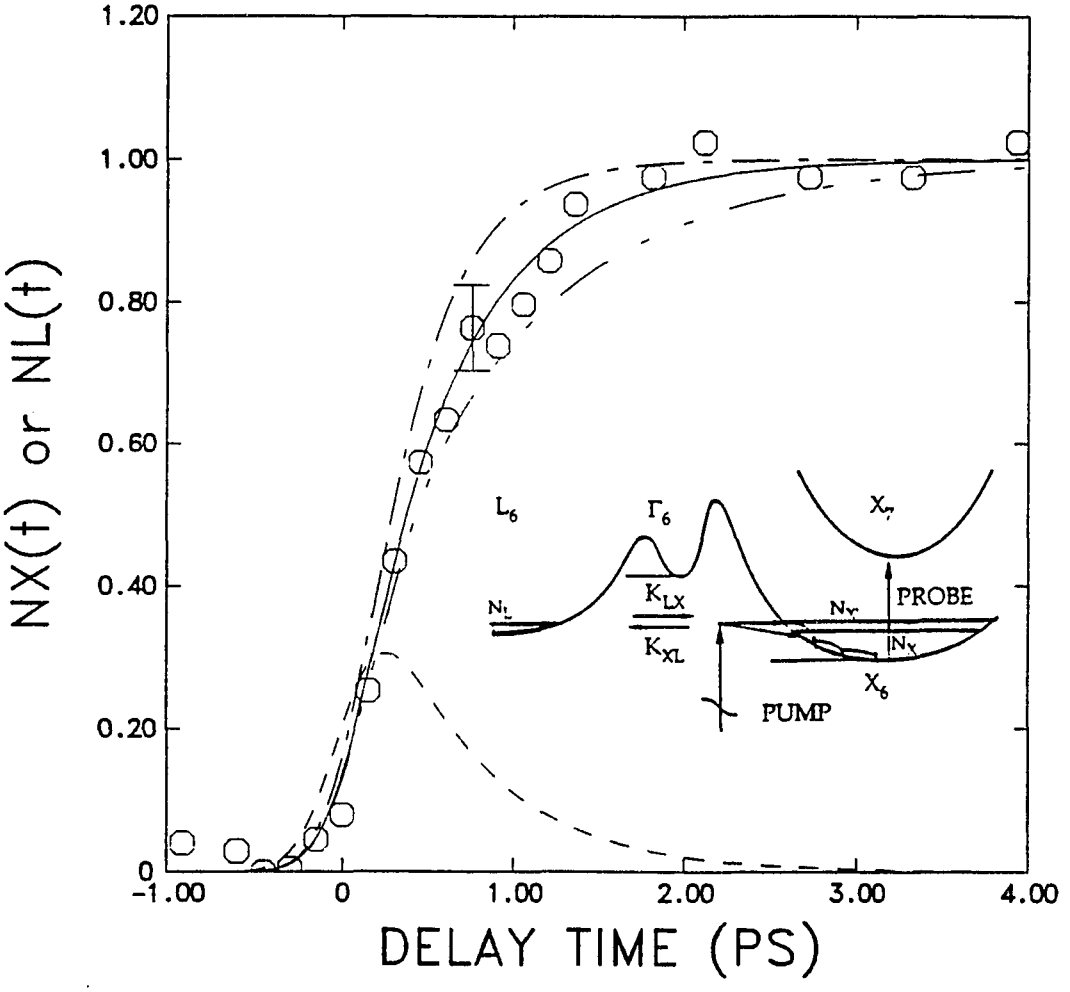

Fig.8.3.4. The time evolution of the population of N_X and N_L. The circles represent the experimental data for N_X. The dot-dash, solid, and dot-dot-dash curves are the computer fits for N_X, from rate equations (8.4.1) to (8.4.3), corresponding to $t_{L\to X}$=100, 200, and 300 fs, respectively. The dashed line is the numerical solution for N_L with t_{LX}=200 fs. The inset shows the relevant scattering processes.[6]

valley and the energy of the electrons in the X valley will decrease to less than 2.089 eV. These electrons in the X valley will then decay to the bottom of the X valley through intravalley scattering.

The rate equations governing the dynamics of the hot carriers through inter-and-intravalley scattering are: [6]

$$dN_L(t)/dt=-K_{LX}N_L(t)+K_{XL}N_{X'}(t)+\alpha_L dP(t) \quad (8.4.1)$$

$$dN_{X'}(t)/dt = K_{LX}N_L(t)-K_{XL}N_{X'}(t)+\alpha_{X'}dP(t)-K_{XX}N_{x'}(t) \quad (8.4.2)$$

$$dN_X(t)/dt = K_{XX}N_{X'}(t)-K_{XV}N_X(t) \quad (8.4.3)$$

where $N_L(t)$=instantaneous population density of electrons(IPDE) in the L valley; $N_{x'}(t)$=IPDE in the X valley whose energies are above 2.089 eV; N_x=IPDE in the bottom of the X valley; P(t)=pump photon flux density; $K_{ij}=1/t_{ij}$ for i,j=L,X, inter-or-intravalley scattering rate shown in Fig.8.1.1, and t_{ij} = intervalley scattering time from the i to j valleys for i≠j, t_{xx}=average time for the X electrons to undergo an energy loss from the above 2.089 eV to the bottom of the X valley by intravalley scattering in the X valley; $K_{XV}=1/t_{XV}$, recombination rate of the X electrons and holes in the valence bands, which can be neglected because t_{XV} is much longer than our experimental range of ~50 ps; α_i (i=L, X) =absorptance of the sample for the pump pulse at 585 nm.

The rate equations (8.4.1) to (8.4.3) were solved for $N_X(t)$ numerically by using the Runge-Kutta method. The values of $\alpha_{X'}$ and α_L can be obtained from the steady-state absorption measurement of the sample. The

value of t_{XX} and the relationship between t_{XL} and t_{LX} can be obtained using the previously determined intravalley decay constant [14], the intra-and-intervalley scattering theory [13], and the parameters of $m_X=0.766m_0$, $m_L=0.566m_0$, $\varepsilon_{oX}=2.023$ eV, $\varepsilon_{OL}=2.089$ eV, $\hbar\omega_l=32.94$ meV for $Al_{0.6}Ga_{0.4}As$ [12]. Substituting the above values for the coefficients in the rate equations leaves only t_{LX} unknown which was treated as a variable parameter to fit the numerical solution for $N_X(t)$ to the experimental data. As examples of fitting, the three curves of the solution of $N_X(t)$ for the three values of t_{LX} = 0.1, 0.2, and 0.3 ps are shown in Fig.8.3.4. Comparison of fitting curves with the experimental data gives a value of t_{LX} = 200 fs for the best fit. The uncertainty in this determined value t_{LX} was estimated to be < $\pm$100 fs by considering the experimental error bars and the uncertainty of the parameters used for solving the rate equations.

The time evolution of the population of electrons in the L valley can also be obtained by solving the rate equations (8.4.1) to (8.4.3) for N_L at a value of t_{LX}. The solution of N_L with t_{LX}=200 fs is displayed in Fig.8.3.4 by the dashed curve.

8.5. Deformation Potential Between the L and X Valleys

The determined L→X intervalley scattering time of t_{LX}=200 fs for $Al_{0.6}Ga_{0.4}As$ is attributed to both phonon-assisted (deformation potential related) [13,15] and alloy-disorder-assisted (zero-phonon transition) [16,17] intervalley scatterings. The intervalley scattering by carrier-phonon interaction

involves an emission or absorption of a zone-edge or near-zone-edge phonon for momentum conservation. This phonon-assisted intervalley scattering is usually the only transfer process of electrons among different valleys in III-V semiconductors such as GaAs. However, in ternary semiconductors such as AlGaAs, there exist another mechanism called alloy-disorder-induced intervalley scattering besides the phonon-assisted one.

In $Al_xGa_{1-x}As$ and other alloys, alloy disorder, i.e. the random distribution of the alloy components on the lattice sites will result in the microscopic violation of the translational symmetry and the fluctuation of the periodic lattice potential energy which may mix states at different points in k-space. As a result, the absence of the periodicity of the potential energy can cause a transition between the bands located at different points in k-space without an emission or absorption of a phonon. Therefore, these alloy-disorder-induced intervalley transition is also called zero-phonon or non-phonon intervalley scattering.

The recent measurements of Kalt et al [17] show that (1) zero-phonon transitions are efficient in $Al_xGa_{1-x}As$ but negligible in GaAs; (2) in $Al_{0.38}Ga_{0.62}As$, the intervalley scattering time for the alloy-disorder-related transfer, t_{alloy}, is about four times longer than that for phonon-assisted transfer, t_{phonon}; and (3) the effect of the disorder for higher x values can be estimated using the simplified formula $(1/t_{alloy}) \alpha$ x(1-x). Since the product of x(1-x) is about 2% higher for our sample with x=0.6 than that for their sample with x=0.38, it is reasonable to choose t_{alloy} to be also about

four times longer than t_{phonon} for $Al_{0.6}Ga_{0.4}As$. The total L→X intervalley scattering time, t_{LX}, can be expressed by the equation of $1/t_{LX}=1/(t_{phonon})_{LX}+1/(t_{alloy})_{LX}$. Substituting the relation of $(t_{alloy})_{LX}=4(t_{phonon})_{LX}$ and the determined value of t_{LX}=200 fs into this equation yields the value of $(t_{phonon})_{LX}$=250 fs for $Al_{0.6}Ga_{0.4}As$.

This phonon-assisted L→X intervalley scattering time $(t_{phonon})_{LX}$, can be used to determine the deformation potential between the L and X valleys from the equation [13,15]

$$\frac{1}{t_{ij}}=\frac{D_{ij}^{2}N_j m_j^{3/2}}{2^{1/2}\pi\hbar^3\rho\omega_{ij}}[(N_{ij}+1)(\varepsilon-\hbar\omega_{ij}-\varepsilon_{oj})^{1/2}+N_{ij}(\varepsilon+\hbar\omega_{ij}-\varepsilon_{oj})^{1/2}] \quad (8.5.1)$$

where t_{ij} is the phonon-assisted intervalley scattering time of electrons from the initial ith valley with energy ε to the final jth valley, N_j the number of equivalent valleys (1 for Γ, 3 for X, and 4 for L), m_j effective mass of electrons in the jth valley, ρ density of the crystal, $\hbar\omega_{ij}$ phonon energy for the i→j intervalley scattering, N_{ij} the number of intervalley scattering phonons, ε_{oj} energy in the bottom of the jth valley, and D_{ij} deformation potential between the ith and jth valleys. The first and the second terms in the angular bracket represent transitions involving emission and absorption of phonons, respectively. All of the values of above-mentioned parameters for $Al_{0.6}Ga_{0.4}As$, except D_{ij}, can be obtained from the literature [12] and our experimental conditions. Substituting all of the known values of the parameters and the determined value of

$(t_{phonon})_{LX}$=250 fs into equation (8.5.1) yields the value of D_{LX}=2.7 × 10^8 eV/cm.

Zollner [15] has calculated the L-X intervalley deformation potential D_{LX} for GaAs as well as for AlAs. The total D_{LX}, considering all of the possible phonon modes were calculated to be 3.8×10^8 eV/cm for GaAs and 3.2×10^8 eV/cm for AlAs. These results indicate that D_{LX} in $Al_xGa_{1-x}As$ changes slightly with x. Therefore, the theoretical value of D_{LX} for $Al_{0.6}Ga_{0.4}As$ can be approximately estimated to be 3.44×10^8 eV/cm which is slightly higher but in good agreement with our experimental value.

The determined value of $(t_{phonon})_{LX}$=250 fs for $Al_{0.6}Ga_{0.4}As$ can be used to estimate the upper limit of the L→X intervalley scattering time t_{LX} for GaAs. Since $(m_X)_{GaAs} > (m_X)_{Al_{0.6}Ga_{0.4}As}$ [12] and $(D_{LX})_{GaAs} > (D_{LX})_{Al_{0.6}Ga_{0.4}As}$ [15], $(t_{LX})_{GaAs}$ should be smaller [13] than $(t_{LX})_{Al_{0.6}Ga_{0.4}As}$, that is t_{LX} < 250 fs for GaAs. Comparing this result with Shah's determination [1] of $t_{L\Gamma}$=2.0 ps shows that $t_{LX} << t_{L\Gamma}$ in GaAs. Therefore, electrons scatter back-and-forth between the L and X valleys more frequently than between the L and Γ valleys. Consequently, the L-X intervalley scattering is more efficient to control the rate of energy relaxation of the energetic hot electrons in the Γ valley for GaAs and more important for high speed hot carrier devices.

REFERENCES

[1] J. Shah, B. Deveaud, T. C. Damen, and W. T. Tsang, A. C. Gossard, and P. Lugli, Phys. Rev. Lett., 59 , 2222 (1987).

[2] A. Katz, and R. R. Alfano, Appl. Phys. Lett., 53 , 1065 (1988).

[3] W. B. Wang, N. Ockman, M. Yan, and R. R. Alfano, J. of Lumin., 50 , 347 (1992).

[4] D. N. Mirlin, I. Ya. Karlik, and V. F. Sapega, Solid State Commun., 65 ,171 (1988).

[5] Since subscript for all of the bands under discussion is labled #6, this #6 will be deleted from here on unless noted otherwise.

[6] W. B. Wang, Kai Shum, R. R. Alfano, D. Szmyd, and A. J. Nozik, Phys. Rev. Lett., 68 , 662 (1992).

[7] T. M. Jedju, and L. Rothberg, Appl. Optics, 27 , 615 (1988).

[8] Kai Shum, W. B. Wang, R. R. Alfano, D. Szmyd, and A. J. Nozik, Phys. Rev. Lett., 68 , 3904 (1992).

[9] W. B. Wang, N. Ockman, M. A. Cavicchia, and R. R. Alfano, Appl. Phys. Lett., 57 , 395(1990).

[10] R. Braunstein, and L. Magid, Phys. Rev., 111 , 480 (1958).

[11] J. S. Blakemore, J. Appl. Phys., 53 , R123 (1982).

[12] Sadao. Adachi, J. Appl. Phys., 58 , R1 (1985).

[13] E. M. Conwell and M. O. Vassell, IEEE Trans. Electron. Devices, ED-13 , 22 (1966).

[14] J. A. Kash, J. C. Tsang, and J. M. Hvam, Phys. Rev. Lett., 54 , 2151 (1985).

[15] S. Zollner, S. Gopalan, and M. Cardona, Appl. Phys. Lett., 54 , 614 (1989).

[16] A. N. Pikhtin, Sov. Phys. Semicond., 11 , 245 (1977).

[17] H. Kalt, W. W. Ruhle, K. Reimann, M. Rinker, and E. Bauser, Phys. Rev., B43 , 12364 (1991).

Chapter 9

DETERMINATION OF THE CRITICAL VALUE x_c FOR DIRECT-TO-INDIRECT BAND GAP TRANSITION IN $Al_xGa_{1-x}As$

9.1. Introduction

The $Al_xGa_{1-x}As$ alloy system is important for several photonic devices as well as high speed electronic devices.[1] The design of these advanced devices relies on the accurate knowledge of the energy band structure of $Al_xGa_{1-x}As$ as a function of x, in particular on the critical value x_c which corresponds to the direct-to-indirect band gap transition[2]. However, the values of x_c determined from recent fluorescence and other measurements[2-6] span a large range of 0.37-0.45. One could not design and construct high quality $Al_xGa_{1-x}As$ devices with such an uncertainty in x_c. Therefore, the precise determination of an accurate value of x_c remains very important for semiconductor physics and device design. Since the probability for indirect transitions is several orders of magnitude smaller than that for direct transitions, the intensity of fluorescence from the satellite valley is much weaker than that from the central valley. Therefore, it is difficult to monitor small changes of the electron distribution among different valleys with x, and to accurately determine x_c by measuring fluorescence from $Al_xGa_{1-x}As$ [1].

I have measured time-resolved IR absorption for $Al_xGa_{1-x}As$, and used a new approach to determine the accurate value of x_c. The measured

change of the photoinduced IR absorption monitors the change of the number of electrons in the X valley which increases significantly when x approaches x_c. The profile of the measured IR absorption enables us to distinguish between direct and indirect band gap structures for samples. The values of $\alpha=\Delta(E_g)^{\Gamma}/\Delta x$ = 13.40 meV/% and x_c=0.412±0.009 were determined with a high degree of accuracy from the measured x-dependence of the short decay component of the IR absorption. [7]

9.2. Measured Profiles of the IR Absorption

Five undoped 2μm-thick $Al_xGa_{1-x}As$ epilayer samples used in our measurements were grown by the Metal Organic Chemical Vapor Deposition process in a vertical reactor at a temperature of 725 °C with a growth rate of 12-14 A/sec. [7] The Al contents of the samples were determined by electron microprobe analysis and gas phase composition measurements in the growth reactor to be 0.358, 0.380, 0.408, 0.439, and 0.595, respectively, with an uncertainty of ±0.005. The GaAs substrate for each sample was completely removed to eliminate excitation and absorption from the substrate. The steady-state IR transmission spectrum of each sample was measured and found to have no appreciable absorption at the IR probe wavelengths.

A femtosecond visible-pump and IR-probe setup mentioned in Section 4.2 was used for this measurement. A 585 nm, ~400 fs pulse was used to pump samples to create hot electrons and holes, and a ~ 3.3μm, ~500 fs

IR probe pulse was used to monitor the photoinduced IR absorption.

The measured growth and decay of the photoinduced IR absorption as a function of x and delay time, t_d, between pump and probe pulses for the $Al_xGa_{1-x}As$ samples at room temperature are displayed in Fig.9.2.1. The salient features of the curves are: the decay of the induced total absorption for samples with x≥0.439 is flat within the experimental time range of ~45 ps; however, the decay for samples with x≤0.408 has both short and long flat components. At the peak position of each curve, the percentage of OD for the short decay portion in the induced total absorption decreases with increasing x for x≤0.408 samples, and goes to zero for x≥0.439 samples.

9.3. Temporal Characteristics of the $X_6 \rightarrow X_7$ Absorption

An explanation for the induced total IR absorption has been previously discussed [8,9]. The induced total IR absorption is attributed to interconduction band absorption (ICA), free carrier absorption (FCA), and intervalence band absorption (IVA). Since the calculated values of OD for IVA [9] at λ≥3.3 μm are much smaller than the observed values of OD for the corresponding samples, IVA can be neglected in our considerations.

The decay of FCA is flat because the radiative and Auger recombination time of electrons and holes in $Al_xGa_{1-x}As$ is at least several nanoseconds [10] which is much longer than our experimental time scale. The flat decay of FCA has been previously observed in our measurements for

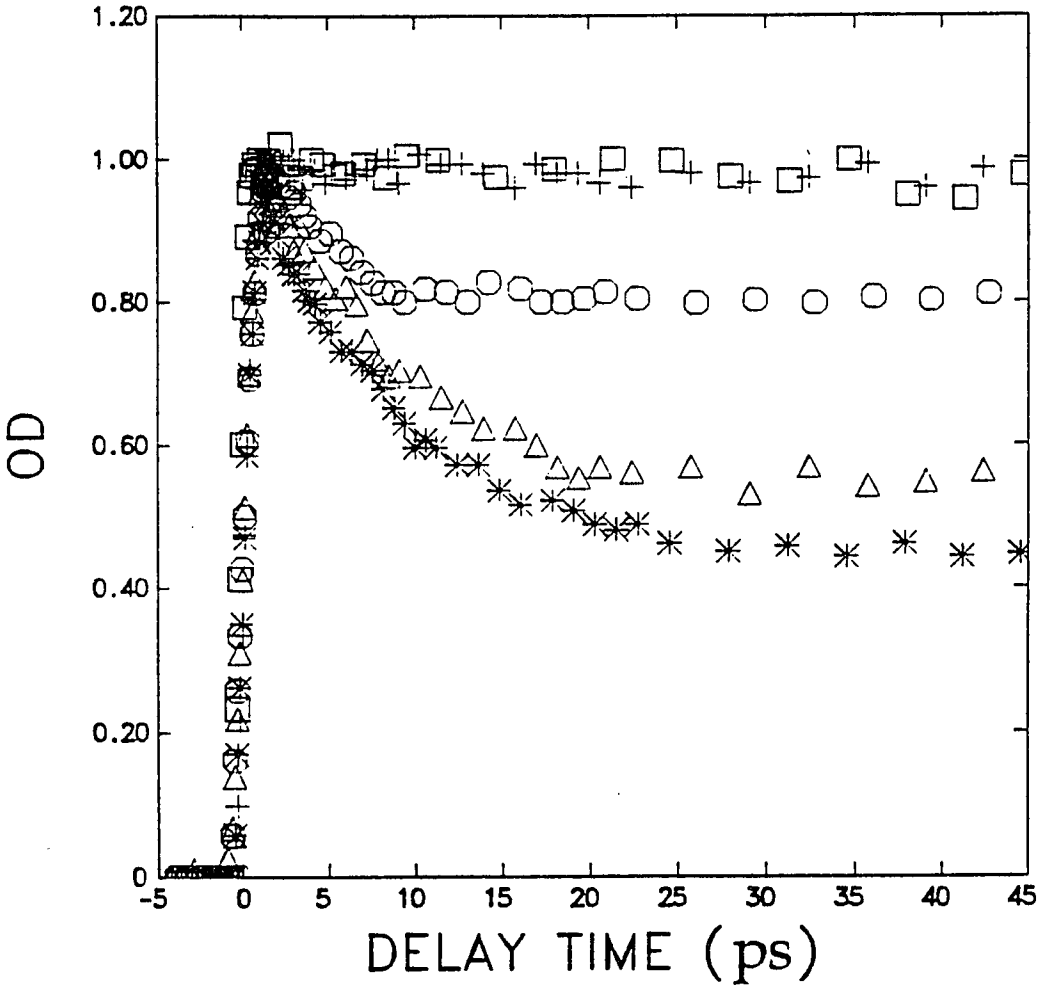

Fig.9.2.1. The measured change in induced optical density (OD) versus delay time at λ_{probe}=3.3 μm for $Al_xGa_{1-x}As$ with x=0.358 (stars), 0.380 (triangles), 0.408 (circles), 0.439 (pluses), and 0.595 (squares), respectively. In order to clearly show their decay behavior, the maximum value of each curve has been normalized to unity. [7]

GaAs at a long probe wavelength of 3.9 μm [11] in which only FCA is possible because the probe photon of 3.9 μm has insufficient energy to make the $X_6 \rightarrow X_7$ transition.

The temporal characteristics of the $X_6 \rightarrow X_7$ ICA in $Al_xGa_{1-x}As$ depends on its band structure as discussed in section 3.5: (1) a sample with $x<x_c$ has a GaAs-like direct band gap, and its N_X and the $X_6 \rightarrow X_7$ ICA as a function of t_d has a short decay; (2) a sample with $x>x_c$ has an AlAs-like indirect band gap, and the decay of the $X_6 \rightarrow X_7$ ICA is flat; and (3) for a sample with $x \approx x_c$, the $X_6 \rightarrow X_7$ ICA has both short and flat decay components as shown in Fig.3.5.4. When the energy difference between the X and Γ mimina, $\Delta E_{X\Gamma}=E_g{}^X-E_g{}^\Gamma$, decreases, the number of electrons in the X valley relative to the total number of electrons in the thermal equilibrium will increase, and as a result, the flat decay portion of ICA will become larger, and the short decay portion of ICA will decrease. Consequently, the measured percentage of the short decay portion of ICA relative to the total absorption, defined as a parameter

$$K_{short}=(OD)_{short}/(OD)_{total}, \qquad (9.3.1.)$$

directly reflects the value of $\Delta E_{X\Gamma}$ for an $Al_xGa_{1-x}As$ alloy. The critical value of x_c for which $\Delta E=0$ can be obtained from the measured x dependence of ΔE.

As discussed in Section 3.6, the parameter K_{short} can be written as

$$K_{short}=[1/(\sigma_{FC}/\sigma_{IC}+p_X)][p_X-f_X], \qquad (9.3.2)$$

where σ_{FC} and σ_{IC} are cross sections for FCA and ICA, respectively; p_X and f_X are fractions of the carrier density in the X valley relative to the total carrier density at the delay times of t_{peak} and t_{flat} corresponding to the absorption peak and the flat absorption region, respectively (see Fig.3.5.4).

The expression for $p_X(x)$ is given by [12]

$$p_X(x)=[1/t_{\Gamma X}(x)]/[1/t_{\Gamma X}(x)+1/t_{\Gamma L}(x)+1/t_{\Gamma\Gamma}(x)], \qquad (9.3.3)$$

where $t_{\Gamma X}(x)$, $t_{\Gamma L}(x)$, and $t_{\Gamma\Gamma}(x)$ are inter-and-intravalley scattering times, and vary with Al content x and the experimental conditions such as crystal temperature, kinetic energy of electrons, and so on.

The x-dependence of the effective mass, the deformation potentials, and the alloy-disorder intervalley scattering rates, discussed in Section 3.6, enable us to obtain the x-dependence of the scattering rates and to calculate $p_X(x)$ as a function of x.

The expression for $f_X(x)$ can be written as [4]

$$f_X(x)=1/[1+(\frac{t_X}{t_\Gamma})(\frac{m_\Gamma}{m_X})^{3/2}e^{\Delta E_{X\Gamma}/K_BT}+(\frac{t_X}{t_L})(\frac{m_L}{m_X})^{3/2}e^{\Delta E_{XL}/K_BT}], \quad (9.3.4)$$

where t_i and m_i are the lifetime and density of states effective mass of electrons in the ith valley, respectively, where i=Γ, L, and X; K_B is the Boltzmann constant; $\Delta E_{X\Gamma} = (E_g)^X-(E_g)^\Gamma$; and $\Delta E_{XL}=(E_g)^X-(E_g)^L$. The previous band-gap determinations suggest a linear dependence [2,12] of $(E_g)^\Gamma(x)$ for $x<x_c$ by: $(E_g)^\Gamma(x)=1.424+\alpha x$. Since the value of $(E_g)^\Gamma(x)$

varies greatly [12] from 1.424 eV for GaAs (x=0) to 3.018 eV for AlAs (x=1), and the previously determined values of α scatter in the large range from 12.50 meV% [5] to 16.1 meV% [13], α has to be kept as an unknown parameter to be determined. The value of $(E_g)^X$ changes slightly from 1.90 eV for GaAs to 2.168 eV for AlAs, and the difference of its calculated values using different determined expressions of $(E_g)^X$ is small [12]. Therefore, we chose the most used expression [14] of $(E_g)^X(x)=1.90+0.125x+0.143x^2$ for $(E_g)^X$(x). For a similar reason, we chose [14] $(E_g)^L(x)=1.704+0.642x$ for $(E_g)^L$(x). Substituting the expressions of t_i(x), m_i(x), $(E_g)^i$(x) (i=Γ, L and X) into equation (9.3.4), f_X(x) was obtained with one unknown parameter α.

The ratio of σ_{FC}/σ_{IC} was found to be 0.418 from equation (9.3.2) using the calculated values of p_X and f_X, and the measured value of K_{short}=0.56 for GaAs (x=0). [7] Substituting the expressions of p_X(x) and f_X(x), and the value of σ_{FC}/σ_{IC} into equation (9.3.2) shows K_{short} to be a complex function of x with an unknown parameter α.

9.4. Determination of the Critical Value x_c

The measured values of K_{short}(x) for a series of $Al_xGa_{1-x}As$ and GaAs samples are displayed in Fig.9.4.1. The change of K_{short}(x) from 0.56 for x=0 to 0.0 for x=0.439 mainly arises from f_X(x) because the

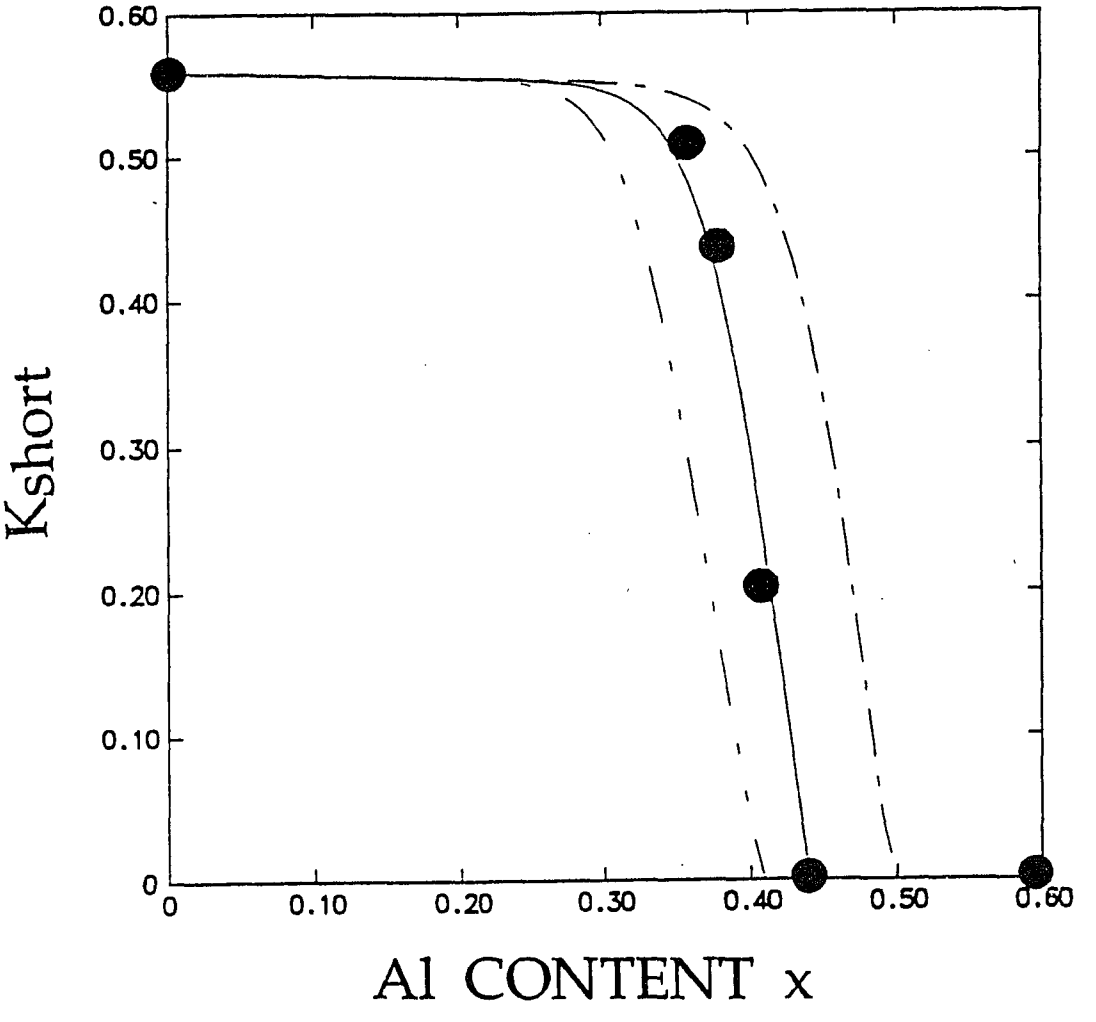

Fig. 9.4.1. K_{short} versus x. The solid curve shows the best fit of the calculated values of K_{short} from equation (9.3.2) to the experimental data (filled circles) with α=13.40 meV/% and x_c=0.412. The dot-dash and dot-dot-dash curves indicate the calculated values of K_{short} obtained by using the values [14] of α=12.47 meV/% and x_c=0.45, and that [2] of α=14.55 meV/% and x_c=0.37, respectively. [7]

calculated corresponding values of p_X(x) change less than 4%. In order to fit the calculated values of K_{short}(x) from equation (9.3.2) to (9.3.4) to their experimental values, α was treated as a variable parameter. The least square fit was used and the best fit, which is shown in Fig.9.4.1, yields a value of α = 13.40 meV/%. The critical value of x_c was then determined to be 0.412 by solving the equation of $(E_g)^X(x_c)= (E_g)^\Gamma(x_c)$.

Since the number of electrons in the X_6 valley, in thermal equilibrium, relative to the total number of electrons increases significantly when x approaches to x_c (i.e. $\Delta E \rightarrow 0$), the change in $(ICA)_{short}$ is extremely sensitive to the change in ΔE, and consequently to the determination of α and x_c. The sensitivity in the determination of x_c by measuring K_{short} can be estimated by calculating the derivative dK_{short}/dx from equation (9.3.2). The value of dK_{short}/dx at x=0.408 was found to be 7.19, which means that if the value of x changes 0.01, the value of K_{short} will change 7.19% which is large enough to be measured. Since the relative standard probable error was $\pm$0.07 for the experimental value of K_{short}=0.193 at x=0.408, the corresponding experimental uncertainty in x_c was determined to be $\pm$0.002 from the relationship dK_{short}/dx.

The contribution of errors in the parameters used in fitting the data for the determination of x_c was also considered. For example, uncertainties in the previously measured inter-and-intravalley scattering times[10,15,16] of $t_{\Gamma X}$=55$\pm$11 fs, $t_{\Gamma L}$=100$\pm$20 fs, and $t_{\Gamma\Gamma}$=165$\pm$20 fs for GaAs could change

the value of p_X for GaAs from 0.44 calculated using the maximum value of $t_{\Gamma X}$=66 fs and the minimum values of $t_{\Gamma L}$=80 fs and $t_{\Gamma\Gamma}$=145 fs, to 0.62 calculated using the minimum value of $t_{\Gamma X}$=44 fs, and the maximum values of $t_{\Gamma L}$=120 fs and $t_{\Gamma\Gamma}$=185 fs. This variation will affect the expression of the x dependence of p_X(x) for $Al_xGa_{1-x}As$, and will change the determined value of x_c corresponding to the best fit. As mentioned above, based on the values of $t_{\Gamma X}$=55 fs, $t_{\Gamma L}$=100 fs, and $t_{\Gamma\Gamma}$=165 fs for GaAs, and the x dependence of the effective mass [12], the deformation potential [17], the alloy-disorder intervalley scattering [18], and the energy gaps [12] for $Al_xGa_{1-x}As$, the fitting yielded x_c=0.412. However, the fitting gave a value of x_c=0.417 using one of the extreme set of values of $t_{\Gamma X}$=66 fs, $t_{\Gamma L}$=80 fs, and $t_{\Gamma\Gamma}$=145 fs for GaAs, and the corresponding x dependence of the parameters in equations (9.3.2) to (9.3.4) for $Al_xGa_{1-x}As$, and a value of x_c=0.407 for the opposite extreme set of values of $t_{\Gamma X}$=44 fs, $t_{\Gamma L}$=120 fs, and $t_{\Gamma\Gamma}$=185 fs for GaAs, and the related x dependence for $Al_xGa_{1-x}As$. All other determined values of x_c from the fitting using other combinations of those measured values were found to fall in the range from 0.407 to 0.417. Therefore, the contribution of errors of the used inter-and-intravalley scattering times was determined to be $\pm$0.005 for x_c. Similar analyses were done for errors in other parameters in equations (9.3.2) to (9.3.4). The total contribution of errors in all the parameters used in the fitting was found to give an uncertainty in x_c of $\pm$0.007.

In addition, the uncertainty in determining the Al content x for the samples was ± 0.005. Consequently, the total uncertainty in x_c arising from the measurement for K_{short}, the determination of Al content x, and the errors of the parameters used for fitting was estimated to be $\pm\sqrt{0.002^2+0.005^2+0.007^2} = \pm 0.009$.

For a comparison of our experimental result with the previously measured values of x_c, the calculated values of K_{short} as a function of x obtained by using the values [14] of $\Delta(E_g)^{\Gamma}/\Delta x$ = 12.47 meV/% and x_c=0.45, and that [2] of $\Delta(E_g)^{\Gamma}/\Delta x$ = 14.55 meV/% and x_c=0.37, are also displayed in Fig.9.4.1. Our experimental data clearly show that the critical value x_c is neither as large as 0.45 nor as small as 0.37, but 0.412.

In conclusion, the observed decay profiles of the induced IR absorption for $Al_xGa_{1-x}As$ reflect the type of band structure gaps. From the change of K_{short} with x, I have determined the values of $\Delta(E_g)^{\Gamma}/\Delta x$ = 13.40 meV% and x_c=0.412 with a high degree of accuracy.

REFERENCES

[1] H. A. Zarem, J. A. Lebens, K. B. Nordstrom, P. C. Sercel, S. Sanders, L. E. Eng, A. Yariv, and K. J. Vahala, Appl. Phys. Lett., 55 , 2622 (1989).

[2] T. F. Kuech, D. J. Wolford, R. Potemski, J. A. Bradley, and K. H. Kelleher, App. Phys. Lett., 57 , 505 (1987).

[3] W. W. Ruhle, K. Leo, and E. Bauser, Phys. Rev., B40 , 1756 (1989).

[4] J. Shah, B. I. Miller, and A. E. DiGiovanni, J. Appl. Phys, 43 , 3434 (1972).

[5] E. E. Mendez, E. Calleja, and W. I. Wang, Phys. Rev., B34 , 6026 (1986).

[6] H. J. Lee, L. Y. Juravel, and J. C. Woolley, Phys. Rev., B21 , 659 (1980).

[7] W. B. Wang, R. R. Alfano, D. Szmyd, and A. J. Nozik, Phys. Rev. B46 , 15828 (1992).

[8] W. B. Wang, N. Ockman, M. A. Cavicchia, M. Yan, and R. R. Alfano, SPIE, 1282 , 86 (1990).

[9] W. B. Wang, Kai Shum, R. R. Alfano, D. Szmyd, and A. J. Nozik, Phys. Rev. Lett., 68 , 662 (1992).

[10] J. Shah, B. Deveaud, T. C. Damen, and W. T. Tsang, A. C. Gossard, and P. Lugli, Phys. Rev. Lett., 59 , 2222 (1987).

[11] W. B. Wang, N. Ockman, M. A. Cavicchia, and R. R. Alfano, Appl. Phys. Lett., 57 , 395(1990).

[12] Sadao. Adachi, J. Appl. Phys., 58 , R1 (1985).

[13] B. Monemore, K. K. Shih, and G. D. Pettit, J. Appl. Phys., 47 , 2604 (1976).

[14] H. C. Casey, Jr., J. Appl. Phys., 49 , 3684 (1978).

[15] P. C. Becker, H. L. Fragnito, C. H. Brito Cruz, J. Shah, R. L. Fork, J. E. Cunningham, J. E. Henry, and C. V. Shank, Appl. Phys. Lett., 53 , 2089 (1988).

[16] J. A. Kash, J. C. Tsang, and J. M. Hvam, Phys. Rev. Lett., 54 , 2151 (1985).

[17] S. Zollner, S. Gopalan, and M. Cardona, Appl. Phys. Lett., 54 , 614 (1989).

[18] H. Kalt, W. W. Ruhle, K. Reimann, M. Rinker, and E. Bauser, Phys. Rev., B43 , 12364 (1991).

Chapter 10
FUTURE RESEARCH DIRECTIONS

10.1. Introduction

This thesis work has shown that a femtosecond visible-pump and IR-probe absorption spectroscopy can be used to measure transient hot carrier dynamics in a satellite K≠0 valley which is useful in determination of the X-valley-involved intervalley scattering rates as well as in determination of band structure parameters in semiconductor systems. In the future, we will continue our study on GaAs to measure the temperature dependence of the $X \rightarrow \Gamma$ intervalley scattering time, and will extend our research to some important low dimensional structures (LDS), such as Si-Ge and InP/GaInP superlattices (SLS) or quantum wells (QWS) by the novel pump-IR-probe absorption spectroscopy.

We plan to measure the hot carrier relaxation time in the X valley in GaAs as a function of temperature, and to determine the temperature dependence of the $X \rightarrow \Gamma$ intervalley scattering time.

We plan to extend our pump-IR-probe absorption measurements to strained Si-Ge superlattice systems and to determine whether they have a direct band gap, which is very important for optical communication and computation.

We also plan to extend our measurements to $Ga_xIn_{1-x}P$ to determine its critical value of x_c for the direct-to-indirect band gap transition, and to

InP/GaInP SLS and QWS to investigate the effect of intervalley scattering on the hot carrier relaxation and electron collection in these structures. Such materials will be useful to make high efficiency hot carrier solar photoconverters.

10.2. Investigation of the Temperature Dependence of the $X \rightarrow \Gamma$ Intervalley Scattering Time in GaAs

The crystal temperature dependence of the intervalley scattering time is useful to understand the effect of lattice temperature on the electron-phonon interaction and hot carrier relaxation in semiconductors. As an example, the $X \rightarrow \Gamma$ intervalley scattering time, $t_{X\Gamma}$, as a function of crystal temperature at ε = 0.55 eV and $D_{X\Gamma}$=4.0×10^8 eV/cm for GaAs , calculated using equation (2.4.12), is shown in Fig.10.2.1. The value of $t_{X\Gamma}$ at low temperature is about 3 times larger than that at room temperature. Therefore, the hot carrier relaxation at low temperature is expected to be much slower than that at room temperature.

We plan to measure the time evolution of the population of electrons in the X_6 valley for different crystal temperatures by a femtosecond pump-IR-probe absorption spectroscopy. This time evolution data will be used to determine the back scattering time, $t_{X\Gamma}$, for each temperature, to obtain the temperature dependence of $t_{X\Gamma}$, and to investigate the effect of lattice temperature on carrier-phonon interaction.

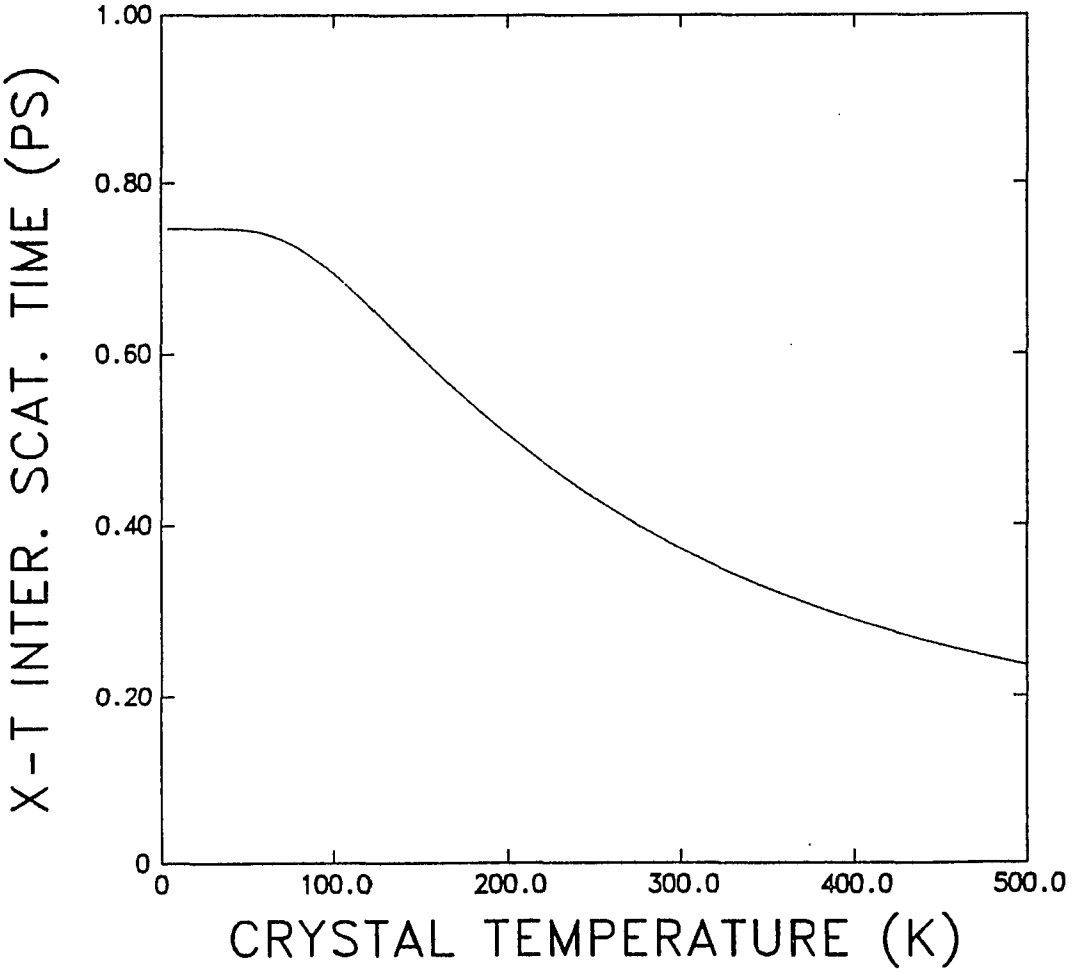

Fig.10.2.1. The calculated $X \rightarrow \Gamma$ intervalley scattering time as a function of crystal temperature for GaAs.

10.3. Investigation of the Direct Band Gap in Strained Si-Ge Superlattices

The band structures of Si and Ge are displayed in Fig.10.3.1 and 10.3.2, respectively.[1] Both of them have indirect band gap structures with the lowest conduction bands at the X point for Si, and at the L point for Ge. However, a strained Si-Ge superlattice system may have a direct band gap since the conduction band minimum at the X point would be "zone-folded" back to the Γ point by long range periodicity[2-4] as shown in Fig.10.3.3. A calculated electronic band structure of the Si_6Ge_4 SLS by Cardona's group[2] is shown in Fig.10.3.4. The possibility of a direct gap has also been shown[3] for Si_4Ge_4/Ge. These strained Si-Ge SLS with direct band gaps have potential importance for optical computation.

It has been pointed out that the speed of silicon Very Large Scale Integrated (VLSI) systems is limited by inter-chip and inter-board communication times between components on chips and off-chip III-V semiconductor optoelectronics components.[5] The latter are needed for generating, transmitting and detecting optical signals with greater efficiency and sensitivity than Si. A strained Si-Ge superlattice system with a direct band gap can perform these functions better than the III-V components. In particular, the generation of intense on-chip optical signals appears to be possible in appropiately strained Ge_nSi_m superlattice systems[2-4] which may have direct energy band gaps. With regard to high speed detector response, strained $Si_{1-x}Ge_x$ SLS have shown a response time of 300 ps at

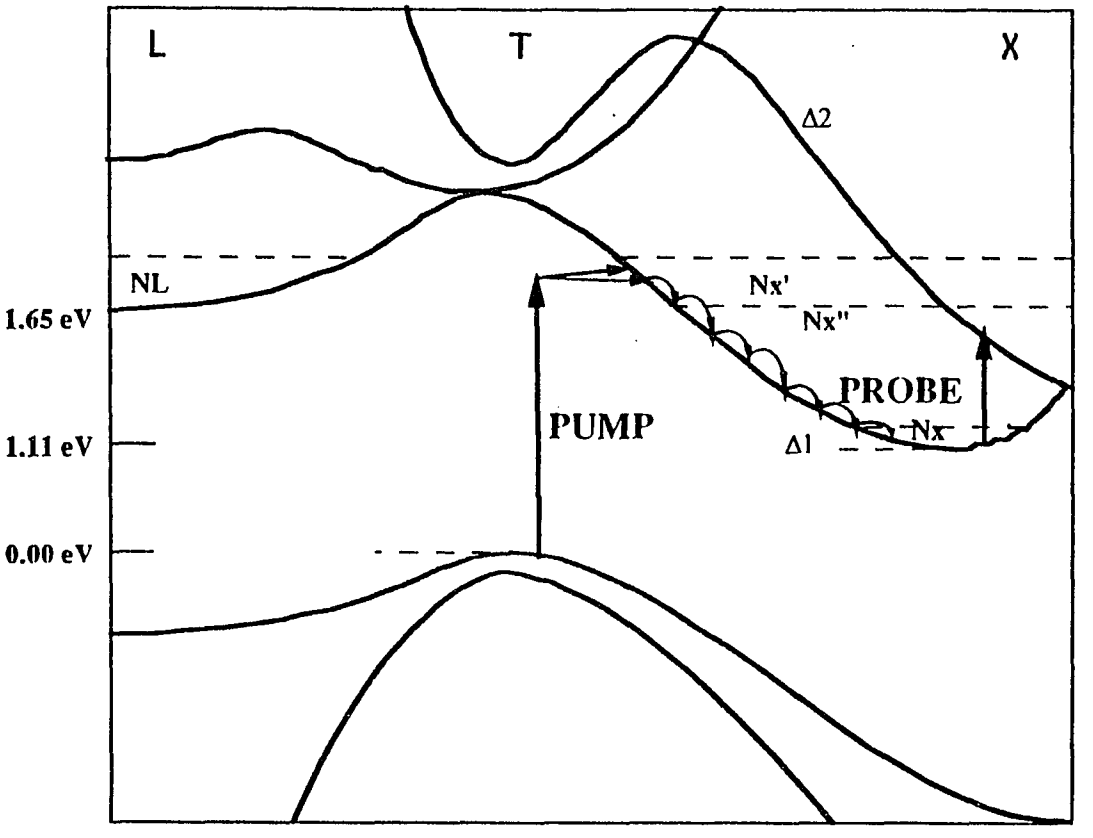

The Band Structure of Si

Fig.10.3.1. Energy band structure for Si. [1]

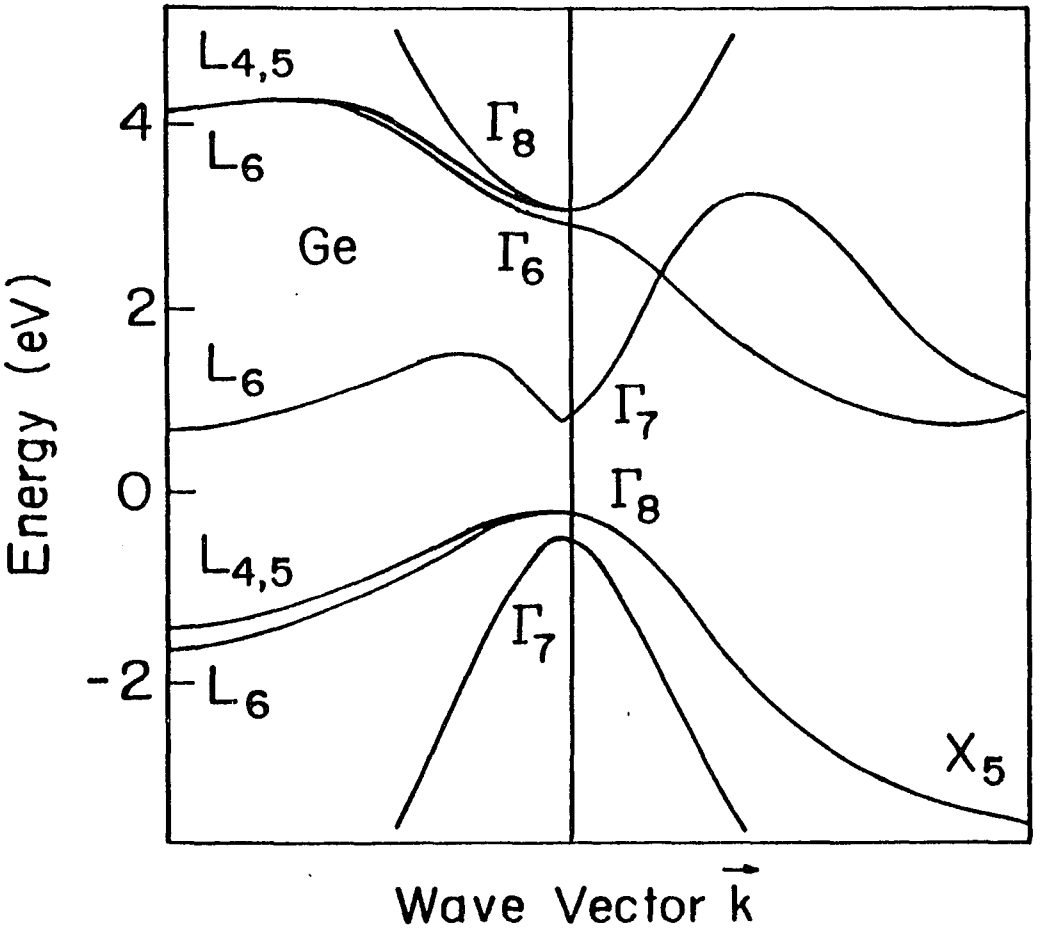

Fig.10.3.2. Energy band structure for Ge. [1]

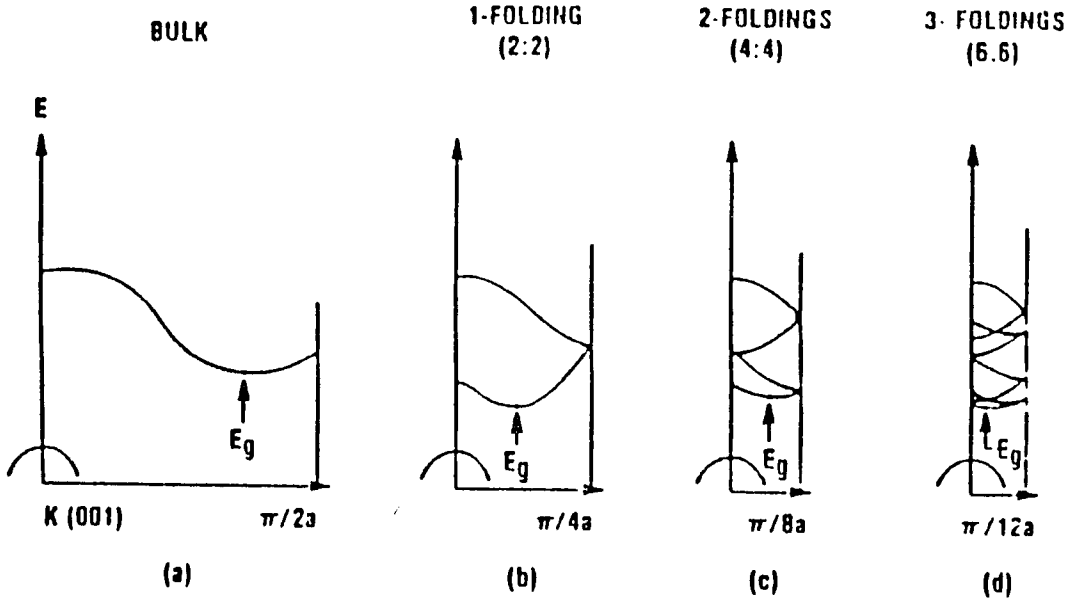

Fig.10.3.3. Schematic representation of zone folding of a Si-like band structure.

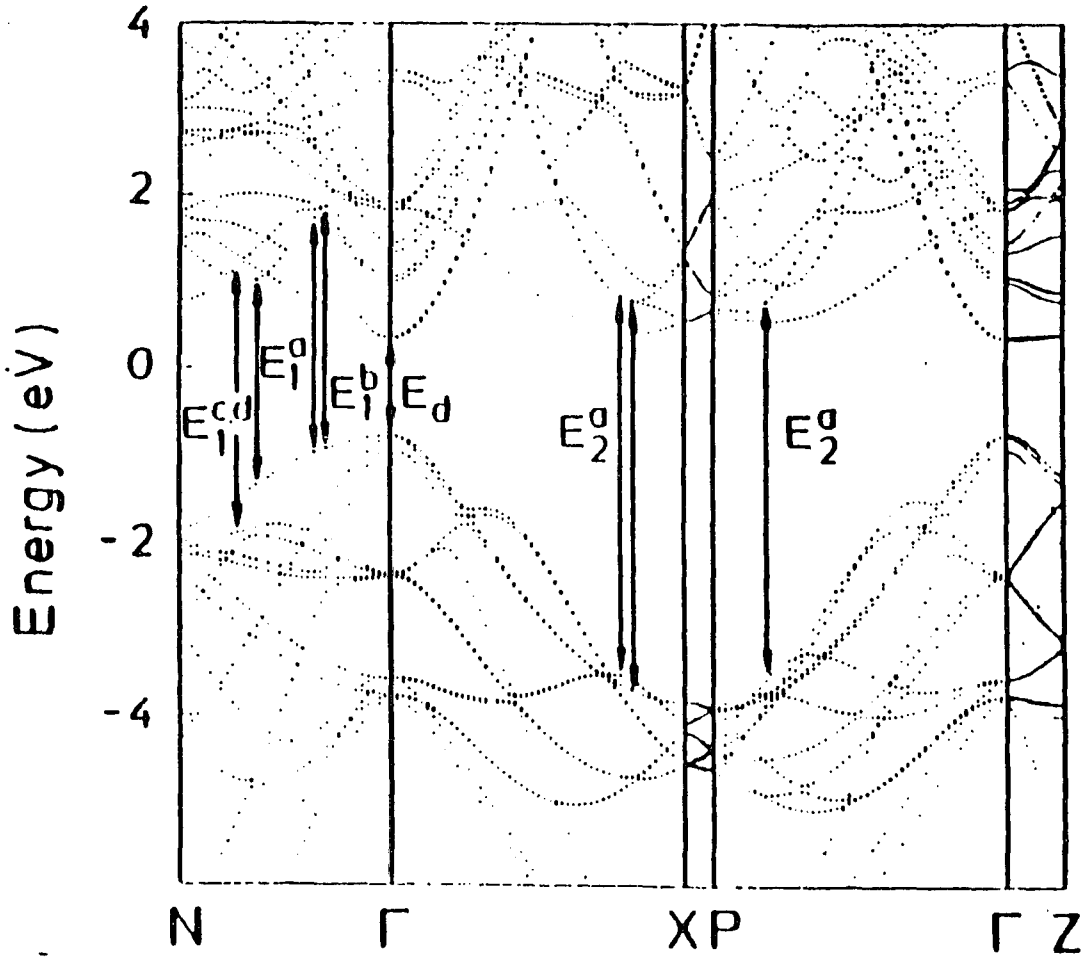

Fig.10.3.4. Calculated electronic band structure (including spin-orbit splitting) of the "free-standing" Si_6Ge_4 SLS along lines of high symmetry. [2]

1.3 μm.[6] Therefore, the possibility of being able to incorporate intense light sources and ultrafast detectors in chips using only Si-Ge technology has been proposed.

Despite their potential importance, there have been, so far, very limited investigations on the band structures and hot carrier dynamics in strained $(Si)_n(Ge)_m$ superlattice systems. All of the experiments to date have not clearly shown a direct band gap structure for strained Si-Ge SLS.[7]

As shown in this thesis work, a successful method to identify a direct or indirect band gap structure for a semiconductor system is to measure hot carrier dynamics in a satellite $K \neq 0$ valley.[2] Therefore, we plan to measure the carrier dynamics in strained Si-Ge superlattices such as Si_6Ge_4 and Si_4Ge_4/Ge by pump-IR-probe absorption spectroscopy. The measured results will be used to investigate whether a strained Si-Ge superlattice system has a direct band gap, and to obtain hot carrier relaxation times in these materials.

10.4. Measurements on Hot Carrier Dynamics in InP/GaInP Low Dimensional Structure

Low dimensional InP/GaInP systems are one of the most important materials for making high efficiency hot carrier solar cells. [10] Therefore, it has become more interesting to investigate the band structure of $Ga_xIn_{1-x}P$, and hot carrier dynamics in InP/GaInP superlattice and quantum wells.

The energy band structure of InP and GaP are shown in Fig.10.4.1, and Fig.10.4.2, respectively. [11] The former has a direct band gap, whereas the later has an indirect band gap. In $Ga_xIn_{1-x}P$ ternary alloys, both of the energy gaps of $(E_g)^\Gamma$ and $(E_g)^X$ increases with x, but $(E_g)^\Gamma$ increases much faster than that of $(E_g)^X$ as shown in Fig.10.4.3. [12] A pump-IR-probe absorption measurement will be performed for several $Ga_xIn_{1-x}P$ samples with different x. The measured results will enable us to determine the accurate critical value of x_c which corresponds to the direct-to-indirect band gap transition as shown at the cross point of $(E_g)^\Gamma$ and $(E_g)^X$ in Fig.10.4.3. The measured value of x_c will be one of the most important parameters for designing the desired InP/GaInP superlattices or quantum well structures.

Intervalley scattering times in superlattices and quantum well structures were measured to be much longer than that in bulk semiconductors [13]. The reason for this is that hot electrons experience a real space transfer from one layer to another layer when they scatter between

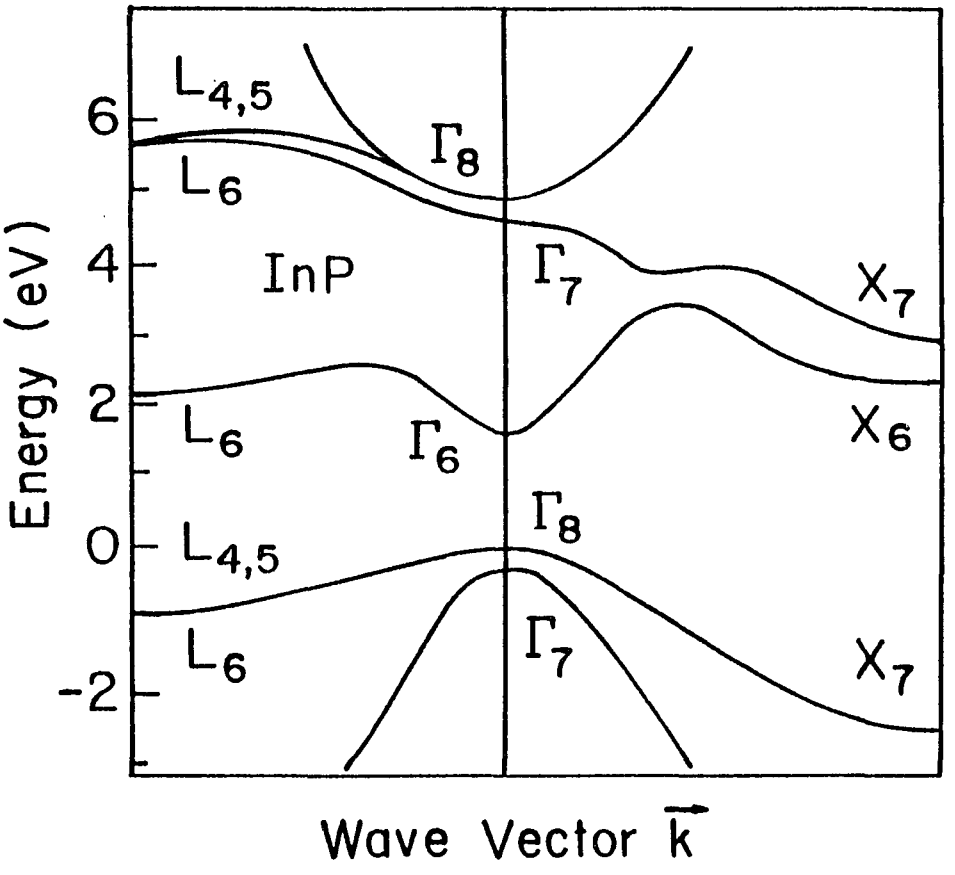

Fig.10.4.1. The energy band structure for InP. [11]

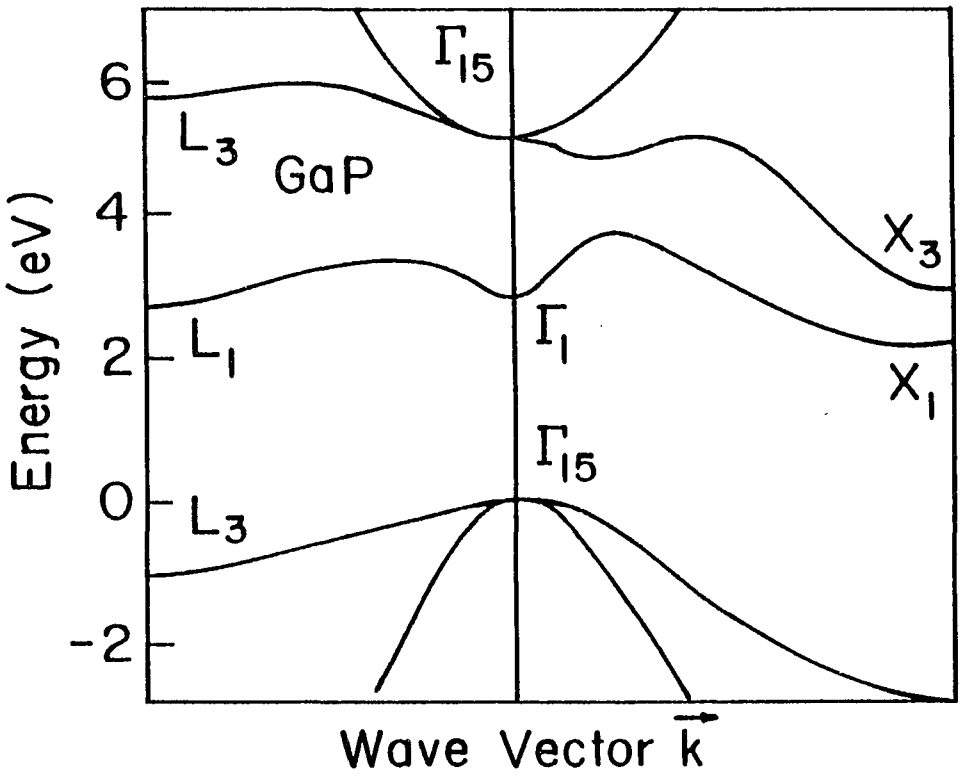

Fig.10.4.2. The energy band structure for GaP. [11]

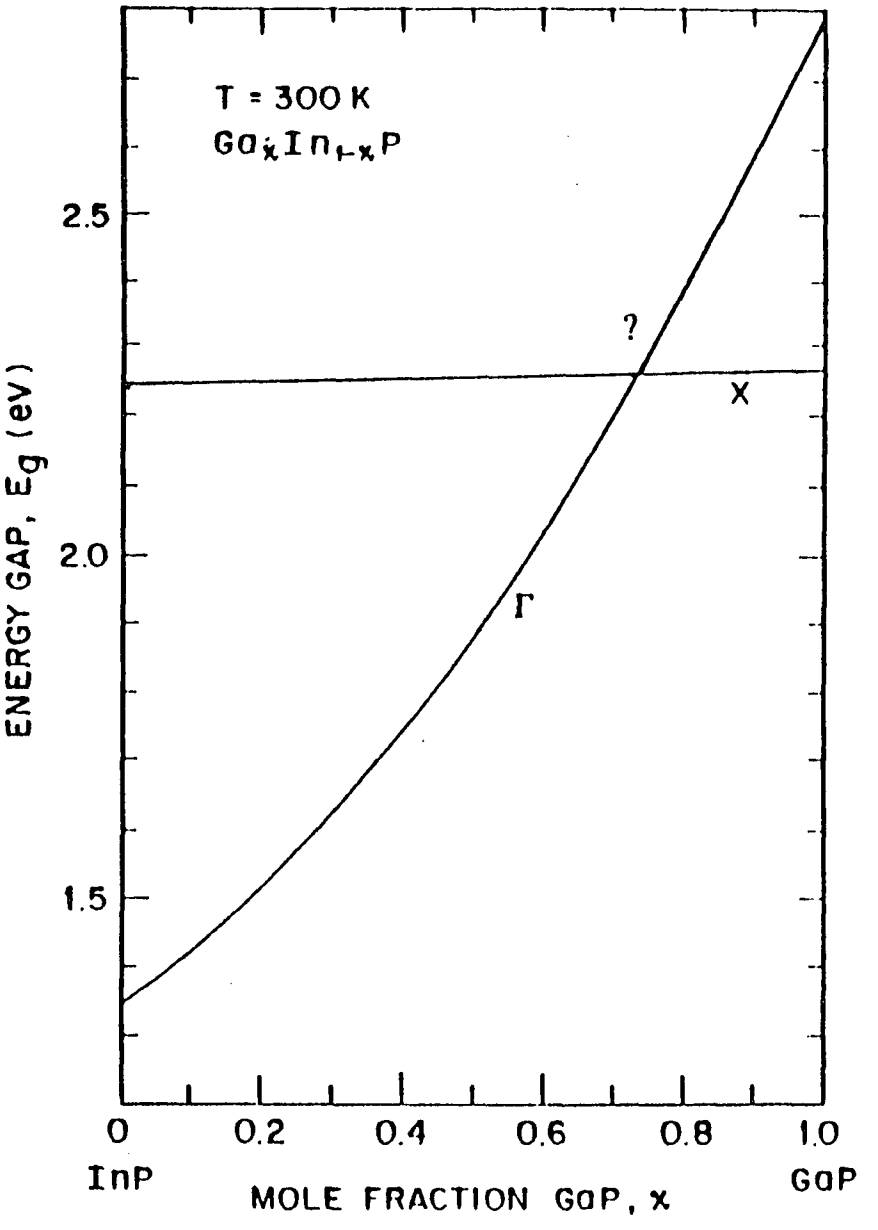

Fig.10.4.3. Schematic diagram for the energy gaps of $(E_g)^{\Gamma}$ and $(E_g)^{X}$ increasing with Ga composition x in $Ga_xIn_{1-x}P$. [12]

different conduction valleys. This intervalley scattering time also shows a strong dependence on layer-thickness. For example, it was found that the intervalley scattering time can be increased by a factor of 5 if the well layer-thickness increased by a only factor of 1.7 [13].

We plan to extend our pump-IR-probe measurements to samples of $(InP)_m(Ga_xIn_{1-x}P)_n$ short period superlattices and quantum well structures with appropriate values of x, m, and n (m, n stand for the number of monolayers in the slabs of InP and $Ga_xIn_{1-x}P$, respectively) so that the GaInP has an indirect band gap, and the lowest lying energy states of the conduction band are confined to the GaInP layers, whereas the lowest lying hole-states of the valence band are confined to the InP layers. After photoexcitation of hot electrons and holes in the confined Γ conduction- and valence-band states of the InP layers, the holes stay in the InP layers during relaxation. In contrast, the electrons scatter from the Γ-related states of a InP layer to the energetically lower X related states of the GaInP layer. Energy relaxation and thermalization of electrons thus involve a real space transfer from the InP layer across the interface to the GaInP layer. The time evolution of the population of hot electrons in the confined lowest X_6 valley of GaInP will be obtained from the time-resolved $X_6 \rightarrow X_7$ IR absorption for a proper IR probe wavelength, and will be used to determine the corresponding intervalley scattering time which is expected to be longer than the scattering time in bulk InP.

It has also been shown that hot carrier cooling rates in superlattice and quantum well structures vary with both well and barrier layer-thickness [13–15]. Therefore, the experiments will also be extended to several InP/GaInP samples with different well and barrier thicknesses to obtain the layer-thickness dependence of the real space involved-intervalley scattering times.

REFERENCES

[1] J. I. Pankove, "Optical processes in Semiconductors", Dover Publication Inc., New York, (1971).

[2] U. Schmid, F. Lukes, N.E. Christensen, M. Alouani and M. Cardona, Phys. Rev. Lett., 65 , 1933 (1990).

[3] S. Satpathy, R. M. Martin and C. G. Van de Walle, Phys. Rev., B38 , 13237 (1988).

[4] H. Okumura, K. Miki, S. Misawa, K. Sakamoto, T. Sakamoto, and S. Yoshoda, Japanese Journal of Appl. Phys., 28 , L 1893 (1989).

[6] H. Temkin, T. P. Pearsall, J. C. Bean, R. L. Logan, and S. Luryi, Appl. Phys. Lett., 48 , 963 (1986).

[7] J. C. Sturm, P. Pruenal, Y. M. Liu, H. Manoharan, Q. MI, P. V. Schwartz, and X. Xiao, IEEE Princeton Section Meeting, March, 1991.

[8] W. B. Wang, Kai Shum, R. R. Alfano, D. Szmyd, and A. J. Nozik, Phys. Rev. Lett. 68 , 662 (1992).

[9] W. B. Wang, R. R. Alfano, D. Szmyd, and A. J. Nozik, Phys. Rev. B46 , 15828, (1992).

[10] K. W. J. Barnham, and G. Duggan, J. Appl. Phys., 67 , 3490 (1990).

[11] B. K. Ridley, "Quantum Processes in Semiconductors", Oxford University Press., (1988), Ch.1.

[12] H. C. Casey, Jr. and M. B. Panish, "Heterostructure Lasers", Part A, Academic press. Inc., New York, (1978), Ch5.

[13] J. Feldmann, R. Sattman, E. O. Gobel, J. Nunnenkamp, J. Kuhl, J. Hebling, K. Ploog, R. Muralidharan, P. Dawson, and C. T. Foxon, Solid State Electron. 32 , 1713 (1989).

[14] K. Leo, W. W. Ruhle, and K. Ploog, Phys. Rev., B38 , 1947 (1988).

[15] A. J. Nozik, C. A. Parsons, D. J. Dunlary, B. M. Keyes, and R. K. Ahrenkiel, Solid State Comm., 75 , 297 (1990).

APPENDIX

```
c                de1.f

c       This is a program to solve numerically a series of
c       differental equations used to determine intervalley
c       scattering times by rate equation analysis

        character * 12 anam,lnam
        parameter(n1=2000)
        common/per/t23,t32,t33
        real tt(n1),yy(n1),zz(n1),t23,t32,t33
        print *, "the L to X scattering time t23"
        read *,t23
        print *, "the X to L scattering time t32"
        read *,t32
        print *, "the X1 to X2 scattering time t33"
        read *,t33
        print *, "name of output datafile for Nx1"
        read *,anam
        open (2, file=anam)
        print *,"name of output detafile for Nx2"
        read *,lnam
        open (3, file=lnam)

        call rk1id(nn,tt,yy,zz)
        do 20 i=1,1000
        write(2,*)tt(i),yy(i)
        write(3,*)tt(i),zz(i)
20      continue
        stop
        end

c       This subroutine is to give initial conditions
```

```
c       of the differential equations.
        subroutine rk1id(nn,tt,yy,zz)
        parameter(n1=4000)
        parameter(n=4)
        dimension tt(n1),yy(n1),zz(n1)
        dimension y(n),dy(n),b(n),c(n)
        y(1)=-4.98
        y(2)=0
        y(3)=0
        y(4)=0
        h=0.02
        n2=1
        call rk1(4,h,0,y,dy,b,c)
        tt(1)=y(1)
        yy(1)=y(3)
        zz(1)=y(4)
1       call rk1(4,h,1,y,dy,b,c)
        n2=n2+1
        tt(n2)=y(1)
        yy(n2)=y(3)
        zz(n2)=y(4)
        if(y(1).lt.25.0000001) go to 1
        nn=n2
        return
        end


c       This subroutine is to calculate the integratal
c       according to the Runge-Kutta formula(1) given
c       on I, P389.

        subroutine rk1(n,h,l,y,dy,b,c)
        dimension a(4),y(n),dy(n),b(n),c(n)
        a(1)=h/2
```

```
      a(2)=a(1)
      a(3)=h
      a(4)=h
      if(l) 2,2,4
2     do 3 i=1,n
3     b(i)=y(i)
      call dery(n,y,dy)
      return
4     do 5 k=1,3
      do 6 i=1,n
      c(i)=b(i)+a(k)*dy(i)
6     y(i)=y(i)+a(k+1)*dy(i)/3
5     call dery(n,c,dy)
      do 7 i=1,n
7     y(i)=y(i)+a(1)*dy(i)/3
      go to 2
      end

c     This subroutine is to give the
c     differential equations.
      subroutine dery(n,y,dy)
      dimension y(n),dy(n)
      common/per/t23,t32,t33
      dy(1)=1
      dy(2)=y(3)/t32-y(2)/t23+0.5*exp(-(y(1)/0.2)**2/2)/sqrt(6.28)/0.2
      dy(3)=y(2)/t23-y(3)/t32+0.5*exp(-(y(1)/0.2)**2/2)/sqrt(6.28)/0.2-y(3)/t33
      dy(4)=y(3)/t33
      return
      end
```

```
c               int1.f

c       This program is to do integral for any function
c       with fixed lower limit and variable upper limit
c       used to calculate the time evolution of the
c       population of hot electrons in the bottom of the X balley
        character * 8,lname
        external pn,simps

        print *, "name of output datafile "
        read *,lname
        open (2, file=lname)
        do 50 j=1,240
        t=-4.0+j*0.05
        tau1=simps(-4.0,t,j,pn)
        write (2,*) t, tau1
50      continue
        close (2,status="keep")
        stop
        end

        function pn(t)
        pn=exp(-t**2/0.25)
        return
        end

        FUNCTION SIMPS(A,B,N,F)
C       THE FUNCTION SIMPS USES N APPLICATIONS OF SIMPSON'S RULE
C       TO CALCULATE NUMERICALLY THE INTEGRAL OF F(X)*DX BETWEEN
C       INTEGRATION LIMITS A AND B.  SUMEND IS THE SUM OF ALL
c       F(X(I))FOR EVEN I (EXCEPT FOR F(X(2*N)) WHILE SUMMID IS
c       THE SUM OF ALL F(X(I)) FOR I ODD.  H IS THE STEPSIZE
c       BETWEEN ADJACENT X(I) AND TWOH IS THE LENGTH OF THE
c       INTERVAL OF INTEGRATION FOR EACH INDIVIDUAL APPLICATION
```

```
c       OF SIMPSON'S RULE.  K IS THE INTEATION COUNTER.
C
        ..... INITIALLIZE PARAMETERS .....
        TWOH=(B-A)/N
        H=TWOH/2.0
        SUMEND=0.
        SUMMID=0.
C
C       ..... EVALUATE SUMEND AND SUMMID .....
        DO 1 K=1,N
        X=A+FLOAT(K-1)*TWOH
        SUMEND=SUMEND+F(X)
        SUMMID=SUMMID+F(X+H)
1       CONTINUE
C
C       ..... RETURN ESTIMATED VALUE OF THE INTEGRAL .....
        SIMPS=(2.0*SUMEND+4.0*SUMMID-F(A)+F(B))*H/3.
        RETURN
C
        END
```

```
c                txT.f
c
c       This program txT.f is to calculate the t-x intervalley
c       scatting time as a function of lattice temperature where
c       x(i)---T, y(i)---tau(inter. scat. time. unit: ps)

        real x(500), u(500), v(500), y(500), D
        character * 12 anam
        print *, "name of output file"
        read *, anam
        print *,"input D"
        read *,D
        print *,"input n"
        read *,n
        open (1,file=anam)
        do 50 i=4,n
        x(i)=i*1
       u(i)=1/(exp(334/x(i))-1)
       v(i)=0.5667*(u(i)+1)+0.6155*u(i)
       y(i)=0.58/(D**2)/v(i)
50      continue
        do 100 i=4,n
        write (1,*) x(i),y(i)
100     continue
        end
```

```
c                txE.f
c
c       This program txE.f is to calculate the t-x intervalley
c       scatting time as a function of kinetic energy of
c       electrons where
c       x(i)---E, y(i)---tau (inter. scat. time. unit: ps)

        real x(500), u(500),y(500), D
        character * 12 anam
        print *,"name of output file"
        read *,anam
        print *,"input D"
        read *,D
        print *,"input n"
        read *,n
        open (1,file=anam)
        do 50 i=51,n
        x(i)=i*0.01
        u(i)=1.489*sqrt(x(i)-0.5088)+0.489*sqrt(x(i)-0.4512)
        y(i)=580/(D**2)/u(i)
50      continue
        do 100 i=51,n
        write (1,*) x(i),y(i)
100     continue
        end
```

```
c                ttT.f
c
c       This program is to calculate the
c       intravalley polar optical phonon scatting time as
c       a function of temperature of lattice
c       x(i)---T, y(i)---tau(intra. pol. opt.. phon. scat.)
c       z(i)---log tau
        real y(500),x(500),z(500)
        character * 12 onam
        print *, "name of output file"
        read *, onam
        print *,"please input n"
        read *,n
        open (1,file=onam)
        do 50 i=20,n
        x(i)=i
       y(i)=(1E-12)*0.894/((2/(exp(418/x(i))))+1)
       z(i)=log(y(i))/2.3
50      continue
        do 60 i=20,n
        write (1,*) x(i),y(i)
60      continue
        end
```

```
c                ttE.f
c
c       This program is to calculate the
c       intravalley polar optical phonon scatting time as
c       a function of kinetic energy of electrons
c       x(i)---E, y(i)---tau(intra. pol. opt.. phon. scat.)
c       z(i)---log tau
        real y(500),x(500),z(500)
        character * 12 onam
        print *, "name of output file"
        read *, onam
        print *,"please input n"
        read *,n
        open (1,file=onam)
        do 50 i=5,n
        x(i)=i*0.01
       y(i)=(1E-12)*(sqrt(x(i)))/1.66
       z(i)=log(y(i))/2.3
50      continue
        do 60 i=5,n
        write (1,*) x(i),y(i)
60      continue
        end
```

```
c              kshort.f
c
c       This program is to calculate K short(x)  in AlGaAs
c       using Casey, Wang, and Kuech's formula.
        character * 12 anam
        real n,m
        dimension x(100),a(100),y(100),t(100),z(100)

        print *, "input n"
        read *,n
        print *, "input m"
        read *,m
        print *," name of output datafile "
        read *,anam
        open (2, file=anam)
        do 50 i=1,60
        x(i)=0.01*i
        a(i)=(sqrt((0.85-0.14*x(i))/(1.477+0.043*x(i))))**3
        y(i)=(0.476-n*x(i)+m*(x(i)**2))/0.026
        t(i)=0.5303-a(i)*exp(-(y(i)))
        if (t(i).le.0) t(i)=0
        z(i)=1.054*t(i)
       write (2,*) x(i),z(i)
50      continue
        close (2)
        end
```

```
c              fcnl.f
c
c       This subroutine is used for main program of
c       taurosv.f for a fitting of calculated
c       direct and indirect transitions to fluorescence data of
c       Intensity versus wavelengths
        subroutine fcn(npar, g,f,x,iflag)
        implicit double precision ( a-h, o-z)
        character * 12 anam
        dimension a(100), b1(100), b(100), c(100), d(100), e1(100),
        dimension e(100), g(100),h(100), x(4), eya(100), u(100),
        demension v(100), y(100), z(100)
        go to (10,60,60,60,120) iflag

 10     print *, "name of experimental datafile"
        read  *, anam
 21     format (a10)
        open(1,file=anam)
        do 50 i=1,28
        read (1,*)h(i),c(i)
        d(i)=h(i)
       y(i)=c(i)
 50     continue
 60     do 62 i=1,28
        a(i)=1242.56/d(i)-2.067
        if (a(i).le.0) a(i)=0
       b1(i)=1242.56/d(i)+x(4)-2.04
       if (b1(i).le.0) b1(i)=0
        b(i)=0.542*((b1(i))**2)
       e1(i)=1242.56/d(i)+x(4)-2.094
        if (e1(i).le.0) e1(i)=0
        e(i)=1.542*((e1(i))**2)
        g(i)=2.067-1242.56/d(i)
        if (g(i).eq.0) g(i)=0.0001
```

```
62    continue
64    do 65 i=1,28
      u(i)=0
      v(i)=0
66    do 68 k=1,28
     dent=x(2)/3.1416/((1242.56/d(k)-1242.56/d(i))**2+x(2)**2)
     u(i)=u(i)+4*x(1)*sqrt(a(k))*dent/d(k)
     bdent=x(3)/3.1416/((1242.56/d(k)-1242.56/d(i))**2+x(3)**2)
     v(i)=v(i)+4*x(1)*0.000305*(b(k)+e(k))*bdent/(g(k)**2)/d(k)
68    continue
      z(i)=u(i)+v(i)
65    continue
      f=0.0
      do 70 i=1,28
      if(y(i).lt.1.0e-10) go to 75
     eya(i)=(z(i)-y(i))
      f=f+(y(i)-z(i))**2
70    continue
75    if (iflag.ne.3) return
120   open(2,file="flueya.dat")
      open(3,file="fluy.dat")
      open(4,file="fluz.dat")
      write (2,*) x(1),x(2),x(3),x(4)
      do 500 i=1,28
      write(2,*)d(i),eya(i)
      write(3,*)d(i),y(i)
      write(4,*)d(i),z(i)
500   continue
      end
```

LIST OF PUBLICATIONS

[1] W. B. Wang, Kai Shum, A. A. Alfano, D. Szmyd, and A. J. Nozik, "L_6-X_6 Intervalley Scattering Time and Deformation Potential for $Al_{0.6}Ga_{0.4}As$ Determined by Femtosecond Time-Resolved Infrared Absorption Spectroscopy", Phys. Rev. Lett., 68 , 664 (1992).

[2] Kai Shum, W. B. Wang, R. R. Alfano, and K. M. Jones, "Observation of the 1P Excitonic State in Cd(S, Se)-Glass Quantum Dots", Phys. Rev. Lett., 68 , 3904 (1992).

[3] W. B. Wang, R. R. Alfano, D. Szmyd, and A. J. Nozik, " "Determination of the Critical value of x_c for the Direct-to-Indirect Band-gap Transition in $Al_xGa_{1-x}As$ by Measuring Hot-carrier Dynamics in the X Valley", Phys. Rev., B46 , 15828 (1992).

[4] W. B. Wang, N. Ockman, M. Yan, and R. R. Alfano, "Determination of X_6 Valley Hot Electron Dynamics and the Intervalley $X_6 \rightarrow \Gamma_6$ Scattering Time in GaAs", J. of Lumin., 50 , 347 (1992).

[5] W. B. Wang, Kai Shum, A. A. Alfano, D. Szmyd, and A. J. Nozik, "Investigation of the L_6-X_6 Intervalley Scattering in $Al_{0.6}Ga_{0.4}As$ by Measuring Hot Carrier Dynamics in a $K \neq 0$ Satellite Valley", Semicond. Sci. Techno., 7 , B173 (1992).

[6] W. B. Wang, R. R. Alfano, D. Szmyd, and A. J. Nozik, "Effect of Al Mole Fraction on Decay Profile of Photoinduced IR Absorption in $Al_xGa_{1-x}As$", invited paper, SPIE, 1677 , 85 (1992).

[7] N. Ockman, W. B. Wang, and R. R. Alfano, "Ultrafast Laser Spectroscopy for Characterizing Semiconductors", Modern Phys., B5 , 3165 (1991).

[8] W. B. Wang, Kai Shum, A. A. Alfano, D. Szmyd, and A. J. Nozik, "Hot Carrier Dynamics in a K≠0 Satellite Valley in $Al_xGa_{1-x}As$", SPIE, 1599 , 106 (1991).

[9] S. K. Gayen, W. B. Wang, V. Petricevic, S. G. Demos, and R. R. Alfano, "Nonradiative Transition Dynamics in Emerald", J. of Lumin., 47 , 181 (1991).

[10] W. B. Wang, N. Ockman, M. A. Cavicchia, and R. R. Alfano, "The Density of States Effective Mass and the Energy Minimum of the X_7 Conduction Band in GaAs Determined from the $X_6 \rightarrow X_7$ Absorption Spectrum", Appl. Phys. Lett., 57 , 395 (1990).

[11] W. B. Wang, N. Ockman, M. A. Cavicchia, M. Yan, and R. R. Alfano, "Ultrafast Pump-Probe X-Valley Absorption Spectroscopy in GaAs", in "Ultrafast Phenomena VII", Edited by C. B. Harris, E. P. Ippen, G. A. Mourou, and A. H. Zewail, (Springer-Verlag, New York, 1990), P 309.

[12] W. B. Wang, N. Ockman, M. A. Cavicchia, M. Yan, and R. R. Alfano, "Determination of the Back Intervalley Scattering Time from the X Valley and the Density of States Effective Mass of the X_7 Band in GaAs by Picosecond Time-Resolved Absorption Spectroscopy", invited paper, SPIE, 1282 , 86 (1990).

[13] W. B. Wang, N. Ockman, M. Yan, and R. R. Alfano, "Intervalley $X_6 \rightarrow \Gamma_6, L_6$ Scattering Time in GaAs Measured by Pump-IR-Probe Absorption Spectroscopy", Solid States Electronics, 32 , 1337 (1989).

[14] N. Ockman, R. Dorsinville, W. B. Wang, and R. R. Alfano, "Time-Resolved picosecond Infrared Absorption Induced by High-Density photogenerated Carrier in Ge and CdSe", IEEE J. Quantum Electron, QE-23 , 2008 (1987).

[15] S. K. Gayen, W. B. Wang, V. Petricevic, K. M. Yoo, and R. R. Alfano, "Picosecond Excite-and-Probe Absorption Measurement of Intra-$^2E_g E_{32}$-State Vibrational Relaxation Time in $Ti^{3+}:Al_2O_3$", Appl. Phys. Lett., 50 , 1494 (1987).

[16] S. K. Gayen, W. B. Wang, V. Petricevic, and R. R. Alfano, "Nonradiative Transition Dynamics in Alexandrite ", Appl. Phys. Lett., 49 , 437 (1986).

[17] S. K. Gayen, W. B. Wang, V. Petricevic, and R. R. Alfano, " onradiative Relaxation in Tunable Solid State Laser Crystals", in the Proceedings of the International Conference on Lasers, '85,

Edited by C. P. Wang (STS Press, Mcleam, VA, 1986), P 622.

[18] S. K. Gayen, W. B. Wang, V. Petricevic, and R. R. Alfano, "Picosecond Time-Resolved Studies of Nonradiative Relaxation in Ruby and Alexandrite", in the Proceedings of the First International Laser Science Conference, Edited by W. C. Stwalley and M. Lapp, (American Institute of Physics, 1986), P 206.

[19] S. K. Gayen, W. B. Wang, V. Petricevic, R. Dorsinville, and R. R. Alfano, "Picosecond Excite-and-Probe Absorption Measurement of the $^4T_2$-State Nonradiative Lifetime in Ruby", Appl. Phys. Lett., 47 , 455 (1985).

[20] H. J. Zarrabi, W. B. Wang, and R. R. Alfano, "Time-Resolved Kinetics of e-h Plasma in GaAsP under Intense Picosecond Laser Pulse Excitation", Appl. Phys. Lett., 46 , 513 (1985).

[21] W. B. Wang, Y. Takiguchi, and R. R. Alfano, "Temperature Dependence of the Intervalley Scattering Time in GaAs", submitted for publication.

[22] W. B. Wang, N. Ockman, A. A. Alfano, "Determination of the X-L Intervalley Deformation Potential in Si by Femtosecond Pump-Probe Infrared Absorption Spectroscopy", to be submitted for publication.

BIBLIOGRAPHY

Adachi, S., J. Appl. Phys., 58 , R1 (1985).

Alfano, R. R., and S. L. Shapiro, Phys. Rev. Lett., 29 , 1655 (1972).

Aspnes, D. E., Phys. Rev, B14 , 5331 (1976).

Aspnes, D. E., C. G. Olson, and D. W. Lynch, Phys. Rev. Lett., 378 , 766 (1976).

Aspnes, D. E., and A. A. Studna, Phys. Rev. B7 , 4605 (1973).

Barnham, K. W. J., and G. Duggan, J. Appl. Phys., 67 , 3490 (1990).

Becker, P. C., H. L. Fragnito, C. H. Brito Cruz, J. Shah, R. J. Fork, J. E. Cunningham, J. E. Henry, and C. V. Shank, Appl. Phys. Lett., 53 , 2089 (1988).

Berthold, K., A.F.J.Levi, J. Walker, and R. J. Malik, Appl. Phys. Lett, 54 , 813 (1989).

Birman, J. L., Phys. Rev., 131 , 1489 (1963).

Birman, J. L., M. Lax and R. London, Phys. Rev., 145 , 620 (1966).

Blakemore, J. S., J. Appl. Phys., 53 , R123 (1982).

Braunstein, R., and L. Magid, Phys. Rev., 111 , 480 (1958).

Casey, H. C., Jr., J. Appl. Phys., 49 , 3684 (1978).

Casey, H. C., Jr, and M. B. Ponish, " Heterostructure lasers", Part A,

Academic Press. Inc., New York, 1978, Ch.5.

Conwell, E. M., in "High Field Transport in Semiconductors", Academic Press, New York, (1967), Ch.3 & 5.

Conwell, E. M., and M. O. Vassell, IEEE Trans. Electron. Devices, ED-13 , 22 (1966).

Doukas, A. G., J. Buchert, and R. R. Alfano, in "Biological Events Probed by Ultrafast Laser Spectroscopy," edited by R. R. Alfano, Academic Press, New York, (1982), Ch.17.

Delfyett, P.J., S. K. Gayen, and R. R. Alfano, "Encyclopedia of Physical Science and Technology", 14 , Academic Press. Inc. 169, (1987).

Ehrenreich, H., Phys. Rev., 120 , 1951 (1960).

Ehrenreich, H., H. R. Philipp, and J. C. Philips, Phys. Rev. Letts, 8 , 59 (1962).

Feldmann, J., R. Sattman, E. O. Gobel, J. Nunnenkamp, J. Kuhl, J. Hebling, K. Ploog, R. Muralidharan, P. Dawson, and C. T. Foxon, Solid State Electron. 32 , 1713 (1989).

Gayen, S. K., W. B. Wang, V. Petricevic, R. Dorsinville, and R. R. Alfano, Appl. Phys. Lett., 47 , 455 (1985).

Gayen, S. K., W. B. Wang, V. Petricevic, K. M. Yoo, and

R. R. Alfano, Appl. Phys. Lett. 50 , 1494 (1987).

Greenaway, D. L., Phys. Rev. Lett. 9 , 97 (1962).

Gunn, J. B., Solid State Commun., 1 , 88 (1963).

James, L. W., R. C. Eden, J. L. Moll, and W. E. Spicer, Phys. Rev. 174 , 909 (1968).

Jedju, T. M., and L. Rothberg, Appl. Optics, 27 , 615 (1988).

Jedju, T. M., and L. Rothberg, Appl. Optics, 26 , 2877 (1988).

Kalt, H., W. W. Ruhle, K. Reimann, M. Rinker, and E. Bauser, Phys. Rev., B43 , 12364 (1991-II).

Kann, M. J., A. M. Kriman, and D. K. Ferry, Phys. Rev., B41 , 12659 (1990).

Kash, J. A., J. C. Tsang, and J. M. Hvam, Phys. Rev. Lett., 54 , 2151 (1985).

Katz, A., and R. R. Alfano, Appl. Phys. Lett., 53 , 1065 (1988).

Kuech, T. F., D. J. Wolford, R. Potemski, J. A. Bradley, and K. H. Kelleher, App. Phys. Lett., 57 , 505 (1987).

Laubereau, A., L. Greiter, and W. Kaiser, Appl. Phys. Lett., 25 , 87 (1974).

Lee, H. J., L. Y. Juravel, and J. C. Woolley, Phys. Rev., B21 , 659 (1980).

Leheny, R. F., J. Shah, R. L. Fork, C. V. Shank, and A. Migus, Solid State Commun., 31 , 809 (1979).

Leo, K., W. W. Ruhle, and K. Ploog, Phys. Rev., B38 , 1947 (1988).

Lin, W. Z., M. J. LaGasse, R. W. Schoenlein, B. Zysset, and J. G. Fujimoto, SPIE, 942 , (March, 1988).

Mendez, E. E., E. Calleja, and W. I. Wang, Phys. Rev., B34 , 6026 (1986).

Mirlin, D. N., I. Ya. Karlik, and V. F. Sapega, Solid State Commun., 65 , 171 (1988).

Monemore, B., K. K. Shih, and G. D. Pettit, J. Appl. Phys., 47 , 2604 (1976).

Nichols, K. H., C. M. L. Yee, and C. M. Wolfe, Solid State Electron, 23 , 109 (1980).

Nozik, A. J., C. A. Parsons, D. J. Dunlary, B. M. Keyes, and R. K. Ahrenkiel, Solid State Comm., 75 , 297 (1990).

Oberli, D. Y., J. Shah, and T. C. Daman, Phys. Rev., B40 , 1323 (1989-I).

Ockman, N., R. Dorsinville, W. B. Wang, and R. R. Alfano, IEEE Quantum Electron, QE-23 , 2008 (1987).

Ockman, N., W. B. Wang, and R. R. Alfano, Internat. J. Modern

Physics, B5 , 3165 (1992).

Okumura, H., K. Miki, S. Misawa, K. Sakamoto, T. Sakamoto, and S. Yoshoda, Japanese Journal of Appl. Phys., 28 , L 1893 (1989).

Osman, M. A., and D. K. Ferry, Phys. Rev. B36 , 6018 (1987).

Pankove, J. I., "Optical processes in Semiconductors", Dover Publication Inc., New York, (1971).

Paul, W., J. Appl. Phys, 32 , 2082 (1961).

Pikhtin, A. N., Sov. Phys. Semicond., 11 , 245 (1977).

Pitt, G. D., and J. Lees, Phys. Rev. B2 , 4144 (1970).

Reggiani, L., in " Hot-Electron Transport in Semiconductors ", edited by L. Reggiani, Springer-Verlag, New York, (1984), ch.2.

Ridley, B. K., "Quantum Processes in Semiconductors", the Second Edition, Oxford Science Publications, Oxford, 1988, Ch.1 & 3.

Ruhle, W. W., K. Leo, and E. Bauser, Phys. Rev., B40 , 1756 (1989).

Satpathy, S., R. M. Martin and C. G. Van de Walle, Phys. Rev., B38 , 13237 (1988).

Schiller, N. H., in "Semiconductors Probed by Ultrafast Laser Spectroscopy, Vol.II, edited by R. R. Alfano, Academic Press., (1984).

Schmid, U., F. Lukes, N.E. Christensen, M. Alouani and M. Cardona, Phys. Rev. Lett., 65 , 1933 (1990).

Schoenlein, R. W., W. Z. Lin, E. P. Ippen, and J. G. Fujimoto, Appl. Phys. Lett., 51 , 1442 (1987).

Seeger, K., "Semiconductor Physics", Springer-Verlag, Vienna, 1973, Ch. 6 & 7.

Seymour, R. J., M. R. Junnarkar, and R. R. Alfano, Solid State Commun, 41 , 657 (1982).

Shah, J., B. I. Miller, and A. E. DiGiovanni, J. Appl. Phys, 43 , 3434 (1972).

Shah, J., B. Deveaud, T. C. Damen, and W. T. Tsang, A. C. Gossard, and P. Lugli, Phys. Rev. Lett., 59 , 2222 (1987).

Shum, Kai, W. B. Wang, R. R. Alfano, D. Szmyd, and A. J. Nozik, Phys. Rev. Lett., 68 , 3904 (1992).

Sizer, T., J. D. Kafka, I. N. Duling, C. W. Gabel, and G. A. Mourou. IEEE, QE-19, , 506 (1983).

Sturm, J. C., P. Pruenal, Y. M. Liu, H. Manoharan, Q. MI, P. V. Schwartz, and X. Xiao, IEEE Princeton Section Meeting, March, 1991.

Tanaka, S., H. Kobayashi, H. Saito, and S. Shionoya, Solid State

Commun., 33 , 167 (1980).

Temkin, H., T. P. Pearsall, J. C. Bean, R. L. Logan, and S. Luryi, Appl. Phys. Lett., 48 , 963 (1986).

Thompson, A. G., M. Cardona, K. L. Shaklee, and J. C. Woolley, Phys. Rev. 146 , 601 (1966).

Tsang, J. C., and J. A. Kash, Phys. Rev., B34 , 6003 (1986).

Ulbrich, R. G., J. A. Kash, and J. C. Tsang, Phys. Rev. Lett., 62 , 949 (1989).

Wang, W. B., R. R. Alfano, D. Szmyd, and A. J. Nozik, Phys. Rev. B46 , 15828, (1992).

Wang, W. B., N. Ockman, M. A. Cavicchia, and R. R. Alfano, Appl. Phys. Lett., 57 , 395 (1990).

Wang, W. B., N. Ockman, M. A. Cavicchia, M. Yan, and R. R. Alfano, SPIE, 1282 , 86 (1990).

Wang, W. B., N. Ockman, M. Yan, and R. R. Alfano, Solid State Electron., 32 , 1337 (1989).

Wang, W, B., N. Ockman, M. Yan, and R. R. Alfano, J. of Lumin., 50 , 347 (1992).

Wang, W. B., Kai Shum, R. R. Alfano, D. Szmyd, and A. J. Nozik, Phys. Rev. Lett., 68 , 662 (1992).

Wang, W. B., K. Tokiguchi, and R. R. Alfano, submitted for publication.

Wise, F. W., I. A. Walmsley, and C. L. Tang, Appl. Phys. Lett., 51 , 605 (1986).

Yariv, A., in "Quantum Electronics", John Wiley*Sons Inc., New York, (1975), ch.10.

Yariv, A., "Optical Electronics", third edition, CBS College Publisher, The Dryden Press., (1985).

Yoffa, E. J., Phys. Rev., B23 , 1909 (1981).

Zarem, H. A., J. A. Lebens, K. B. Nordstrom, P. C. Sercel, S. Sanders, L. E. Eng, A. Yariv, and K. J. Vahala, Appl. Phys. Lett., 55 , 2622 (1989).

Zollner, S., S. Gopalan, and M. Cardona, Appl. Phys. Lett., 54 , 614 (1989).

Zollner, S., S. Gopalan, and M. Cardona, SPIE, 1677 , 614 (1990).